

STRUCTURE AND COMPOSITION OF THE SUBCONTINENTAL LITHOSPHERIC MANTLE IN CONVERGENT SETTINGS

*INSIGHTS FROM MANTLE XENOLITHS
HOSTED IN ALKALINE MAGMATISM*

ZOLTÁN KONC



UGR

Universidad
de Granada

Tesis Doctoral 2013

Editor: Editorial de la Universidad de Granada
Autor: Zoltán Konk
D.L.: GR 1910-2013
ISBN: 978-84-9028-615-9



Instituto Andaluz de Ciencias de la Tierra

Universidad de Granada
&
Consejo Superior de Investigaciones Científicas



**STRUCTURE AND COMPOSITION OF THE SUBCONTINENTAL
LITHOSPHERIC MANTLE IN CONVERGENT SETTING:**

INSIGHTS FROM MANTLE XENOLITHS HOSTED IN ALKALINE MAGMATISM

ZOLTÁN KONC

Ph. D. Thesis • Tesis Doctoral • Doktori értekezés

*Memoria de Tesis Doctoral presentada por el Licenciado en Geología
D. Zoltán Konc para optar al Grado de Doctoral por la Universidad de Granada*

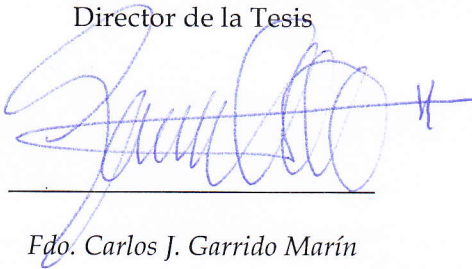
*Esta Tesis Doctoral ha sido dirigida por el Dr. Carlos Jesús Garrido Marín, Científico Titular del
CSIC, Instituto Andaluz de Ciencias de la Tierra (CSIC-UGR)*

1 de marzo de 2013
Granada, Spain

El doctorando Zoltán Konc y el director de la tesis Carlos J. Garrido garantizamos, al firmar esta tesis doctoral, que el trabajo ha sido realizado por el doctorando bajo la dirección de los directores de la tesis y hasta donde nuestro conocimiento alcanza, en la realización del trabajo, se han respetado los derechos de otros autores a ser citados, cuando se han utilizado sus resultados o publicaciones.

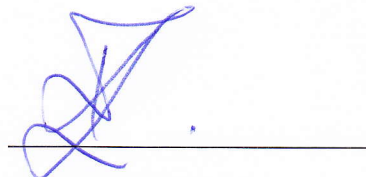
Granada, 1 de marzo de 2013

Director de la Tesis



Fdo. Carlos J. Garrido Marín

Doctorando



Fdo. Zoltán Konc

OMNIA MEA MECUM PORTO

Szüleimnek • To my Parents • A mis Padres

Abstract

Convergent – destructive – margins – where two plates converge forming either subduction or continental collision zones – are one of the main tectonic scenarios along plate boundaries. Despite the enormous success of the plate tectonic theory in modern Earth sciences, essential questions still remain open concerning the evolution of continents in convergent settings and their role in the dynamics of the Earth's lithospheric mantle. The subcontinental lithospheric mantle (SCLM) is the part of the lithosphere below the crust up to asthenospheric depths. Small samples of this region – known as mantle xenoliths – can be entrained by volcanic rocks and provide direct sample of the SCLM from different tectonic settings such as intracontinental rifts and – less commonly – convergent settings. Thus, mantle xenoliths afford a unique opportunity to investigate petrology, structure and chemical composition of the SCLM.

The originality of this work relies on the multidisciplinary study of two mantle xenolith occurrences in convergent settings: the Sangilen Plateau of Tuva in Siberia and the SE Iberian Volcanic Province in South East Spain. The Tuva and SE Iberian Volcanic Province xenoliths give insight into ancient Ordovician and Neogene SCLM in different convergent geodynamic settings, respectively.

In this thesis I studied mantle xenoliths hosted in alkaline rocks produced during the latest stages of orogenic convergence, thereby providing a snapshot of the deformation, melting and metasomatism in these settings. I combined detailed petrological and petrostructural characterization of mantle xenoliths with geochemical characterization including bulk and mineral major, trace element, Sr-Nd-Pb radiogenic isotope and in situ Re-Os isotope analyses. These data are combined and mined to unveil the thermal, petrostructural and seismic characteristic of the SCLM beneath these regions, as well as used to identify the age and inheritance of melting events, melt-rock reaction and metasomatic processes involved in the compositional modification of the SCLM in convergent settings.

Key Words: *Subcontinental lithospheric mantle, mantle xenoliths, Tuva, Betic-Rif Cordillera, SE Iberian Volcanic Province, Eastern Betic, convergent setting, subduction, petrology, deformation, geochemistry, EBSD-textural analysis, Sr-Pb-Nd isotopes, trace elements.*

Resumen

Los contextos geodinámicos convergentes y destructivos, donde dos placas litosféricas convergen generando zonas de subducciones y/o colisión continental, constituyen uno de los principales contextos tectónicos de la tectónica de placas terrestre. A pesar del enorme éxito que la teoría de la tectónica de placas ha tenido en Ciencias de la Tierra para explicar estos procesos tectónicos, aún quedan por esclarecer cuestiones esenciales sobre la evolución de las raíces litosféricas de los continentes y el papel del manto litosférico en la dinámica y evolución tectono-magmática de los márgenes convergentes. El manto litosférico subcontinental (MLSC) es la parte de la litosfera continental que se encuentra entre la corteza y la astenosfera. Esta porción del manto aparece muestreada como pequeñas rocas - conocidas como enclaves mantélicos- englobadas por los magmas durante su ascenso por la litosfera y luego expuestas a la superficie terrestre durante las erupciones volcánicas. Estos enclaves mantélicos constituyen muestras directas del manto en diferentes contextos geodinámicos, como zonas extensionales intracontinentales y, en menor medida, márgenes convergentes. Los enclaves mantélicos representan, por tanto, una oportunidad única para investigar la naturaleza y procesos que ocurren en el MLSC desde el punto de vista petrológico, petrofísico y geoquímico.

La originalidad de esta tesis se debe a su enfoque multidisciplinar sobre los enclaves mantélicos en dos márgenes convergentes: el plateau de Sangilen en la región de Tuva (Siberia) y la Provincia Volcánica del Sureste de España, que se formaron a lo largo de 440 millones de años. Los enclaves de Tuva y del Sureste de España proporcionan información respectivamente sobre el MLSC Ordovícico y Neógeno en un contexto geodinámico convergente.

En esta tesis se han estudiado enclaves mantélicos muestreados por lavas alcalinas producidas durante las últimas etapas magmáticas en un contexto convergente, y que por lo tanto constituyen un registro de la deformación, fusión parcial y metasomatismo en el manto durante este estadio. Se han combinado una detallada caracterización petrológica y petro-estructural de los enclaves mantélicos con su estudio geoquímico, incluyendo elementos mayores, elementos en traza e isótopos radiogénicos de Sr-Nd-Pb en minerales y roca total y análisis minerales in situ del sistema Re-Os. Estos datos se han interpretado para describir las características térmicas, petro-estructurales y sísmicas del MLSC por debajo de estas regiones, así como para identificar la edad y la impronta de los eventos de fusión parcial, de

reacción fundido-roca y de los procesos metasomáticos que han afectado el MLSC en estos contextos.

Palabras Clave: *Manto litosférico subcontinental, enclaves mantélicos, Tuva, Cordillera Bético-Rifeña, Provincia Volcánica del Sureste de España, Cordillera Bética Oriental, contexto convergente, subducción, petrología, deformación, geoquímica, análisis microestructural por EBSD, isotopos radiogénicos de Sr-Nd-Pb-Os, elementos en traza*

Acknowledgements

I am grateful to:

- ☞ my demanding supervisor, **CARLOS J. GARRIDO** (*Instituto Andaluz de Ciencias de la Tierra, CSIC-UGR, Spain*), and my tutors, especially **DELPHINE BOSCH** and **ANDREA TOMMASI** (*Géoscience Montpellier, UM2, France*), **CSABA SZABÓ** (*Lithosphere Fluid Research Lab, ELTE, Hungary*), **FERNANDO GERVILLA** (*Universidad de Granada, Spain*), **JEAN-LOUIS BODINIER** (*Géoscience Montpellier, UM2, France*) for their help, patience, constructive criticism and all the fruitful discussions and ideas that we shared; **VICTOR V. SHARYGIN** (*V.S. Sobolev Institute of Geology and Mineralogy, SB RAS, Russia*) for the availability of the Tuva mantle rock samples, as well as his help;
- ☞ the members of the Ph.D. dissertation examining committee: **ALAIN VAUCHEZ**, **DELPHINE BOSCH** (*Géoscience Montpellier, UM2, France*), **FERNANDO GERVILLA**, **GUILLERMO BOOTH-REA** (*Universidad de Granada, Spain*), **CSABA SZABÓ** (*Lithosphere Fluid Research Lab, ELTE, Hungary*), **VICENTE LÓPEZ SÁNCHEZ-VIZCAÍNO** (*Universidad de Jaen, Spain*), **JOAQUÍN PROENZA** (*Universidad de Barcelona, Spain*), and **ANTONIO GARCÍA-CASCO** (*Universidad de Granada, Spain*);
- ☞ the following people, who helped us during sample preparations and analytical runs: **MARIA ROSARIO REYES GONZÁLEZ** (*Instituto Andaluz de Ciencias de la Tierra, CSIC-UGR, Spain*) in thin-section preparation; **MIGUEL ANGEL HIDALGO LAGUNA** (*Centro de Instrumentación Científica, UGR, Spain*), **CLAUDE MERLET** (*Sciences et Techniques du Languedoc, UM2, France*) and **KÁROLY HIDAS** (*Instituto Andaluz de Ciencias de la Tierra, CSIC-UGR, Spain*) in EMPA analysis; **OLIVIER BRUGUIER**, **OLIVIER ALARD** (*Géoscience Montpellier, UM2, France*) and **KÁROLY HIDAS** (*Instituto Andaluz de Ciencias de la Tierra, CSIC-UGR, Spain*) in LA-ICP-MS analysis; **ANDREA TOMMASI**, **ALAIN VAUCHEZ**, **FABRICE BAROU** (*Géoscience Montpellier, UM2, France*), **LUIZ FERNANDO GRAFULHA MORALES** (*Helmholtz Centre Potsdam, GFZ, Germany*) and **JOSÉ ALBERTO PADRÓN-NAVARTA** (*Research School of Earth Sciences, ANU, Australia & Géoscience Montpellier, UM2, France*) in EBSD analysis; **ISABEL SÁNCHEZ ALMAZO** (*Centro de Instrumentación Científica, UGR, Spain*) and **KÁROLY HIDAS** (*Instituto Andaluz de Ciencias de la Tierra, CSIC-UGR, Spain*) in SEM imaging; **MARIA ISABEL MORENO VIDA** (*Centro de Instrumentación Científica, UGR, Spain*) and **CLAUDIO MARCHESI** (*Instituto Andaluz de Ciencias de la Tierra, CSIC-UGR, Spain*) in whole rock - major (XRF) and trace element

(ICP-MS) – analyses; Delphine Bosch, **BÉATRICE GALLAND** (*Géoscience Montpellier, UM2, France*), **PROF. WILLIAM L. GRIFFIN**, **JOSÉ MARÍA GONZÁLEZ-JIMÉNEZ** (*GEMOC, Macquarie University, Australia*), **PATRICK VERDOUX** (*Centre Universitaire de Formation et de Recherche de Nîmes, UNIMES, France*), **PHILIPPE TELOUK** (*l'ENS de Lyon, France*) and **BRUNO DHUIME** (*School of Earth Sciences, University of Bristol, UK*) in radiogenic isotope (MC-ICP-MS, MC-TIMS) analyses... **and many other people** who accidentally have left out from this list (*sorry*);

- ☞ **the former and present members of the Instituto Andaluz de la Ciencias de la Tierra and the Faculty of Science of the University of Granada (Spain)**, especially **AMEL BARICH**, **MARIA ISABEL VARAS**, **ERWIN FRETS**, **KÁROLY HIDAS** and **CLAUDIO MARCHESI** – *members of the Granada Dream Team* –, **JOSÉ ALBERTO PADRÓN-NAVARTA**, **ANTONIO ACOSTA VIGIL**, **VANESA NIETO**, **GIORDANA GENNARI**, **AITOR CAMBESES** and members of the Marine Geology Group; **of the Géoscience Montpellier of the University Montpellier 2 (France)**, especially **KATE HIGGIE**, **ROBERTO AGRUSTA**, **VINCENT SOUSTELLE**; **of the Lithosphere Fluid Research Lab (ELTE, Hungary)**, especially **ZSANETT PINTÉR**, **ÁKOS BOROS**;
- ☞ **the Crystal2Plate community** for their constructive ideas;
- ☞ **the secretary of the Instituto Andaluz de Ciencias de la Tierra (CSIC-UGR, Spain)** for their help in every administrative work;
- ☞ **everybody that I meet during field trips, short courses, scholarships and my study at IACT and Géoscience Montpellier**;
- ☞ **my girlfriend ANDI and my friends** living in Hungary, Spain and all around the world.

At last, but not least **special thanks go out to My Parents (GABRIELLA and ZOLTÁN)** for their enthusiasm, support, patience, love and every little care with which they helped me when I needed.

Zoltán Konc

February of 2013

We acknowledge funding from the “Ministerio de Economía y Competitividad” (Grant CGL2010-14848), the “Junta de Andalucía” (research group RNM-131 and grant 2009RNM4495), the International Lithosphere Program (ILP) (CC4-MEDYNA), and the Joint Research of the Russian Academy of Sciences and the Hungarian Academy of Sciences (project #55 to C. Szabó). Z. Konc's Ph.D research is supported by a CSIC JAE-PreDoc fellowship (2008JAEP033) funded by the European Social Fund. This research has benefited from other grants and fellowships funded by the European Fund for Regional Development.

Table of Contents

| | |
|--|------------|
| RESUMEN EXTENDIDO | 3 |
| EL MSCL DE ORÓGENOS COLISIONALES EN ZONAS CIRCUMCRATÓNICAS | 3 |
| EL MSCL EN CONTEXTOS DE SUPRA-SUBDUCCIÓN Y DELAMINACIÓN CONTINENTAL | 4 |
| PART I | 9 |
| 1. INTRODUCTION | 11 |
| 1.1. LITHOSPHERIC PLATES | 11 |
| 1.2. THE SUBCONTINENTAL LITHOSPHERIC MANTLE (SCLM) | 13 |
| 1.3. THE PETROLOGICAL COMPOSITION AND STRUCTURE OF THE SCLM | 14 |
| 1.4. THE COMPOSITION OF THE SCLM | 17 |
| 1.5. THERMAL STRUCTURE AND TEXTURE OF THE SCLM AS DERIVED FROM MANTLE XENOLITH STUDIES | 21 |
| 1.6. MANTLE XENOLITH AS PROBE OF THE SCLM: TYPES AND OCCURRENCES | 23 |
| 1.7. MODIFICATION OF THE SCLM MANTLE BENEATH CONVERGENT SETTINGS: CASES OF STUDY | 24 |
| 2. AIMS AND STRUCTURE OF THE THESIS | 31 |
| 2.1. AIMS OF THE THESIS | 31 |
| 2.2. OUTLINE OF THE THESIS | 31 |
| 3. METHODOLOGY | 35 |
| 3.1. SAMPLING AND SAMPLE PREPARATION | 35 |
| 3.2. ELECTRON PROBE MICROANALYSES (EPMA) | 37 |
| 3.3. LASER ABLATION INDUCTIVELY COUPLED PLASMA MASS SPECTROMETER (LA-ICP-MS) | 39 |
| 3.4. SCANNING ELECTRON MICROSCOPY (SEM) | 40 |
| 3.5. ELECTRON BACKSCATTERED DIFFRACTION (EBSD-SEM) | 42 |
| 3.6. X-RAY FLUORESCENCE (XRF) | 46 |
| 3.7. INDUCTIVELY COUPLED PLASMA MASS SPECTROMETER (ICP-MS) | 47 |
| 3.8. ANALYSES OF RADIOGENIC ISOTOPES BY MASS SPECTROMETRY (MC-ICP-MS & TIMS) | 47 |
| PART II | 55 |
| 4. STRUCTURE AND COMPOSITION OF THE SUBCONTINENTAL LITHOSPHERIC MANTLE BENEATH THE SANGILEN PLATEAU (TUVA, SOUTHERN SIBERIA, RUSSIA): EVIDENCE FROM LAMPROPHYRE-HOSTED SPINEL PERIDOTITE XENOLITHS | 57 |
| 4.1. INTRODUCTION | 59 |
| 4.2. SAMPLING AND PETROGRAPHY | 59 |
| 4.3. MINERAL CHEMISTRY | 61 |
| 4.4. DISCUSSION | 64 |
| 4.5. CONCLUSION | 73 |
| 5. DEFORMATION RECORD, SEISMIC PROPERTIES AND FLOW OF THE SHALLOW UPPER MANTLE IN THE WESTERNMOST MEDITERRANEAN: INSIGHTS FROM MANTLE XENOLITHS IN PLIO-PLEISTOCENE ALKALI BASALTS FROM THE EASTERN BETIC CORDILLERA (SE SPAIN) | 75 |
| 5.1. INTRODUCTION | 77 |
| 5.2. SAMPLING AND SAMPLE PREPARATION | 78 |
| 5.3. MINERAL CHEMISTRY | 80 |
| 5.4. LITHOLOGY AND TEXTURE | 80 |
| 5.5. GEOTHERMOMETRY | 84 |
| 5.6. CRYSTAL PREFERRED ORIENTATION | 85 |
| 5.7. SEISMIC PROPERTIES | 91 |
| 5.8. DISCUSSION | 94 |
| 5.9. CONCLUSION | 113 |
| 6. ISOTOPIC AND GEOCHEMICAL COMPOSITION OF THE SUBCONTINENTAL LITHOSPHERIC MANTLE IN THE WESTERNMOST MEDITERRANEAN: CONSTRAINTS FROM PERIDOTITE XENOLITHS IN PLIO-PLEISTOCENE ALKALI BASALTS (EASTERN BETIC CORDILLERA, SE SPAIN) | 115 |
| 6.1. INTRODUCTION | 117 |

| | |
|---|------------|
| 6.2. SAMPLING, LITHOLOGY AND TEXTURE OF EASTERN BETICS XENOLITHS | 117 |
| 6.3. RESULTS | 119 |
| 6.4. DISCUSSION | 129 |
| 6.5. CONCLUSION | 140 |
| 7. THE ARCHITECTURE OF THE EUROPEAN-MEDITERRANEAN LITHOSPHERE: A SYNTHESIS OF THE RE-OS EVIDENCE | 147 |
| 7.1. INTRODUCTION | 149 |
| 7.2. GEOLOGICAL SETTING AND SAMPLE BACKGROUND | 149 |
| 7.3. RESULTS AND INTERPRETATION | 150 |
| PART III | 159 |
| 8. CONCLUSIONS | 161 |
| 8.1. SCLM INVOLVING CIRCUMCRATONIC MANTLE IN COLLISIONAL OROGENS | 161 |
| 8.2. SCLM IN SUPRA-SUBDUCTION AND CONTINENTAL DELAMINATION SETTINGS | 162 |
| PART IV | 165 |
| 9. REFERENCES | 167 |
| PART V | 195 |
| SAMPLE LIST | 197 |
| WHOLE ROCK MAJOR ELEMENTS | 202 |
| MINERAL MAJOR ELEMENTS | 203 |
| WHOLE ROCK TRACE ELEMENTS | 206 |
| CLINOPYROXENE TRACE ELEMENTS | 208 |

Resumen Extendido

El principal objetivo de esta Tesis Doctoral ha sido la investigación de la estructura, composición geoquímica y evolución del manto subcontinental litosférico (MSCL) en contextos convergentes de placas a través del estudio de los enclaves de peridotitas que son muestreados por el magmatismo alcalino postorogénico. En la Tesis se investigan dos ejemplos de enclaves en estos contextos: (i) el de enclaves del MSCL circumcratónico en orógenos colisionales (Meseta de Sangilen, Tuva, Rusia); y (ii) el de enclaves del MSCL que ha registrado eventos tectónicos y magmáticos en un contexto de suprasubducción y delaminación continental durante la evolución Terciaria Alpina de la Cordillera Bético-Rifeña (provincia volcánica del sureste Ibérico, Murcia, España).

El MSCL de orógenos colisionales en zonas circumcratónicas

En este apartado se han investigado los enclaves de peridotitas que aparecen en diques de lamprófidos del Ordovícico Superior de la Meseta de Sangilen (Tuva, Rusia) y que forman parte de la cadena orogénica circumcratónica de Asia Central (sur de Siberia). Estos enclaves nos han permitido investigar la composición química y la estructura térmica del MLSC circumcratónico que compone el microcontinente de Tuva-Mongolia. Estos enclaves proporcionan una información de la composición del manto en esta área circumcratónica. Esta información es complementaria a la proporcionada por los enclaves que aparecen en basaltos alcalinos Neógenos y que muestrean el manto cratónico adyacente de este orógeno de colisión.

El estudio petrológico y geoquímico de los enclaves de peridotitas con espinela de la Meseta de Sangilen nos ha permitido alcanzar las siguientes conclusiones: (i) los enclaves registran un gradiente térmico (*ca.* 1000–1100 °C) compatible con un muestreo del MSCL a profundidades de 43 a 53 km (1.3–1.6 GPa); (ii) la variación de la composición del Mg# (87.9–90.9) del olivino y el Cr# (9.5–45.7) de la espinela muestra que estos enclaves son muestras del de

un manto residual que ha sufrido un máximo de 10% de fusión parcial a partir de una fuente mantélica empobrecida; (iii) el alto contenido en Yb_N de algunos clinopiroxenos (muestra 5H-10) y la fraccionación variable de los contenidos de LREE-MREE relativas a las HREE en los clinopiroxenos de los enclaves, muestran que han sufrido procesos metasomáticos de enriquecimiento en elementos trazas posteriores a la fusión parcial. Estos procesos metasomáticos consistieron en episodios de percolación y reacción de pequeñas fracciones de fundidos alcalinos precursores de los fundidos que formaron los lamprófidos alcalinos en la región (lamprófidos de Agardag); (iv) La ausencia de correlación entre la profundidad de procedencia de los enclaves con sus variaciones modales, tipos texturales y grado de fusión parcial -deducido a partir de la concentración de los HREE más compatibles- muestran que en el Ordovícico no existía en el MSCL de la Meseta de Sangilen una estructuración tectónica y/o composicional en profundidad. Como demuestran los modelos cuantitativos de percolación-reacción, estas variaciones composicionales indican que el MSCL fue metasomatizado por una red de diques por los que circulaban fundidos alcalinos máficos que estaban distribuidos heterogéneamente en el manto litosférico después de los eventos colisionales que originaron el MSCL circumcratónico.

El MSCL en contextos de supra-subducción y delaminación continental

Los basaltos alcalinos del Plioceno y Pleistoceno (2-3 Ma) que afloran en centros volcánicos de las zonas internas de las Béticas orientales (centros volcánicos de Tallante, Murcia) contienen numerosos enclaves de peridotitas que proporcionan una oportunidad única para investigar la estructura y composición del manto litosférico en la terminación noreste del arco que rodea el mar de Alborán en el Mediterráneo occidental (Cordillera Bético-Rifeña, sur de España). Estos enclaves de peridotitas registran la deformación del manto de un área tectónicamente compleja y, además, proporcionan información complementaria a la obtenida por los estudios sísmicos de la cordillera.

Una síntesis de los datos de isótopos de Os en muestras de peridotitas

muestran que el manto subcontinental de las Cordillera Bético-Rifeña y los Apeninos poseen edades máximas de empobrecimiento en Re (TRD) diferentes a las edades más antiguas (Paleo-Proterozoicas; 1.8 Ga) que aparecen de forma generalizada en el manto Europeo y Africano. Las muestras de manto de los dominios Alpinos poseen edades TRD más antiguas, y en el caso de los enclaves mantélicos de Tallante registran edades Neo-Arcaicas (2.6 Ga). Estas edades máximas diacrónicas desvelan la presencia—hasta ahora desconocida—de dominios de MSCL de origen Arcaico en el Mediterráneo occidental y central. Estas observaciones indican que fragmentos de manto arcaico empobrecido han jugado un papel fundamental en la evolución y construcción de la litosfera Mediterránea durante la orogenia Alpina. Las edades arcaicas registradas (TRD) en los sulfuros de los enclaves de Tallante son idénticas a las edades U-Pb más antiguas encontradas en circones heredados en magma anatéticos de las Béticas orientales, y son similares a las edades más antiguas en las peridotitas de Ronda (TRD) y en los circones heredados de las unidades corticales de alto grado suprayacentes en las unidades Alpujárrides de las Béticas occidentales. Estas similitudes probablemente muestran que el manto litosférico y la corteza inferior de las Béticas orientales tienen una procedencia no Ibérica, y proceden de la litosfera del dominio de Alborán expuesta en los Alpujárrides occidentales. A pesar de tener la misma procedencia, los enclaves de peridotitas de las Béticas orientales muestrean un MSCL que es composicionalmente más fértil y con un estilo y una edad más joven de deformación que el MSCL muestreado por las peridotitas orogénicas de Ronda en las Béticas orientales.

El estudio microestructural y de las orientaciones cristalográficas preferentes (OCP) de los minerales de los enclaves de peridotitas de las Béticas orientales proporcionan nuevas claves para comprender el significado y edad de la deformación del manto en el mediterráneo occidental. Las OCP de ortopiroxenos en venas de ortopiroxenitas -formadas ente 2.2 y 4.4 Ma por la reacción de fluidos/fundidos ricos en sílice con peridotitas litosféricas—

muestran que este proceso metasomático fue sincinemático con la deformación dúctil por mecanismos por flujo de dislocaciones de las peridotitas encajantes. Esta observación demuestra que las deformaciones dúctiles registradas en los enclaves de peridotitas de las Béticas orientales sucedieron al final del Neógeno. Las OCP de los olivinos en los enclaves de peridotitas muestra patrones de deformación de tipo axial-[100]. Estos patrones son característicos de deformación por un mecanismo de cizalla simple en un régimen tectónico transtensional. La textura y composición de los enclaves registra una fuerte descompresión desde profundidades mínimas de 55-60 km hasta la base de la corteza inferior a 19-20 km. La secuencia sincinemática de asociaciones minerales desde facies de lherzolitas con granate hasta facies de lherzolitas con espinela y plagioclasa, demuestra que la descompresión fue acomodada de forma continuada durante el cizallamiento y adelgazamiento dúctil del manto litosférico. El adelgazamiento litosférico registrado en los enclaves de las Béticas orientales es compatible un factor de adelgazamiento de 1.5 y tasas de deformación de $9\cdot7\cdot10^{-13}$ s⁻¹. Estos valores son característicos de la extensión rápida del MSCL asociada a altos gradientes geotérmicos (>100 mW·m⁻²).

Tal y como se deduce de las propiedades sísmica calculadas a partir de la OCP de los enclaves de peridotitas, la dirección actual N 69° detectada en los estudios de anisotropía sísmica de ondas SKS y Pn en las Béticas orientales puede explicarse por una fábrica tectónica del manto litosférico superficial con una orientación de los ejes [100] del olivino subhorizontal que es paralela a las direcciones de flujo (actual o heredada) del manto. El espesor del manto superior actual (40-80 km) y el tiempo de retardos entre las ondas SKS polarizadas en las Béticas orientales pueden explicarse solamente si la foliación de las peridotitas del MLSC es subvertical y la lineación subhorizontal; esta geometría de la fábrica tectónica del manto litosférico implica un flujo del manto—activo o fósil—con un componente en salto en dirección paralelo al paleo-margen ibérico. Esta configuración puede reflejar una deformación del manto litosférico heredada entre los márgenes de Iberia y el Dominio exótico de Alborán durante la retirada hacia el O-SO en el Mioceno

inferior de la laja de subducción del Tethys occidental que originó el arco de Gibraltar. Los perfiles composicionales en los minerales de los enclaves de peridotitas muestra que el inicio del adelgazamiento dúctil del MLSC pudo ocurrir entre 6.2 y 9.4 Ma. Este periodo de tiempo coincide con numerosos procesos tectónicos y magmáticos de origen profundo en las Béticas orientales tales como la iniciación de la fusión parcial de la corteza inferior (*ca.* 9 Ma) y el cambio del estilo del magmatismo desde tipo subducción hasta tipo intraplaca (6.3-4.8 Ma). Estos eventos magmáticos fueron contemporáneos con el levantamiento generalizado de la región que originó la crisis de salinidad del Mesiniense en el Mediterráneo, y que algunos autores atribuyen al ascenso diapírico de la astenosfera mantélica asociada a la delaminación del margen Ibérico durante los procesos de estiramiento en la zona de trasera de arco durante la migración hacia el oeste de la zona de subducción del Tethys occidental. La delaminación del borde del margen continental de Iberia pudo originar la descompresión del manto litosférico caliente extendido de Alborán y su flujo lateral hacia el oeste para rellenar los márgenes delaminados de Iberia siguiendo la anisotropía O-SO del MLSC heredada de los procesos tectónicos del Mioceno inferior. Este proceso explicaría la Moho subhorizontal, el calentamiento y fusión cortical, el cambio de estilo del magmatismo, y el levantamiento regional en el Mioceno superior. La delaminación del manto litosférico subducido y su remplazamiento por manto y corteza inferior de tipo Alborán proveniente del oeste explicaría la procedencia de Alborán del manto y la corteza inferior en las Béticas orientales. Este paroxismo geológico fue contemporáneo con la apertura E-O de la cuenca oceánica Argelino-Balear en el Mioceno medio-superior. La existencia de una fábrica heredada en el MLSC con un fuerte componente en salto en dirección puede estar gobernando algunos procesos geológicos profundos en las Béticas orientales.

El estudio geoquímico detallado de la composición en elementos mayores, traza e isótopos de Nd-Sr-Pb de los enclaves de peridotitas de las Bética orientales proporciona, además, información sobre cómo los procesos tectónicos y magmáticos asociados a la orogenia Alpina han modificado la

composición del manto subcontinental en el Mediterráneo occidental. Las variaciones de la concentración de los elementos mayores, junto al quimismo mineral, de los enclaves de peridotitas revelan la existencia de diferentes grupos composicionales con un grado variable de fertilidad. Estos grupos abarcan desde peridotitas empobrecidas (Grupo I con un Mg# de hasta 0.915) hasta lherzolitas extremadamente fértiles (Grupo III con Mg# entre 0.868-0.889; y Wehrlitas con Mg# entre 0.867-0.874), pasando por lherzolitas de composiciones intermedias (Grupo II con Mg# de hasta 0.906). La composición en elementos mayores de los minerales de las peridotitas muestra que éstas registraron entre un 10 y 12% de fusión parcial. La composición en elementos traza e isótopos revelan que los enclaves han sufrido procesos metasomáticos de enriquecimiento en elementos trazas incompatibles posteriores a la fusión parcial. Estos procesos metasomáticos conllevaron a un enriquecimiento de los elementos de las tierras raras ligeras (LREE) en las peridotitas del Grupo II y III, y en las wehrlitas. Contrariamente a los elementos mayores y trazas, los isótopos radiogénicos de Nd-Sr-Pb muestran una variabilidad independientemente. Los enclaves de peridotitas de las Béticas orientales muestran variaciones isotópicas entre los componentes DMM y EM2, con una contribución de un componente isotópico derivado de sedimentos Atlánticos. La composición geoquímica de los enclaves de las Béticas orientales puede explicarse por procesos de refertilization del manto de tipo Alboran asociados a metasomatismo de fundidos derivados de la subducción oceánica probablemente relacionada con la subducción del Tethys en el Mioceno inferior en el Mediterráneo occidental.

Part I

*Introduction, Aims & Thesis Structure
and Methodology*

1. Introduction

1.1. Lithospheric Plates

Plate tectonics theory—the theory that describes the large-scale movements of Earth's lithosphere—builds on the concepts of continental drift, developed during the first decades of the 20th century. A key concept of the plate tectonic theory is that of lithospheric plate. The outermost solid layer of the Earth is divided into lithosphere and asthenosphere. This difference is not always patent and is mainly based on the mechanical properties and the way heat is transferred. Mechanically, the lithosphere is cooler and more rigid part that can sustain long-term stresses, whereas the asthenosphere is hotter and flows under long-term applied stresses. In terms of heat transfer, the lithosphere is the part that transfers heat by conduction, whereas has a nearly adiabatic temperature gradient and heat transfer mostly happens by convection.

The Earth's lithosphere is formed by seven major lithospheric plates (African, Antarctic, Eurasian, Indo-Australian, North American, Pacific and South American Plates) and many other minor plates (e.g. Arabian, Caribbean, Indian, Juan de Fuca, Nazca Plates) (Fig. 1).

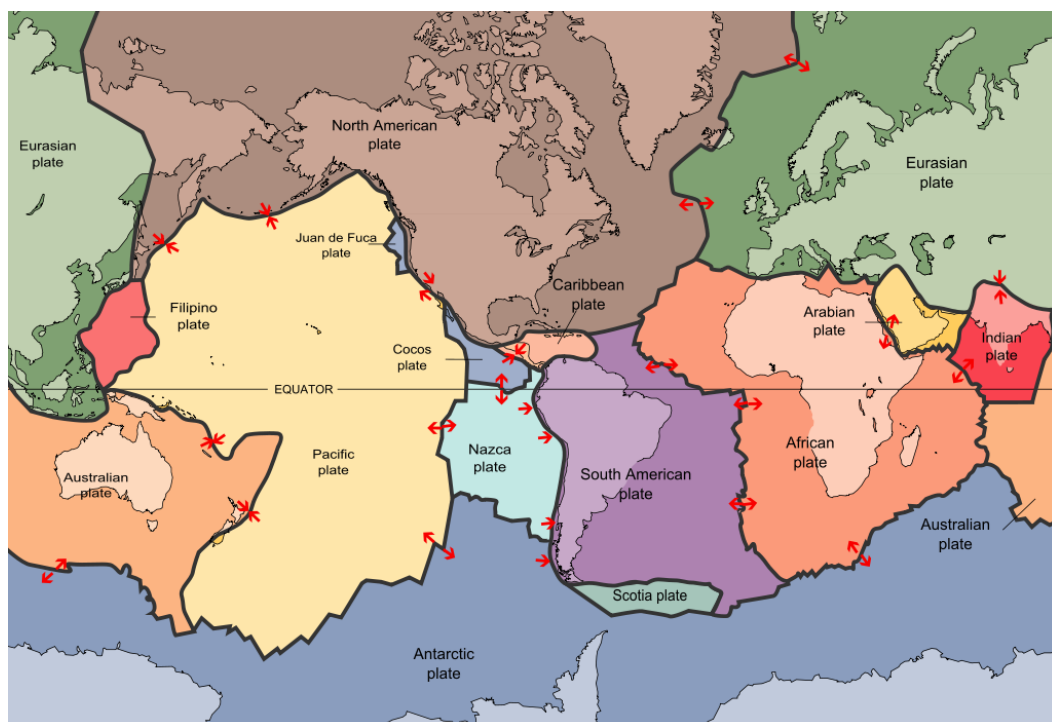


Fig. 1 The tectonic plates of the Earth were mapped in the second half of the 20th century (after Kious and Tilling, 1994)

Lithospheric plate boundaries are the loci where plates meet: formation of mountains, oceanic ridges, and seismic and magmatic activities commonly takes places along these plate boundaries, where new lithosphere can be generated or consumed. Depending on the relative motion of plates along these boundaries, they can be classified into transform plate boundaries (e.g. San Andreas Fault in California, USA), convergent (usually destructive) plate boundaries, which occur where two plates converge forming either subduction zones or continental collision orogenic zones; and divergent (constructive) boundaries (Fig. 2), which occur where two plates move apart (e.g. mid-ocean ridges such as Mid-Atlantic Ridge or active zones of rifting such as East African Rift).

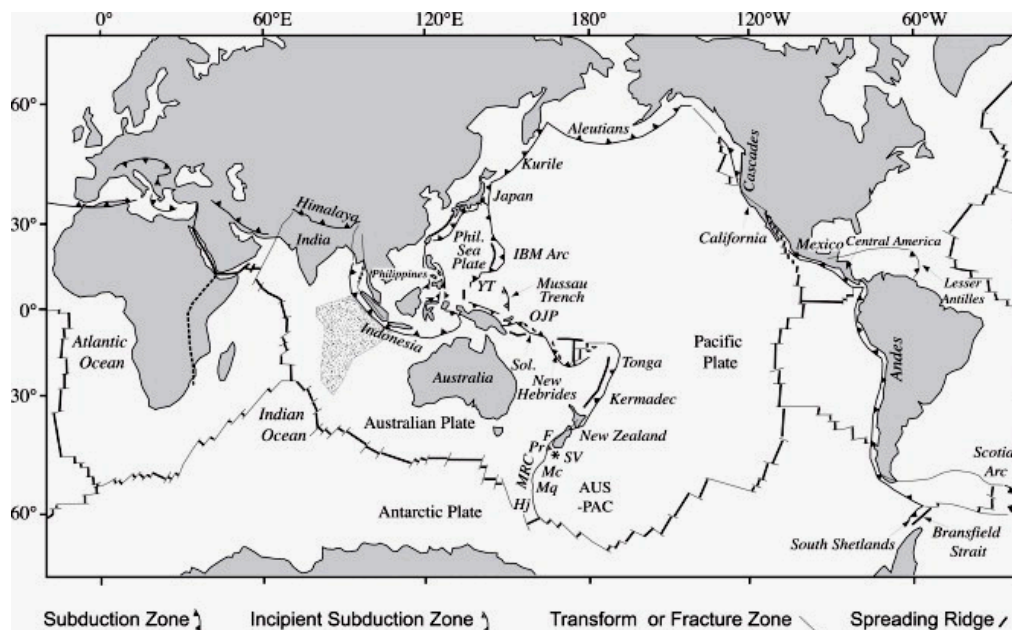


Fig. 2 Map showing location of subduction zones and where new subduction zones form (after Stern, 2004). YT=Yap Trench, Sol.=Solomon Arc, OJP=Ontong-Java Plateau. Stippled area in Indian Ocean between India and Australia is diffuse plate boundary of Royer and Gordon (1997). Area south of New Zealand is part of the MRC and Fiordland (F), including associated deeps: Puysgur (Pr), McDougall (Mc), Macquarie (Mq) and Hjort (Hj). General location of the pole of rotation for the Australian and Pacific plates is also shown (AUS-PAC).

In spite of the great successes of plate tectonic theory in modern Earth science, fundamental questions still remain concerning the evolution of continents and their role in the dynamics of the Earth's lithosphere and mantle. The growth process of continents, their thickness and the dynamic coupling with the underlying mantle are topics requiring focused attention from a series of sub-disciplines, including, among others, mantle petrology and geochemistry, local and global seismology and numerical geodynamics. Equally important questions remain to be solved concerning mechanisms controlling continental tectonics and their effects on vertical movements, dynamic topography, and sedimentary basin formation. Vital in this respect are the dynamics of splitting and formation of continents; particularly on

how one plate dives beneath another at a subduction zone, and how mountains are built and their effects on boundary processes between oceans and continents. In order to quantify these essential processes involved in solid Earth science, it is fundamental to understand the processes that compositionally and geologically modified the subcontinental lithospheric mantle—the largest portion of the continental part of lithospheric plates—at convergent plate boundaries and how these processes are coupled both to internal and external forcing.

1.2. The Subcontinental Lithospheric Mantle (SCLM)

The lithospheric mantle is the part of the lithosphere below the crust (*ca.* 0-10 km in the oceans and *ca.* 30-50 km on the continents) up to asthenospheric depths. The depth of the base of the mantle lithosphere – the lithosphere-asthenosphere boundary – is variable and depends on how asthenosphere is defined; lithosphere and asthenosphere constitute the upper mantle, which extends up to depths of the transition zone (410-660 km). Below, the lower mantle occurs between 660 and 2890 km (Fig. 3). The mineralogy and composition of the uppermost mantle is constrained by the petrology of mantle-derived, ultramafic rocks, as well as from seismological and geophysical observations of the Earth's interior and from meteoritic analogies.

The Subcontinental Lithospheric Mantle (SCLM) is defined as the portion of the lithospheric mantle beneath continents. Fragments of the SCLM can be found in the Earth's crust as tectonically emplaced, mantle peridotite massifs (Fig. 4) that are broadly known as orogenic peridotite massifs (*e.g.* the Ronda, Beni Bousera, and Lanzo peridotite massifs) and that usually crop out at plate boundaries and/or in orogenic belts. Orogenic peridotites provide large exposures of SCLM rocks – up to 300 km² – allowing detailed investigations of the composition and structure of the SCLM at kilometeric scales (*e.g.* Menzies et al., 1991; Pearson and Nowell, 2002; Bodinier and Godard, 2003). Smaller portions – up to a few meters – of the SCLM can be found as fragments – known as mantle xenoliths – entrained by volcanic rocks during eruption (Fig. 4) (Nixon, 1987; Pearson et al., 2003). These mantle xenoliths are the only direct samples of the SCLM available in some tectonic settings such as intracontinental rifts and, less commonly, convergent settings. In addition to furnish samples of parts of the SCLM unavailable elsewhere, mantle xenoliths provide a snapshot of the thermal, compositional and tectonic structure of the SCLM at the time of eruption; this information is inaccessible by the study of orogenic peridotites and is complementary to the information provided by geophysical methods.

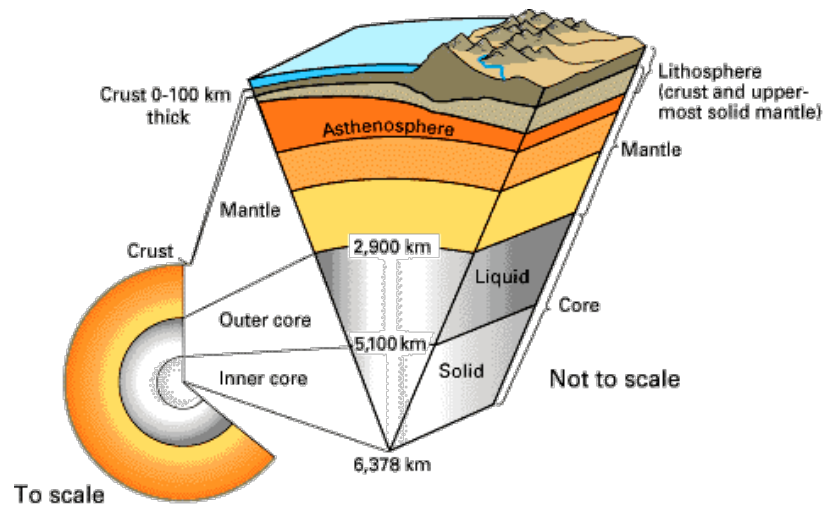


Fig. 3 Simplified sketch of the Earth's structure (after Kious and Tilling, 1996)

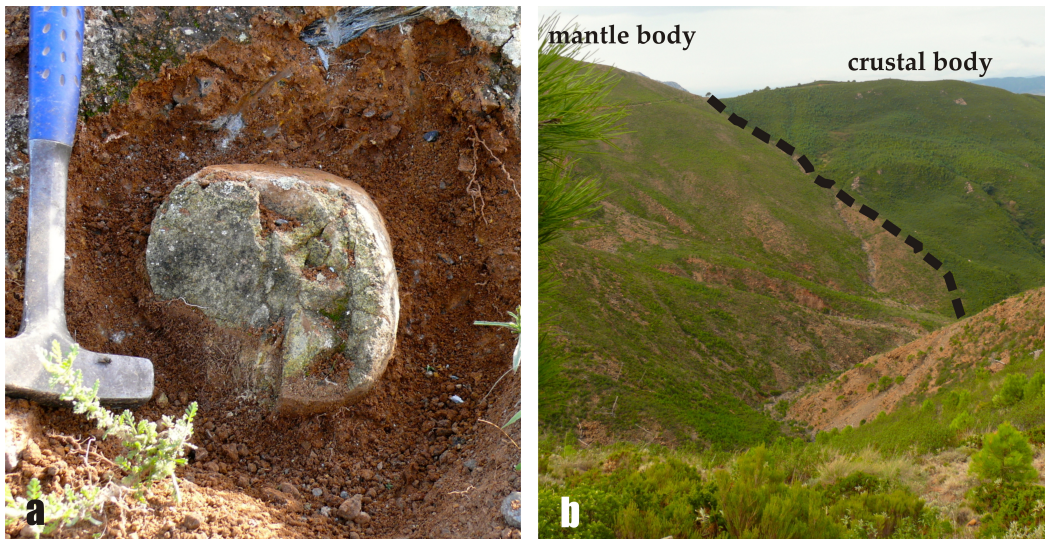


Fig. 4 Field pictures of (a) a mantle xenolith in a porphyroclastic flow from the Tallante alkaline volcanic center in the SE IVP (Murcia, Spain) and (b) the crust-mantle transition in the Ronda peridotite massif (Betic Cordillera, Malaga, S. Spain). (b) The black dashed line marks the tectonic boundary between mantle (reddish) and overlying crustal (grayish) rocks. (Photos were taken by the author during field work campaigns in 2008).

1.3. The Petrological Composition and Structure of the SCLM

The SCLM mantle is predominantly composed of magnesium-rich olivine and orthopyroxene with lesser amount of calcium-bearing clinopyroxene and an aluminous minerals varying from plagioclase to spinel to garnet. Pyroxenite is thought to be only a minor component of SCLM mantle.

The nomenclature of peridotite and pyroxenite is summarized in Fig. 5 (e.g. Streckeisen, 1974, 1976; Le Bas and Streckeisen, 1991). Peridotite is made up of olivine (> 60 vol%) and pyroxenes. If the olivine exceeds 90 vol%, the peridotite is termed dunite; if it consists almost exclusively of olivine and orthopyroxene, it is called harzburgite; wehrlite is peridotite consisting almost exclusively of olivine and clinopyroxene; finally, lherzolite is peridotite with greater amounts of both pyroxenes. On the other hand, pyroxenite contains less than 60 vol% of olivine. In addition to olivine and pyroxene, SCLM peridotite usually contains an aluminum-bearing mineral, such as spinel, plagioclase or garnet, which nature strongly depends on the equilibration pressure and hence the depth of provenance of the peridotite sample. Garnet and plagioclase peridotites sample the deepest and shallowest parts of the SCLM, respectively. Because plagioclase is only stable in lherzolite at depths below c. 30 km (*i.e.* those depths expected for the continental crust) lherzolite peridotites are rare in SCLM xenoliths and generally reveal settings with an anomalously thin SCLM.

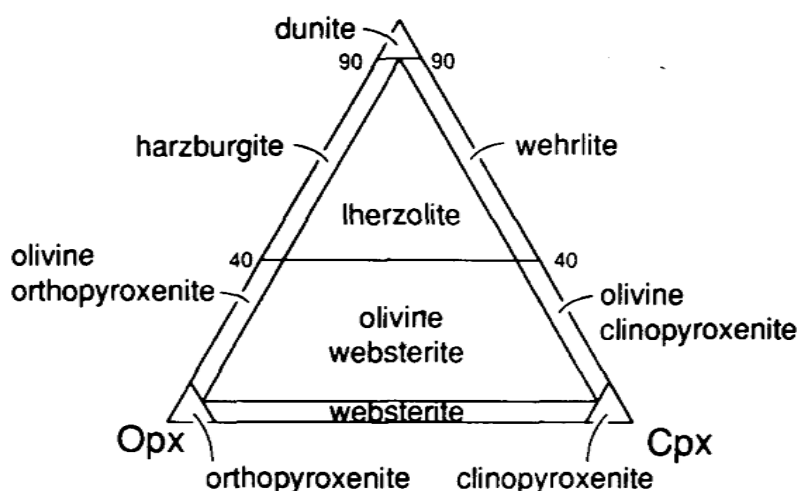


Fig. 5 Classification and nomenclature of the ultramafic rocks (mafic minerals > 90%) based on the modal proportions of olivine (Ol), orthopyroxene (Opx) and clinopyroxene (Cpx) (Streckeisen, 1976).

The composition of the SCLM is thought to be dominated by lherzolite; however, its composition varies depending upon the specific continental setting (*e.g.* cratons, continental shields, and circum-cratonic areas) and its age of formation. Any estimate of SCLM composition should match that obtained from mantle samples (Fig. 4) and geophysical constraints (Fig. 6). However, the differentiation between SCLM and oceanic mantle in terms of compositional and geophysical constraints is not everywhere straightforward. On the basis of the seismic velocity, at shallow depth (*e.g.* < 125 km) the transition from continental to oceanic mantle lithosphere is reasonably well discerned because of the relatively higher

seismic shear wave velocity (V_s) of the SCLM (Fig. 7). The high V_s of the SCLM further supports that the most abundant rock type is peridotite (Bina, 2003).¹

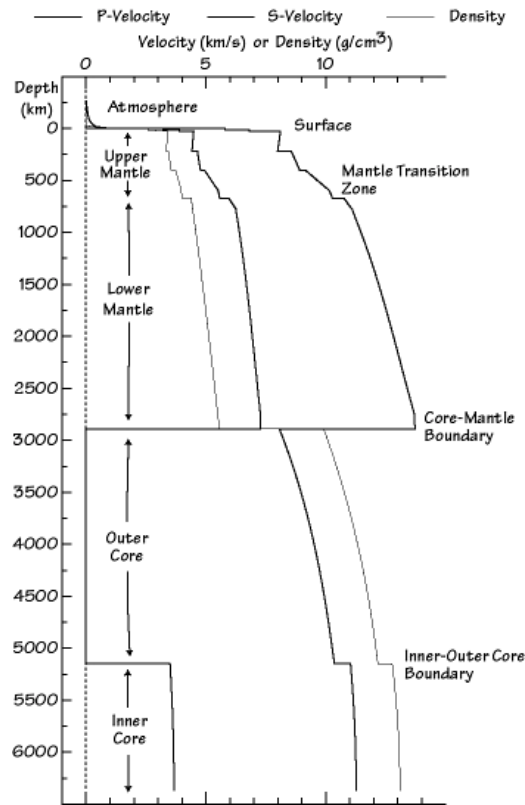


Fig. 6 The diagram is a plot of the P- and S-wave velocities and the density as a function of depth into the Earth based on seismic observations.

Although generally higher than in oceanic mantle, seismic velocities of the SCLM vary noticeably and correlate best with the age of last tectonomagmatic activity in the region instead of with the age of the overlying crust (Carlson et al., 2005). SCLM domains can hence be classified in terms of the tectonomagmatic age of the overlying crust (Griffin et al., 1999, 2009). According to this classification, we can differentiate the SCLM domains into Archons, where the crust has not been affected by large-scale, tectonomagmatic events since ≥ 2.5 Ga; Protons, which have experienced tectonomagmatic events at 2.5-1.0 Gyr; and Tectons, which have been formed and/or modified less than 1.0 Ga ago (Griffin et al., 2009). Generally, shallow upper mantle beneath actively deforming continental areas (Tectons), such as continental basins, usually shows the lowest-velocity of both compressional (V_p) and shear (V_s) seismic waves. The highest velocity of the SCLM underlies the cores of Archean cratons (Archon); whereas lower V_s are observed in the SCLM beneath regions where Proterozoic thermal and magmatic events have affected crust and mantle (Proton).

¹ Peridotite gives the majority of mantle rock retrieved as a xenolith (Nixon, 1987; Pearson et al., 2003), with eclogite (the high pressure equivalent of basalt) of secondary abundance (Carlson et al., 2005 and references therein).

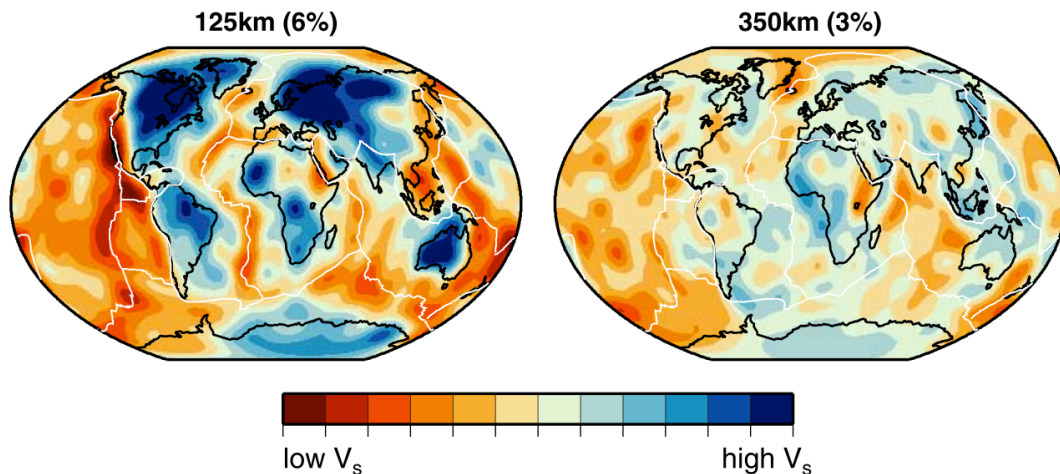


Fig. 7 Map of shear wave (V_s) seismic velocity variation in the upper mantle at depths of (left) 125 and (right) 350 km (Ritsema et al., 2004; Carlson et al., 2005). The total range in velocities at 125 km is $\pm 6\%$ and $\pm 3\%$ at 350 km depth. White solid lines are plate boundaries; continents are outlined in black.

However, this tectonomagmatic classification is oversimplified because, besides temperature, the composition—and notably the bulk content of Fe in peridotite—plays a significant role in the variation of seismic velocities of the peridotitic upper mantle (Lee, 2003; James et al., 2004). According to Goes et al. (2000), the estimated change in seismic velocity per 100 °C temperature is ca. 0.5-2% for V_p and ca. 0.7-4.5% for V_s . A 2% increase in seismic velocity can be due to a 120 °C decrease in the mantle potential temperature or, alternatively, to a 7.5% or 15% depletion in Fe and Al, respectively, relative to the depleted upper mantle composition (Godey et al., 2004). As the bulk Fe content of peridotite depends on the degree and average pressure of melting, other factors related to the genesis and the differentiation of the SCLM may come into play into the formation of different SCLM domains.

1.4. The Composition of the SCLM

Estimation of the composition of the upper mantle relies on studies of the composition of mantle xenoliths. Several estimates for the major and minor element composition of the upper mantle made over the last decades show that relatively to CI chondrite (Table 1) the upper mantle is depleted in the alkaline elements (*e.g.* K and Na) (White, 2005). The depletion in moderately volatile elements is also visible by comparing strontium isotope ratios if the mantle and chondrites: $^{87}\text{Sr}/^{86}\text{Sr}$ ratios in the mantle imply Rb/Sr ratios more than an order of magnitude lower than C1 chondrite. Some of the Rb depletion of the mantle can be explained by extraction of the Rb into the Earth's crust.

The chemical characteristics of SCLM allow further discriminations of the mantle-derived rocks and give also hints about its geochemical evolution. SCLM are usually classified as fertile or depleted concerning their composition has been modified by extraction of partial melts (Fig. 8). A number of methods have been used to estimate the composition of the SCLM before any melting has occurred (*e.g.* Ringwood, 1969; Jagoutz et al., 1979; McDonough and Sun, 1995; Palme and O'Neill, 2003). During mantle melting, certain elements such as calcium and aluminum move into the melt whereas other elements, particularly magnesium, stay in the solid residue. Those elements that move into the melt are known as incompatible elements. Note that during dry melting at low pressure (< 3 GPa) and during water-saturated melting at higher pressure, iron is nearly equally partitioned between melt and solid (Kinzler and Grove, 1992; Walter, 1998; Kawamoto and Holloway, 1997; Gaetani and Grove, 1998).

Table 1 Comparison of estimated silicate Earth compositions (after White, 2005)

| | CI Chondrites | CI Chondritic Mantle & Core ¹ | Hart & Zindler LOSIMAG ² | Ringwood ³ Pyrolite | McDonough & Sun ⁴ Pyrolite | Allegre et al. ⁵ PRIMA |
|--------------------------------|------------------|---|--|-----------------------------------|--|--------------------------------------|
| SiO ₂ | 22.77 | 49.52 | 45.96 | 44.76 | 45.0 | 46.12 |
| Al ₂ O ₃ | 1.64 | 3.56 | 4.06 | 4.46 | 4.45 | 4.09 |
| FeO | 24.49 | 7.14 | 7.54 | 8.43 | 8.05 | 7.49 |
| MgO | 16.41 | 35.68 | 37.78 | 37.23 | 37.8 | 37.77 |
| CaO | 1.30 | 2.82 | 3.21 | 3.60 | 3.55 | 3.23 |
| Na ₂ O | 0.67 | 0.292 | 0.332 | 0.61 | 0.36 | 0.36 |
| K ₂ O | 0.067 | 0.028 | 0.032 | 0.029 | 0.029 | 0.034 |
| Cr ₂ O ₃ | 0.39 | 0.412 | 0.468 | 0.43 | 0.384 | 0.38 |
| MnO | 0.256 | 0.115 | 0.130 | 0.14 | 0.135 | 0.149 |
| TiO ₂ | 0.073 | 0.159 | 0.181 | 0.21 | 0.20 | 0.18 |
| NiO | 1.39 | 0.244 | 0.277 | 0.241 | 0.25 | 0.25 |
| CoO | 0.064 | 0.012 | 0.013 | 0.013 | 0.013 | 0.07 |
| P ₂ O ₅ | 0.274 | 0.018 | 0.019 | 0.015 | 0.021 | |
| Sum | 69.79 | 100.0 | 100.0 | | | |
| HVE ⁶ | 30.21 | 30.21 | 30.21 | | | |
| MVE ⁷ | | 1.258 | 1.258 | | | |
| SVE ⁸ | | | 5.33 | | | |
| Fe | 74.44 | 85.62 | | | | 79.39 |
| Ni | 4.53 | 5.16 | | | | 4.87 |
| Co | 0.2081 | 0.237 | | | | 0.253 |
| S | | | | | | 2.3 |
| O | | 20.81 | 8.99 | | | 4.10 |
| Core Sum | | 100.0 | 100.0 | | | |
| Total | 99.9 | 99.7 | 99.4 | | | |

¹ Removing HVE, MVE and siderophiles and some oxygen from mantle to form core; renormalizing silicate mantle and core separately (Hart and Zinder, 1986). ² Low-Si-Mg Earth with siderophiles and some oxygen removed from mantle to form; renormalizing silicate mantle and core separately (Hart and Zindler, 1986). ³ Estimated Primitive Upper Mantle (PUM) composition (Ringwood, 1991). ⁴ Estimated Primitive Mantle (PM) composition (McDonough and Sun, 1995). ⁵ Primitive Mantle (PRIMA) (Allégre et al., 1995). ⁶ HVE – Highly Volatile Elements, includes H₂O, S, C, organics and so on. ⁷ MVE – Moderately Volatile Elements, includes Na, K, P, Cr, Mn. ⁸ SVE – Slightly Volatile Elements, Si and Mg.

The transition from fertile to depleted peridotite is characterized first by the loss of clinopyroxene and garnet (Fig. 8)—the main hosts for incompatible elements in mantle

peridotite—and then orthopyroxene, resulting in the transition from lherzolite to harzburgite, and finally dunite (Fig. 5).

It has long been recognized that Archean SCLM is more depleted than younger SCLM (Boyd, 1989). Although disputed, it also seems to be characterized by Si-enriched composition that is manifested in higher average modal contents of orthopyroxene. Average Archean mantle is ca. 2.5% less dense than fertile mantle (Jordan, 1975), while the composition of ‘young’ mantle sampled for instance at Phanerozoic rifts can be fairly similar to the fertile mantle. These differences in mantle composition are related to the process of individualization and formation of SCLM from asthenosphere, and generally record a protracted multistage evolution since the first formation of SCLM.

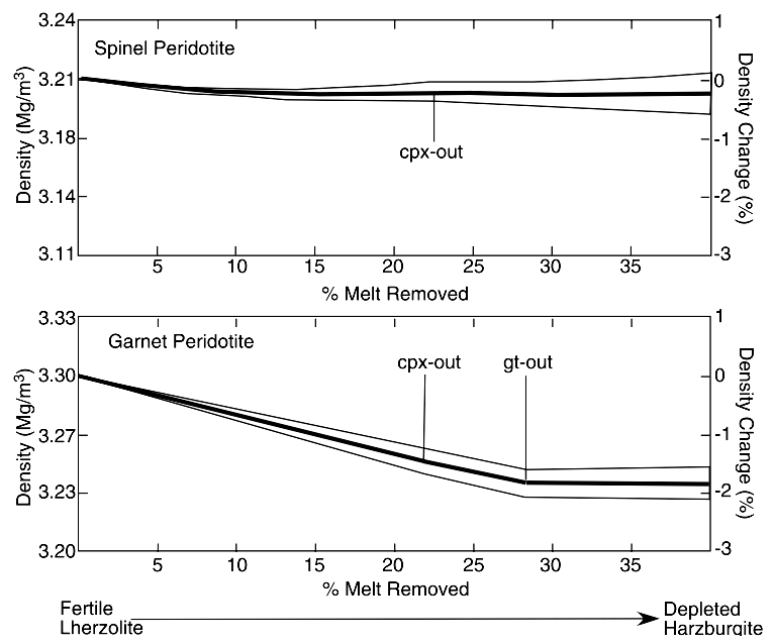


Fig. 8 Density change in spinel and garnet peridotite (at room temperature and pressure) due to melt extraction (Carson et al., 2005; Schutt and Lesher, 2006). Also indicated on the plots in the percentage of melting where clinopyroxene (cpx-out) and garnet (gt-out) are fully consumed. The bold line shows the density change in function of the percentage of melt extracted with the shaded band indicating the error margin of density.

The pristine mantle composition of the SCLM can be modified by melt-rock reactions processes (mostly via nominally anhydrous, silicate melts) associated with thermal perturbations related to the movement of the asthenosphere-lithosphere boundary during large tectonic events (e.g. continental rifting, continental subduction, etc.), and/or be modified by near-solidus or subsolidus mantle metasomatic agents, process often referred to as mantle metasomatism (Menzies and Hawkesworth, 1987). Melt-rock interaction and

metasomatism can lead to substantial post-accretion modification of the major and trace element composition of the SCLM; these modifications are attested by the addition of major and/or trace elements to the SCLM relative to the depleted upper mantle composition, leading to its fertilization or refertilization. Where is modally patent, the fertilization is accompanied by textural and/or mineralogical evidence in the form of crystallization of secondary minerals from melts, mostly secondary clinopyroxene and amphibole depending on the temperature and nature of the metasomatic agent (*e.g.* alkaline low melt fractions, carbonatite melts and hydrous, silicate melts). This modal metasomatism can be erased by recrystallization and deformation. Compositional refertilization may also occur without modifications of the mode of peridotite (*i.e.* cryptic metasomatism).

The chemical fingerprint of mantle fertilization associated with melt-rock interaction and metasomatism is highly variable and depends on the details of the melt-rock fractionation mechanism and the composition and nature of the metasomatic/melt agent involved. In terms of major elements, refertilization of refractory (depleted) lithospheric mantle (generally harzburgite) metasomatized by asthenospheric partial melts may result in a secondary lherzolitic mantle, leading to addition of Fe, Ca and Al to depleted, harzburgitic protoliths (*e.g.* Nicolas and Dupuy, 1984; Rampone et al., 1994, 1997; Garrido and Bodinier, 1999; Lenoir et al., 2001; Beyer et al., 2006; Le Roux et al., 2007). In terms of trace elements, the chemical fingerprint of metasomatism and melt-rock reaction is chiefly recorded in the normalized trace element pattern—particularly that of the Rare Earth Element (REE) signatures— of mantle peridotite and their clinopyroxenes (Bodinier and Godard, 2003 and reference therein). Trace element geochemical signatures of refertilization reactions may include transient (chromatographic), convex-upward normalized REE patterns in clinopyroxene, nearly constant concentration of moderately incompatible elements in lherzolite minerals (*e.g.* titanium in clinopyroxene) and anomalously high nickel content in olivine (Bodinier et al., 2004).

In terms of radiogenic isotopes, SCLM shows extensive overlap with oceanic mantle for the isotopic compositions of lithophile elements such as Sr and Nd (Menzies, 1990; Pearson, 1999). For Nd isotopes, the SCLM ranges from highly radiogenic compositions (relatively high values of $^{143}\text{Nd}/^{144}\text{Nd}$; high ϵNd) to highly enriched compositions (relatively low values of $^{143}\text{Nd}/^{144}\text{Nd}$; low ϵNd). Furthermore, the dominant Nd isotopic characteristic of SCLM is not 'enriched' but close to—or slightly more depleted than—bulk Earth (Pearson and Nowell, 2002). Further isotopic studies on mantle rocks include the Pb-Pb (^{204}Pb , ^{206}Pb , ^{207}Pb , ^{208}Pb) system that is a powerful tracer of nature of the metasomatic agents. In the other

hand, Re-Os ($^{187}\text{Re}/^{188}\text{Os}$) radiogenic isotopes provide a unique, multistage record of the melting events recorded by the SCLM and are hardly perturbed by metasomatic events.

1.5. Thermal Structure and Texture of the SCLM as Derived from Mantle Xenolith Studies

As pointed out above, mantle xenoliths provide a snapshot of the structure and thermal state of the SCLM at the time of eruption. The thermal structure of the SCLM beneath a given volcanic region can hence be investigated through the geothermobarometry of peridotite xenoliths. Geothermobarometry is the estimation of the temperatures (T) and pressures (P) recorded by mineral chemical equilibria. At high temperature mantle conditions, elements diffuse quickly and, hence, it is generally admitted that mineral equilibrium in peridotite mantle xenoliths records the ambient mantle temperature at a given depth at the time of eruption (Finnerty and Boyd, 1987; Brey et al., 1990). Thermobarometry of mantle xenoliths can thus provide the depth interval and minimum thickness of the lithosphere sampled by volcanism. Furthermore, as xenoliths are random samples of the SCLM, the temperature and pressure derived from geothermometric studies may offer a spatial information (*i.e.* depth of lithospheric provenance) among population of xenoliths that can be used to reveal textural and/or compositional zoning of the SCLM beneath volcanic centers. Finally, geothermobarometry of mantle xenoliths can be useful to characterize (paleo-) geothermal gradients of the SCLM, which ultimately depends on the tectonomagmatic activity at the time of eruption.

Several experimentally calibrated thermobarometers based on exchange and net-transfer metamorphic reactions are available to determine the P-T equilibration conditions of polymineralic mantle peridotites (Table 2). Geobarometry of peridotite xenoliths is generally well established for garnet-facies peridotites; particularly, the pressure dependence of Al solubility in pyroxenes coexisting with garnet is an excellent and well-calibrated geobarometer for most peridotite compositions (McGregor, 1974; Nickel and Green, 1985; Brey et al., 1990; Nimis and Taylor, 2000; Nimis and Grütter, 2010 and reference therein). On the other hand, there are not accurate geobarometers for spinel- and plagioclase-facies peridotites. Although the exchange of calcium between clinopyroxene and olivine is pressure dependent, it is also sensitive to thermal perturbations; ergo, late stage short heating events common in xenoliths may highly affect pressure estimations based on this geobarometric formulation.

Although the use of geothermometry and/or geobarometry using appropriate mineral assemblages in mantle xenoliths may allow reconstruction of the geotherm characteristic of the underlying lithosphere at the time of xenolith entrainment (Boyd, 1973), some problems may arise from the possible lack of equilibration between phases due to slow diffusion rate of some components. This can lead to freezing-in of reactions and hence on memory effects of P and T at different times for different mineral constituents or depth ranges upon cooling, resulting in spurious geothermal gradients (Fraser and Lawless, 1978). However, these effects can be avoided by careful integration of petrological, geochemical and geophysical data to unravel the stratigraphy of the SCLM, the nature of the Moho² and the thermal evolution of the SCLM during the time span of the volcanic activity that entrained xenoliths.

Table 2 Some geothermobarometers applicable to xenoliths. Only the most commonly used are listed, for a more extensive list see Taylor (1998), Brey et al. (1990) and Nimis and Grütter (2010).

| Method ¹ | Assemblage | Equilibrium | Comment | Accuracy ² |
|---------------------|------------|----------------|---|-----------------------|
| <i>Barometers</i> | | | | |
| P _{BKN} | gt - opx | Al exchange | gt-facies only | 0.5 GPa |
| P _{NT} | cpx - gt | Cr/Al exchange | gt-facies only | 0.3 GPa |
| P _{KB} | ol - cpx | Ca exchange | Analytically challenging | 0.7 GPa |
| <i>Thermometers</i> | | | | |
| T _{WS} | opx - spl | Al exchange | sp-facies only | 30 °C |
| T _{Ball} | ol - spl | Fe-Mg exchange | Fast diffusion | 30 °C |
| T _{BKN} | opx - cpx | Ca-Mg exchange | Insensitive to Fe ³⁺ | 60 °C |
| T _{TA} | opx - cpx | Ca-Mg exchange | Insensitive to Fe ³⁺ | 62 °C |
| T _{Ca-opx} | opx | Ca-Mg exchange | Insensitive to Fe ³⁺ | 60 °C |
| T _{KR} | cpx - gt | Fe-Mg exchange | Fe ³⁺ sensitive ³ | 100 °C |
| T _{OW} | ol - gt | Fe-Mg exchange | Fe ³⁺ sensitive ³ | 180 °C |
| T _{HA} | opx - gt | Fe-Mg exchange | Fe ³⁺ sensitive ³ | 92 °C |
| T _{LG} | opx - gt | Fe-Mg exchange | Fe ³⁺ sensitive ³ | 96 °C |

¹ P_{BKN}, T_{BKN}, T_{Ca-opx} - Brey and Köhler (1990); P_{KB} - Köhler and Brey (1990); P_{NT} - Nimis and Taylor (2000); T_{WS} - Witt-Eickschen and Seck (1991); T_{Ball} - Ballhaus et al. (1991); T_{TA} - Taylor (1998); T_{KR} - Krogh (1988); T_{OW} - O'Neill and Wood (1979); T_{HA} - Harley (1984); T_{LG} - Lee and Ganguly (1988). ² The 2 σ accuracies are based on ability to reproduce experimental data (Brey and Köhler, 1990; Taylor, 1998). ³ The sensitivity to Fe³⁺ content of one or both phases is reviewed by Canil and O'Neill (1996).

² The Mohorovičić discontinuity usually referred to as the Moho, is the boundary between the Earth's crust and the mantle.

Mantle xenoliths are metamorphic tectonites whose textures reflect the temperature, pressure and differential stress conditions of the SCLM; the grain size, orientation and interrelationships among different minerals with varying strength in peridotites vary depending on the deformation history experienced by the sample, and are used to classify the texture of the rock according to set criteria. Nixon and Boyd (1973) were some of the first workers to note the relationship between chemistry and texture in peridotite xenoliths. Various classifications of texture type have been developed (*e.g.* Mercier and Nicolas, 1975; Boullier and Nicolas, 1975; Harte et al., 1975) but the terminology of Harte (1977) is used in most cases.

Mantle xenoliths most commonly display coarse granular or porphyroclastic textures, and transition between these two end-members. The coarse granular texture is characterized by lack of a grain shape orientation and average olivine grain sizes greater than *ca.* 2 mm; these textures are generally equigranular. Porphyroclastic textures cannot be retained for long periods at high temperatures in the mantle lithosphere, due to the fast rate of olivine recrystallization and coarsening (Goetze, 1975). Porphyroclastic textures are therefore a 'transient' phenomena experienced by mantle rocks on a 'short' timescale before entrainment in their host magma, as may be also indicated by mineral zoning (Smith and Boyd, 1992).

1.6. Mantle Xenolith as Probe of the SCLM: Types and Occurrences

As discussed previously, mantle xenoliths are transported to the surface via volcanic rocks. To date there are known over 3500 mantle xenolith localities (Pearson et al., 2003). Nixon (1987) summarized the geology of many of these mantle xenolith localities. Further historical perspective on their study is presented by Menzies (1990). Lithospheric mantle xenoliths from several tectonic setting are mainly found in pyroclastic flows of volcanic eruptions, less commonly in lava flows, and rarely in subplutonic to subvolcanic intrusions. They are often associated with alkali basalts *sensu lato*—generally comprising alkaline basalt-basanites and more evolved derivatives—nephelinites, and melilitites. Less commonly, mantle xenoliths occur in lamphropyres and related magmas (*e.g.* minettes, monchiquites, and camptonites; Rock, 1991) and lamproites. Kimberlites (Group I and II, and orangeites; Mitchell, 1995) are particularly rich in mantle xenoliths. Finally, rare occurrences of mantle xenoliths have been described in more evolved magmas such as phonolites and trachytes (Irving and Price, 1981). Generally, the type of mantle xenoliths at a given locality varies with type of the host rock; spinel-facies xenoliths mostly occur in alkaline and potassic mafic magmas, whereas

kimberlites erupt both spinel- and garnet-facies peridotite mantle xenoliths (Nixon, 1987; Harte and Hawkesworth, 1989; Pearson et al., 2003).

The types of SCLM mantle xenoliths show a systematic variation depending on the age of the crust and the tectonomagmatic record of the continental lithosphere. This variability of mantle xenoliths reveals first-order compositional and structural differences of the SCLM beneath continents. Mantle xenoliths from cratonic and circumcratonic areas are noticeably different in petrology and geochemistry from those of continental areas that have undergone significant lithospheric rifting and thinning – generally related to non-cratonic crust – in their recent geological history. Mantle xenoliths in (Archean) cratonic regions (*e.g.* Kaapvaal craton: Boyd and Nixon, 1978; Gurney and Harte, 1980; Nixon, 1987; Boyd, 1989; Grégoire et al., 2005; Baptiste et al., 2012; Udachnaya, Siberia: Sobolev et al., 1973; Pokhilenko et al., 1993; Ashchepkov et al., 2010; Kimberley: Dawson and Smith, 1977; Boyd et al., 1983; Grégoire et al., 2002; Lazarov et al., 2009) are characterized mainly by garnet-facies peridotites, which include SCLM samples from depth ranging from crustal levels to over 200 km (Pearson et al., 2003). On the other hand, non-cratonic mantle xenoliths are derived from depths less than 140 km; garnet-facies mantle xenoliths are scarce in these localities (Pearson et al., 2003). There are elusive differences between mantle xenoliths erupted in cratons and those in circum-cratonic stable areas of Proterozoic crust. For instance, the maximum depth of provenance of circum-cratonic peridotite suites are shallower than for cratonic mantle samples (Pearson et al., 2003 and references therein). The xenoliths sampled from ‘young’ active tectonomagmatic environment (*e.g.* Victoria, SE Australia: Frey and Green, 1974; O’Reilly and Griffin, 1988; Yaxley et al., 1991; Powell et al., 2004; Vitim: Ionov et al., 1993; Litasov et al., 2000; Ashchepkov et al., 2011; Pannonian Basin: Embey-Isztin, 1976; Bali et al., 2002; Szabó et al., 2004; Coltorti et al., 2007; Kovács et al., 2012) fall into the loose category of non-cratonic xenoliths (*cf.* Griffin et al., 1999 for a more comprehensive description of SCLM xenoliths). Among these later, rare mantle xenoliths are found in settings recording recent subduction near-cratons, or in Phanerozoic mobile belts and orogenic areas recording processes of thinning and destruction of the SCLM. The latter, allows investigating the processes responsible for the modifications of the SCLM in convergent settings.

1.7. Modification of the SCLM Mantle Beneath Convergent Settings: Cases of Study

As described above, in order to quantify and understand the mechanisms involve in the generation and modification of tectonic plates – and particularly those related with

continents—it is fundamental to understand the processes that compositionally and rheologically modify the subcontinental lithospheric mantle at convergent plate boundaries. Convergent plate margins (> 55 000 km) (Lallemand, 1999; Stern, 2002 and references therein) cover almost the same extension as that of mid-ocean ridges (60 000 km). Subduction zones are convergent plate margins where material is either recycled to the surface through arc volcanism or transferred deep into the mantle. Subduction zones play a significant role in the generation of explosive volcanic activity, high-magnitude earthquakes, rapid geomorphological evolution and inverted geotherms (Poli and Schmidt, 2002). The effect of subduction zones on crustal evolution is preserved in the overriding plate where at some distance from the trench occurs an arcuate chain of volcanoes—the volcanic arc—formed by magmas produced by dehydration melting of the mantle wedge above the incoming subducting slab. In contrast to other tectonic settings, arc magmatic rocks are characterized by a large compositional diversity as shown by their wide distribution on standard classification schemes (*e.g.* Streckeisen 1974, 1976; Le Maitre et al. 2002); their composition ranges from mafic to felsic such as tholeiitic (low K) (mostly in island arcs) and calc-alkaline (medium to high K) series (mostly in continental arcs). Both lava series show a complete spectrum of rock types ranging from basalt through rhyolite. However, most of these volcanic suites are mantle xenolith barren, and hence do not provide samples of the SCLM.

Although rare, alkaline magmatism also occurs and usually records the latest evolutionary stages of subduction zones associated with asthenospheric upwelling through slab “windows” produced by break off or tearing of the slab. This alkaline volcanism commonly entrains to the surface mantle and crust xenoliths, which provide a unique opportunity to investigate geochemical processes and the petrophysical nature of the lithospheric mantle beneath these convergent settings. Most xenoliths are spinel lherzolite and its metasomatized variants such as wehrlite; composite xenoliths also occur. Typical metasomatic phases may include pargasite or kaersutite, phlogopite, apatite, and grain-boundary oxides, *e.g.* rutile. Some well-known type localities are Itinome-Gata (Japan; Aoki, 1971) and Simcoe (USA; Brandon et al., 1999).

In this Thesis, I investigated the processes related to the compositional and structural modifications of the SCLM in convergent settings as revealed by the petro-structural and geochemical study of mantle xenoliths hosted in alkaline magmatism in two cases studies from the Sangilen Plateau and the SE Iberian Volcanic Province (Fig. 9). The first case study are rare, mantle xenoliths hosted in lamprophyres from Tuva in the Sangilen Plateau (Fig. 9) that characterize the circum-cratonic SCLM areas recording modification of the SCLM

around cratons and associated to subduction and continental collision. The second case study are mantle xenoliths from the SE Iberian Volcanic Province (Fig. 9) that characterize an anomalously thin SCLM strongly modified by a protracted evolution recording supra-subduction magmatism and strong lithospheric thinning related to subcontinental delamination. The SE Iberian Volcanic province exemplifies a boundary plate setting between Iberia and the Alboran lithosphere where the SCLM has been strongly compositionally and tectonically modified acquiring thicknesses more akin to those of oceanic lithosphere, and hence allowing the investigation of the processes allied to the destruction of SCLM; this locality is one of the few worldwide localities where samples of plagioclase-facies peridotite mantle xenoliths are found. Below I provide more details about the geological setting of these two unique SCLM mantle xenolith occurrences.

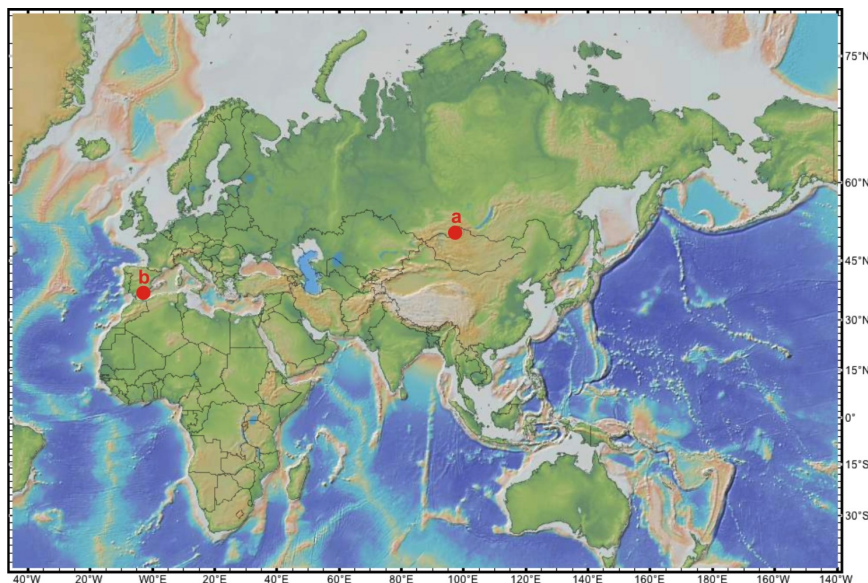


Fig. 9 A general view of the studied locations, the Sangilen Plateau (a) in Tuva (Russia) and SE Iberian Volcanic Province (SE IVP; b) in Murcia (Spain) are marked with red dots.

1.7.1. The Sangilen Plateau (Tuva, Russia) Mantle Xenoliths

The Central Asian orogenic belt was formed by accretion of continental, oceanic and island arc tectonic blocks at the southern edge of the Siberian craton during the Neoproterozoic and Paleozoic (Berzin et al., 1994; Mossakovskii et al., 1993). One of the largest blocks accreted during this orogeny was the Tuva-Mongolian microcontinent, whose southwestern part is constituted by the Sangilen Plateau (Fig. 10) (Vladimirov et al., 2005). This plateau is primarily made up of amalgamated metamorphic and igneous complexes (Fig. 10) that were first interpreted as the Archean-Paleoproterozoic basement of the Tuva-Mongolian microcontinent (Ilyin, 1990; Zonenshain et al., 1990). However, later studies have shown that

these rocks are not related to the Proterozoic accretion, but they are Cambrian-Ordovician metamorphic and plutonic complexes (Izokh et al., 2001). These complexes are intruded by ultramafic to felsic igneous rocks (Izokh et al., 2001; Vladimirov et al., 2005) (Figure 10). One of the youngest igneous episodes (447–441 Myr) formed the Agardag alkaline lamprophyre dike complex (Gibsher et al., 2012; Izokh et al., 2001; Vladimirov et al., 2005) (Fig. 10; dark triangles).

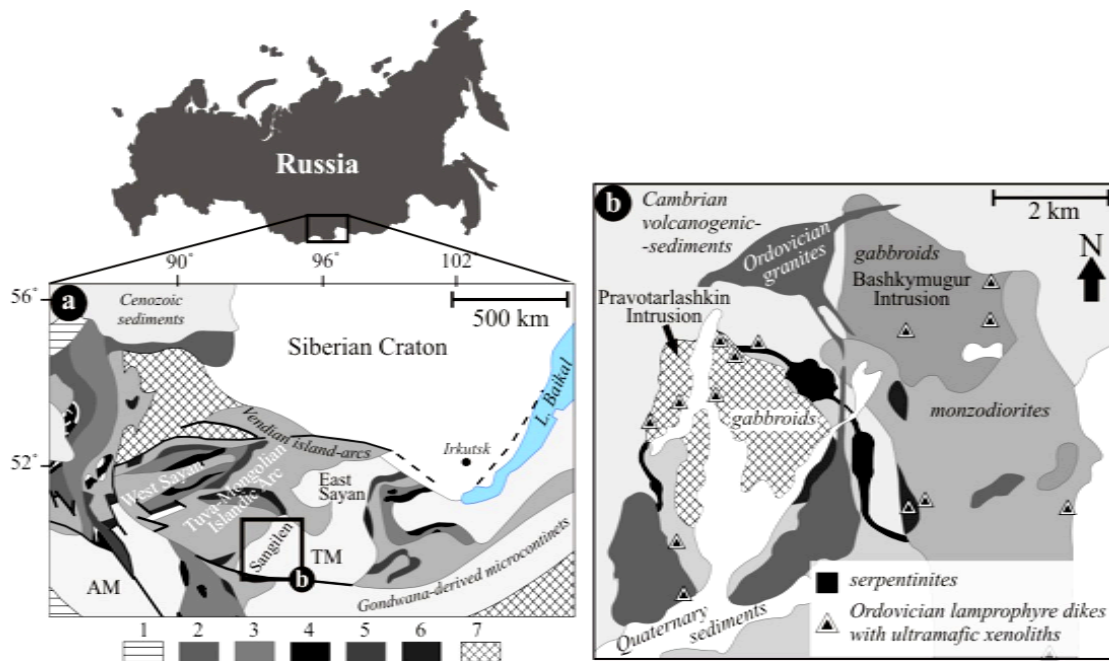


Fig. 10 (a) Simplified geological map of the Central Asian Orogenic Belt in southern Russia (inset) (modified after Dobretsov and Buslov, 2007). AM and TM refers respectively to the Gondwana derived micro-continents of Altai-Mongolian and Tuva-Mongolian. Legend of tectonic units: 1-Hercynides; 2-Cambrian island arc calc-alkaline volcanic series; 3-Neoproterozoic-Cambrian accretionary prisms; 4-Neoproterozoic-Cambrian ophiolites; 5-Neoproterozoic supra-subduction ophiolites; 6-Neoproterozoic-Cambrian ophiolitic basalts; 7-Middle-Late Paleozoic volcano-sedimentary basins. (b) Simplified geological map of the Sangilen Plateau (see inset in Fig. a) showing the location of the intrusive Ordovician Agardag lamprophyre dikes containing mantle peridotite xenoliths (modified after Egorova et al., 2006).

Agardag alkaline lamprophyres are camptonites (Izokh et al., 2001); in terms of total alkalis ($\text{Na}_2\text{O} + \text{K}_2\text{O}$) versus SiO_2 content they are characterized by high alkalis and low SiO_2 contents similar to foidite and basanite lavas (Rock, 1991). These lamprophyre dikes are intrusive into the Moren metamorphic complex, the Cambrian volcanogenic-sedimentary units, the Pravotarlashkin troctolite-anorthosite-gabbro complex, and the Ordovician Bashkymugur gabbro-norite and monzodiorite (Fig. 10b) (Izokh et al., 2001; Vladimirov et al., 2005). These lamprophyre dikes contain rare mantle xenoliths (Egorova et al., 2006) that are the subject of the present study and will be referred below to as Sangilen xenoliths.

1.7.2. Mantle Xenoliths Hosted in Alkaline Basalts from the SE Iberian Volcanic Province (Murcia, Spain)

The Betic Cordillera is part the Betic-Rifean orogenic belt (or peri-Alboran orogenic system), an arc-shaped collisional mountain belt bordering the Alboran Sea, which constitutes the westernmost segment of circum-Mediterranean Alpine orogenic system in southwestern Europe (Fig. 11). This orogen was generated during the convergence of the Nubia and European plates in Tertiary times (Dewey et al., 1989) and underwent large-scale extensional collapse in the Early Miocene (e.g. Platt and Vissers, 1989; Galindo-Zaldívar et al., 1989).

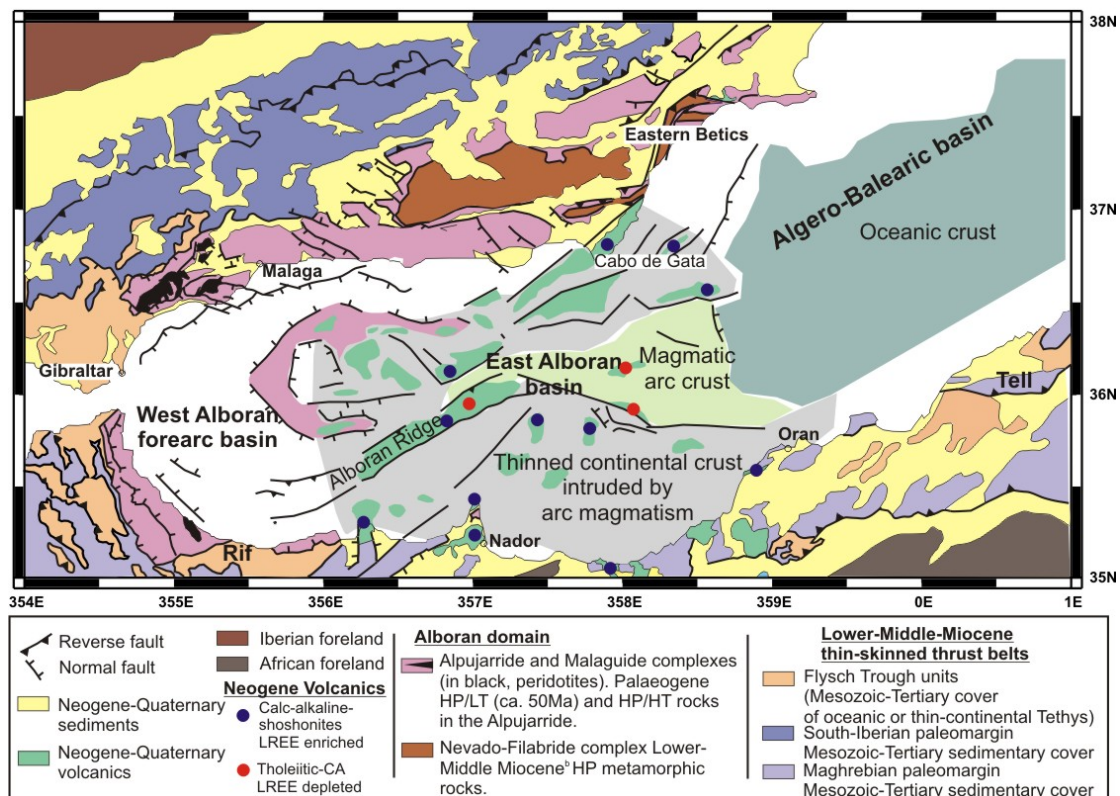


Fig. 11 Simplified geological map showing the main tectonic domains and the different three major areas formed by oceanic, magmatic arc and continental crust of the Western Mediterranean, with igneous geochemical data and age of metamorphism (after Booth-Rea et al., 2007 and reference therein).

This arched orogenic belt is characterized by a thrust of high-grade metamorphic rocks (Fig. 11) including plurifacial high-pressure peridotite complexes, and Neogene-Quaternary arc-like volcanism (Fig. 11 & 12). Three main paleo-geographic domains can be distinguished in the chain: the south Iberian plate and the Maghrebian (Africa foreland) paleomargins (also called 'External Zones'); the Flysch trough units composed of deep-water sediments; and the metamorphic complexes of the Alboran Domain (traditionally called 'Internal Zones'). The Alboran Domain has been traditionally divided into three metamorphic domains that from

bottom to top, are: the Nevado-Filábride, the Alpujárride and the Maláguide complexes; however, recent studies indicate that the deepest Nevado-Filábride complex underwent middle-Miocene HP-LT, subduction metamorphism and it is currently interpreted as the remnants of the Iberian paleomargin subducted beneath the Alboran domain and rapidly uplifted in the Miocene along a NE-SW striking core complex currently exposed in the Sierra Nevada extensional dome (Fig. 11). Therefore, strictly speaking, only the Maláguide (Blumenthal, 1929) and the Alpujárride complexes—which consist mainly of metasedimentary Mesozoic and pre-Mesozoic rocks (Egeler and Simon, 1969; Gómez-Pugnaire et al., 1982)—and their equivalents in the Rif Belt—the Ghormarides and Septides complexes—constitute the Alboran domain (Fig. 11). These metamorphic complexes underwent pervasive Alpine deformation and metamorphism that obliterated most of the effects of pre-Alpine deformational events.

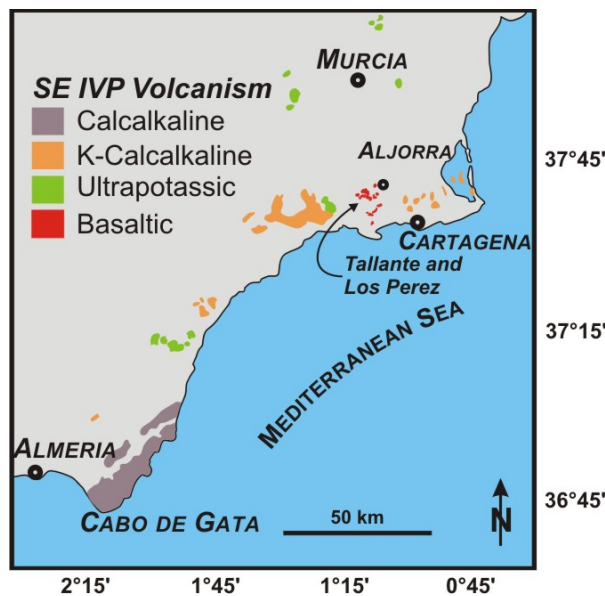


Fig. 12 Geological sketch displaying the distribution of alkaline basalts of Tallante and Los Perez volcanic centers within the SE Iberian Volcanic Province (modified after Cebriá et al., 2009).

Cenozoic post-orogenic volcanism is widespread in SE Iberia, the Alboran basin and SE African branch of the Betic-Rif belt. Many geochemical, isotopic and geochronological studies have been published on the Cenozoic volcanic rock from this area. In the Betic-Rif belt, the oldest Alpine magmatic rocks correspond to 33.6-17 Myr tholeiitic dike swarms intruding in the Maláguide complex (Torres-Roldán et al., 1986; Turner et al., 1999; Duggen et al., 2004) and late Oligocene andesitic-like volcanism intruding in the Ronda peridotite (Marchesi et al., 2012). Most other volcanism occurred in the Miocene and was broadly

coeval with extension and subsidence of the Alborán Sea Basin—Early to Middle Miocene—and orogenesis in the surrounding arcuate Betic-Rif mountain belt (Comas et al., 1999; Jolivet and Faccenna, 2000; Lonergan and White, 1997; Booth-Rea et al., 2007). Neogene-Quaternary volcanism in the Alboran Basin includes Middle to Late Miocene tholeiitic to calc-alkaline lavas in the present day Alboran Sea Basin (Fig. 11), and Neogene to Quaternary Alborán Island and coastal volcanic complexes in southeastern Spain, here collectively referred to as the South East Iberian Volcanic Province (SE-IVP) (Fig. 12), and coastal volcanic complexes in the Rif and Tell chains (Fig. 11) (Benito et al., 1999; Coulon et al., 2002; Duggen et al., 2005, 2004, 2003; El Bakkali et al., 1998; Gill et al., 2004; Hoernle et al., 1999; Turner et al., 1999).

Neogene to Quaternary continental margin igneous activity in the SE IVP includes Late Miocene to Plio-Pleistocene shoshonitic igneous rocks and basanites/alkali basalts and their derivatives (Fig. 11) (Benito et al., 1999; Duggen et al., 2005, 2004, 2003; Gill et al., 2004; Hoernle et al., 1999; Turner et al., 1999). In the SE IVP, alkali basalts contain abundant crustal high-grade metamorphic, mafic and ultramafic xenoliths and megacrysts (Vielzeuf, 1983; Dupuy et al., 1986; Arai et al., 2003; Beccaluva et al., 2004; Shimizu et al., 2004, 2008; Rampone et al., 2010; Bianchini et al., 2011). Alkali basalt at the volcanic centers of Cabezo Negro de Tallante and Los Perez host many lithospheric mantle xenoliths that have been the subject of study of the present Thesis (*cf.* Part 2) (Fig. 12).

Numerous geodynamic models have been proposed to account for the Cenozoic tectonomagmatic evolution of the Betic-Rif belt; these models can be subdivided into six major groups (Doblas et al., 2007): Subduction models combining nearly all of possible scenarios (*e.g.* Morales et al., 1999; Puga et al., 2002; Duggen et al., 2003, 2004), compressional models (Fontboté, 1986; Piqué et al., 1998), purely extensional models (Platt and Vissers, 1989; Turner et al., 1999) related with detachment lithospheric roots or subducting slabs (Houseman, 1996; Platt et al., 1998; Turner et al., 1999; Calvert et al., 2000), transtensional models (*e.g.* López-Ruiz et al., 2002; 2004) and in situ mantle upwelling models (Weijermars, 1991). These geodynamic models will be discussed in more detail in the light of the results of our study of mantle xenoliths hosted in alkali basalts from the SE IVP.

2. Aims and Structure of the Thesis

2.1. Aims of the Thesis

The main goal of the present PhD. Thesis is to investigate the petrophysical nature, geochemical composition and evolution of the SCLM beneath convergent settings as sampled by mantle xenoliths entrained by alkaline magmatism. As introduced earlier, alkaline magmatism often occur in the latest evolutionary stages of convergent settings providing rather unique samples of the SCLM that record the tectonomagmatic processes that modify the SCLM during the convergence stage. In this Thesis I will focus on two cases of study exemplifying the evolution of the SCLM in different convergent settings (i.) involving circumcratonic SCLM (Tuva, Sangilen Plateau, Russia) and (ii.) involving highly attenuated SCLM recording supra-subduction and slab delamination tectonomagmatic processes related to the Tertiary Alpine evolution and formation of the Alboran Sea Basin in the westernmost Mediterranean (Murcia, South-Eastern Iberian Volcanic Igneous Province, SE Spain). These two localities provide a unique opportunity to investigate the SCLM of different age affected by convergent setting tectonomagmatic processes. In both localities, alkaline magmatism was the latest magmatic event of the convergent stage and sampled numerous mantle xenoliths that provide a snapshot of the deformation, melting and metasomatism record of the SCLM beneath this setting. In order to investigate the petrophysical nature and geochemical composition and evolution of the SCLM beneath these convergent settings I will combined detailed petrological and petrostructural studies of mantle xenoliths with geochemical characterization including bulk and mineral major, trace and Sr-Nd-Pb radiogenic isotopic and *in situ* Re-Os isotopic analyses using state-of-the-art laboratory and instrumental techniques. These data are combined and mined to unveil the thermal, petrostructural and seismic characteristic of the SCLM beneath these regions, as well as used to identify the age and inheritance of melting events, and the melt-rock reaction and metasomatic processes involved in the compositional modification of the SCLM in these settings.

2.2. Outline of the Thesis

The Thesis is subdivided into five major parts:

In **PART I**, the Introduction (Chapter 1) I have provided some introductory notions to acquaint the reader with the main subject of the Thesis and gain a better grasp of the aims and motivation behind this work. I summarized some basic concepts, starting with a brief

introduction about the Earth's plate tectonics and convergent settings, with emphasis on subduction zones. Furthermore, I introduced the notion of the subcontinental lithospheric mantle, particularly our knowledge on lithospheric (upper) mantle by means of mantle xenoliths (structure, lithology, equilibrium temperature and pressure, geochemical features and so on). I also briefly recalled the main types of mantle xenolith occurrences, and I have introduced the geological setting of the xenolith occurrences investigated here. The current section, Aims & Thesis Structure (Chapter 2), presents the main objectives and motivation of the Thesis and its structure. This section is followed by the description of the Methodology (Chapter 3), highlighting the multidisciplinary approaches and state-of-the-art analytical methodologies that have provide an extensive and novel database of the petrostructure and composition of the studied mantle xenoliths. These approaches encompass different geochemical and instrumental techniques (*e.g.* EPMA, LA-, MC-ICP-MS, TIMS) and petrophysical and classical petrological methods (*e.g.* EBSD, SEM, microscopy).

PART II presents the main Results of this Thesis and is subdivided into three major chapters. Chapter 4 presents the studies of lamprophyre hosted mantle xenoliths from Sangilen Plateau (Tuva, Russia). This chapter has been published in *LITHOS*—a top ranked journal in the research field of Mineralogy—and I am the first and corresponding author. Chapters 5 to 7 deal with the study of upper mantle xenoliths from the SE IVP in Spain. Chapter 5 deals with the petrostructural and petrophysical study of these xenoliths. The study is aimed at investigating the structure, deformation record and seismic characteristics of the SCLM beneath SE IVP, and the interpretation of the dataset in the light of recent regional seismic anisotropy surveys. Chapter 6 presents a detailed geochemical characterization of SE IVP SCLM. This comprehensive study encompasses major, trace element and radiogenic isotopes data of peridotite mineral and whole rocks; in addition to Sr-Nd isotopes, it provides the first Pb dataset of xenoliths from the SE IVP. These dataset is used to decipher the melting and metasomatic events recorded by the SCLM beneath this area, and related them to the complex geodynamic evolution recorded by the Alboran orogenic system. Chapters 5 and 6 have been submitted as papers to *Geochemistry*, *Geophysics*, *Geosystems (G3)* and *Chemical Geology*, respectively, both first-quartile, ISI journals in the research fields of Geophysics and Geochemistry; in both papers, I am the first and corresponding author. Finally, Chapter 7 shows the result of collaborative study wherein I have contributed with the in situ Re-Os study of sulfides in SE IVP xenoliths as part of a broader a study of the provenance of the westernmost Mediterranean SCLM. I am a co-

author of this study, which has been published in *GEOLOGY*, a first-rank journal in the research field of Geology.

Finally, **Part III** contains the main conclusions of the present Thesis (Chapter 8). **Part IV** presents the references cited (Chapter 9), and **Part V** includes the appendixes providing sample location and the extensive dataset obtained during this work not presented elsewhere in the Thesis.

3. Methodology

3.1. Sampling and Sample Preparation

3.1.1. Sampling

Mantle xenoliths from Tuva (southern Siberia, Russia) were collected from Agardag alkaline lamprophyre dikes of Sangilen Plateau (*cf.* Part 4 for further details) by Professor Victor V. Sharygin, who made them available for our study. Mantle xenoliths hosted in alkali basalts of SE IVP (Murcia, Spain) were collected from the volcanic centers of the Cabezo Negro de Tallante and Los Perez during field campaigns in 2008; the two volcanic centers are 3 km far from each other. Mantle xenoliths were selected on the basis of the lack of macroscopic or microscopic signs of contamination by their host magma, and their representativeness in terms of their macroscopic texture and modal composition.

3.1.2. Thin-section Preparation

Selected xenoliths were cut into slabs with a diamond saw (University of Granada, Spain). In each slab, one of several chips representative of the main textural and compositional features of the xenolith were marked and cut. Thin section chips were grinded and then polished using 3 μm diamond grit using Buehler™ polishing pads, then glued onto a 26x46 mm size thin-section glass with two-component petrological epoxy. Mounted thick sections were cut with a slow speed, high precision diamond saw to obtain a *ca.* 80-100 μm thick section. The thick sections were subsequently grinded and polished using Buehler™ polysynthetic diamond at 3 and 1 μm grit steps; if necessary they were further polished using a 0.25 μm diamond grit step.

For EBSD-SEM measurement (see later), thin sections required additional polishing. Diamond polishing induces damage to crystals in the uppermost surface of the thin section that must be removed to obtain high-quality Kikuchi diffraction patterns under the EBSD-SEM. Thus, standard diamond polished thin sections were further polished during 5 min. with a chemical and mechanical procedure using Buehler™ and Mastermet™ colloidal silica suspension.

3.1.3. Preparation of Whole Rock Powders and Clinopyroxene Separates

Samples were processed at the rock-crushing laboratory of the Department of Mineralogy and Petrology (University of Granada, Granada, Spain) and Geosciences Montpellier (University of Montpellier 2, Montpellier, France). After removal of altered surfaces with a

diamond saw, rock specimens were cut into 3-4 cm cubic chips and then ultrasonically washed in water during 15 minutes. Once dried, they were crushed in a steel jaw crusher. Representative samples of crushates for powdering were obtained using a riffle-splitter. The crushate leftover was stored for subsequent mineral separation.

Whole rock powders ($< 2 \mu\text{m}$ mesh sieve) were obtained by milling crushates in an agate ring mill for about ca. 30 minutes; the precise duration of milling depended on the rock type. In order to avoid cross-contamination, before milling a new sample the ring mill was carefully cleaned with compressed air, alcohol, and by milling quartz chips. For each sample, powder was split into three representative subsamples and stored in distinct clean PVC vials for X-Ray Fluorescence (XRF), Inductively Coupled Plasma-Mass Spectrometry (ICP-MS) and whole rock isotopic analyses.

Ultraclean, nominally inclusion-free clinopyroxene separates were obtained from peridotite crushates in several sequential steps. In the first step, seven grain fractions were sieved and separated: $< 63 \mu\text{m}$, $63\text{-}125 \mu\text{m}$, $125\text{-}250 \mu\text{m}$, $250\text{-}500 \mu\text{m}$, $500\text{-}720 \mu\text{m}$, $720\text{-}1000 \mu\text{m}$ and $> 1000 \mu\text{m}$. Fractions in mesh sieves coarser than $250 \mu\text{m}$ were further milled and sieved until sample depletion to obtain enough fine fractions suited for manual separation of clean clinopyroxene crystals. After processing each sample, sieves were carefully cleaned by compressed air, plastic brush, metallic needle and alcohol to avoid cross-contamination and remove any grain from the previous sample. The $125\text{-}250 \mu\text{m}$ mesh fraction was then ultrasonically cleaned with ultrapure water, dried and then processed by magnetic separation in a Frantz® Magnetic Barrier Laboratory Separator (Model LB-1; Fig. 13) to obtain clinopyroxene concentrates. Clean clinopyroxene were handpicked from concentrates immersed in alcohol under a binocular zoom microscope to remove composite and altered grains, as well as grains hosting visible inclusions.

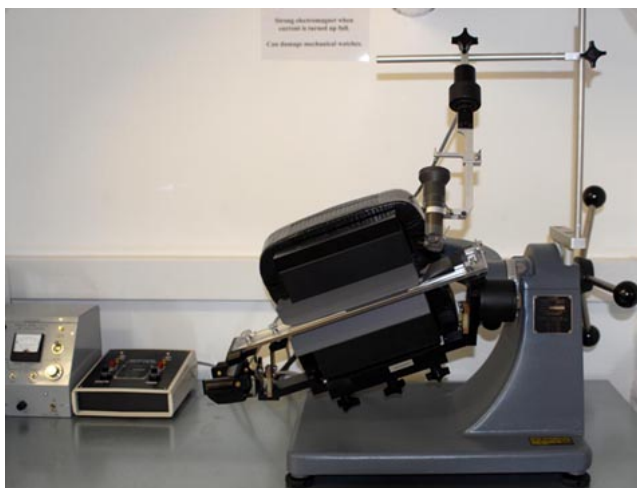


Fig. 13 Frantz® Magnetic Barrier Laboratory Separator.

3.2. Electron Probe Microanalyses (EPMA)

An electron probe microanalyzer (Fig. 14) is a microbeam instrument used primarily for the *in situ* non-destructive chemical analysis of minute solid samples. It is fundamentally the same as an SEM (see later), with the added capability of chemical analysis (Reed, 1995, 2005). The primary importance of an EPMA is the ability to acquire precise, quantitative elemental analyses at very small spot sizes (as little as 1-2 microns), primarily by wavelength-dispersive spectroscopy (WDS). The spatial scale of analysis, combined with the ability to produce detailed images of the sample, makes it possible to analyze geological materials *in situ* and to resolve complex chemical variation within single phases.

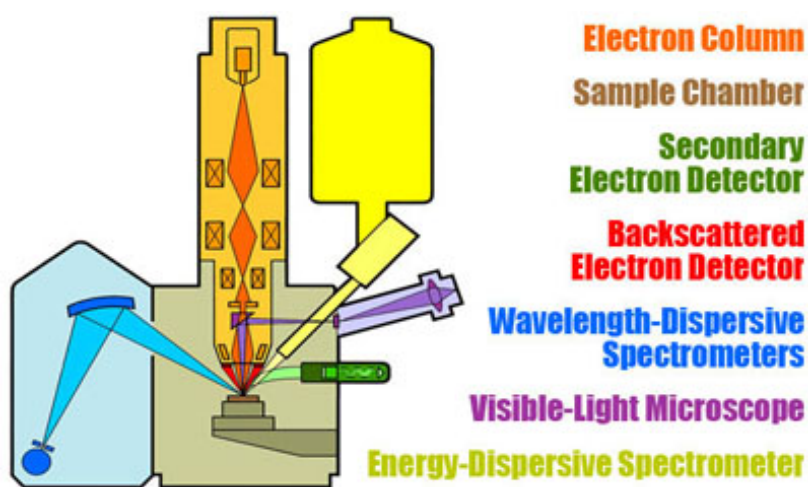


Fig. 14 Schematic diagram of a typical microprobe (after John Goodge).

3.2.1. Wavelength Dispersive (X-Ray) Spectroscopy (WDS)

Once an electron beam of sufficient energy interacts with a sample target it produces X-rays, as well as derivative electrons (*e.g.* secondary, back-scattered, auger; Fig. 15). A wavelength-dispersive spectrometer uses the characteristic X-Rays generated by individual elements to enable quantitative analyses (down to atomic number 5, boron) to be measured at spot sizes as small as a few micrometers (Reed, 1995, 2005). WDS can also be used to create element X-Ray compositional maps. Together, these potentials offer fundamental quantitative compositional information for a wide range of solid materials, and an EPMA typically has an array of numerous WDS spectrometers for synchronized measurement of various elements.

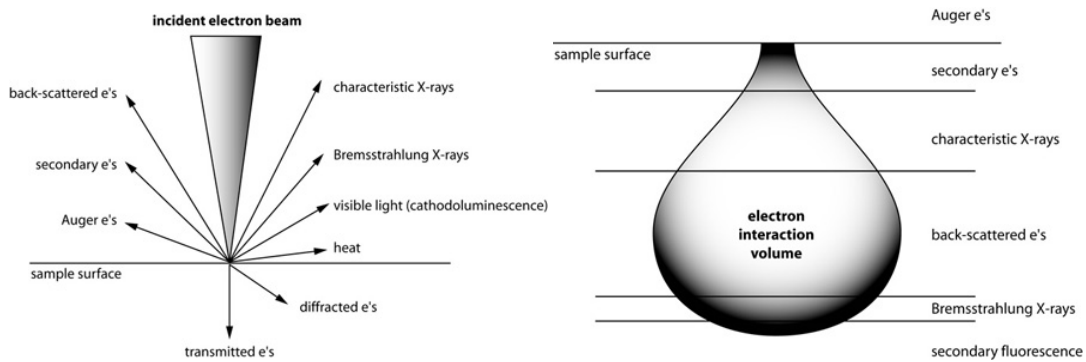


Fig. 15 Type of interactions between electrons and a material (**left**) with their volume within the sample (**right**). (Figures are after Darrell Henry.)

3.2.2. Fundamental Principle of EPMA

An electron microprobe runs under the principle that if an accelerated and focused electron beam attacks a solid material, the incident electron beam has sufficient energy to release both matter and energy from the sample. These electron-sample interactions principally liberate heat, but they also yield both derivative electrons and X-Rays. Of most common interest in the analysis of geological materials are secondary and back-scattered electrons, which are practical for imaging a surface or obtaining an average composition of the material. X-Ray generation is produced by inelastic collisions of the incident electrons with electrons in the inner shells of atoms in the sample; when an inner-shell electron is ejected from its orbit, leaving a vacancy, a higher-shell electron falls into this vacancy and must shed some energy (as an X-Ray) to do so (Reed, 2005). These quantized X-Rays are characteristic of the element. EPMA analysis is considered to be non-destructive; that is, X-Rays generated by electron interactions do not lead to volume loss of the sample, so it is possible to re-analyze the same materials more than one time.

EPMA consists of four major components, from top to bottom (Reed, 2005): **(i.)** an electron source, regularly a W-filament cathode referred to as a 'gun'. **(ii.)** A series of electromagnetic lenses located in the column of the instrument, used to condense and focus the electron beam emanating from the source; this comprises the electron optics and operates in an analogous way to light optics. **(iii.)** A sample chamber, with movable sample stage (x, y, z), that is under a vacuum to prevent gas and vapor molecules from interfering with the electron beam on its way to the sample; a light microscope allows for direct optical observation of the sample. **(iv.)** A variety of detectors arranged around the sample chamber that are used to collect X-Rays and electrons emitted from the sample.

Major element composition of minerals were obtained by Electron Probe Microanalyses (EPMA) in *ca.* 80 μm thick, standard thin sections, using the following microprobes from different institutions:

- JEOL Superprobe JXA8100 and CAMECA SX50 instruments at the Institute of Geology, Siberian Branch of the Russian Academy of Science in Novosibirsk (Russia).
- CAMECA SX100 instrument at the Centro de Instrumentación Científica (CIC) in the University of Granada in Granada (Spain).
- CAMECA SX100 instrument at the Geosciences Montpellier of the CNRS and the University of Montpellier 2 in Montpellier (France).

The following measurement conditions were used; the accelerating voltage were 15 kV at Granada and 20 kV at Novosibirsk and Montpellier, sample current 7, 10 and 15 nA and beam diameter 5 μm . Counting times were 10-30 s. Natural and synthetic silicate and oxide standards were used for calibration and ZAF correction.

3.3. Laser Ablation Inductively Coupled Plasma Mass Spectrometer (LA-ICP-MS)

In Laser Ablation Inductively Coupled Plasma Mass Spectrometry (LA-ICP-MS) the sample is directly analyzed by ablating with a pulsed laser beam (Fig. 16). In the latter, solid aerosols are transported into the core of inductively coupled argon plasma (ICP), which generates temperature of approximately 8000 °C. The plasma in ICP-MS is used to generate ions that are afterward introduced to the mass analyzer. These ions are then separated and collected according to their mass to charge ratios. ICP-MS offers extremely high sensitivity to a wide range of elements. Depending on the analytical measurement system, very small amount of sample quantities may be sufficient for this technique. In addition, a focused laser beam allows spatial characterization of heterogeneity in solid samples, with typically micron resolution both in terms of lateral and depth conditions.

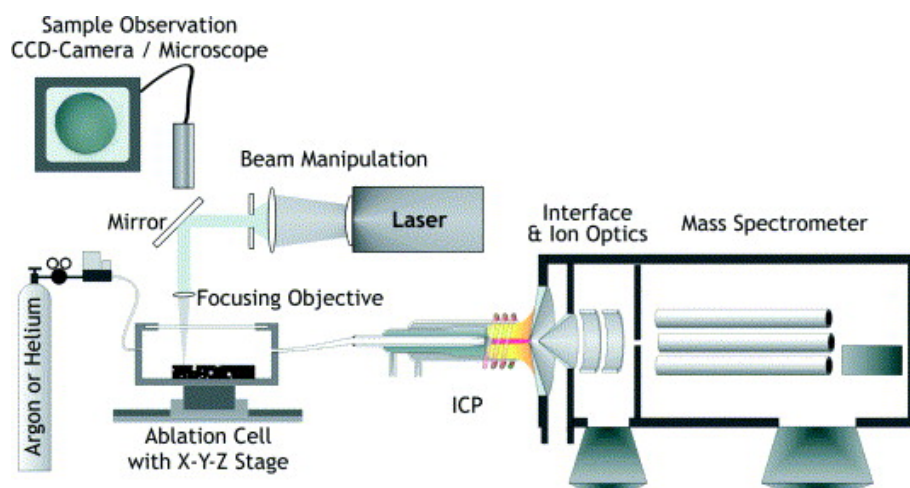


Fig. 16 Schematic set-up of Laser Ablation Inductively Coupled Plasma Mass Spectrometer (LA-ICP-MS) (after Günther and Hattendorf, 2005)

In situ trace element analyses of clinopyroxene were carried out by LA-ICP-MS. Analyses were performed at Geosciences Montpellier (France) using a ThermoFinnigan ELEMENT XR sector field ICP-MS coupled with a Geolass (Microlas) automated platform housing a 193 nm wavelength Complex 102 laser from LambdaPhysik. Ablation was conducted in a cell of ca. 30 cm³ in He atmosphere, which enhances sensitivity and reduces inter-element fractionation. Signals were acquired devoting 2 minutes for the background blank and 1 minute for measurement of the sample. The laser was fired at an energy fluency of 15 J/cm² and a frequency of 6 and 8 Hz using circular spot sizes of 80-120 μm in diameter, respectively.

Concentrations were calibrated against the NIST Certified Reference rhyolite glass 612, using the values compiled by Pearce et al. (1997). Data were subsequently reduced using the GLITTER software (Van Achtebergh et al., 2001) by inspecting the time-resolved analyses to check for lack of heterogeneities in the analyzed volume. CaO was used as internal standard and BIR 1G (USGS basaltic glass reference sample) was shot in every procedure for analytical quality control.

3.4. Scanning Electron Microscopy (SEM)

The scanning electron microscope (SEM; Fig. 17) uses a focused beam of high-energy electrons to generate a variety of signals at the surface of solid specimens (Fig. 15). The signals, which derive from electron-sample interactions, show information about the sample including external morphology (texture), chemical composition, and crystalline structure and orientation of materials making up the sample. In most applications, data are collected

over a selected area of the surface of the sample, and a 2-dimensional image is generated, which displays spatial variations in these properties. Areas ranging from approximately 1 cm to 5 microns in width can be imaged in a scanning mode using conventional SEM techniques (magnification ranging from 20x to approximately 30,000x, spatial resolution of 50 to 100 nm) (Goldstein, 2003). The SEM is also capable of performing analyses of selected point locations on the sample; this approach is especially useful in qualitatively or semi-quantitatively determining chemical compositions (using EDS), crystalline structure, and crystal orientations (using EBSD, see later).

3.4.1. Energy Dispersive (X-Ray) Spectroscopy (EDS)

An energy dispersive detector is used to split the characteristic X-Rays of different elements into an energy spectrum, and EDS system with a given software is used to evaluate the energy spectrum in order to determine the abundance of specific elements. EDS can be used to find the chemical composition of materials down to a spot size of a few microns, and to create element composition maps. An EDS detector contains a crystal that absorbs the energy of incoming X-Rays by ionization, yielding free electrons in the crystal that become conductive and produce an electrical charge bias (Goldstein, 2003). The X-Ray absorption thus converts the energy of individual X-Rays into electrical voltages of proportional size; the electrical pulses correspond to the characteristic X-Rays of the element.

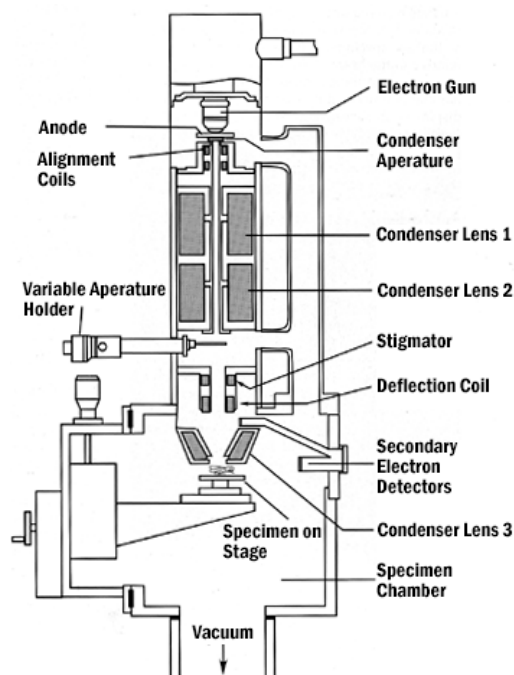


Fig. 17 Schematic set-up of construction of a Scanning Electron Microscope (SEM) with the main elements. (Image was taken form the webpage of The University of Iowa.)

Scanning electron microscope (SEM) observations were performed by secondary and back-scattered electron imaging in carbon-coated, polished, thin sections, using LEO 1430-VP equipped with energy dispersive spectrometer (EDS) at the Centro de Instrumentación Científica (UGR, Granada, Spain; <http://cic.ugr.es>). EDS Mineral inclusions (*e.g.* Apatite in Part 2) were identified using EDS spectrums and 2048x1886 pixel images under an acceleration voltage of 20 kV, a beam current of 20 nA, and a sample distance of 10 mm.

3.5. Electron Backscattered Diffraction (EBSD-SEM)

Accelerated electrons in the primary beam of a scanning electron microscope (SEM) can be diffracted by atomic layers in crystalline materials (Prior et al., 1999). These diffracted electrons are detected when they impose on a phosphor screen and generate detectable lines, called Kikuchi bands (Fig. 18), or 'EBSP's' (electron backscatter patterns). These patterns are actually projections of the geometry of the lattice planes in the crystal, and they give direct information about the crystalline structure and crystallographic orientation of the grain from which they originate. When used in combination with a database that includes crystallographic structure information for phases of interest and with software for processing the EPSP's and indexing the lines, the data can be used to identify minerals based on crystal structure and also to perform fabric analyses on polycrystalline rocks.

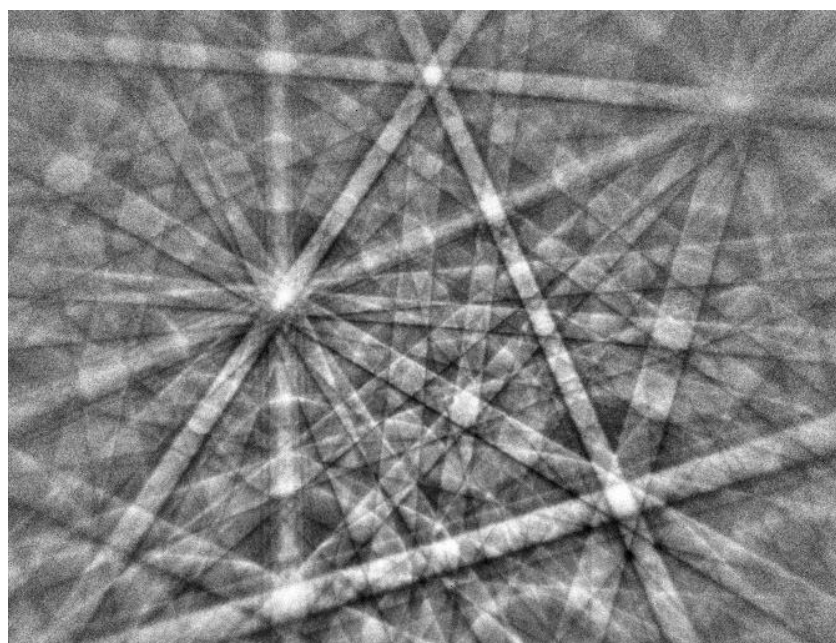


Fig. 18 The Kikuchi bands of Silicon (Si) in the initial diffraction pattern.

The polished thin-section is placed in the SEM and inclined approximately 70° relative to normal incidence of the electron beam. The detector is essentially a camera equipped with

a phosphor screen integrated with a digital frame grabber (Fig. 19). The camera resides on a horizontally mounted motorized carriage. It is inserted to within several mm of the surface of the inclined thin-section. The pattern of Kikuchi lines on the phosphor screen is electronically digitized and processed to recognize the individual Kikuchi lines (Fig. 19).

These data are used to identify the phase, to index the pattern, and to determine the orientation of the crystal from which the pattern was generated. Individual mineral grains can be chosen for identification and determination of crystal orientation, or data may be acquired on a grid over a selected area of the surface of the sample to determine the identity, orientations, and spatial relations between a large numbers of grains (Fig. 19). These data can be used to make statistical studies of the microstructure of the sample, to show systematic textural relations between individual grains or phases; and even to determine relative abundances of phases in a polyphase sample.

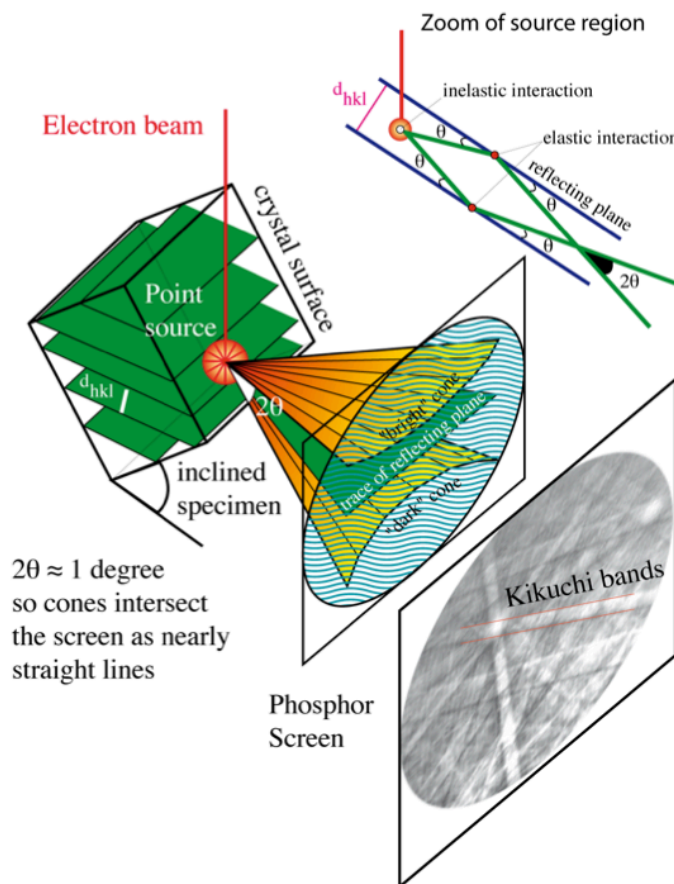


Fig. 19 Illustration of the 3D nature of the Kikuchi cones that project on the EBSD phosphor screen as nearly straight lines due to the very small Bragg angles for electrons at typical SEM accelerating voltages. The detailed geometry near the source region is shown at the top right (after D. Mainprice).

Crystal preferred orientation (CPO) of olivine, orthopyroxene and clinopyroxene were measured by indexing backscattered pattern diffraction or Kikuchi patterns. Backscattered diffraction is one of a variety of possible interactions produced, when a sample is incited by

high-energy electrons of an electron beam (Prior et al., 1999) with an acceleration voltage of 20 kV. EBSD patterns were acquired by using the SEM-EBSD systems (Fig. 20) at Geosciences Montpellier (France).

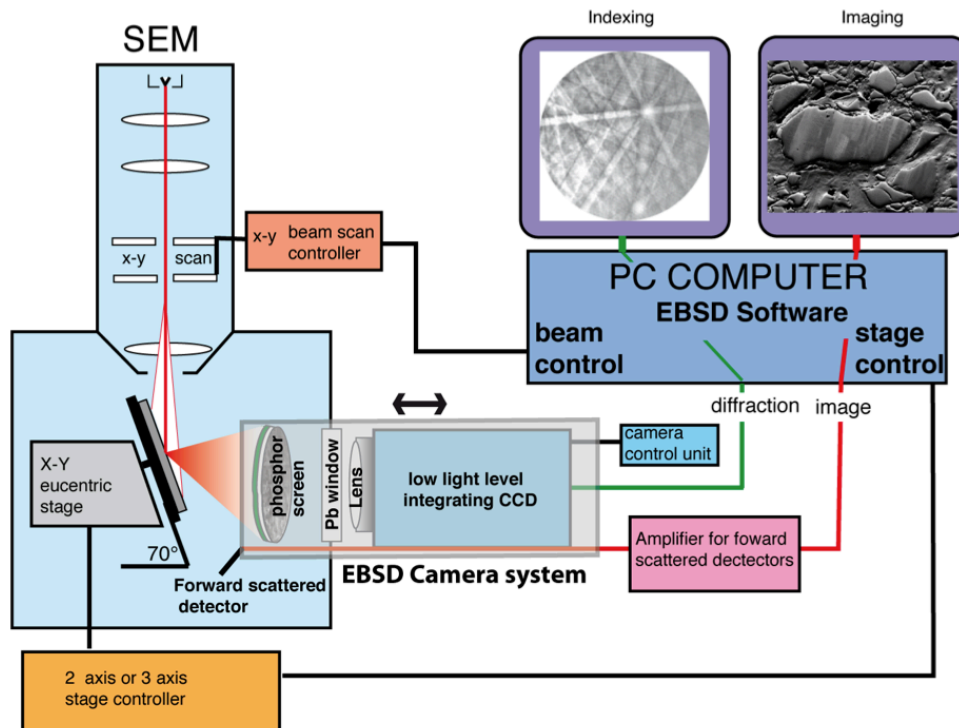


Fig. 20 Generic SEM-EBSD system at Geosciences Montpellier (France) showing all the elements essential for EBSD (after D. Mainprice)

Indexing was performed by automatic EBSD mapping of whole thin sections on a JEOL JSM 5600 (Fig. 20), using a regular grid step of 20-100 μm . Indexation rates are range from 57 to 91%. Very low indexation rate (25%) was also obtained only one time at one sample.

EBSD patterns were indexed automatically using CHANNEL 5 software package from HKL Technology. Lattice orientation by CHANNEL 5 software is achieved by automatic indexation of Kikuchi patterns, using the Hough transform and six to nine detected band edges and their zones axis in the diffraction pattern.

Post-acquisition data treatment (*cf.* Tommasi et al., 2008) allowed us to increase further the indexation rate by (i.) filling the non-indexed pixels that have up to eight identical neighbors with this orientation, (ii.) repeating this operation using respectively seven, six and five identical neighbors, (iii.) identifying the grains (*i.e.* continuous domains characterized by an internal misorientation $<15^\circ$), and (iv.) within each olivine crystal,

searching and correcting for systematic indexation errors caused by olivine hexagonal pseudo-symmetry that results in similar diffraction patterns for orientations differing by a rotation of 60° around [100].

Because the foliation and lineation could not be determined macroscopically in many samples, most thin-sections were cut in random orientation. To allow a comparison between the CPO of different samples, all the CPO measurements were rotated to have the maximum concentrations of olivine [100] and [010] axes parallel to east-west and north-south directions, respectively (Fig. 21). To avoid over-representation of large crystals, CPO is plotted as one measurement per grain (average orientation of the crystal). In order to obtain data compatible with the format of most of the already published EBSD analyses on upper mantle material (e.g. Mainprice and Silver, 1993; Ben Ismail and Mainprice, 1998; Tommasi et al., 1999; Mainprice et al., 2000; Vachez and Garrido, 2001; Vonlanthen et al., 2006; Soustelle et al., 2010), we have chosen the Unicef Careware software package (D. Mainprice) to generate orientation distribution functions (ODF) and calculate seismic properties (Fig. 21).

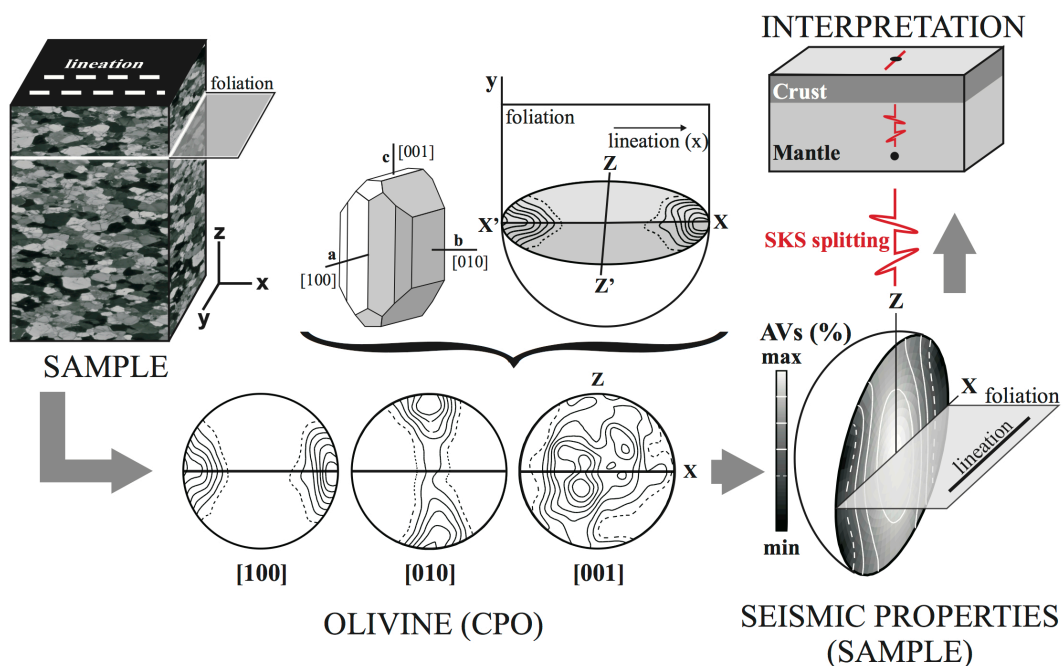


Fig. 21 General sketch about EBSD data treatment, and reading and evaluation of the pole figures (olivine) – calculated from ODF and rotated to the best axes – and the seismic properties of the bulk rock sample as well.

3.6. X-Ray Fluorescence (XRF)

An X-ray fluorescence (XRF) spectrometer is an X-Ray instrument used for routine, relatively non-destructive chemical analyses of rocks, minerals and sediments. It works on wavelength-dispersive spectroscopic principles that are similar to an electron microprobe (EPMA). However, an XRF cannot generally make analyses at the small spot sizes characteristic of EPMA work (2-5 microns), so it is typically used for bulk analyses of larger fractions of geological materials.

The analysis of major and minor transition elements in geological materials by X-Ray fluorescence is made possible by the behavior of atoms when they interact with radiation (Fitton, 1997). When materials are energized with high-energy, short wavelength radiation (*e.g.* X-Rays), they can become ionized. If the energy of the radiation is sufficient to remove a tightly held inner electron, the atom becomes unstable and an outer electron replaces the missing inner electron (Fitton, 1997). When this happens, energy is released due to the decreased binding energy of the inner electron orbital compared with an outer one. The emitted radiation is of lower energy than the primary incident X-Rays and is termed fluorescent radiation. Because the energy of the emitted photon is characteristic of a transition between specific electron orbitals in a particular element, the resulting fluorescent X-Rays can be used to detect the abundances of elements that are present in the sample (Fitton, 1997).

Whole rock major and minor transition elements (V, Cr and Ni) in mantle peridotites from SE IVP (Part 2) were analyzed at the Centro de Instrumentación Científica (Spain) by BRUKER D8 ADVANCE X-Ray Fluorescence (XRF) instrument equipped with six analyzer (LiF200, LiF220, Ge, PE, PX1, PX2) using standard sample preparation and analytical procedures.

Whole rock powders were mixed with a lithium tetraborate ($\text{Li}_2\text{B}_4\text{O}_7$) / metaborate (LiBO_2) flux and fused in a platinum-gold alloy crucible in an induced furnace for 20-40 minutes. The resultant glass disk was placed in a sample holder and excited with a rhodium anode tube operating at 3 or 4 kW. Usual detection limits are 0.01% for major elements and 1-5 ppm for trace elements. Loss on ignition (LOI) was directly determined only on several samples by drying 0.5 grams of whole rock powder at 110 °C and placing it in a furnace at 1000 °C for 1 hour.

3.7. Inductively Coupled Plasma Mass Spectrometer (ICP-MS)

Inductively Coupled Plasma (ICP) analytical techniques can quantitatively measure the elemental content of a material from the ppt (pg/g) to the wt% range. Solid samples are dissolved or digested in a liquid, usually an acidic aqueous solution and the sample solution is then sprayed into the core of an inductively coupled argon plasma, which can reach temperatures of approximately 8000 °C. At such high temperature, all chemical constituents are atomized, ionized and thermally excited, and they can then be detected and quantified with a mass spectrometer (MS). ICP-MS measures the masses of the element ions generated by the high temperature argon plasma. The ions created in the plasma are separated by their mass to charge ratios. ICP-MS offers extremely high sensitivity (*i.e.* low detection limits) for a wide range of elements.

Whole-rock trace elements (Rb, Sr, Y, Zr, Nb, Cs, Ba, REE, Hf, Ta, Pb, Th and U) in the SE IVP mantle rocks were analyzed (Part 2) by a ThermoFinnigan ELEMENT XR high resolution (HR) ICP-MS at the Geosciences Montpellier laboratory (France).

Dissolution was performed following the HF-HClO₄ digestion procedure described by Ionov et al. (1992). Element concentrations were determined by external calibration except for Nb and Ta that were calibrated by using Zr and Hf as internal standards, respectively. This technique was applied to avoid memory effects due to the intake of concentrated Nb-Ta solutions in the instrument and it is an implementation to ICP-MS analysis of the method described by Jochum et al. (1990) for Nb measurement by spark-source mass spectrometry. The assessment of the analysis precision of a given element was made using 3-run measurements in the same solution and estimating the standard deviation (σ_s) from the standard deviations of the sample (σ_s), instrumental (σ_i) and procedural blank (σ_p) measurements (*cf.* Godard et al., 2000). The compositions of the reference samples BIR-1, UB-N and JP-1, analyzed as unknowns during the analytical runs, show good agreement with working values for these international standards (Govindaraju, 1994) and the reproducibility is better than 10% for the UB-N serpentinite.

3.8. Analyses of Radiogenic Isotopes by Mass Spectrometry (MC-ICP-MS & TIMS)

3.8.1. Ultraclean Lab Chemical Procedures

Analysis of samples for radiogenic isotope ratios of different elements, such as strontium (Sr), neodymium (Nd) and lead (Pb), require ultraclean laboratory procedures for purification of these elements and preparation for their analysis via mass spectrometry (Fig.

22). The clean laboratory has to be adapted to special requirements, particularly cleanliness to avoid external contamination of the studied samples, and elements separation by chromatography.



Fig. 22 Overview of the clean lab at Geoscience Montpellier with an 'anteroom' where the precision balance and clean lab-clothes are located (left), and the over-pressurized clean lab (right).

3.8.2. Pb, Nd & Sr Chromatographic Extractions

All the reagents used in the analytical procedures were three times sub-boiling distilled Merck® Suprapur acids. Water has been purified by a Millipore MilliQ Element Elix3 device with electric resistance larger than 18.3 M Ω (Fig. 23). The disposable pipette pits were discarded after single used. PTFE tubes were washed in several one-day baths of hot HCl 30% and HNO₃ 30% and rinsed with ultrapure water. Previously to sample treatment, Teflon beakers were first cleaned with acetone after filled with concentrated HNO₃ and put in ultrasonic cleaner for a while. After rinsing with ultra-pure water, the Teflon beakers were submerged in three HNO₃ diluted solutions, left on the hotplate (Fig. 24) during 24 hours for each bath, and carefully rinsed afterward. At last, the vessels were washed in two baths of double distilled HCl 6.4N and ultra-pure water, closed and heated in hotplate (Fig. 24) during 24 hours, and then rinsed and dried.

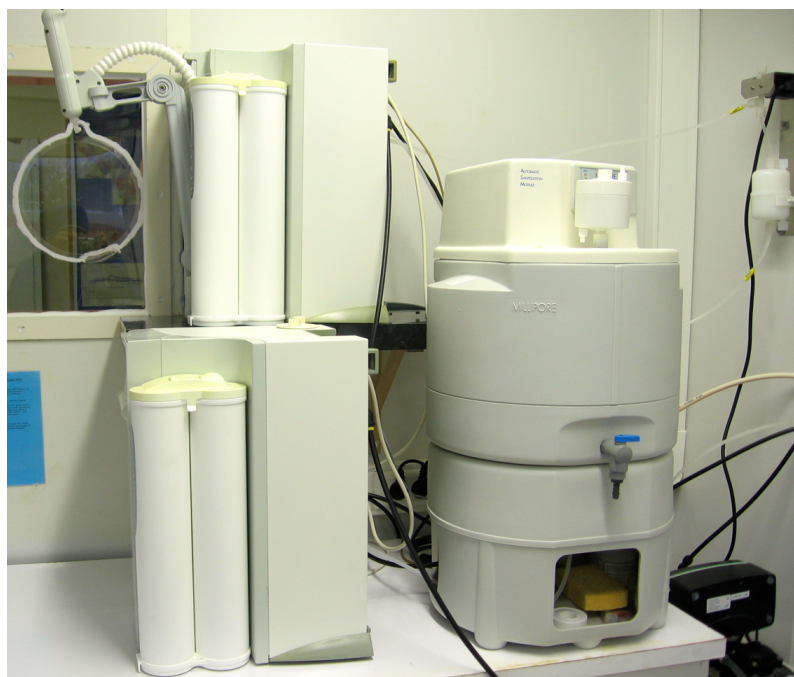


Fig. 23 Part of Millipore ultrapure water cleaning system at the Géosciences Montpellier Ultra-clean Radiogenic Isotope Laboratory.

The sample processing was continuously performed on over-pressurized laminar vertical flow hoods to prevent incidental external contamination. Clean digestion vessels were loaded with approximately 400-1000 mg of whole rock powder or 200 mg of clinopyroxene separate. However, the loaded materials were strongly depending on the Pb, Nd and Sr contents in the sample. To get highly precise isotopic outcomes, a minimum abundance of 400 ng is required for each element to be analyzed; but the quantity of the sample that can be processed should not be more than 1 g in order to prevent matrix effects during the chemical separations.



Fig. 24 Hotplates for evaporation in closed system evaporation cabinets with injection of HEPA prefiltered air and independent air exhaustion system (Géosciences Montpellier ultraclean lab).

For Pb extraction by liquid chromatography, 0.3 ml of 8N HBr was added to the samples and kept at 70 °C for 2-3 hours, moved in ultrasonic bath and subsequently evaporated. Afterwards, 0.8 ml HBr 0.5N was added to the residues that were left in ultrasonic cleaner for several minutes. Sample solutions were then transferred to tubes and centrifuged for approximately 10 minutes. The chemical separation of Pb was done in Teflon columns using 50 µl of anion exchange resin (AG1X8, 200-400 mesh) and samples were loaded and washed in 0.5N HBr. Before the chemical separation, the initiation of the resin was preceded and followed by three washing cycles with alternate HCl 6N and ultra-pure water. 1 ml HBr 0.5N was then added to the resin and after percolation a vessel was placed below the columns to recover the leaching solution. Then, the solution was evaporated for recovering of Sr and Rare Earth Elements (REE). Pb was finally extracted from the samples adding 1 ml HCl 6N and the leaching solution was recovered in a dedicated vessel, and then evaporated on hotplates. Lead blanks were lesser than 40 pg/g and are considered negligible for the present analyses.

Sr and REE pre-concentration were done using cationic exchange resin (AG50WX12, 200-400 mesh) firstly cleaned by four cycles of alternate ultra-pure water and HCl 6N. 0.5 ml HCl 6N was introduced in beakers kept on the hotplate for *ca.* 30 minutes and evaporated afterward. 2 ml HCl 1.5N was then added to the samples and solutions moved to ultrasounds, transferred to tubes and centrifuged for *ca.* 10 minutes. 4 ml HCl 1.5N was subsequently added to the resin and after its percolation a sample solution was carefully introduced to each Teflon column. Samples were then leached with 6 ml HCl 1.5N and 4 ml HCl 2.5N in order to remove major elements. After this step, a phial was placed under each column to recover the alkali and alkaline earth elements (*e.g.* K, Rb, Sr, Ba) by leaching twice with 4 ml HCl 2.5N, which was finally evaporated on a hotplate. 2 ml HCl 4N was afterwards introduced in the columns and REE were finally recuperated in a second beaker by elution and subsequent evaporation of 7.5 ml HCl 6N.

Following the extraction chromatographic method modified by Pin et al. (1994), Sr separation was done using the Eichrom™ Sr Spec exchange; 2 ml HNO₃ 2N was initiate into the beakers and the sample solutions were then moved by ultrasounds, transferred to tubes and centrifuged for *ca.* 10 minutes. The resin was firstly washed by six cycles of alternate HCl 6N and HNO₃ 0.05N and conditioned with 3 ml HNO₃ 2N. A sample solution was then carefully introduced in each Teflon column. First of all, K and Rb were extracted by leaching twice with 1 ml HNO₃ 2N, followed by Ba that was eluted with 3 ml HNO₃ 7N and 0.5 ml

HNO₃ 3N. Sr was finally recuperated adding 6 ml HNO₃ 0.05N, which was then evaporated on hotplate. Average total Sr content in procedural blanks was lesser than 50 pg/g.

Nd isotopes were separated following Richard et al. (1976) including a first step of REE separation (using AG50WX12 cation exchange resin) followed by two steps of Nd purification using the HDEHP technique (Fig. 25). The organic acid HDEHP fixed on the surface of microscopic Teflon balls (diameter *ca.* tens μm) set on silica columns. 0.5 ml HCl 0.3N was placed in the beakers and the sample solutions were treated by ultrasounds. Teflon balls were preconditioned with 3 ml HCl 0.3N and after its percolation a sample solution was gently introduced into each column. An adjustable volume of HCl 0.3N (ranging between 3.1 and 4.3 ml depending on the calibration of each column) was added to firstly elute the LREE (La, Ce, Pr). Nd was subsequently recover by leaching with a second variable volume of HCl 0.3N (from 3.2 to 6.3 ml) that was finally evaporated. The Teflon balls were washed by the percolation of 8 ml HCl 6N. Nd total procedural blanks were lesser than 15 pg/g and 20 pg/g.

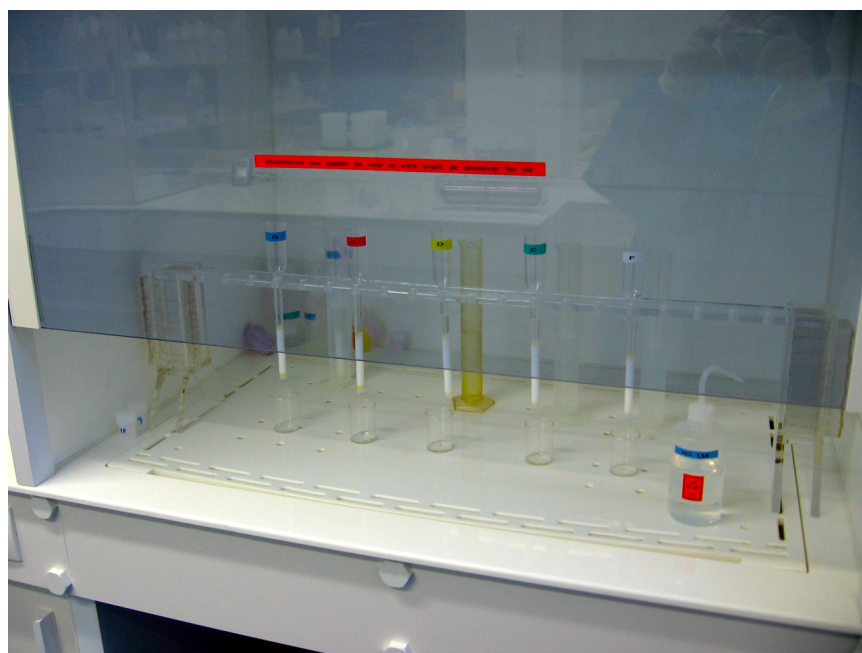


Fig. 25 Columns for Nd separation using HDEHP techniques in over-pressurized vertical laminar flow cabinet at Géosciences Montpellier.

3.8.3. Multicollector Inductively Coupled Plasma Mass Spectrometer (MC-ICP-MS)

MC-ICP-MS is an analytical instrument for high precision measurement of isotope ratios which are commonly used in geochemistry and geochronology. Pb (²⁰⁶Pb, ²⁰⁷Pb, ²⁰⁸Pb/²⁰⁴Pb) and Nd (¹⁴³Nd/¹⁴⁴Nd) radiogenic isotopic ratios were measured in whole rocks and in clinopyroxene concentrates by a VG Plasma 54 and NuPlasma 500 Multi-Collector

Inductively Coupled Plasma Mass Spectrometer (MC-ICP-MS; Fig. 26) at the École Normale Supérieure de Lyon (ENS, Lyon, France).

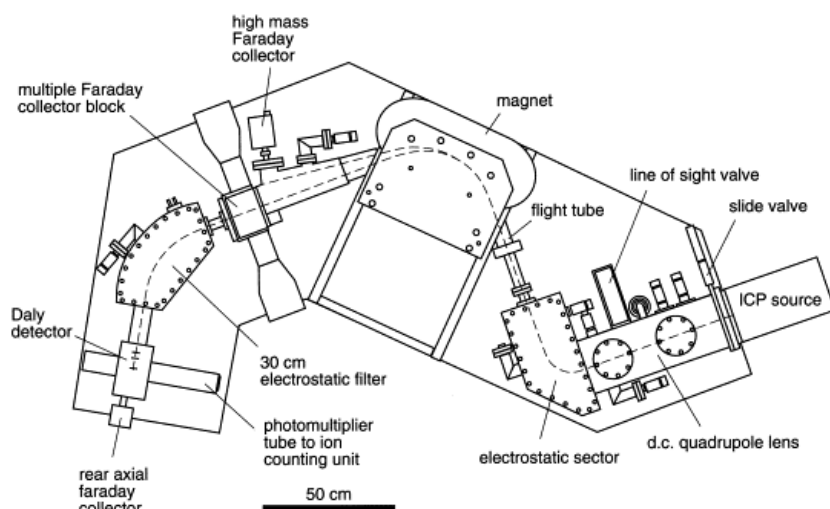


Fig. 26 Sketch of the VG Elemental Plasma 54 MC-ICP-MS (Halliday et al., 1998)

A MC-ICP-MS is a combined mass spectrometer that joins the advantages of superior ionization of an inductively coupled plasma source and the accurate measurements of a magnetic sector multicollector mass spectrometer. The primary improvement of the MC-ICP-MS is its ability to analyze a broader range of elements, including those with high ionization potential that are difficult to analyze by TIMS (see later). The ICP source also permits flexibility in how samples are introduced to the mass spectrometer and allows the analysis of samples introduced either as an aspirated solution or as an aerosol produced by laser ablation.

For Pb analyses, samples were dissolved in *ca.* 0.75-1 ml HNO₃ 0.05N containing 50 µg/l of Tl (following the normalization method of White et al., 2000), stayed some minutes on hotplate, then moved by ultrasounds and transferred into a tube. Two rinsing solution of 3 vol.% HNO₃ and HNO₃ 0.05N were used at the end of each measurement. NBS 981 standard was measured after each batch of two samples during the whole Pb analytical session. After the measurements, an external correction was applied to the standard according to the values reported by Todt et al. (1996). Pb isotopic ratios of the samples are not most affected by errors on the third decimal (10⁻³).

For Nd radiogenic isotope ratios, the analyses followed the method described by Luais et al. (1997). Samples were dissolved in *ca.* 0.75-1 ml and HNO₃ 0.05N, kept some minutes on hotplate after that transferred into a tube. Every two samples were bracketed between the 'Lyon-in-house' Nd standard with an average of ¹⁴³Nd/¹⁴⁴Nd = 0.512134 ± 24 (2σ, n=102).

3.8.4. Thermal Ionization Mass Spectrometer (TIMS)

Sr radiogenic isotopic ratios ($^{87}\text{Sr}/^{86}\text{Sr}$) were measured by a ThermoFinnigan Triton T1 Multi Collector Thermal Ionization Mass Spectrometer (MC-TIMS; Fig. 27) at the Centre Universitaire de Formation et de Recherche de Nîmes (France).



Fig. 27 Finnigan TRITON TIMS from Thermo Fisher Scientific Inc. (www.thermoscientific.com)

A TIMS is a magnetic sector mass spectrometer that is suitable of making very precise measurements of isotope ratios of elements that can be ionized thermally, usually by passing a current through a thin (Re) metal filament (Fig. 28) under vacuum. The ions formed on the filament are accelerated across an electrical potential gradient (up to 10 KV) and focused into a beam via a series of slits and electrostatically charged plates. This ion beam after that passes through a magnetic field and the original ion beam is dispersed into separate beams on the basis of their mass to charge ratio. These mass-resolved beams are then directed into collectors where the ion beam is converted into voltage. Comparison of voltages corresponding to individual ion beams yields precise isotope ratios.

For the Sr isotopic analyses by Thermal Ionization Mass Spectrometry (TIMS), samples were firstly dissolved in 2 μl HNO_3 0.1N and carefully positioned onto a Re filament (Fig. 28). The deposition of the sample solution on the filament was preceded and followed by the evaporation of 2 μl TaCl_5 that regulates the emission of Sr in the analysis. During the analytical sessions, filaments were heated in 3 steps up to approximately 1460 $^\circ\text{C}$ before the onset of the analysis that consisted of 5 cycles of 15 runs each. $^{87}\text{Sr}/^{86}\text{Sr}$ ratios were corrected for mass discrimination by normalizing to $^{86}\text{Sr}/^{88}\text{Sr} = 0.1194$ and for interference with ^{87}Rb by measuring ^{85}Rb . Results on NBS 987 Sr standard yielded a mean value of $^{87}\text{Sr}/^{86}\text{Sr} = 0.710256$

± 10 (2σ , $n=22$). Sr isotopic ratios of the samples are at most affected by errors on the fifth decimal (10^{-5}).



Fig. 28 Re filament ribbons for deposition and loading of samples in TIMS (after Marchesi, 2006; photo by V. Bennett).

Initial isotopic compositions of the whole dataset were corrected an age of *ca.* 3 Ma obtained by Duggen et al. (2005) that corresponds to the alkaline magmatism of Tallante (Part 2).

Part II

Results

4. Structure and Composition of the Subcontinental Lithospheric Mantle Beneath the Sangilen Plateau (Tuva, Southern Siberia, Russia): Evidence from Lamprophyre-hosted Spinel Peridotite xenoliths

Z. Konc^a, C. Marchesi^a, K. Hidas^a, C.J. Garrido^a, Cs. Szabó^b & V.V. Sharygin^c

Abstract

We present new data on spinel peridotite xenoliths hosted in Agardag alkaline lamprophyres from the Sangilen Plateau (Tuva, South Siberia, Russia), sampling at ~450 Ma the subcontinental lithospheric mantle of the Tuva-Mongolian micro-continent that belongs to the accretionary Central Asian orogenic belt at the southern edge of the Siberian craton. Xenoliths are spinel lherzolites principally showing poikilitic and subordinately coarse granular and coarse equigranular textures. Geothermobarometric calculations for pyroxene yield a narrow range of equilibration temperature (*ca.* 1000–1100 °C) that corresponds to lithospheric depths from 43 to 53 km (1.3–1.6 GPa) along a hot intracontinental geotherm. Variation of mean Mg# [$100 \cdot \text{Mg}/(\text{Mg}+\text{Fe})$] of olivine (87.9–90.9) with mean Cr# [$100 \cdot \text{Cr}/(\text{Cr}+\text{Al})$] of spinel (9.5–45.7) indicates that spinel lherzolites are mostly residues of up to 10% melting of a fertile peridotite source. In terms of normalized REE (Rare Earth Element) and incompatible trace element patterns of clinopyroxene, the Sangilen xenoliths can be classified into three types: Type I characterized by convex-upward REE patterns depleted in LREE ($0.10 \leq \text{La}/\text{Yb}_N \leq 0.49$), and with relative negative anomalies of Rb, Pb, Hf, Zr and Ti and positive spikes of U and Sr; Type II displaying variable LREE/HREE ratios ($0.53 \leq \text{La}/\text{Yb}_N \leq 2.17$), but generally flatter REE patterns and similar abundances of other trace elements compared to Type I; and Type III showing a LREE enriched pattern [$(\text{La}/\text{Sm})_N = 2.22$; $(\text{La}/\text{Yb})_N = 8.42$], high REE contents and no relative anomalies of U and Sr. The elevated Yb_N concentration of one Type II clinopyroxene and the variable fractionation of LREE-MREE relative to HREE in most xenolith types indicate Sangilen xenoliths underwent variable metasomatic enrichment. This enrichment is well accounted by percolation-reaction between depleted peridotite and small-melt fractions of alkaline mafic melts precursor to the Agardag alkaline lamprophyres. The lack of correlation with depth of modal variations, textural types, inferred degrees of melting and trace element patterns in xenoliths indicates the absence of a texturally or compositionally layered lithospheric mantle sampled by

Ordovician lamprophyres beneath the Sangilen plateau. The observed compositional variations are better accounted by depleted lithosphere variably metasomatized along a network of percolating alkaline mafic melts heterogeneously distributed throughout the Sangilen lithospheric mantle section.

^a *Instituto Andaluz de Ciencias de la Tierra (IACT), Consejo Superior de Investigaciones Científicas & Universidad de Granada (CSIC & UGR), Avenida de las Palmeras, 418100-Armilla (Granada), Spain*

^b *Lithosphere Fluid Research Lab (LRG) Department of Petrology and Geochemistry, Eötvös University, Pázmány Péter sétány, I/C, Budapest, H-117, Hungary*

^c *V.S. Sobolev Institute of Geology and Mineralogy, Siberian Branch of the Russian Academy of Sciences, pr. Akademika Koptyuga 3, Novosibirsk, 630090, Russia*

4.1. Introduction

Our knowledge of the composition and magmatic record of the subcontinental upper mantle comes from the investigation of peridotite from a variety of tectonic settings including mantle sections tectonically obducted as orogenic peridotite massifs, peridotite—primarily spinel peridotite—erupted in tectono-magmatically active areas away from cratons, and peridotite xenoliths—spinel and garnet peridotite—carried by kimberlites erupted through both Archean and middle to early Proterozoic crust (Bodinier and Godard, 2006; Carlson et al., 2005; Downes, 2001; Pearson et al., 2003; and references therein). In particular, the trace element geochemistry and microstructure of mantle xenoliths hosted in Paleozoic lamprophyre and lamproite at the southern edge of the Siberian craton are poorly known, and their study hence provides a unique opportunity to investigate the nature of the subcontinental mantle beneath these terrains.

In this paper we present new data on spinel xenoliths hosted in Early Ordovician alkaline lamprophyres from the Sangilen Plateau (Tuva, Russia) in the accretionary Central Asian orogenic belt, (southern Siberia). These lamprophyre-hosted spinel peridotite xenoliths allow us to investigate the composition and thermal structure of the circumcratonic subcontinental lithospheric mantle of the Tuva-Mongolian micro-continent (Griffin et al., 1999b). Sangilen mantle xenoliths therefore offer complementary information on the Central Asia subcontinental mantle lithosphere to that provided by mantle xenoliths in younger Neogene basalts that sample the subcontinental mantle beneath the Baikal rift and Mongolia (*e.g.* Ionov, 2002; Litasov et al., 2000; Wiechert et al., 1997).

4.2. Sampling and Petrography

The studied Sangilen xenoliths were sampled from different localities of the Agardag alkaline lamprophyre dike complex and are invariably spinel lherzolites. Peridotite xenoliths in these dikes can be up to 10 cm in diameter, they are commonly highly altered and friable. Fresh peridotite xenoliths are uncommon and small, limiting the availability of samples for the present study and preventing their bulk rock analysis. For this study, we selected highly fresh peridotite xenoliths (up to 4 cm in size) representative of the textural and modal variations of the suite (Table 3). The modal composition of xenoliths was estimated by image analyses of thin sections (Table 3).

Table 3 Average major element compositions (wt.%) of minerals, modal abundances and calculated equilibrium temperatures of the studied Sangilen xenoliths

| Sample | 3H-2 | | | | 3H-4 | | | | 3H-8 | | | | 5H-2 | | | |
|--------------------------------------|-----------------------------------|------|--------|--------|------------------------------|------|--------|--------|------------------------------|-------|--------|--------|---------------------------------------|-------|--------|--------|
| | Spinel lherzolite coarse granular | | | | Spinel lherzolite poikilitic | | | | Spinel lherzolite poikilitic | | | | Spinel lherzolite coarse equigranular | | | |
| Mineral | ol | opx | cpx | spl | ol | opx | cpx | spl | ol | opx | cpx | spl | ol | opx | cpx | spl |
| SiO ₂ | 40.9 | 55.8 | 53.1 | 0.07 | 40.7 | 54.2 | 51.5 | 0.15 | 40.5 | 53.7 | 51.0 | 0.06 | 40.0 | 54.1 | 51.3 | 0.06 |
| TiO ₂ | b.d.l. | 0.05 | 0.13 | 0.22 | b.d.l. | 0.14 | 0.55 | 0.18 | b.d.l. | 0.18 | 0.59 | 0.19 | b.d.l. | 0.14 | 0.53 | 0.14 |
| Al ₂ O ₃ | b.d.l. | 2.79 | 3.49 | 29.4 | b.d.l. | 5.70 | 7.64 | 57.8 | b.d.l. | 5.20 | 7.03 | 55.6 | b.d.l. | 5.04 | 7.20 | 57.2 |
| Cr ₂ O ₃ | b.d.l. | 0.70 | 1.27 | 36.8 | b.d.l. | 0.42 | 0.73 | 9.07 | b.d.l. | 0.40 | 0.78 | 9.99 | b.d.l. | 0.39 | 0.84 | 10.3 |
| FeO ^{tot} | 9.86 | 6.21 | 3.06 | 16.1 | 10.2 | 6.48 | 3.43 | 10.9 | 10.8 | 6.92 | 3.57 | 11.9 | 10.27 | 6.58 | 3.33 | 11.1 |
| MnO | 0.13 | 0.12 | 0.09 | 0.12 | 0.15 | 0.13 | 0.10 | 0.11 | 0.13 | 0.15 | 0.09 | 0.10 | 0.18 | 0.18 | 0.13 | 0.22 |
| MgO | 48.8 | 32.5 | 16.9 | 16.0 | 47.2 | 31.1 | 15.0 | 20.2 | 48.2 | 31.4 | 15.0 | 20.2 | 48.8 | 32.6 | 15.8 | 20.7 |
| NiO | 0.32 | 0.09 | b.d.l. | 0.19 | 0.34 | 0.11 | b.d.l. | 0.36 | 0.33 | 0.12 | b.d.l. | 0.33 | 0.39 | 0.11 | b.d.l. | 0.39 |
| CaO | 0.09 | 1.08 | 19.6 | b.d.l. | 0.11 | 1.01 | 19.2 | b.d.l. | 0.09 | 0.962 | 18.9 | b.d.l. | 0.08 | 0.85 | 18.6 | b.d.l. |
| Na ₂ O | b.d.l. | 0.08 | 0.87 | b.d.l. | b.d.l. | 0.15 | 1.67 | b.d.l. | b.d.l. | 0.15 | 1.69 | b.d.l. | b.d.l. | 0.14 | 1.75 | b.d.l. |
| Total | 100.2 | 99.4 | 98.5 | 99.0 | 98.8 | 99.4 | 99.9 | 98.7 | 100.1 | 99.2 | 98.7 | 98.3 | 99.8 | 100.1 | 99.6 | 100.1 |
| mg# | 89.8 | 90.3 | 90.7 | 63.9 | 89.2 | 89.5 | 89.9 | 78.2 | 88.9 | 89.0 | 88.3 | 74.6 | 89.4 | 89.9 | 89.5 | 77.0 |
| cr# | | | | 45.7 | | | | 9.52 | | | | 10.7 | | | | 10.8 |
| vol.% | 63.4 | 26.5 | 7.6 | 2.5 | 51.1 | 32.7 | 15.2 | 1.0 | 52.8 | 31.9 | 15.0 | 0.3 | 54.7 | 29.1 | 15.7 | 0.5 |
| T _{Cpx-Opx} (± 31 °C) | 1096 °C | | | | 1031 °C | | | | 1019 °C | | | | 1042 °C | | | |
| T _{Ca-Opx} (± 16 °C) | 1075 °C | | | | 1060 °C | | | | 1047 °C | | | | 1014 °C | | | |
| T _{Ca-Opx-mod} (± 25–45 °C) | 1072 °C | | | | 1055 °C | | | | 1041 °C | | | | 1003 °C | | | |
| T _{Cr-Al-Opx} (± 15 °C) | 1020 °C | | | | 1038 °C | | | | 1009 °C | | | | 999 °C | | | |

| 5H-3 | | | | 5H-7 | | | | 5H-9 | | | | 5H-10 | | | | 5H-13 | | | |
|------------------------------|---------|--------|--------|------------------------------|---------|--------|--------|------------------------------|---------|--------|--------|-----------------------------------|---------|--------|--------|------------------------------|-------|--------|--------|
| Spinel lherzolite poikilitic | | | | Spinel lherzolite poikilitic | | | | Spinel lherzolite poikilitic | | | | Spinel lherzolite coarse granular | | | | Spinel lherzolite poikilitic | | | |
| ol | opx | cpx | spl | ol | opx | cpx | cpx | ol | opx | cpx | spl | ol | opx | cpx | spl | ol | opx | cpx | spl |
| 40.5 | 53.8 | 51.8 | 0.06 | 40.7 | 55.0 | 52.7 | 0.05 | 40.3 | 54.6 | 51.7 | 0.05 | 41.1 | 54.9 | 52.0 | 0.12 | 40.9 | 56.2 | 53.2 | 0.06 |
| b.d.l. | 0.04 | 0.11 | 0.06 | b.d.l. | 0.07 | 0.23 | 0.08 | b.d.l. | 0.16 | 0.48 | 0.28 | b.d.l. | 0.11 | 0.31 | 0.21 | b.d.l. | 0.08 | 0.19 | 0.24 |
| b.d.l. | 4.64 | 5.52 | 50.2 | b.d.l. | 4.80 | 6.53 | 54.0 | b.d.l. | 4.68 | 6.03 | 48.7 | b.d.l. | 4.18 | 5.95 | 44.7 | b.d.l. | 2.88 | 3.95 | 31.1 |
| b.d.l. | 0.55 | 0.92 | 16.17 | b.d.l. | 0.53 | 1.03 | 14.43 | b.d.l. | 0.61 | 1.06 | 17.4 | b.d.l. | 0.63 | 1.38 | 22.82 | b.d.l. | 0.77 | 1.64 | 37.02 |
| 9.9 | 6.17 | 3.15 | 11.7 | 10.1 | 6.37 | 3.10 | 11.1 | 11.73 | 7.45 | 3.90 | 14.2 | 9.9 | 6.27 | 3.12 | 13.4 | 8.81 | 5.57 | 2.75 | 14.0 |
| 0.13 | 0.14 | 0.09 | 0.08 | 0.16 | 0.17 | 0.13 | 0.27 | 0.18 | 0.18 | 0.13 | 0.33 | 0.14 | 0.15 | 0.09 | 0.15 | 0.15 | 0.16 | 0.12 | 0.54 |
| 48.8 | 31.5 | 16.4 | 19.5 | 48.9 | 32.8 | 16.0 | 20.1 | 47.6 | 31.9 | 16.4 | 18.5 | 48.2 | 32.0 | 15.4 | 18.2 | 49.6 | 33.7 | 17.2 | 16.5 |
| 0.32 | 0.09 | b.d.l. | 0.28 | 0.39 | 0.10 | b.d.l. | 0.36 | 0.37 | 0.10 | b.d.l. | 0.31 | 0.36 | 0.10 | b.d.l. | 0.27 | 0.38 | 0.11 | b.d.l. | 0.20 |
| 0.10 | 1.09 | 20.0 | b.d.l. | 0.07 | 0.88 | 19.1 | b.d.l. | 0.09 | 1.03 | 19.0 | b.d.l. | 0.08 | 0.96 | 19.3 | b.d.l. | 0.08 | 0.96 | 19.8 | b.d.l. |
| b.d.l. | 0.10 | 0.92 | b.d.l. | b.d.l. | 0.13 | 1.59 | b.d.l. | b.d.l. | 0.09 | 1.19 | b.d.l. | b.d.l. | 0.15 | 1.61 | b.d.l. | b.d.l. | 0.08 | 1.14 | b.d.l. |
| 99.7 | 98.1 | 98.9 | 98.1 | 100.4 | 100.8 | 100.5 | 100.3 | 100.4 | 100.8 | 99.9 | 99.9 | 99.8 | 99.4 | 99.3 | 99.8 | 99.9 | 100.5 | 100.1 | 99.7 |
| 89.8 | 90.1 | 90.3 | 74.9 | 89.6 | 90.2 | 90.2 | 76.4 | 87.9 | 88.4 | 88.2 | 70.0 | 89.7 | 90.1 | 91.0 | 74.0 | 90.9 | 91.5 | 91.8 | 67.8 |
| | | | 17.8 | | | | 15.2 | | | | 19.4 | | | | 25.5 | | | | 44.4 |
| 65.5 | 20.1 | 13.4 | 1.1 | 68.4 | 20.7 | 9.8 | 1.1 | 72.6 | 20.9 | 6.3 | 0.2 | 81.5 | 11.2 | 6.9 | 0.4 | 82.5 | 10.9 | 6.1 | 0.5 |
| 1082 °C | 1065 °C | | | | 1093 °C | | | | 847 °C | | | | 1063 °C | | | | | | |
| 1083 °C | 1021 °C | | | | 1062 °C | | | | 1047 °C | | | | 1043 °C | | | | | | |
| 1081 °C | 1012 °C | | | | 1057 °C | | | | 1041 °C | | | | 1037 °C | | | | | | |
| 1048 °C | 1038 °C | | | | 1059 °C | | | | 1056 °C | | | | 1041 °C | | | | | | |

b.d.l. – below detection limit

Using thermometers: $T_{Cpx-Opx}$ – Taylor, 1998; T_{Ca-Opx} – Brey and Köhler, 1990; $T_{Ca-Opx-mod}$ – Nimis and Grütter, 2010; $T_{Cr-Al-Opx}$ – Witt-Eickschen and Seck, 1991

The selected xenoliths lack any vein or modal layering and are spinel lherzolites with variable modal proportions of olivine, orthopyroxene and clinopyroxene (Table 3). Sangilen xenoliths show principally poikilitic texture (e.g. Downes et al., 1992; Grégoire et al., 1997; Mercier and Nicolas, 1975; Xu et al., 1998) characterized by coarse (3–4 mm) orthopyroxene enclosing olivine (1–2 mm) (Fig. 29a); less common coarse equigranular texture has homogeneous (0.5–2 mm) grain size (Fig. 29b), and coarse granular texture (Lenoir et al., 2000; Mercier and Nicolas, 1975) has relatively large olivine (up to 3 mm) and pyroxenes (1–2 mm) (Fig. 29c). Coarse equigranular and coarse granular xenoliths not only differ in terms of olivine grain size but also in the shape of grain boundaries, which is, respectively, straight (Fig. 29b) and curvilinear (Fig. 29c). Pyroxenes show no exsolution lamellae and round subhedral spinel grains occur either interstitially (sometimes with holy-leaf shape) or as inclusions in silicates (Fig. 29b, c). Spinel grains are always smaller (0.5–1 mm) than other rock-forming minerals. Sulfide blebs (30–300 μm) are common in all samples.

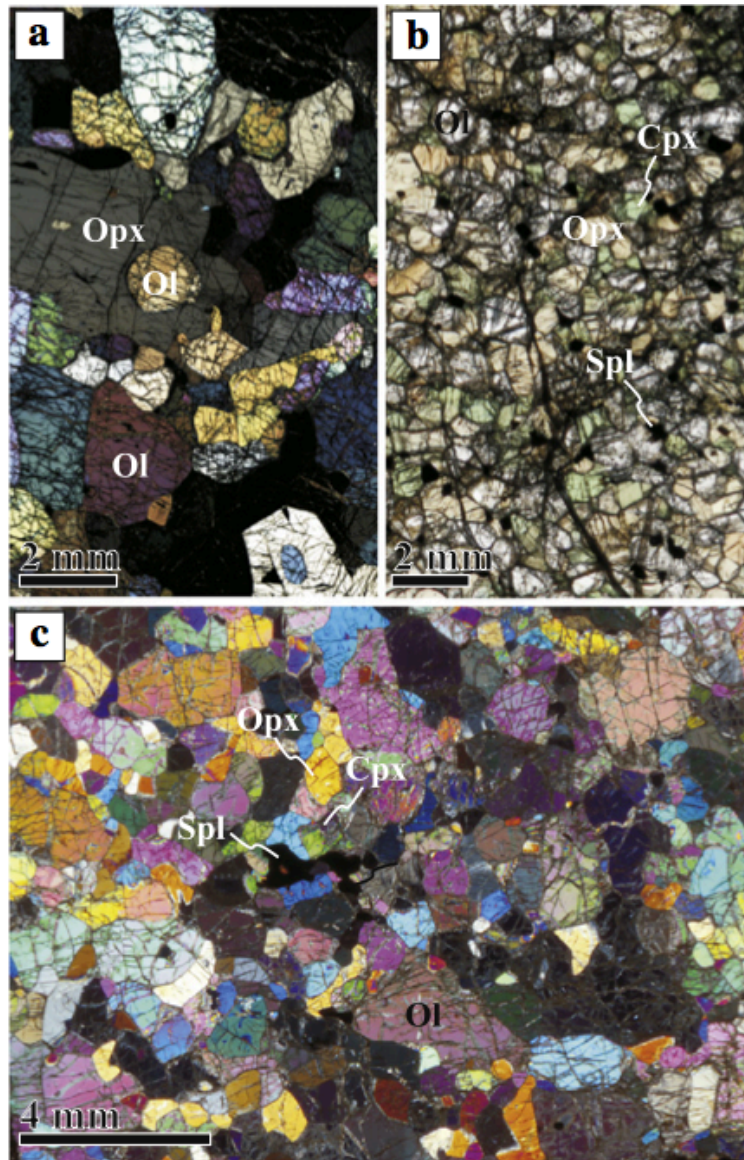


Fig. 29 Photomicrographs of representative textures of Sangilen mantle xenoliths: (a) poikilitic texture with olivine enclosed in large orthopyroxene (sample 5H-9); (b) coarse-grained equigranular texture with straight grain boundaries (sample 5H-2); (c) coarse granular texture with curvilinear grain boundaries (sample 3H-2). Cpx: clinopyroxene; Ol: olivine; Opx: orthopyroxene; Spl: spinel.

4.3. Mineral Chemistry

4.3.1. Major Elements

In terms of major elements, olivine, orthopyroxene, clinopyroxene and spinel are homogenous at the thin section scale. Average Mg# [$100 \cdot \text{Mg} / (\text{Mg} + \text{Fe})$] of olivine is uncorrelated with the textural type of xenoliths and ranges from 87.9 to 90.9 as characteristic for fertile lherzolite (Fig. 30). Average Mg# of orthopyroxene ranges from 88.4 to 91.5, CaO from 0.85 to 1.08 wt.%, and Al_2O_3 from 4.18 to 5.70 wt.% except in lherzolites 3H-2 and 5H-13

where the Al₂O₃ content is significantly lower (2.79-2.88 wt.%) (Table 3). Clinopyroxene (Mg-augite) has an average Mg# ranging from 88.2 to 91.8 and highly variable Al₂O₃ content (3.49-7.64 wt.%). Cr₂O₃ and Na₂O contents span from 0.73 to 1.64 wt.% and 0.87 to 1.75 wt.%, respectively (Table 3). Average Cr# [100*Cr/(Cr + Al)] of spinel (Mg-Al chromite) is highly variable (9.5-45.7) (Fig. 30) and Mg# ranges between 63.9 and 78.2. These compositions are similar to those reported in previous studies of major elements in minerals from the Sangilen xenoliths (Egorova et al., 2006; Gibsher et al., 2008) and are typical of mantle-derived spinel lherzolite xenoliths (e.g. Maaloe and Aoki, 1977; Pearson et al., 2003).

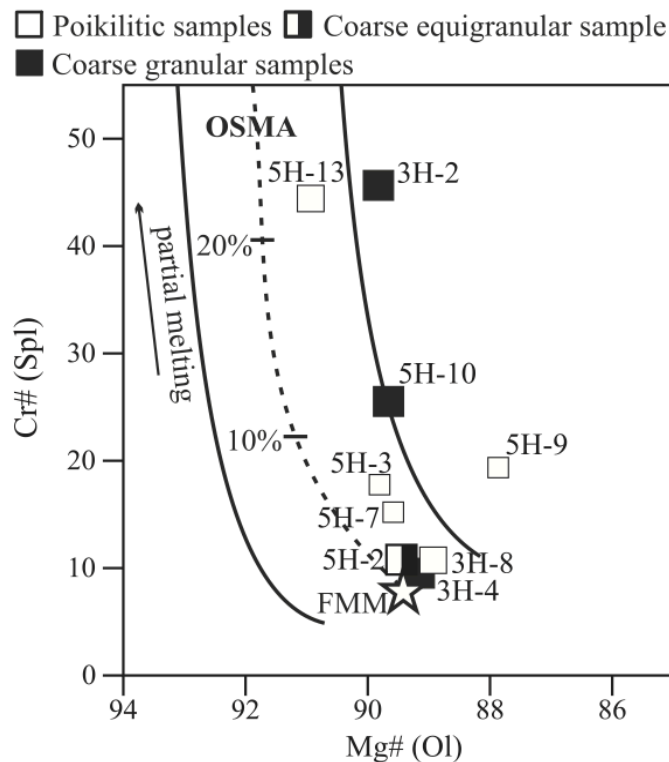


Fig. 30 Plot of spinel Cr# [100*Cr/(Cr+Al)] versus olivine Mg# [100*Mg/(Mg+Fe)]. The Olivine-Spinel Mantle Array (OSMA) and degrees of partial melting are from Arai (1994). FMM (open star) is the Fertile MORB Mantle after Pearce et al. (2000). Ol: olivine; Spl: spinel.

4.3.2. Trace Elements in Clinopyroxene

Clinopyroxene has homogenous trace element composition in each sample (Table 4). Three types of chondrite-normalized (Sun and McDonough, 1989) rare earth element (REE) patterns of clinopyroxene can be differentiated:

- (i) Type I: characterized by convex-upward patterns depleted in light REE (LREE) with $0.12 \leq (La/Sm)_N \leq 0.45$ and $0.10 \leq (La/Yb)_N \leq 0.49$ in samples 3H-4, 3H-8, 5H-7 and 5H-9 (Fig. 31a);

- (ii.) Type II: characterized by relatively flat REE patterns with $0.65 \leq (\text{La}/\text{Sm})_N \leq 1.59$ and $0.53 \leq (\text{La}/\text{Yb})_N \leq 2.17$ in samples 3H-2, 5H-2, 5H-3 and 5H-10 (Fig. 31b);
- (iii.) Type III: characterized by enriched LREE patterns with average $(\text{La}/\text{Sm})_N = 2.22$ and $(\text{La}/\text{Yb})_N = 8.42$ in xenolith 5H-13 (Fig. 31c).

The shape of normalized patterns of clinopyroxene is unrelated to its modal abundances and/or textural type of xenoliths.

Table 4 Average trace element abundances (ppm) of clinopyroxenes from the Sanglilen xenoliths.

| Sample | 3H-2 (st. dev.) | | 3H-4 (st. dev.) | | 3H-8 (st. dev.) | | 5H-2 (st. dev.) | | 5H-3 (st. dev.) | | 5H-7 (st. dev.) | | 5H-9 (st. dev.) | | 5H-10 (st. dev.) | | 5H-13 (st. dev.) | |
|----------------------|-----------------|---------|-----------------|-------|-----------------|-------|-----------------|-------|-----------------|-------|-----------------|---------|-----------------|---------|------------------|-------|------------------|---------|
| Li | 0.992 | 0.104 | | | 1.50 | 0.09 | 1.27 | 0.16 | 1.27 | 0.25 | 1.21 | 0.07 | 1.16 | 0.01 | 371 | 194 | 1.00 | 0.10 |
| Rb | 0.043 | 0.038 | 0.024 | 0.008 | 0.032 | 0.012 | 0.247 | 0.238 | 0.019 | 0.011 | 0.054 | 0.062 | 0.157 | 0.128 | 0.263 | 0.133 | 0.018 | 0.014 |
| Th | 0.039 | 2.1E-04 | 0.013 | 0.005 | 0.031 | 0.002 | 0.060 | 0.001 | 0.033 | 0.001 | 0.006 | 3.4E-04 | 0.006 | 0.000 | 1.16 | 0.07 | 0.668 | 0.019 |
| U | 0.013 | 0.003 | 0.005 | 0.002 | 0.012 | 0.003 | 0.016 | 0.001 | 0.016 | 0.007 | 0.010 | 0.013 | 0.012 | 0.016 | 0.359 | 0.060 | 0.171 | 0.020 |
| Nb | 0.291 | 0.009 | 0.102 | 0.054 | 0.279 | 0.006 | 0.648 | 0.017 | 0.311 | 0.007 | 0.063 | 0.003 | 0.079 | 0.004 | 10.3 | 0.4 | 2.70 | 0.02 |
| Ta | 0.035 | 0.002 | 0.006 | 0.004 | 0.037 | 0.002 | 0.037 | 0.005 | 0.032 | 0.002 | 0.007 | 0.001 | 0.004 | 3.7E-04 | 1.07 | 0.06 | 0.479 | 0.012 |
| La | 1.36 | 0.02 | 0.319 | 0.013 | 1.21 | 0.02 | 1.35 | 0.04 | 0.88 | 0.01 | 0.331 | 0.003 | 0.141 | 0.008 | 27.0 | 1.2 | 8.09 | 0.20 |
| Ce | 3.72 | 0.05 | 2.15 | 0.03 | 4.32 | 0.09 | 3.68 | 0.14 | 2.25 | 0.03 | 1.27 | 0.09 | 0.688 | 0.038 | 76.7 | 4.8 | 18.5 | 0.7 |
| Pb | 0.043 | 0.010 | 0.034 | 0.025 | 0.046 | 0.021 | 0.043 | 0.021 | 0.045 | 0.034 | 0.021 | 0.003 | 0.024 | 0.004 | 0.270 | 0.034 | 0.080 | 0.005 |
| Sr | 50.4 | 1.7 | 60.0 | 1.1 | 60.7 | 0.5 | 75.5 | 3.0 | 25.9 | 0.6 | 41.2 | 0.3 | 19.7 | 5.6 | 496 | 17 | 158 | 2 |
| Pr | 0.579 | 0.008 | 0.545 | 0.008 | 0.790 | 0.022 | 0.577 | 0.012 | 0.293 | 0.006 | 0.244 | 0.003 | 0.176 | 0.012 | 12.2 | 1.1 | 2.41 | 0.08 |
| Nd | 3.13 | 0.04 | 3.82 | 0.08 | 4.68 | 0.12 | 3.31 | 0.04 | 1.28 | 0.02 | 1.51 | 0.01 | 1.36 | 0.08 | 67.8 | 6.7 | 10.6 | 0.3 |
| Hf | 0.531 | 0.010 | 0.982 | 0.023 | 0.853 | 0.010 | 0.798 | 0.021 | 0.105 | 0.005 | 0.182 | 0.006 | 0.495 | 0.042 | 6.89 | 1.34 | 1.34 | 0.08 |
| Zr | 15.3 | 0.2 | 26.7 | 0.4 | 25.9 | 0.2 | 23.0 | 0.3 | 4.60 | 0.03 | 7.85 | 0.05 | 9.49 | 0.80 | 268 | 36 | 52.4 | 1.5 |
| Sm | 1.01 | 0.01 | 1.74 | 0.07 | 1.72 | 0.06 | 1.34 | 0.01 | 0.36 | 0.01 | 0.655 | 0.015 | 0.777 | 0.029 | 21.3 | 2.2 | 2.35 | 0.10 |
| Eu | 0.362 | 0.005 | 0.730 | 0.021 | 0.675 | 0.013 | 0.571 | 0.018 | 0.142 | 0.002 | 0.292 | 0.003 | 0.312 | 0.020 | 8.697 | 0.808 | 0.752 | 0.020 |
| Gd | 1.20 | 0.01 | 2.73 | 0.10 | 2.45 | 0.05 | 2.16 | 0.04 | 0.65 | 0.02 | 1.09 | 0.02 | 1.30 | 0.08 | 23.7 | 2.2 | 2.27 | 0.05 |
| Tb | 0.190 | 0.003 | 0.509 | 0.013 | 0.436 | 0.006 | 0.413 | 0.005 | 0.139 | 0.002 | 0.222 | 0.003 | 0.237 | 0.014 | 4.46 | 0.29 | 0.320 | 0.008 |
| Ti | 722 | 18 | 3788 | 25 | 3841 | 17 | 3067 | 178 | 955 | 37 | 1707 | 82 | 3106 | 279 | 24224 | 2939 | 1991 | 98 |
| Dy | 1.16 | 0.01 | 3.79 | 0.09 | 3.11 | 0.04 | 3.04 | 0.05 | 1.20 | 0.02 | 1.79 | 0.02 | 1.66 | 0.09 | 29.0 | 1.6 | 1.94 | 0.03 |
| Ho | 0.223 | 0.002 | 0.805 | 0.028 | 0.666 | 0.011 | 0.672 | 0.013 | 0.285 | 0.003 | 0.421 | 0.008 | 0.342 | 0.024 | 5.95 | 0.29 | 0.347 | 0.008 |
| Y | 5.26 | 0.07 | 20.0 | 0.6 | 16.8 | 0.2 | 16.7 | 0.6 | 7.46 | 0.10 | 10.8 | 0.1 | 8.41 | 0.61 | 144.0 | 5.4 | 8.65 | 0.10 |
| Er | 0.559 | 0.008 | 2.35 | 0.07 | 1.92 | 0.02 | 1.93 | 0.06 | 0.896 | 0.007 | 1.29 | 0.01 | 0.931 | 0.057 | 15.5 | 0.7 | 0.877 | 0.006 |
| Tm | 0.074 | 0.001 | 0.338 | 0.010 | 0.274 | 0.004 | 0.281 | 0.007 | 0.141 | 0.003 | 0.201 | 0.004 | 0.129 | 0.011 | 2.15 | 0.09 | 0.116 | 1.9E-04 |
| Yb | 0.448 | 0.006 | 2.21 | 0.07 | 1.79 | 0.03 | 1.81 | 0.06 | 0.950 | 0.024 | 1.37 | 0.02 | 0.804 | 0.049 | 14.0 | 0.5 | 0.689 | 0.018 |
| Lu | 0.065 | 0.002 | 0.314 | 0.009 | 0.253 | 0.004 | 0.265 | 0.009 | 0.143 | 0.002 | 0.204 | 0.004 | 0.117 | 0.008 | 2.00 | 0.07 | 0.097 | 0.003 |
| (La/Sm) _N | 0.85 | | 0.11 | | 0.44 | | 0.63 | | 1.54 | | 0.32 | | 0.11 | | 0.79 | | 2.16 | |
| (La/Yb) _N | 2.06 | | 0.10 | | 0.46 | | 0.51 | | 0.63 | | 0.16 | | 0.12 | | 1.31 | | 7.99 | |

The subscript N denotes chondrite-normalized element ratio (Sun and McDonough, 1989)

Primitive upper mantle (PUM) normalized (Sun and McDonough, 1989) multi-element patterns of clinopyroxene in Sanglilen xenoliths also vary according to the groups differentiated on the basis of REE: (i.) Type I xenoliths have trace element abundances that generally increase towards the least incompatible elements from ~ 0.01 to $10 \times$ PUM. Exceptions to this trend are relative negative anomalies of Rb, Pb, Hf, Zr and Ti and positive spikes of U and Sr (Fig. 31d), (ii.) Type II xenoliths display concentrations and spikes similar to Type I in the PUM normalized multi-element diagrams but less patent positive anomalies of U (Fig. 31e); the trace element abundances of clinopyroxene in 5H-10 are remarkably higher than in other samples, mostly $> 10 \times$ PUM; finally, (iii.) Type III xenolith 5H-13 generally displays trace element concentrations between 1 and $10 \times$ PUM with no relative anomalies of U and Sr, and a negative Nb spike (Fig. 31f).

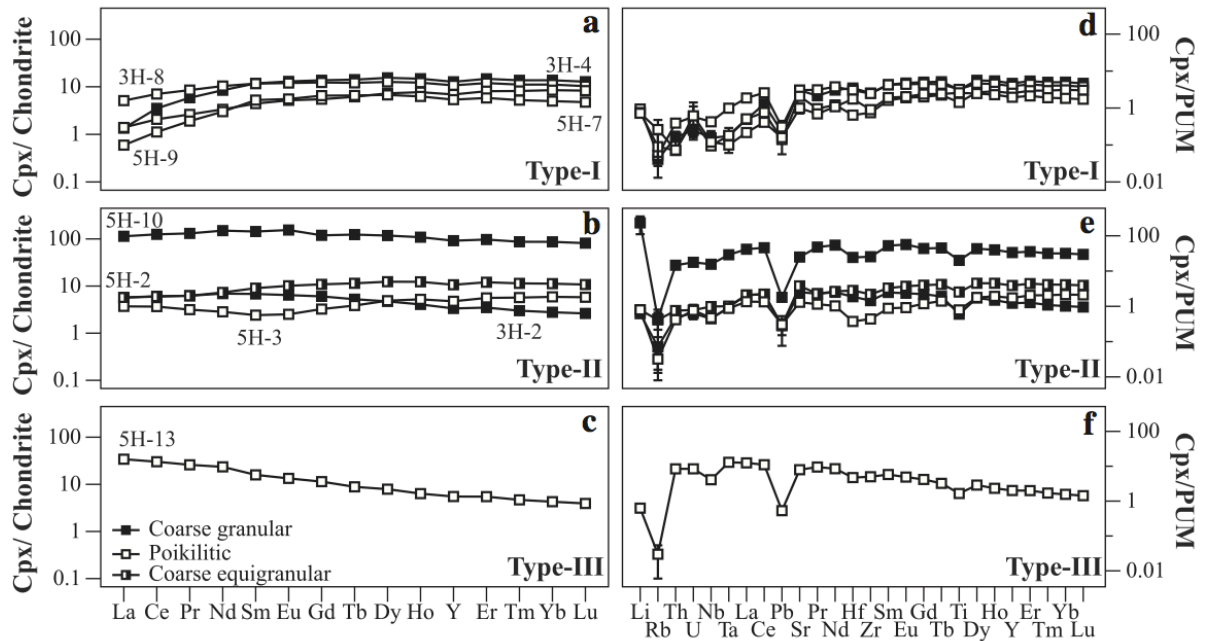


Fig. 31 Geochemical classification of Sangilen spinel peridotite xenoliths based on C1 chondrite-normalized REE patterns (**a-c**) and Primitive Upper Mantle (PUM) normalized trace element patterns (**d-f**) of clinopyroxenes (see text for further details). Reported values are the average composition of several clinopyroxene analyses per sample ($n > 6$). Error bars in panels **d-f** are 2 SD (standard deviation) only shown for analyses where the relative error is larger than 10%. Normalizing values after Sun and McDonough (1998).

4.4. Discussion

4.4.1 Depth of Provenance of Xenoliths and Thermal Structure of the Lithospheric Mantle Beneath the Sangilen Plateau

The spinel lherzolite assemblage of the Sangilen xenoliths indicates they are samples coming from lithospheric depths above the spinel to garnet lherzolite facies transition (Fig. 32) Due to the lack of accurate geobarometric formulations for spinel lherzolite (Nimis and Grütter, 2010; Taylor, 1998; and references therein), the depth of provenance of the Sangilen xenoliths can only be assessed combining the calculated equilibration temperature of mantle xenoliths with the inferred mantle paleogeotherm at the age of intrusion of the Agardag lamprophyres.

Calculated equilibration temperatures of Sangilen xenoliths, obtained using several recommended geothermometric formulations for spinel peridotite, are reported in Table 3 ($T_{\text{Cpx-Opx}}$, two-pyroxene geothermometer of Taylor, 1998; $T_{\text{Ca-Opx}}$, Ca-in-orthopyroxene geothermometer of Brey and Köhler, 1990; $T_{\text{Ca-Opx-mod}}$, $T_{\text{Ca-Opx}}$ formulation modified by Nimis and Grütter, 2010; and $T_{\text{Cr-Al-Opx}}$, the Al-in-orthopyroxene geothermometer of Witt-Eickschen and Seck, 1991). Most geothermometric formulations yield a relatively narrow range of

equilibration temperature (~1000–1100 °C) (Table 3). An exception is sample 5H-10 for which the $T_{\text{Cpx-Opx}}$ geothermometer yields an unusually low equilibration temperature (~850 °C) relative to that obtained from other thermometric formulations (Table 3). This divergence is common in spinel mantle xenoliths and reflects lack of chemical disequilibrium between orthopyroxene and clinopyroxene (Nimis and Grütter, 2010). The lack of textural evidence for secondary clinopyroxene and the high temperature obtained for the $T_{\text{Cr-Al-Opx}}$ and $T_{\text{Ca-in-Opx}}$ formulations in the orthopyroxene core of this sample indicate that the anomalously low $T_{\text{Cpx-Opx}}$ temperature may be the vestige of an older low-temperature event as reported in other xenolith suites (Foley et al., 2006). Egorova et al. (2006) ($T_{\text{Ca-Opx}} = 1020\text{--}1100$ °C) and Gibsher et al. (2008) ($T_{\text{Ca-Opx}} = 970\text{--}1100$ °C) have reported a similar range of equilibration temperatures for the Sangilen peridotite xenoliths.

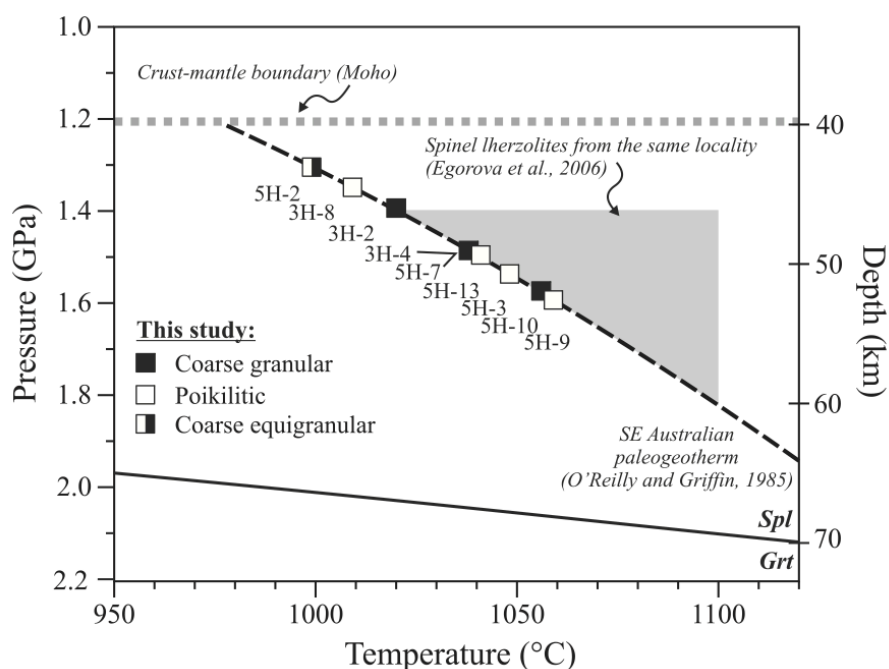


Fig. 32 Estimated equilibrium temperature of Sangilen spinel peridotites plotted along the SE Australia paleogeotherm (dashed black curve) (O'Reilly and Griffin, 1985). This paleogeotherm is taken as representative for intracontinental areas with high heat flow as suggested for the Sangilen plateau lithosphere at the time of intrusion of Ordovician Agardag lamprophyres. The spinel to garnet peridotite transition (solid black line) is calculated for a fertile lherzolite composition (O'Neill, 1981; Webb and Wood, 1986) and the crustal thickness (dashed gray line) is that of off-craton continental crust (Rudnick and Gao, 2003).

Several studies have shown that the Sangilen lithospheric mantle records hotter geothermal regimes than the lithospheric mantle in nearby areas of the Siberian platform (Djomani et al., 2003; Khutorskoy and Yarmolyuk, 1989; Zorin et al., 1990). We hence assume that the paleogeothermal gradient of the Sangilen mantle is first approximated by a

relatively hot geotherm as that derived from studies of spinel mantle xenoliths in intracontinental regions such as southeastern Australia (O'Reilly and Griffin, 1985). Calculated temperatures of Sangilen xenoliths plot along this geotherm at pressures ranging from 1.3 to 1.6 GPa, which correspond to lithospheric depths from ~43 to 53km (Fig. 32). This depth of provenance is in good agreement with the crustal thickness seismically imaged beneath the Sangilen plateau (Djomani et al., 2003; Khutorskoy Yarmolyuk, 1989; Zorin et al., 1990). Likewise, it is in good accordance with the spinel lherzolite nature of the Sangilen xenoliths, as the spinel-garnet peridotite transition at ~1000–1100 °C is approximately and located at 65km (Fig. 32); significantly hotter or cooler paleogeotherms would have resulted in equilibration of some xenoliths at plagioclase lherzolite or garnet lherzolite facies depths, respectively. These results are in good accordance with a Late Ordovician hot paleogeothermal regime inferred for the Sangilen plateau that is similar to that recorded in younger, Neogene basalt-hosted spinel mantle xenoliths from the Baikal rift (Ionov, 2002).

In many suites of spinel peridotite xenoliths, samples with poikilitic texture usually record the highest equilibration temperatures and are commonly ascribed to recrystallization at near-solidus peridotite temperatures under high melt-rock ratios near the lithosphere-asthenosphere boundary (Embey-Isztin et al., 2001; Xu et al., 1998, 2003). The absence of correlation between equilibration temperature, textural and trace element types (Fig. 32) and the coincident high equilibration temperatures of Sangilen poikilitic xenoliths with those of other textural types point to the absence of a layered spatial distribution of the textural types in the sampled Sangilen lithospheric mantle.

4.4.2. Composition of the Sangilen Plateau Lithospheric Mantle: Geochemical Record of Partial Melting and Metasomatism

The partial melting record

The spinel Cr# and olivine Mg# variations in Sangilen peridotite xenoliths indicate they are mostly residues of low to moderate (up to 10%) degrees of partial melting of a fertile peridotite mantle source (Fig. 30). Because clinopyroxene is the main carrier of trace elements in upper mantle anhydrous spinel peridotite (Garrido et al., 2000; McDonough and Frey, 1989; Rampone et al., 1991; Rivalenti et al., 1996; Stosch, 1982), its trace element composition is of particular interest to further constrain the magmatic processes that affected the Sangilen lithospheric mantle.

The Yb_N content of clinopyroxene is particularly a good proxy for depletion of mantle peridotite during spinel lherzolite facies melting because it mainly depends on the total melt

extracted irrespectively of the melting mechanism (*i.e.* batch, fractional or incremental melting) (*e.g.* Johnson et al., 1990; Shaw, 1970) and it is hardly modified by post-melting processes associated with melt porous flow (Bodinier et al., 1988; Godard et al., 1995; Ionov et al., 2002; Lenoir et al., 2001; Ozawa and Shimizu, 1995; Soustelle et al., 2009; Suhr, 1999; Vernières et al., 1997). Fig. 33 displays the (Ce/Dy) (Fig. 33a) and (Sm/Yb) (Fig. 33b) *versus* the Yb_N content of Sangilen peridotite clinopyroxenes and the variation of these parameters calculated for clinopyroxene in spinel peridotite residues of variable degrees of non-modal batch and fractional melting. In good accordance with their olivine and spinel compositions (Fig. 30), the Yb_N content of clinopyroxene in xenoliths 3H-4, 3H-8 and 5H-2 records low degrees of partial melting (Fig. 33). The Yb_N content of clinopyroxene in other Sangilen xenoliths indicates they are residues of up to ~40% batch melting or 15% fractional melting of a depleted mantle source; however, the lherzolite mineral assemblage of Sangilen xenoliths is more consistent with the lower melting degree estimates. The highest inferred melting degree corresponds to Type II 3H-2 and Type III 5H-13 xenoliths (Fig. 33), in good agreement with their highly refractory spinel Cr# (Fig. 30). Only the elevated Yb_N content of clinopyroxene in 5H-10 (Fig. 33) cannot be accounted for by partial melting from usual peridotite mantle sources and it most likely reflects enrichment by post-melting magmatic processes discussed below. So, partial melting alone cannot explain the REE variability of clinopyroxene in Sangilen mantle xenoliths (Fig. 33).

Although the $(Ce/Dy)_N$ of clinopyroxene in Type I xenoliths 5H-7 and 5H-9 is consistent with being melting residues of variable degrees of batch melting (Fig. 33a), batch melting cannot reproduce their $(Sm/Yb)_N$ ratios (Fig. 33b). Furthermore, the $(Ce/Dy)_N$ ratio of clinopyroxene in xenoliths 3H-2, 5H-3 and 5H-13 is higher than that calculated for clinopyroxene residual of different melting mechanisms. These variations of $(Ce/Dy)_N$ and $(Sm/Yb)_N$ in clinopyroxene unexplained by melting most likely indicate that mantle xenoliths underwent post-melting modifications by metasomatism.

Irrespective of the melting mode, the depletion of Sangilen mantle xenoliths is not correlated either with textural type or their depth of provenance (*cf.* Fig. 32 & 33). Some cratonic and circumcratonic xenolith suites reveal compositionally and texturally layered lithospheric mantle related to different mechanisms of accretion of the continental and/or subducted lithosphere (*e.g.* Carlson et al., 2005; Foley et al., 2006; Griffin et al., 1999a, 2003, 2004; Pearson et al., 2007; Rudnick et al., 1993, 1998; Simon et al., 2007). The absence of layered structure in the sampled lithospheric mantle from the Sangilen plateau is instead consistent with growth by the succession of the accretionary tectonic processes associated

with the building of the Tuva-Mongolia micro-continent (Djomani et al., 2003; Khutorskoy and Yarmolyuk, 1989; Zorin et al., 1990).

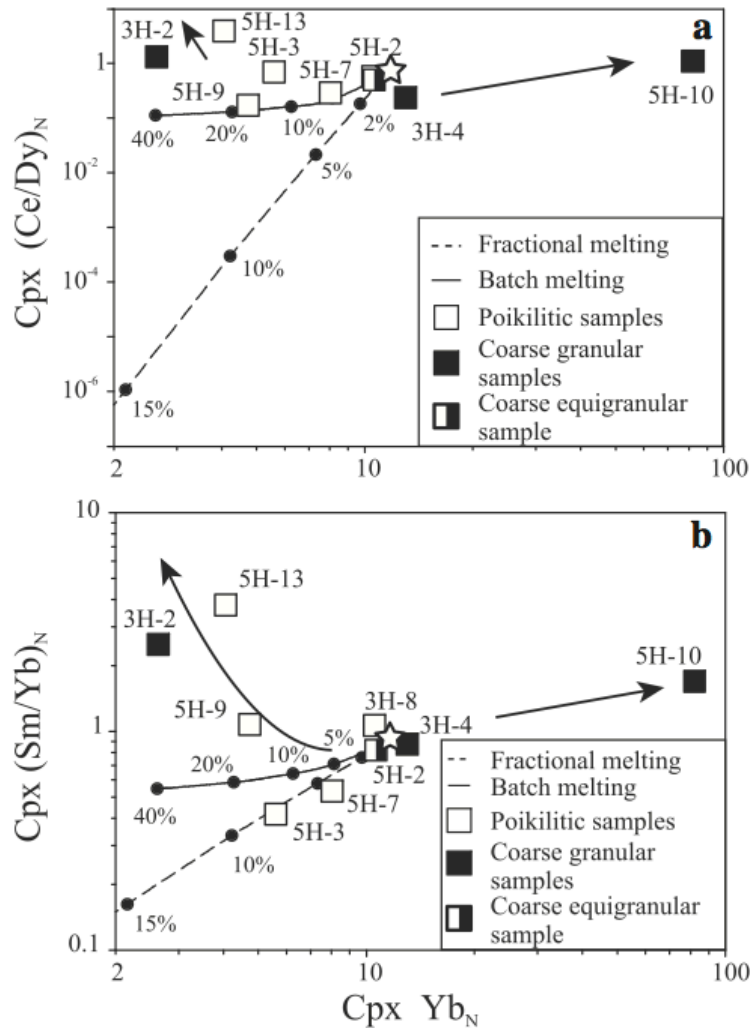


Fig. 33 Yb_N contents versus $(Ce/Dy)_N$ (a) and $(Sm/Yb)_N$ (b) of clinopyroxene (N =chondrite-normalized after Sun and McDonough, 1989) in Sangilen Plateau mantle xenoliths compared with those of spinel peridotite residues of non-modal fractional (dashed lines) and batch (solid curves) melting of depleted MORB mantle (open star) (Salters and Stracke, 2004). The source and melting modal proportions (ol:opx:cpx) are taken for peridotite melting at 2 GPa after Niu (1997) and are, respectively, 0.57:0.28:0.15 and -0.03:0.50:0.53. Number labels in melting curves indicate degrees of partial melting. The bulk composition partition coefficients are taken from Bedini et al. (1997) and Su et al. (2003). Black arrows indicate variations that cannot be accounted for by melting models and are most likely due to post-melting, mantle metasomatism (see text for further details).

The mantle metasomatism record

Enrichments of incompatible trace elements relatively to predictions of partial melting models are commonly observed in mantle-derived peridotite (Bodinier and Godard, 2006; Downes, 2001; Hawkesworth et al., 1984; Pearson et al., 2003 and references therein). These compositional modifications, which are collectively referred to as mantle metasomatism (Menzies and Hawkesworth, 1987a and references therein), are generally ascribed to post-melting magmatic processes caused by melt/rock reactions involving percolation of small fractions of fluids, volatile-rich silicate melts and/or carbonate melts through asthenospheric or lithospheric mantle (*e.g.* Bell et al., 2005; Bodinier et al., 1990; Dautria et al., 1992; Garrido and Bodinier, 1999; Gregoire et al., 2001; Harte et al., 1993; Ionov et al., 2002; Lenoir et al., 2001; McKenzie, 1989; Soustelle et al., 2009). Transient chromatographic chemical fractionation produced by metasomatic melts/fluids percolating through a peridotite matrix may account for the variable fractionation of LREE-MREE relative to HREE observed in Sangilen xenoliths (Fig. 33). According to the chromatographic fractionation model, porous flow of melt/fluid through peridotite generates chromatographic fronts for trace elements of different compatibility; accordingly, LREE chromatographic fronts travel significantly faster than those of more compatible MREE and HREE. This dynamic chemical fractionation creates transient enrichment of incompatible elements in both the percolated peridotite and the metasomatic melt (Bodinier et al., 1990; Godard et al., 1995; Navon and Stolper, 1987; Soustelle et al., 2009; Takazawa et al., 1992; Vernières et al., 1997). For a constant integrated melt/rock ratio and absence of mineralogical reaction, peridotite affected by the highest melt/rock ratio is in closer trace element exchange equilibrium with the primordial metasomatic melt (Navon and Stolper, 1987; Vasseur et al., 1991; Vernières et al., 1997).

A potential candidate for unraveling the trace element composition of the parental metasomatic agent in Sangilen peridotites is Type III xenolith 5H-13. The LREE-enriched normalized pattern of clinopyroxene in this sample (Fig. 31c) is in trace element exchange equilibrium with mantle-derived alkaline melts (Fig. 34). Several studies have reported genetic links between alkali basalts and precursor metasomatic agents that metasomatized their hosted spinel mantle xenoliths (Bedini et al., 1997; Dautria et al., 1992; Downes, 2001); it is hence conceivable that the Sangilen mantle was metasomatized by alkaline melts similar – or precursor – to the Agardag lamprophyres. Carbonate melts are also extremely rich in incompatible trace elements and effective metasomatic agents due to their capability of easily migrating through peridotite owing to low melt-solid dihedral angles (Dautria et al., 1992; Ionov et al., 1993; Rudnick et al., 1993; Watson and Brenan, 1987; Yaxley et al., 1991).

Although clinopyroxene in some Types II and III Sangilen xenoliths is LREE-enriched (Fig. 31b-c), it lacks the trace element signature that characterizes peridotite clinopyroxene metasomatized by carbonate melts; namely, negative anomalies of high field strength elements (Ti, Nb, Ta, Zr and Hf) relative to REE and Th-U, and low Ti/Eu ratios (Fig. 31e-f) (Coltorti et al., 1999; Dautria et al., 1992; Foley et al., 2009; Grégoire et al., 2000; Ionov et al., 1993; Klemme et al., 1995; Rudnick et al., 1993). Although the physical nature of the metasomatic agent that affected Sangilen xenoliths remains mostly unconstrained, trace element variations in clinopyroxene suggest that it was alkaline silicate melt, similarly to spinel peridotite xenoliths from West Eifel (Zinngrebe and Foley, 1995).

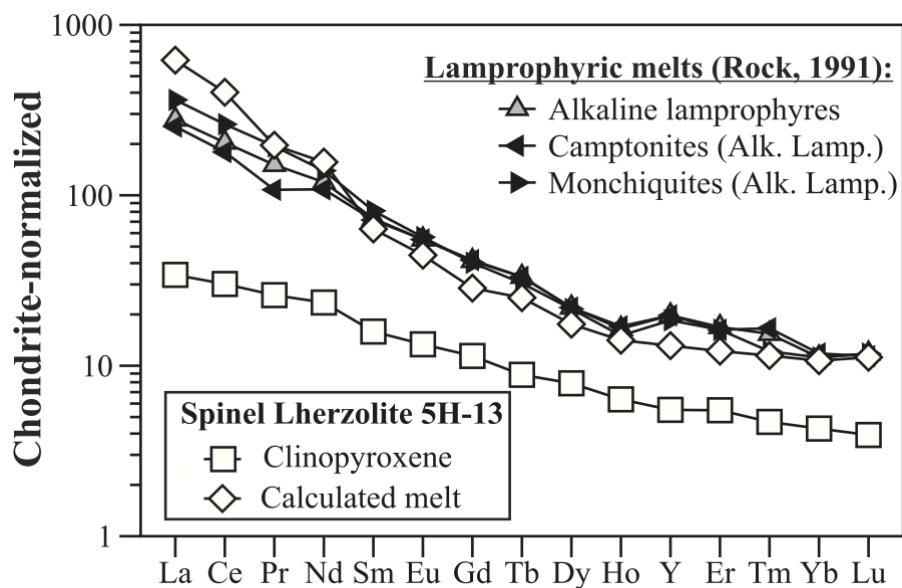


Fig. 34 C1 chondrite-normalized REE patterns of clinopyroxene (open squares) of Sangilen xenolith 5H-13 and the calculated melt (open diamonds; partition coefficients from McKenzie and O’Nions, 1991) in exchange equilibrium with it compared with the REE patterns of common alkaline lamprophyres (after Rock, 1991). Normalizing values after Sun and McDonough (1989).

Fig. 35 shows the results of melt/rock reaction simulation using the plate numerical model of Vernières et al. (1997) aiming to test whether variable REE patterns of clinopyroxene in Sangilen xenoliths (Fig. 31a-c) may be reproduced by reaction between depleted peridotite and a percolating alkaline melt in equilibrium with the clinopyroxene of 5H-13 (Type III sample in Fig. 31c) as shown in Fig. 34. Modeling results show that clinopyroxene REE patterns of Sangilen xenoliths (Fig. 35a) can be reproduced satisfactorily by variable integrated melt/peridotite ratios and constant melt mass of a LREE-rich alkaline parental melt percolating through a depleted lithospheric peridotite (Fig. 35b). Only the clinopyroxene composition of 5H-10 cannot be ascribed to the percolation metasomatic model described above, as its trace element contents are too high (Fig. 35a). In a melt-

peridotite percolation scenario, such high concentrations can be explained by percolation of the same parental metasomatic melt coupled with fractional crystallization and reaction with host peridotites at decreasing melt mass (the percolative fractional crystallization model of Harte et al., 1993). As reported for other mantle spinel peridotites, percolation of metasomatic melts reacting with host peridotite at decreasing melt-rock ratios causes substantial enrichment of trace elements (Bedini et al., 1997; Bodinier et al., 2008; Soustelle et al., 2009) and may account for their high contents in clinopyroxene in 5H-10 (Fig. 31e).

Fig. 36 gives a portrait of a conceptual model for metasomatism by alkaline melts in the Sangilen lithospheric mantle. As for melting-induced compositional variations, trace element variations due to metasomatism in Sangilen xenoliths are not correlated with the xenolith textural type and equilibration temperature and, therefore, depth of provenance (*cf.* Fig. 31, 32 & 35). In contrast with other subcontinental lithospheric mantle sections, where correlation between texture and equilibration temperature of spinel peridotite xenoliths reveals systematic variations of metasomatic reactions with depth at lithospheric length scales (Bedini et al., 1997), Sangilen xenoliths seem to reveal a more heterogeneous metasomatic imprint that may be better explained by variable, vein-related reactions throughout the lithospheric section (Bodinier et al., 1990, 2004; Harte et al., 1993; Wilshire, 1987) (Fig. 36). The absence in Sangilen xenoliths of hydrous minerals distinctive of modal metasomatism, such as amphibole or phlogopite, indicates incompatible trace element enrichments were generated by cryptic metasomatism (Harte et al., 1993; Hawkesworth et al., 1984; Menzies and Hawkesworth, 1987a, 1987b). As hydrous minerals are common liquidus phases in alkaline mafic magmas and lamprophyres at depth of equilibration of spinel peridotites (Foley, 1984, 1990; Foley et al., 2009), cryptic metasomatism further constrains metasomatism at elevated temperature that can only be accounted in the wall rock of veins where super solidus alkaline melt circulated. Near-isothermal, melt-peridotite metasomatic reactions at constant melt mass (Fig. 35 & 36 right panel) along wall peridotite of intrusive dykes may be responsible for variable REE variations observed in clinopyroxenes from Sangilen xenoliths (Fig. 36). Further crystallization of metasomatic melts at decreasing temperature away from dykes would result in over-enrichment of trace elements in metasomatized peridotite as seen in sample 5H-10 (Fig. 36 left panel). Far from intrusive dykes, lithospheric mantle section is characterized by depleted mantle composition. If melt intrusion occurred at temperature above the stability of hydrous phases in the metasomatic alkaline melts, once the magmatic activity ceased no trace of metasomatism would remain other than its cryptic imprint.

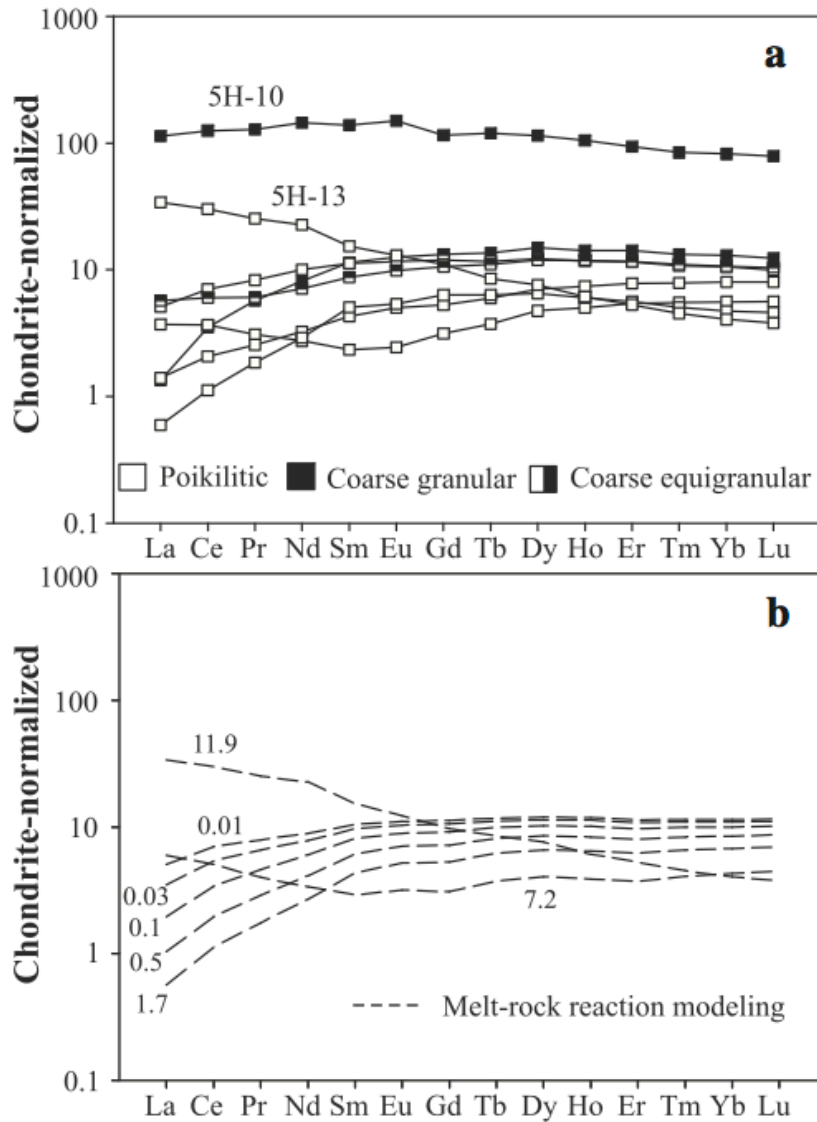


Fig. 35 C1 Chondrite normalized REE patterns of clinopyroxene in the Sangilen spinel lherzolite (**a**) (symbols as in Fig. 30) compared with (**b**) those for clinopyroxene obtained from modeling of melt-peridotite reaction using the plate model of Vernieres *et al.* (1997) for the simulation of the trace element fractionation during partial melting and magma transport in the upper mantle. The REE composition of the melt reacting with mantle peridotite is that in equilibrium with clinopyroxene sample 5H-13 (see Fig. 34). The REE and modal compositions of the peridotite source are those of the depleted MORB mantle (Salters and Stracke, 2004). The melt-rock reaction used in the simulation is: $0.9 \text{ Opx} + 0.45 \text{ Cpx} = 0.35 \text{ Ol} + 1 \text{ Melt}$. The number of reaction cells and dissolution increment (Vernieres *et al.*, 1997) are, respectively, 100 and 0.0024. The curve shows the best fits to clinopyroxene compositions of all Sangilen xenoliths (Fig. 35b) but sample 5H-10; labels on dashed patterns indicate the instantaneous melt/rock ratio. Partition coefficients are from Bedini *et al.* (1997) and Su *et al.* (2003). Normalizing values after Sun and McDonough (1989).

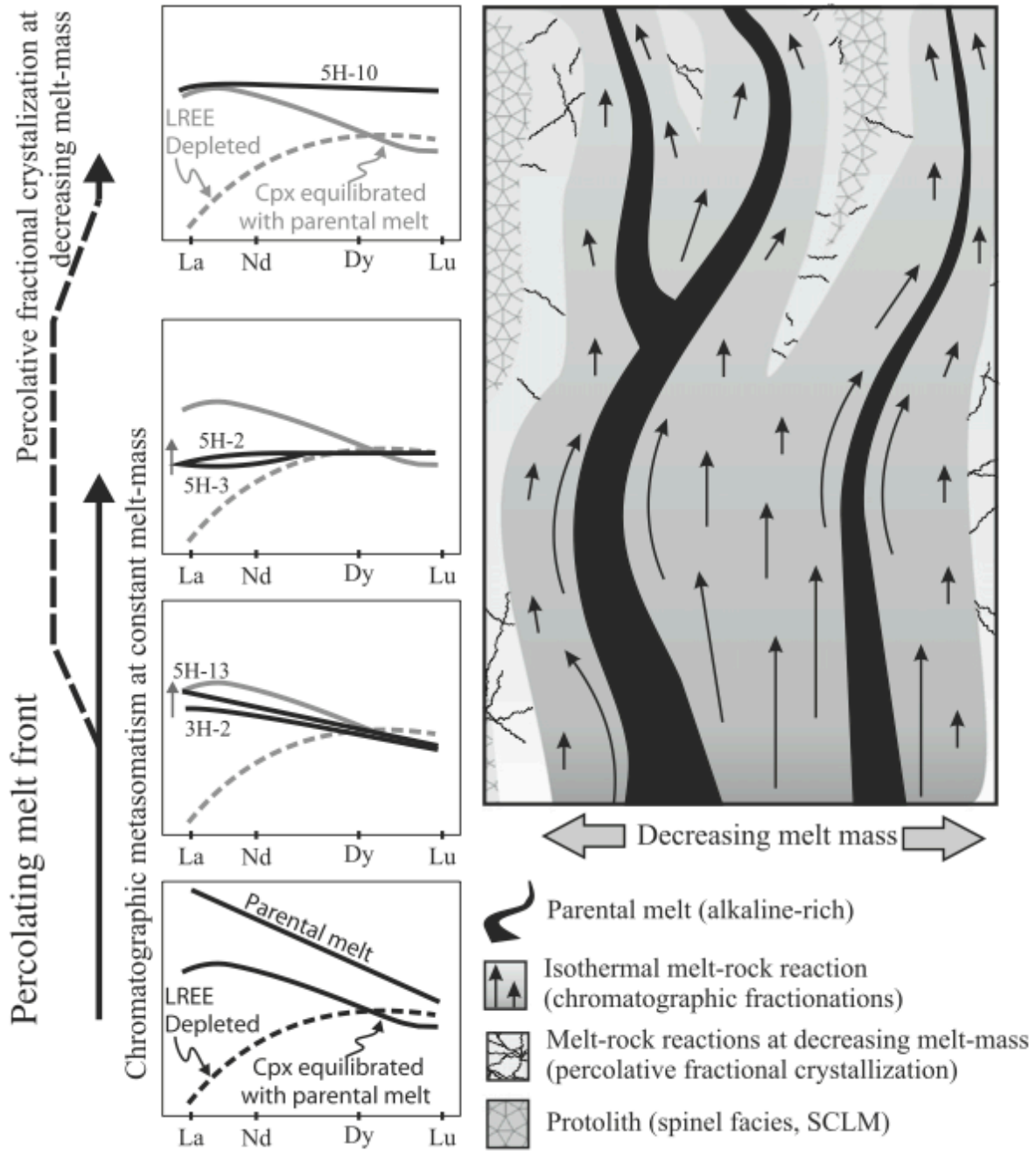


Fig. 36 Cartoon of conceptual model (right panel) to account for the trace element variability of Sangilen plateau peridotite xenoliths by mantle metasomatism produced by a veined network of parental alkaline-rich melts reacting with variable depleted source lithospheric peridotites. See text for further details.

4.5. Conclusion

On the basis of our petrological and geochemical study of Sangilen mantle xenoliths, the following conclusions can be drawn:

- i.** Sangilen xenoliths record a narrow range of equilibration temperature (*ca.* 1000–1100 °C) plotting along a relatively hot intracontinental geotherm at lithospheric depths from ~43 to 53 km (1.3 to 1.6 GPa).
- ii.** Their variation of olivine Mg# (87.9–90.9) with spinel Cr# (9.5–45.7) indicates xenoliths are mostly residues of up to 10% melting of a depleted peridotite source.
- iii.** The elevated Yb_N content of clinopyroxene in sample 5H-10 and the variable fractionation of LREE-MREE relative to HREE in clinopyroxene from other xenoliths indicate they underwent variable metasomatic processes. These processes probably consisted of episodes of percolation-reaction through peridotite of small-melt fractions of alkaline mafic melts precursor to Agardag alkaline lamprophyres.
- iv.** The lack of correlation with depth of modal variations, textural types, inferred degrees of melting and trace element patterns of clinopyroxene indicates the absence of a texturally or compositionally layering in the lithospheric mantle beneath the Sangilen plateau sampled by Ordovician lamprophyres. The observed compositionally variation of xenoliths is better accounted by depleted lithosphere variably metasomatized along a network of percolating alkaline mafic melts heterogeneously distributed throughout the Sangilen lithospheric mantle section.

5. Deformation Record, Seismic Properties and Flow of the Shallow Upper Mantle in the Westernmost Mediterranean: Insights from mantle xenoliths in Plio-Pleistocene Alkali Basalts from the eastern Betic Cordillera (SE Spain)

Z. Konc^a, C.J. Garrido^a, A. Tommasi^b, K. Hidas^a, A. Vauchez^b, J.A. Padrón-Navarta^{b,c}, A. Acosta-Vigil^a, Cs. Szabó^d & C. Marchesi^a

Abstract

Peridotite mantle xenoliths in Plio-Pleistocene alkali basalts of the eastern Betic Cordillera (Cartagena area, Murcia, SE Spain) provides a snapshot of the structure and composition of the shallow lithospheric mantle at the northern limb of the Alpine Betic-Rif arched belt in the westernmost Mediterranean. Mantle xenoliths are spinel and plagioclase lherzolite, with minor harzburgite and wehrlite, displaying porphyroclastic to fine- to medium-grained equigranular textures. Regardless composition and texture, the Crystal Preferred Orientation (CPO) of olivine in xenoliths shows an axial-[100] pattern characterized by a strong alignment of olivine [100]-axes near or parallel to the peridotite lineation and a girdle distribution of [010]-axes with a maximum normal to the peridotite foliation. This CPO pattern is consistent with ductile deformation accommodated by dislocation creep with dominant activation of the high temperature [100]{0kl} olivine slip system indicative of deformation by simple shear or combinations of simple shear and pure shear with a transtensional component. Synkinematic deformation of orthopyroxene in veins of composite xenoliths formed by reactive percolation of subduction-related Si-rich melt/fluids shows that deformation in xenoliths occurred in the late Neogene. Synkinematic overprinting of mineral assemblages from the garnet-spinel to the plagioclase facies demonstrates 36-40 km uplift continuously accommodated by ductile shear thinning of the lithospheric mantle.

Calculated seismic properties of mantle xenoliths are characterized by fast propagation of P-waves and polarization of the fast split of S-waves parallel to olivine [100]-axis that are aligned subparallel to mantle flow. The observed SKS and Pn seismic anisotropy beneath eastern Betics can be explained by shallow lithospheric mantle peridotite having a fabric similar to eastern Betic xenoliths and their [100]-axes are subhorizontal and subparallel to the mantle flow direction. The shallow thickness of the mantle lithosphere (40-80 km) and

measured azimuths and delays of polarized SKS waves in the eastern Betics can be explained by a steeply dipping mantle foliation and a subhorizontal lineation with a ca. N 69° strike. This geometry of the lithospheric peridotite fabrics implies active or frozen mantle flow with a dominantly strike-slip component subparallel to the paleo-Iberian margin and most likely reflects an inherited fabric. This fabric was most likely acquired during strike-slip deformation in the early Miocene due the W-SW slab retreat of the Alboran lithosphere at the edge of the Iberian margin. Compositional profiles in xenoliths indicate that initiation of ductile thinning occurred between 6.2 and 9.4 Ma. In the eastern Betics this time span broadly overlaps with significant magmatic and tectonic deep processes such as onset of lower crust anatexis (ca. 9 Ma), the change from subduction-related to intraplate-type volcanism (6.3-4.8 Ma), and uplift associated with the Messinian salinity crisis likely due to mantle upwelling and lithospheric edge delamination of the Iberian margin during westward rollback of the subducted Tethys oceanic lithosphere. The existence of strike-slip inherited mantle fabrics may continue governing some deep processes in the Eastern Betics. We propose that edge delamination of the Iberian margin in the middle Miocene triggered thinning, decompression and westward inflow of hot extended lithosphere of Alboran provenance to fill the detached cold lithosphere following the inherited roll-back S-SW lithospheric anisotropy at the edges of Iberia. This event was likely coeval to the middle to late Miocene E-W opening and oceanic magmatic accretion of the Algero-Balearic basin. Detachment of the subducted lithospheric mantle and westward replacement by Alboran-type hot lower lithosphere would account for the Alboran provenance of mantle and lower crustal in the Eastern Betics.

^a *Instituto Andaluz de Ciencias de la Tierra (IACT), CSIC & UGR, Avenida de las Palmeras 4, 18100 Armilla, Granada, Spain.*

^b *Géosciences Montpellier, Université Montpellier II & CNRS, Place E. Bataillon, 34095 Montpellier, France.*

^c *Research School of Earth Sciences. The Australian National University. Mills Road, Canberra, Australia.*

^d *Lithosphere Fluid Research Lab, IGES, Eötvös Lorán University, Pázmány Péter sétány 1/C, H-1117, Budapest, Hungary.*

5.1. Introduction

Orogenic arcs in the Mediterranean—formed during the Cenozoic convergence of the African and European plates—provide a natural laboratory where to test key plate tectonic hypotheses on the evolution of subduction, nature of lithospheric plates, large scale strike-slip and intraplate deformation and arc volcanism. In the westernmost Mediterranean, the Betic-Rif orogenic belt—an arched orogenic belt arc around the Alboran sea basin—was mainly formed during the Miocene collision between the Alboran domain and the south Iberian and Maghrebian passive margins in the context of N-S to NW-SE Africa-Iberia convergence. Slab rollback and detachment, mantle lithosphere delamination, and convective thinning of overthickened lithospheric roots are among the diverse geodynamic scenarios proposed to account for Tertiary synorogenic extension leading to the opening of the Alboran Sea basin and the current shape and topography of this orogenic belt (Lonergan and White, 1997; Spakman and Wortel, 2004; Booth-Rea et al., 2007 and references therein).

An increasing number of seismological experiments are trying to investigate the current deep mantle structure of the Betic-Rif arc as a mean to elucidate its Tertiary geodynamic evolution (e.g. Calvert et al., 2000; Gurria and Mezcuá, 2000; Serrano et al., 2005; Buontempo et al., 2008; Jolivet et al., 2009; Diaz et al., 2010). Among these, teleseismic shear wave splitting measurements show that the fast direction of SKS splitting is parallel to the limbs of the Betic-Rif arc and rotates around the Gibraltar arc (Buontempo et al., 2008; Díaz et al., 2010). Although these data have been used to support geodynamic hypotheses proposing rollback of a westward retreating slab, the nature, age and geodynamic significance of seismic anisotropy is still uncertain; combination of fossil anisotropy from Eocene subduction and renewed Miocene asthenospheric flow around an Alboran slab are among the hypotheses put forward to account for the seismic anisotropy in the circum-Alboran sea basin. Some difficulties in the interpretation of SKS measurements arise from deciphering the cause of anisotropy and its mantle lithosphere or asthenosphere provenance (Fouch and Rondenay, 2006). Laboratory and theoretical studies indicate that seismic anisotropy in the uppermost mantle results mainly from the Crystal Preferred Orientation (CPO) of mantle olivine (Nicolas and Christensen, 1987; Long and Becker, 2010). Microstructural studies of natural mantle peridotite hence can provide useful information on the nature and significance of mantle seismic anisotropy beneath orogens (e.g. Mainprice et al., 2000; Karato et al., 2008).

Alkali basalts—2-3 Ma—in the inner easternmost Betic Cordillera entrained numerous mantle xenoliths that provide a snapshot of the structure and composition of the lithospheric mantle beneath the NE termination of the Alboran arc system. These mantle xenoliths provide a unique opportunity for the direct observation of the lithospheric mantle and complementary information to seismological investigation about the structure and composition of uppermost mantle beneath this region. Here we report a detailed microstructural and crystal preferred orientation study of mantle spinel peridotite xenoliths hosted in alkaline basalts from the Tallante area volcanic centers (Murcia, SE Spain). We will use these data to unravel the deformation record, constrain the relative age of microstructures and derive the anisotropic seismic properties of the lithospheric mantle beneath SE Iberia. Comparison of the calculated anisotropy and delay times with available seismic data allows us to provide new important insights into the age and significance of seismic anisotropy in the NE termination of the Alboran arc system.

5.2. Sampling and Sample Preparation

The mantle xenoliths collected for the present study come from the alkali basalt volcanic centers of “Cabezo Negro de Tallante” (samples with label prefix TAL)—hereafter referred to as “Tallante”—and “Los Perez” (samples with label prefixes LP08 and LPE) located to the northwest of Cartagena (Murcia, Spain). From a large sampling, we selected 12 and 13 peridotite xenoliths from the Tallante and Los Perez volcanic centers, respectively (Table 5). We selected mantle xenoliths on the basis of their lack of macroscopic evidence for contamination by host magma, their size, and their representativeness in terms of their macroscopic texture and modal composition. We excluded composite peridotite xenoliths containing veins, vein networks, and/or large patches of kaersutitic amphibole that are common in the Tallante volcanic center (Beccaluva et al., 2004; Rampone et al., 2010; Bianchini et al., 2011). These amphibole-bearing composite xenoliths record mantle metasomatism by alkaline melts prior to eruption (Boivin, 1982) that might have obscured the deformation record of peridotite. Study of amphibolite veins in the Lherz peridotite massif shows this type of metasomatic processes are restrained to veins and their wall rocks and are not volumetrically representative of the structure and composition of the massif (Bodinier et al., 1987). We have included a composite xenolith containing millimetric veins of orthopyroxene that have been interpreted as produced by silica-rich, subduction derived mantle metasomatism (Arai et al., 2003; Shimizu et al., 2004; Rampone et al., 2010) that predates alkaline volcanism (Bianchini et al., 2011). This composite xenolith might then

provide relative time constraints between the deformation recorded in peridotite and subduction-related metasomatism in the eastern Betics.

Most xenoliths display no patent macroscopic foliation and/or lineation and thin sections were made from random cuts. In the few with a patent foliation and lineation defined by stretched spinel, thin sections were made from slabs perpendicular to foliation and parallel to the lineation.

To improve the quality of back-scattered diffraction measurements, standard diamond polished (down to 0.25 mm grain size) thin sections were polished for 5 min with a chemical-mechanical procedure using colloidal silica suspension (Buehler™ Mastermet™).

Table 5 Sample description with the estimated equilibrium temperatures

| Sample | Location | Texture | Lithology | Mineral Assemblage (mode %) | T _{solv} (±31 °C) | T _{Ca-Opx} (±16 °C) | T* _{Ca-Opx} (±25-45 °C) | T _{Al-Opx} (±15 °C) |
|----------|-----------|-----------------|-------------|--|-------------------------------|---------------------------------|-------------------------------------|---------------------------------|
| LP08-02 | Los Perez | porphyroclastic | Lherzolite | Ol (64), Opx (21), Cpx (14) [Sp, Plg] | 844 | 932 | 906 | 982 |
| LP08-12 | Los Perez | porphyroclastic | Wehrlite | Ol (82), Cpx (18) [Spl] | | | | |
| LPE-002 | Los Perez | cluster porph. | Lherzolite | Ol (68), Opx (21), Cpx (11) [Sp, Plg] | 867 | 994 | 980 | 949 |
| LPE-008 | Los Perez | composite | Lherzolite | Ol (55), Opx (43), Cpx (2) [Sp, Plg, Amp] | | | | |
| LPE-016 | Los Perez | cluster porph. | Lherzolite | Ol (71), Opx (17), Cpx (19) [Spl] | | | | |
| LPE-025 | Los Perez | equigranular | Lherzolite | Ol (77), Opx (17), Cpx (6) [Spl] | | | | |
| LPE-028 | Los Perez | equigranular | Wehrlite | Ol (85), Cpx (15) [Spl] | | | | |
| LPE-029 | Los Perez | cluster porph. | Lherzolite | Ol (71), Opx (20), Cpx (9) [Sp, Plg] | 986 | 1055 | 1050 | 935 |
| LPE-042* | Los Perez | equigranular | Lherzolite | Ol (68), Opx (20), Cpx (13) [Spl] | 939 | 988 | 973 | 993 |
| LPE-048* | Los Perez | porphyroclastic | Lherzolite | Ol (73), Opx (16), Cpx (10) [Spl] | 977 | 1047 | 1041 | 969 |
| LPE-058 | Los Perez | transitional | Lherzolite | Ol (63), Opx (19), Cpx (18) [Sp, Plg] | | | | |
| LPE-061 | Los Perez | porphyroclastic | Lherzolite | Ol (70), Opx (20), Cpx (11) [Sp, Plg] | 859 | 1124 | 1125 | 1083 |
| LPE-062* | Los Perez | porphyroclastic | Lherzolite | Ol (65), Opx (22), Cpx (13) [Spl] | 1005 | 1054 | 1049 | 976 |
| TAL-001 | Tallante | transitional | Lherzolite | Ol (74), Opx (17), Cpx (10) [Spl] | 872 | 980 | 964 | 933 |
| TAL-014 | Tallante | porphyroclastic | Lherzolite | Ol (68), Opx (23), Cpx (9) [Sp, Plg, Ap] | 894 | 1175 | 1177 | 1070 |
| TAL-047* | Tallante | cluster porph. | Lherzolite | Ol (74), Opx (19), Cpx (7) [Spl] | | | | |
| TAL-056* | Tallante | porphyroclastic | Lherzolite | Ol (76), Opx (17), Cpx (6) [Spl] | 887 | 976 | 959 | 982 |
| TAL-084 | Tallante | transitional | Harzburgite | Ol (78), Opx (17), Cpx (5) [Spl] | 892 | 955 | 935 | 1010 |
| TAL-094 | Tallante | transitional | Lherzolite | Ol (78), Opx (17), Cpx (5) [Sp, Plg] | 905 | 970 | 952 | 1063 |
| TAL-106 | Tallante | transitional | Lherzolite | Ol (74), Opx (16), Cpx (10) [Sp, Plg] | | | | |
| TAL-112 | Tallante | cluster porph. | Lherzolite | Ol (76), Opx (15), Cpx (10) [Spl] | 884 | 956 | 935 | 945 |
| TAL-124 | Tallante | porphyroclastic | Harzburgite | Ol (87), Opx (10), Cpx (2) [Sp, Plg] | | | | |
| TAL-127 | Tallante | porphyroclastic | Lherzolite | Ol (70), Opx (21), Cpx (9) [Sp, Plg] | 1038 | 951 | 930 | 994 |
| TAL-134 | Tallante | cluster porph. | Lherzolite | Ol (70), Opx (19), Cpx (11) [Spl] | 843 | 974 | 957 | 962 |
| TAL-148 | Tallante | porphyroclastic | Lherzolite | Ol (75), Opx (15), Cpx (10) [Sp, Plg, Amp] | | | | |

Ol – olivine, Opx – orthopyroxene, Cpx – clinopyroxene, Sp – spinel, Plg – plagioclase, Amp – amphibole, Ap – apatite
Using thermometers: T_{solv} – Taylor, 1998; T_{Ca-Opx} – Brey and Kohler, 1990; T*_{Ca-Opx} – Nimis and Grutter, 2010; T_{Al-Opx} – Witt-Eickschen and Seck, 1991

porph. – porphyroclastic; * Paten lineation/foliation

We calculated the modal composition of peridotites by mass balance (wt.%) and, where bulk rock analyses were unavailable due to the small size of xenoliths, from EBSD-SEM phase maps (vol.%). Mass balance calculation for modal analysis uses an inversion procedure (Garrido et al., 2000) combining the major element bulk rock (Konc et al., submitted) and the average mineral composition of xenoliths. For most samples, the modal composition retrieved using both procedures compares well (Fig. 37).

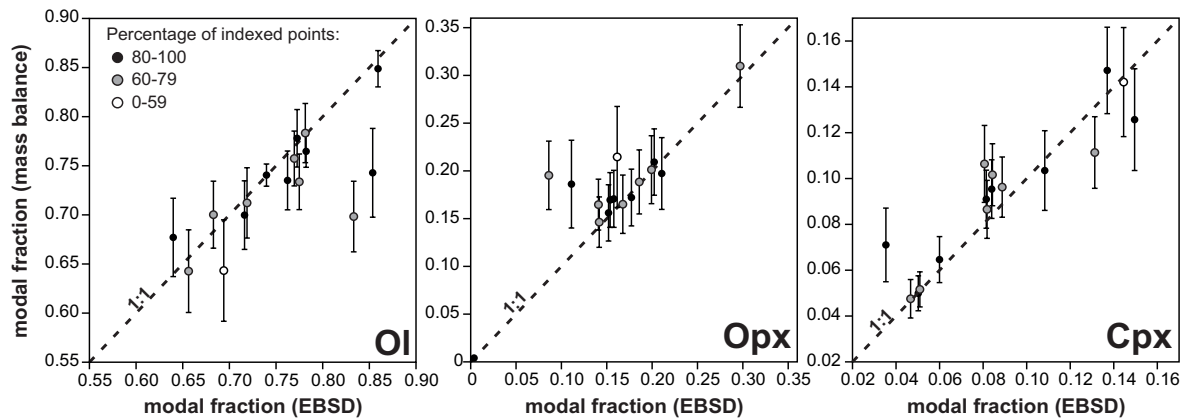


Fig. 37 Plots comparing modal proportions of olivine (Ol), orthopyroxene (Opx) and clinopyroxene (Cpx) obtained from mass balance (wt.%) and EBSD data (vol. %). Mass-balance modes were obtained by inversion of whole rock and mineral major element analyses (Tarantola and Valette, 1982; Garrido et al., 2000). Error bars in wt.% modes are 1s. Error of EBSD modes depends on the indexation rate (white, grey and black symbols indicate, respectively, poor, fair, and good indexation rate).

5.3. Mineral Chemistry

The chemical major element composition of peridotite xenolith minerals is within the range of those previously reported for Tallante mantle xenoliths (Capedri et al., 1989; Beccaluva et al., 2004; Rampone et al., 2010). Konc et al. (submitted) provides a detailed account of the mineral chemistry of the studied xenolith; here we only report general variations of interest for the present study. The composition of mineral grains is homogenous and rather similar among samples regardless of their locality, texture, and metamorphic facies. The average Mg# [$100 \cdot \text{Mg} / (\text{Mg} + \text{Fe})$] of olivine varies between 0.89-0.90 in lherzolites and harzburgites, and it is slightly lower (0.87) in wehrlites. The average Mg# of orthopyroxene of lherzolite and harzburgite ranges from 0.89 to 0.91, and that of clinopyroxene varies from 0.91-0.93 in lherzolites and harzburgites, and 0.89 in wehrlites. The spinel Cr# [$100 \cdot \text{Cr} / (\text{Cr} + \text{Al})$] varies between 0.11-0.24 in lherzolite and harzburgite, and it is relatively higher (0.30-0.33) in wehrlites. The anorthite content of plagioclase is 54.4-59.5.

5.4. Lithology and Texture

Peridotite xenoliths are mainly spinel and spinel-plagioclase lherzolites and, to a lesser extent, spinel-plagioclase harzburgites and spinel wehrlites (Fig. 38; Table 5). In good accordance with previous studies (Bianchini et al., 2011), Tallante xenoliths are clinopyroxene-poor lherzolites and harzburgites (Fig. 38). In addition to rare wehrlites, Los Perez xenoliths are mostly lherzolite with variable clinopyroxene content including clinopyroxene-rich lherzolites with modal compositions near that of the primitive mantle (Fig. 38). The composite xenolith LPE-008 of this volcanic center is composed of

orthopyroxenite veins—with straight and serrated boundaries—within a matrix of amphibole-bearing, spinel-plagioclase lherzolite (Fig. 39). Interstitial accessory volatile-bearing minerals (mostly amphibole and apatite) are present in some samples (Table 3), but these minerals are omitted in the present study because of their low modal abundance.

Regardless of their modal composition and locality, xenoliths are fine ($\leq 1\text{mm}$) to coarse-grained ($\geq 3\text{mm}$) peridotites that can be grouped by their texture into porphyroclastic, equigranular, and transitional peridotites (Fig. 38; Table 5) (see also Boivin, 1982; Beccaluva et al., 2004; Rampone et al., 2010). We only have found equigranular textures in xenoliths from Los Perez volcanic center, but Rampone et al. (2010) have also reported this textural group in Tallante.

Porphyroclastic peridotites (Mercier and Nicolas, 1975) are characterized by large rounded, orthopyroxene and, to a lesser extent, olivine porphyroclasts embedded in a medium- to fine-grained recrystallized granoblastic matrix of olivine, pyroxene, and spinel (Fig. 39a). Porphyroclasts show sharp curvilinear grain boundaries and have a weak shape preferred orientation. With the exception of occasional deformation bands in olivine porphyroclasts (Fig. 39a), porphyroclasts generally show no intracrystalline plastic deformation features and subgrain boundaries. The recrystallized matrix is composed of neoblasts of olivine, orthopyroxene, and clinopyroxene of variable sizes that have generally rounded or poorly elongated aspect ratios and curvilinear grain boundaries. Spinel is generally rounded and interstitial; however, in some samples trails of elongated spinel define a patent lineation (*e.g.* TAL-056 and LPE-061). Where present, plagioclase occurs as polygonal aggregates rimming spinel or in elongated or round patches having sharp boundaries with the surrounding granoblastic matrix. A particular subtype of porphyroclastic peridotites—hereafter refer to as cluster porphyroclastic peridotites—is characterized by the presence of porphyroclastic clusters of coarse orthopyroxene + spinel \pm clinopyroxene aggregates, embedded in a fine recrystallized equigranular matrix of olivine, pyroxene and spinel neoblasts (Fig. 39b). Previous authors (Shimizu et al., 2008; Rampone et al., 2010) have described in detail these textures that they have interpreted as breakdown products of former garnet porphyroclasts.

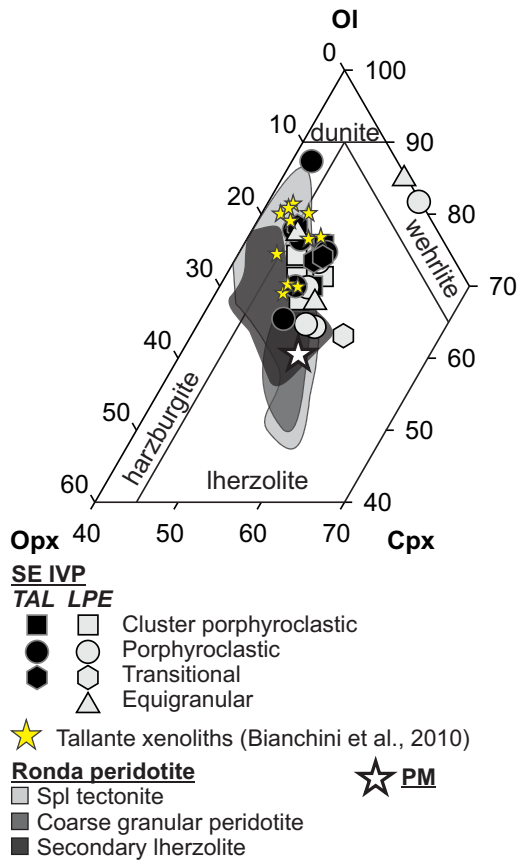


Fig. 38 Strekeissen triangular plot (c.f. Strekeissen, 1974) for the classification of peridotites showing modal composition of Eastern Betic mantle xenoliths (data from this study and from Bianchini et al., 2011) Also shown is the modal composition of peridotites from the different tectono-metamorphic domains of the Ronda peridotite (Van der Wal and Bodinier, 1996; Lenoir et al., 2001; Bodinier et al., 2008; Soustelle et al., 2009)

Equigranular peridotite xenoliths have a medium (1-3 mm) to fine grain polygonal crystals of olivine and pyroxenes with straight grain boundaries and 120° triple junctions (Fig. 39c). Grains show no intracrystalline deformation features or exsolution. Dark brown spinel crystals have irregular, cusped shapes and, less commonly, a holly-leaf shape at the boundaries of rock-forming silicates. Most samples show a mosaic equigranular texture and grains with a near spherical aspect ratio (e.g. wehrlite LPE-028 and lherzolite LPE-042); some samples, however, (lherzolite LPE-025) have a well developed tabular equigranular texture where grains show a larger aspect ratio.

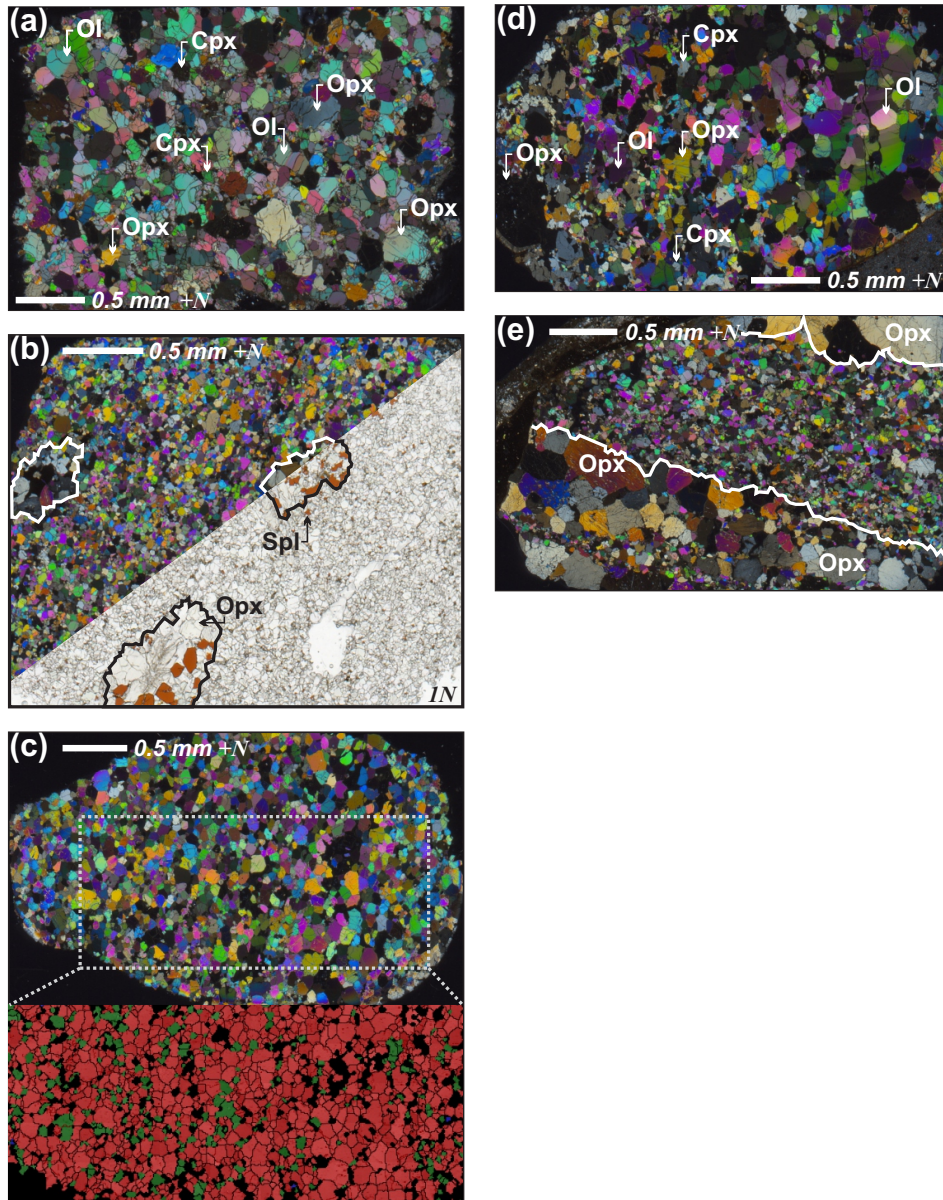


Fig. 39 Micrographs illustrating the different textural groups identified in eastern Betic mantle xenoliths. (a) porphyroclastic spinel-plagioclase lherzolite (TAL-094) with orthopyroxene (Opx) porphyroclasts; (b) cluster porphyroclastic spinel-plagioclase lherzolite (LPE-002) with coarse grained orthopyroxene-spinel clusters marked by white and black solid lines; (c) EBSD phase map of equigranular spinel wehrlite (LPE-028) (olivine, Ol, in red; clinopyroxene, Cpx, in green); (d) transitional spinel-plagioclase lherzolite (LPE-058) showing transition from porphyroclastic (**left**) to granular texture (**right**); (e) composite xenolith (LPE-008) with orthopyroxenite veins composed of large Opx grains in fine-grained porphyroclastic lherzolitic wall-rock (e). (+N – cross-polarized light; 1N – plane-polarized light.)

Transitional peridotites – referred to as porphyroclast-to-granular textures by Rampone et al. (2010) – show microstructures with mixed characteristics between the two above textural groups (Fig. 39d). They have textures reminiscent to normal porphyroclastic peridotite, but with a coarser equigranular matrix composed of olivine and pyroxenes with curvilinear to

straight grain boundaries resembling the equigranular peridotites. Spinel is small and scattered in the samples.

5.5. Geothermometry

Table 5 reports the calculated equilibrium temperatures of peridotite xenoliths obtained applying the two-pyroxene solvus (T_{solv} , Taylor, 1998), the Ca-in-orthopyroxene ($T_{\text{Ca-opx}}$, Brey and Khöler, 1990; $T^*_{\text{Ca-opx}}$, Nimis and Grütter, 2010), and the Al-in-orthopyroxene ($T_{\text{Al-opx}}$, Witt-Eickschen and Seck, 1991) geothermometers. Computation of equilibration temperatures of wehrlites was not possible due to the lack of accurate geothermometric formulations for clinopyroxene-olivine assemblages (*c.f.* Nimis and Grütter, 2010).

We obtain similar equilibration temperatures for different textural groups and lithologies regardless of their locality and metamorphic facies (Table 5). T_{solv} ranges between 844-1038 °C for porphyroclastic peridotites, 843-986 °C for cluster porphyroclastic peridotites, and 872 to 892 °C for transitional peridotites, and yields 939 °C for one equigranular lherzolite. T_{solv} generally results in lower equilibration temperature than any other of the applied formulations, which most likely reflects the lack of equilibration between coexisting clinopyroxene and orthopyroxene pairs. $T_{\text{Al-opx}}$ temperatures ranges between 969-1083 °C for porphyroclastic peridotites, 935-962 °C for cluster porphyroclastic peridotites, and 933-1063 °C for transitional peridotites, and yields 993 °C for one equigranular lherzolite. $T_{\text{Ca-opx}}$ and $T^*_{\text{Ca-opx}}$ are, within the range of uncertainties of these geothermometric formulations, comparable for a given textural groups. With the exception of transitional peridotites, $T_{\text{Ca-opx}}$ and $T^*_{\text{Ca-opx}}$ are higher than temperatures obtained with the other two formulations. $T_{\text{Ca-opx}}$ and $T^*_{\text{Ca-opx}}$ ranges, respectively, between 932-1175 °C and 906-1177 °C for porphyroclastic peridotites, 956-1055 °C and 935-1050 °C for cluster porphyroclastic peridotites, and 955-980 °C and 935-964 °C for transitional peridotites, and yield, respectively, 988 °C and 873 °C for one equigranular lherzolite.

In summary, disregarding T_{solv} , porphyroclastic peridotites tend to yield higher average temperatures ($T_{\text{Ca-opx}}$ & $T^*_{\text{Ca-opx}} = 1032 \pm 92$; $T_{\text{Al-opx}} = 1008 \pm 47$ °C) than cluster porphyroclastic ($T_{\text{Ca-opx}}$ & $T^*_{\text{Ca-opx}} = 987 \pm 44$ °C; $T_{\text{Al-opx}} = 948 \pm 11$ °C) and transitional peridotites ($T_{\text{Ca-opx}}$ & $T^*_{\text{Ca-opx}} = 959 \pm 66$ °C; $T_{\text{Al-opx}} = 1000 \pm 66$ °C), and the equigranular lherzolite ($T_{\text{Ca-opx}}$ & $T^*_{\text{Ca-opx}} = 980 \pm 10$ °C; $T_{\text{Al-opx}} = 988$ °C). These temperature estimates are similar to those reported in previous studies of Tallante xenoliths (920-1020 °C, Seghredi et al., 2002; 830-930 °C for porphyroclastic peridotites, Beccaluva et al., 2004; 950-1020 °C for cluster

porphyroclastic peridotites, Shimizu et al., 2008; and 960-1020°C for all textural groups, Rampone et al., 2010).

5.6. Crystal Preferred Orientation

5.6.1. Olivine

All studied peridotites from Tallante and Los Perez display well-developed olivine CPOs (Fig. 40, 41 & 42). The predominant CPO pattern is axial-[100] (a.k.a. [100]-fiber) characterized by a strong point alignment of olivine [100] axes subparallel to the lineation. The olivine [010] axes show a pronounced girdle distribution normal to the [100] maximum, and the [001] axes display either a weak girdle pattern parallel to the distribution of [010] axes or they have random distribution. Olivine CPOs in some samples (LPE-048, TAL-148, TAL-127, LPE-016, LPE-058, TAL-106 and TAL-001) are transitional towards an orthorhombic pattern characterized by a point-like distribution of all the three axes with [100], [010] and [001] axes with maxima parallel to X (lineation), Z and Y directions, respectively (Fig. 40 & 41). To further characterize the distribution of olivine crystallographic axes we performed eigenvalue analysis. The relative proportion of point, girdle and random components for each olivine axis is calculated from the eigenvectors of the normalized orientation matrix (Vollmer, 1990) (Fig. 43). In the set of studied peridotites, [100] axes exhibit the highest point component and [010] axes are characterized by a patent girdle distribution trending towards the point distribution field. The [001] axes in all cases display a dominantly random component. These observations are consistent with the predominance of axial-[100] olivine CPOs with subordinate occurrence of orthorhombic patterns.

Rotation axes accommodating low-angle ($<15^\circ$) misorientations within olivine crystals are generally distributed normal to [100], displaying two maxima parallel to [001] and [010] (Fig. 44). This indicates dominant slip on $\{0kl\}[100]$ with main activation of $(010)[100]$ and a minor contribution of $(001)[100]$, possibly as edge dislocations in subgrain boundaries. Exceptions are some cluster porphyroclastic (LPE-016 and TAL-134) and a transitional (LPE-058) peridotites where the distribution of rotation axes tends towards [100] (Fig. 44), indicating a possible activation of $(010)[001]$ in addition to $\{0kl\}[100]$. In a previous study of Tallante mantle xenoliths, Rampone et al. (2010) reported the predominance of orthorhombic $(010)[100]$ pattern with minor occurrence of $\{0kl\}[100]$ (A-type and D-type fabrics of Karato et al., 2008, respectively). This discrepancy is likely due to the limited number of grains (≤ 100) measured by universal stage by Rampone et al. (2010) with prevented these author a better identification of fabric types (Fig. 40 & 41).

The strength of mineral CPO can be evaluated quantitatively through the J-index obtained from the integral of the orientation distribution function over the volume of an aggregate; it has a value of unity for a random CPO and tends to infinity for a single crystal. Mantle peridotites have variable olivine J-indices between 2 and 20, with an average value around 8 (Ben Ismail and Mainprice, 1998; Tommasi et al., 2000). The olivine J-index (J^{ol}) of the studied peridotites varies from 2.2 to 8.3 and it is uncorrelated with the modal composition and texture.

5.6.2. Pyroxenes

The CPO of orthopyroxene (Fig. 40 & 42) is less developed than that of the olivine, but it is generally correlated with the olivine fabric. Orthopyroxene CPOs are characterized by strong alignment of [001] axes around the lineation, parallel to olivine [100], and they display a weak girdle of [010] normal to the lineation with a nearly random [100] distribution. Clear maxima of [100] parallel to the Z direction are rare (e.g. TAL-001, TAL-084) (Fig. 40). These observations indicate that the dominant slip direction in orthopyroxene is [001], but the poor orientation of [100] and [010] axes hinders the determination of the slip plane. Rotation axes accommodating low-angle ($<15^\circ$) misorientations in orthopyroxene crystals are often distributed parallel to [010] (Fig. 44), which is consistent with subgrain boundaries formed by the common (100)[001] slip system of orthopyroxene under upper mantle conditions (Coe and Kirby, 1975; McLaren and Etheridge, 1976; Mercier, 1985; Dornbush et al., 1994). However, in cluster porphyroclastic and the equigranular peridotites rotation axes are exclusively concentrated around [001]. Moreover, this direction also occurs in some porphyroclastic peridotites (e.g. LPE-061, TAL-148) in addition to the common rotation axes around [010]. These unusual rotation axes either indicate the activation the unusual (100)[010] slip system (Naze et al., 1987; Dornbush et al., 1994), or result from accumulation of dislocations along deformation twins on the (100) plane, which are commonly split from (100)[001] slip by partial dislocations (Coe and Kirby, 1975; McLaren and Etheridge, 1976), producing further slight rotation around [001] (Frets et al., 2012). Given that orthopyroxene [001] is always correlated with olivine [100], and orthopyroxene [010] has never been observed as parallel to the lineation in the eastern Betics mantle xenoliths, the latter explanation is more plausible. Orthopyroxene CPO with [001] axis subparallel to lineation, and both [100] and [010] axes subnormal to the foliation was reported by Jung et al. (2010) (Type-ABC) who explained their formation by a combined slip system of (100)[001] and (010)[001].

The observed orthopyroxene patterns differ from those of the Ronda peridotite that show characteristic deformation by the activation of the (100)[001] slip system (Vauchez and Garrido, 2001; Soustelle et al., 2009). The orthopyroxene J-indices (J^{opx} , the mean orientation for each grain) are slightly lower than those of the olivine and vary between 1.7 and 6.3. The only exception is a porphyroclastic spinel lherzolite (LPE-048) that shows anomalously high (10.6) J^{opx} .

Most of the clinopyroxenes exhibit moderately developed CPOs, which are correlated with olivine and orthopyroxene crystal axes orientation distributions. Clinopyroxene [001] axes are subparallel to olivine [100] and orthopyroxene [001], and are aligned parallel to the peridotite lineation (Fig. 40 & 41). This observation indicates that [001] is the dominant slip direction in clinopyroxenes. However, similarly to orthopyroxene, slip planes are less clear, because (010) poles either show single maxima parallel to Z direction, or aligned along a girdle perpendicular to the lineation. In both cases clinopyroxene (010) and orthopyroxene [010] are strongly correlated. These CPOs are consistent with deformation of clinopyroxene by dislocation glide on {110}[001] and (100)[001] (Bascou et al., 2002). The J^{cpx} ranges between 4.1-23.6, but it is strongly influenced by the number of analyzed grains due to variation of clinopyroxene modal content among lithologies (Table 6).

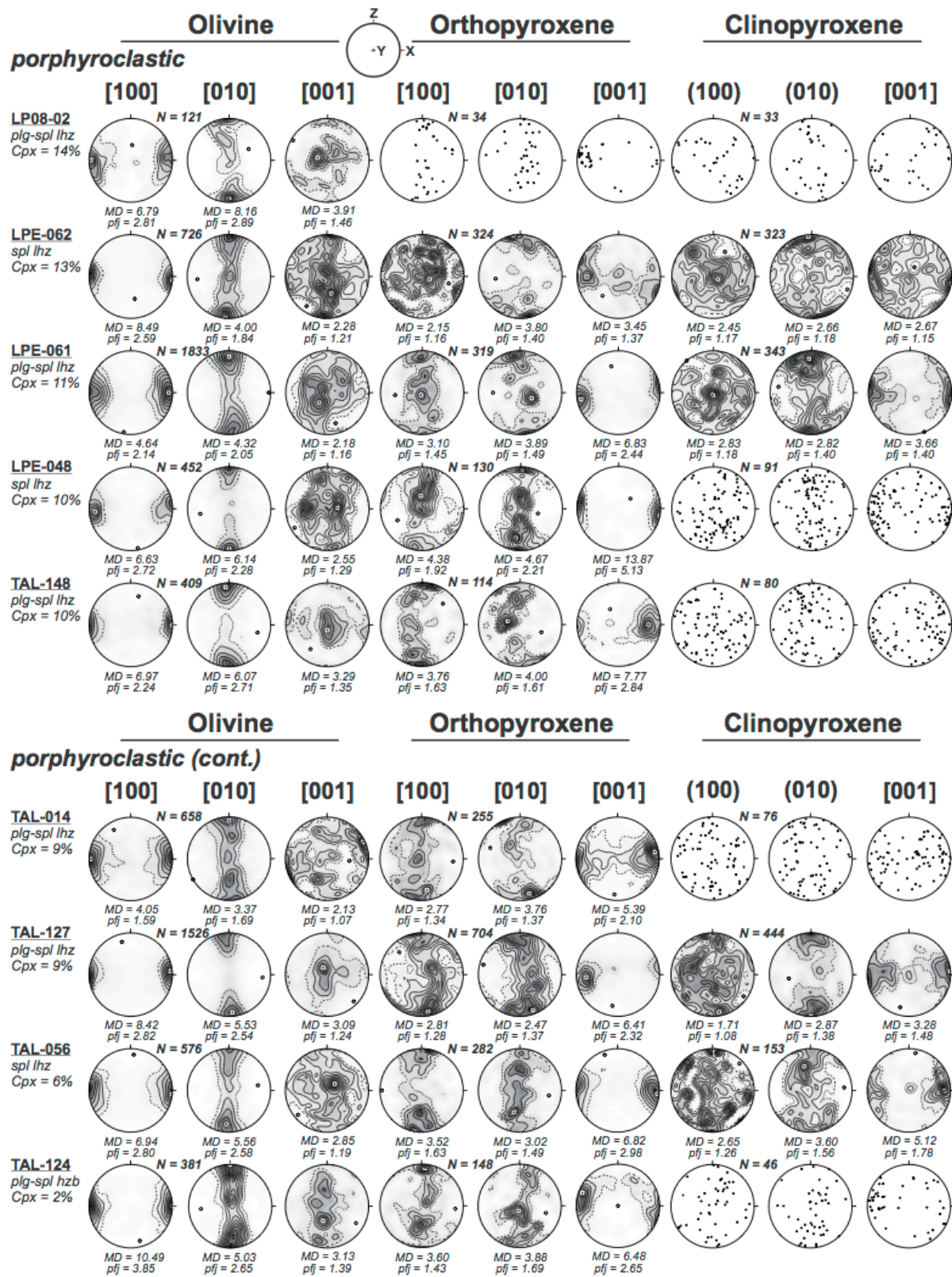


Fig. 40 Lower hemisphere, equal area stereographic plots of the Crystal Preferred Orientation (CPO) of olivine, orthopyroxene and clinopyroxene in eastern Betics lherzolite and harzburgite xenoliths. CPOs are plotted in the structural reference frame (XYZ) derived from the literature for natural peridotites: where [100] is the best fitting to the lineation (X direction) and [010] the best fitting normal to the foliation plane (Z direction). Mantle xenoliths are grouped by textures and decreasing clinopyroxene (Cpx) content. (N – number of measured grains; MD – maximum density and pfj – J index of the pole figure.)

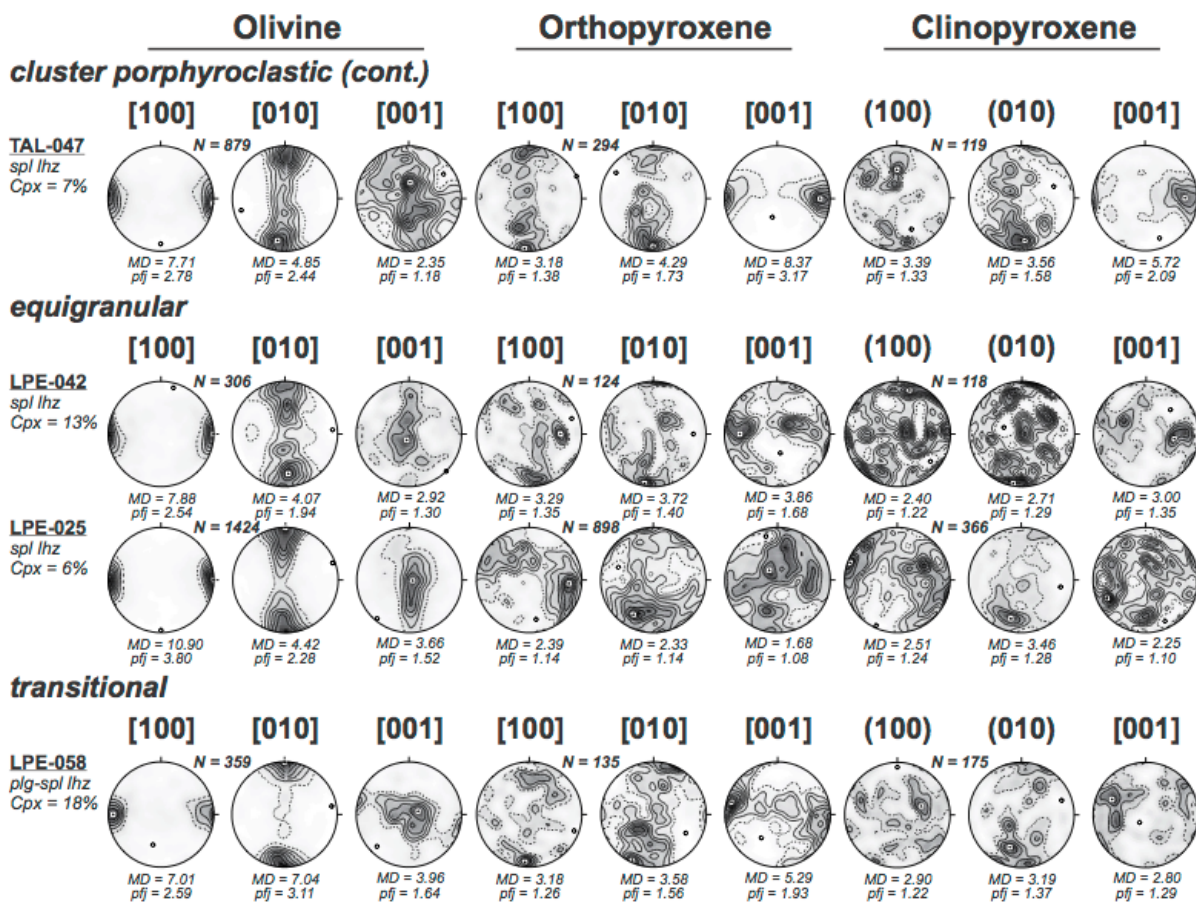
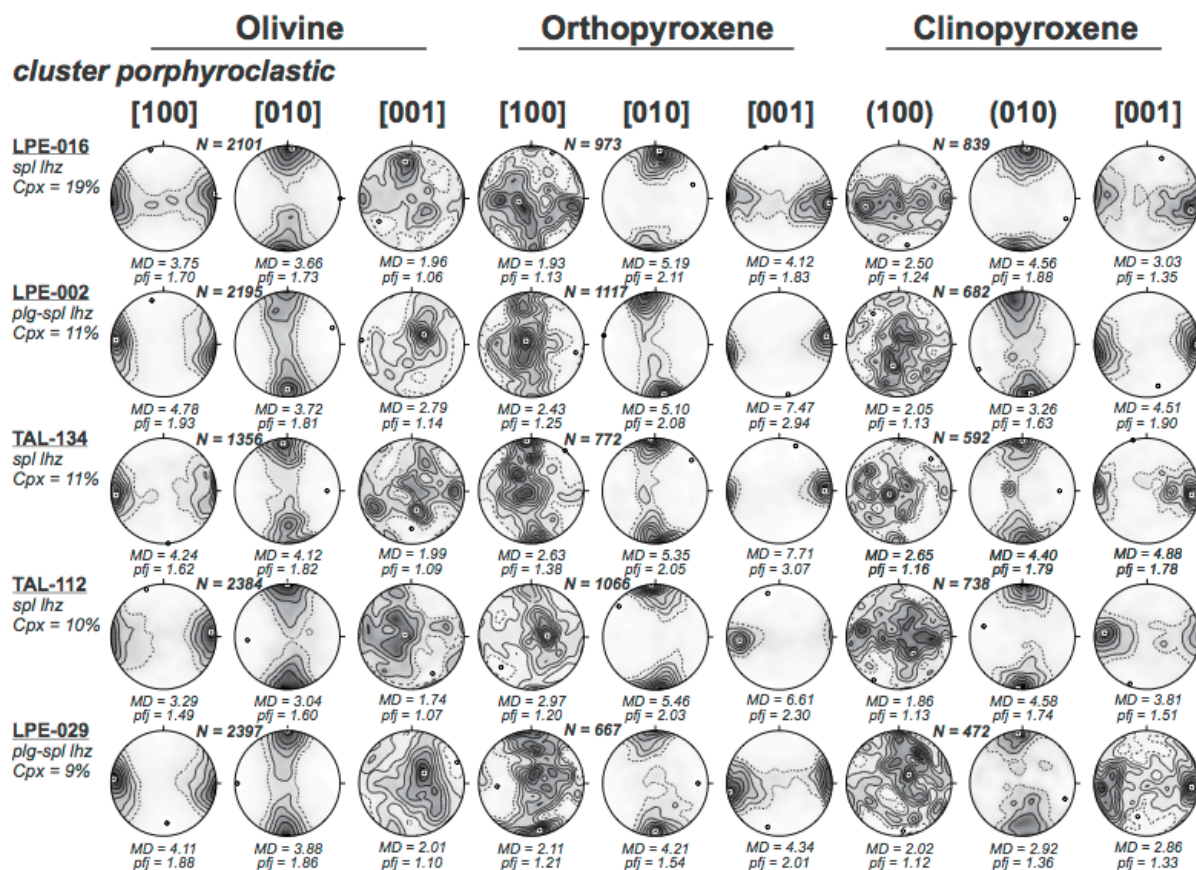


Fig. 40 cont.

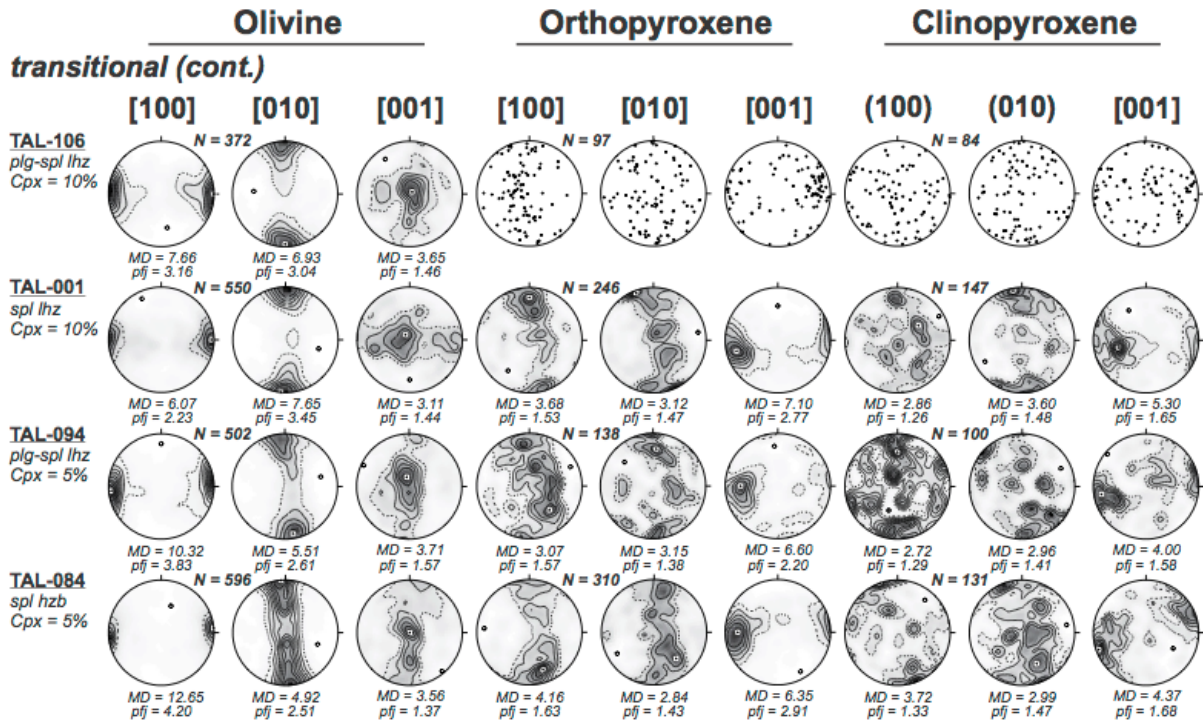


Fig. 40 cont.

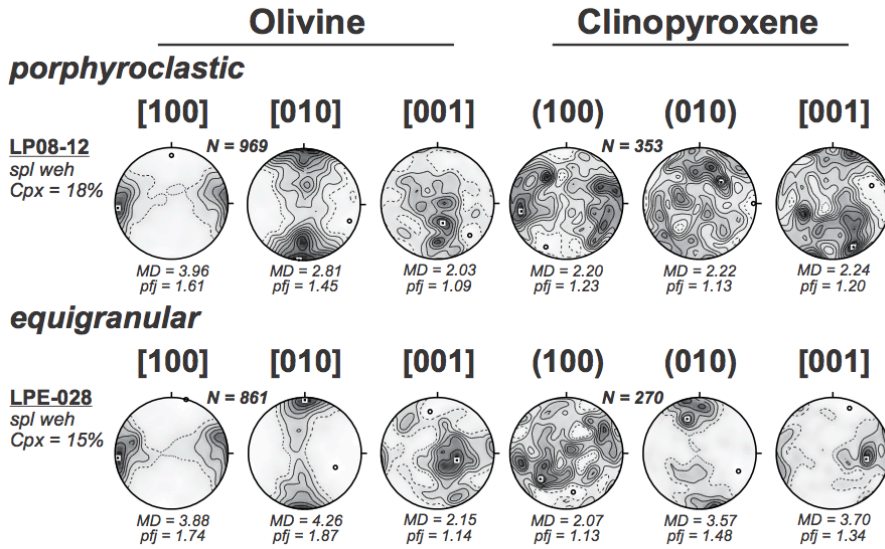


Fig. 41 Lower hemisphere, equal area stereographic plots of the Crystal Preferred Orientation of olivine and clinopyroxene eastern Betics wehrlite xenoliths (structural reference frame and abbreviations as in Fig. 40)

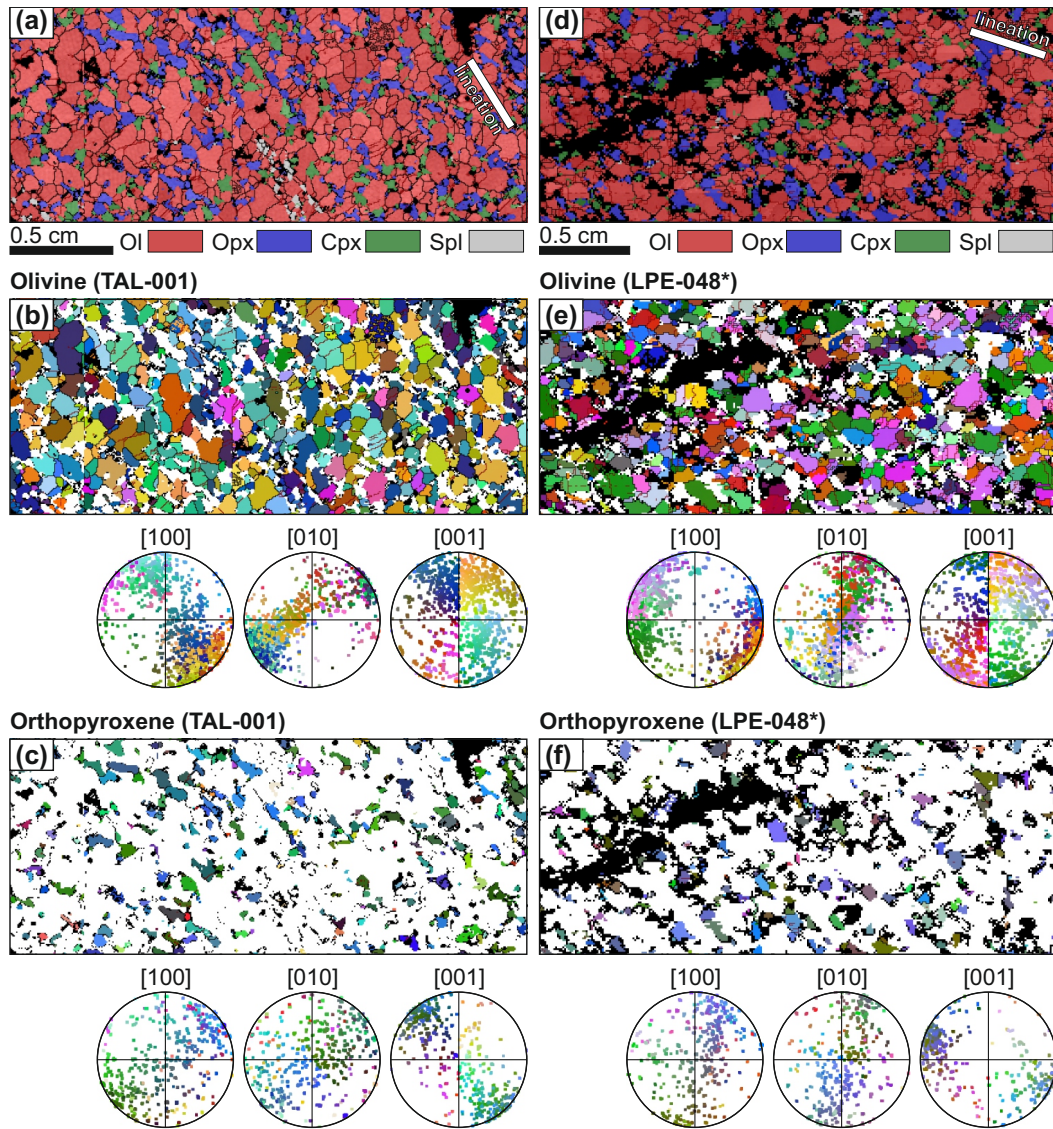


Fig. 42 EBSD phase map (a, d) illustrating the correspondence of xenolith tectonic foliation – defined by flattening of olivine – and stretching lineation – defined by stretched spinel aggregates – and crystallographic orientation map (b-e, c-f) with equal-area lower hemisphere stereographic projections of olivine (Ol) and orthopyroxene (Opx) CPOs in the thin-section reference frame. Data are from samples TAL-001 and LPE-048*. (* - oriented thin-section, Cpx - clinopyroxene, Spl - spinel)

5.7. Seismic Properties

The theoretical seismic properties of mantle xenoliths can be computed from averaging individual grain elastic constant tensor as a function of the CPO – retrieved by EBSD measurements – and the sample modal composition (e.g. Mainprice and Humbert, 1994). Fig. 45 shows the three-dimensional distribution of the P-waves velocity (V_p , km·s⁻¹), the intensity of the S-wave polarization anisotropy ($AV_s = 200 \cdot (VS_1 - VS_2) / (VS_1 + VS_2)$, in %; where VS_1 and VS_2 are, respectively, the velocities of the fast, S_1 , and slow, S_2 , polarized S-

wave), and the polarization direction of S1 for selected samples of different textural groups of eastern Betics xenoliths. For these calculations we used the Voigt-Reuss-Hill averaging method and single-crystal elastic constants tensors of olivine and pyroxenes at ambient conditions (Duffy and Vaughan, 1988; Abramson et al., 1997) (see caption of Fig. 45 for more details). The seismic properties are presented in the structural reference frame (Fig. 45) where the X axis is parallel to the lineation, XY is the plane of foliation, and the Z axis is normal to foliation. The seismic properties are similar for all xenoliths regardless the volcanic center, texture and lithology (Fig. 45). There are only slight differences in AVs that are relatively slower for lherzolite and wehrlite; however, they only have a minor effect in determining the bulk seismic properties of xenoliths. For all xenoliths the propagation of P-waves is fastest parallel to the lineation—subparallel to the olivine (100) axis—where velocity ranges between 8.40-9.01 km·s⁻¹, and is slowest in the plane normal to the foliation, where velocity ranges between 7.91-8.08 km·s⁻¹. S-wave splitting (AVs) is minimal for waves propagating at ~45° to the lineation in the plane perpendicular to foliation, and maximal for waves propagating at or near the perpendicular to the lineation in the foliation plane (Fig. 45). S1 polarized waves propagating normal to the foliation also sample a high birefringence direction. For all propagation directions, the fast S1 wave is polarized along the foliation plane parallel to the lineation (Fig. 45), which corresponds to alignment of olivine (100)-axis. The direction of propagation of S1 (Vs) is polarized along the foliation plane and parallel to the olivine a-axis; and the maximum AVs (3.41-7.52%) is approximately normal to the lineation (Y-axis) (Fig. 45). This seismic anisotropy patterns are characteristic of mantle peridotites where olivine deformation is accommodated by a dislocation creep mechanisms with a dominant activation of the olivine {0kl}[100] slip system (Tommasi et al., 2004; Vauchez et al., 2005).

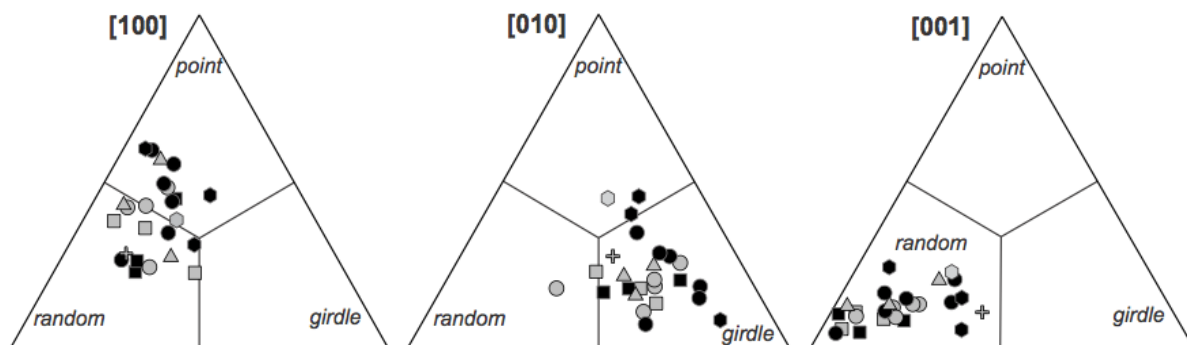


Fig. 43 Olivine CPO symmetry expressed as the proportion of point (P), girdle (G) and random (R) components calculated from the eigenvalues ($\lambda_1, \lambda_2, \lambda_3$) of the normalized orientation matrix (c.f. Vollmer, 1990) for the three principal crystallographic axes: [100], [010] and [001]. ($P = \lambda_1 - \lambda_2$; $G = 2(\lambda_2 - \lambda_3)$; $R = 3\lambda_3$) (Legend is same as in Fig. 38.)

Fig. 45 also shows the seismic properties of the composite xenolith taking only into account the orientation of orthopyroxene in veins formed by Si-rich hydrous metasomatism. The seismic properties are very similar to those of non-metasomatized peridotites, indicating that orthopyroxene addition by reactive percolation of hydrous melts or fluids has no impact on the fast S-waves polarization directions of S-waves splitting (Soustelle et al., 2010).

Table 6 Sample description and the calculated mineral J-indexes with the significant values of the seismic properties

| Sample | Texture | Lithology | Mineral Assemblage (mode %) | J-index (Ol) | J-index (Opx) | J-index (Cpx) | Vp | | | Avs anisotropy | |
|----------|----------------|-------------|--|--------------|---------------|---------------|-------------|-------------|-----------|----------------|----------|
| | | | | | | | min. (km/s) | max. (km/s) | anis. (%) | min. (%) | max. (%) |
| LP08-02 | normal porph. | Lherzolite | Ol (64), Opx (21), Cpx (14) [Sp, Plg] | 7.8 | 16.4 | - | 8.0 | 8.8 | 9.0 | 0.3 | 6.3 |
| LP08-12 | normal porph. | Wehrlite | Ol (82), Cpx (18) [Spl] | 2.2 | - | 4.6 | 8.0 | 8.6 | 7.0 | 0.2 | 4.3 |
| LPE-002 | cluster porph. | Lherzolite | Ol (68), Opx (21), Cpx (11) [Sp, Plg] | 3.9 | 5.8 | 4.7 | 8.0 | 8.7 | 8.0 | 0.1 | 5.4 |
| LPE-008 | composite | Lhz/Hzb | Ol (55), Opx (43), Cpx (2) [Sp, Plg, Amp] | 4.2 | 2.6 | - | 8.1 | 8.4 | 4.2 | 0.1 | 3.4 |
| LPE-016 | cluster porph. | Lherzolite | Ol (71), Opx (17), Cpx (19) [Spl] | 3.0 | 4.0 | 4.2 | 8.0 | 8.6 | 8.0 | 0.1 | 5.0 |
| LPE-025 | equigranular | Lherzolite | Ol (77), Opx (17), Cpx (6) [Spl] | 8.0 | 1.7 | 4.7 | 8.0 | 8.9 | 11.0 | 0.2 | 6.9 |
| LPE-028 | equigranular | Wehrlite | Ol (85), Cpx (15) [Spl] | 3.4 | - | 5.2 | 8.0 | 8.7 | 8.6 | 0.1 | 5.8 |
| LPE-029 | cluster porph. | Lherzolite | Ol (71), Opx (20), Cpx (9) [Sp, Plg] | 3.7 | 3.6 | 4.1 | 8.0 | 8.7 | 8.1 | 0.1 | 5.6 |
| LPE-042* | equigranular | Lherzolite | Ol (68), Opx (20), Cpx (13) [Spl] | 5.2 | 4.5 | 9.6 | 8.0 | 8.7 | 7.9 | 0.1 | 4.9 |
| LPE-048* | normal porph. | Lherzolite | Ol (73), Opx (16), Cpx (10) [Spl] | 5.4 | 10.6 | 12.4 | 8.0 | 8.8 | 9.8 | 0.1 | 7.2 |
| LPE-058 | transitional | Lherzolite | Ol (63), Opx (19), Cpx (18) [Sp, Plg] | 7.7 | 4.5 | 7.4 | 7.9 | 8.7 | 8.8 | 0.3 | 5.8 |
| LPE-061 | normal porph. | Lherzolite | Ol (70), Opx (20), Cpx (11) [Sp, Plg] | 4.5 | 4.9 | 5.2 | 8.0 | 8.7 | 8.5 | 0.1 | 5.8 |
| LPE-062* | normal porph. | Lherzolite | Ol (65), Opx (22), Cpx (13) [Spl] | 4.8 | 2.7 | 4.3 | 8.1 | 8.7 | 7.3 | 0.2 | 4.3 |
| TAL-001 | transitional | Lherzolite | Ol (74), Opx (17), Cpx (10) [Spl] | 7.5 | 5.5 | 8.5 | 7.9 | 8.7 | 9.4 | 0.3 | 6.3 |
| TAL-014 | normal porph. | Lherzolite | Ol (68), Opx (23), Cpx (9) [Sp, Plg, Ap] | 2.7 | 4.0 | 18.1 | 8.1 | 8.6 | 5.8 | 0.1 | 3.9 |
| TAL-047* | cluster porph. | Lherzolite | Ol (74), Opx (19), Cpx (7) [Spl] | 6.0 | 6.2 | 11.8 | 8.0 | 8.8 | 9.9 | 0.3 | 6.5 |
| TAL-056* | normal porph. | Lherzolite | Ol (76), Opx (17), Cpx (6) [Spl] | 5.1 | 5.0 | 8.7 | 8.0 | 8.8 | 10.1 | 0.3 | 6.8 |
| TAL-084 | transitional | Harzburgite | Ol (78), Opx (17), Cpx (5) [Spl] | 5.6 | 4.9 | 9.8 | 8.0 | 8.9 | 10.9 | 0.2 | 7.0 |
| TAL-094 | transitional | Lherzolite | Ol (78), Opx (17), Cpx (5) [Sp, Plg] | 7.5 | 4.4 | 11.9 | 8.0 | 8.9 | 11.0 | 0.1 | 6.8 |
| TAL-106 | transitional | Lherzolite | Ol (74), Opx (16), Cpx (10) [Sp, Plg] | 7.4 | 6.2 | 12.1 | 7.9 | 8.8 | 10.8 | 0.4 | 7.1 |
| TAL-112 | cluster porph. | Lherzolite | Ol (76), Opx (15), Cpx (10) [Spl] | 2.7 | 4.8 | 4.4 | 8.0 | 8.6 | 7.0 | 0.1 | 4.6 |
| TAL-124 | normal porph. | Harzburgite | Ol (87), Opx (10), Cpx (2) [Sp, Plg] | 8.3 | 6.0 | 23.6 | 8.0 | 9.0 | 12.2 | 0.4 | 7.5 |
| TAL-127 | normal porph. | Lherzolite | Ol (70), Opx (21), Cpx (9) [Sp, Plg] | 5.0 | 3.0 | 4.5 | 8.0 | 8.8 | 9.5 | 0.2 | 6.3 |
| TAL-134 | cluster porph. | Lherzolite | Ol (70), Opx (19), Cpx (11) [Spl] | 2.6 | 5.0 | 5.0 | 8.0 | 8.6 | 7.4 | 0.2 | 4.7 |
| TAL-148 | normal porph. | Lherzolite | Ol (75), Opx (15), Cpx (10) [Sp, Plg, Amp] | 6.3 | 6.3 | 12.8 | 8.0 | 8.7 | 9.0 | 0.3 | 6.1 |

Ol – olivine, Opx – orthopyroxene, Cpx – clinopyroxene, Sp – spinel, Plg – plagioclase, Amp – amphibol, Ap – apatite porph. – porphyroclastic; * Paten lineation/foliation

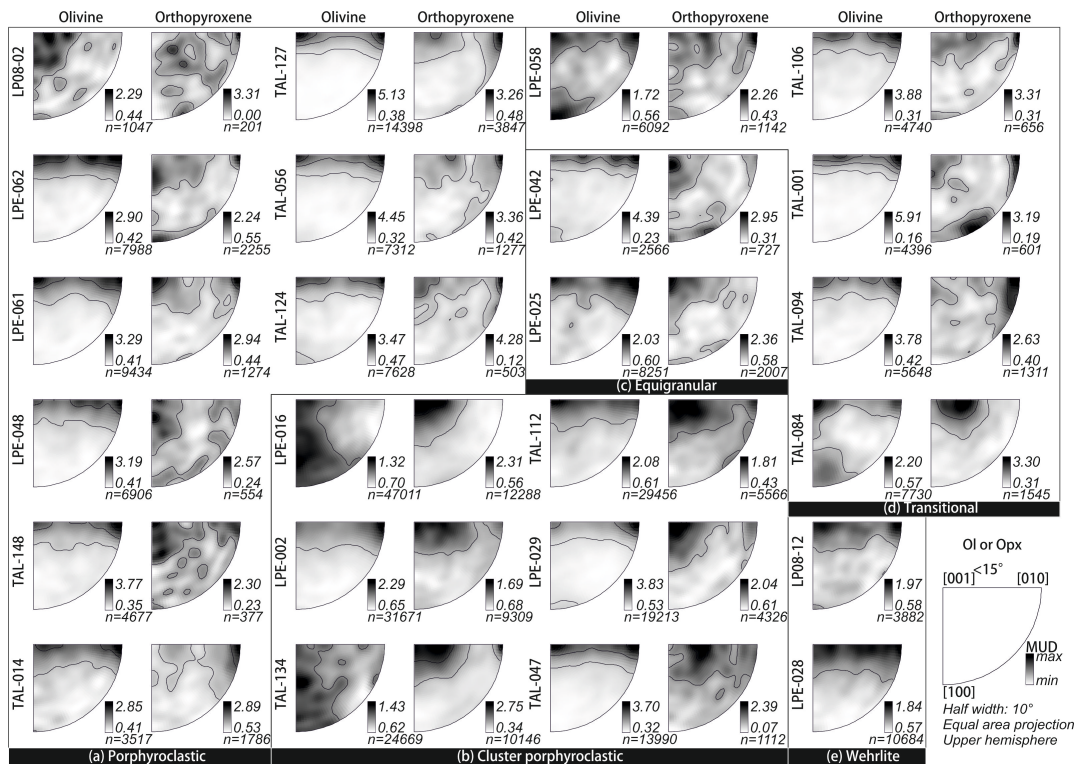


Fig. 44 Rotation axes accommodating misorientation $\leq 15^\circ$ within olivine (Ol) and orthopyroxene (Opx) crystals for all the eastern Betic peridotites sorted by textural groups (a-e).

5.8. Discussion

5.8.1. Provenance and Age of Deformation Recovered of the SCLM in the Eastern Betic Cordillera

Because the recent eruption age—2-3 Ma—of alkali basalts, the studied mantle xenoliths provide a snapshot of the deformation and composition of the subcontinental lithospheric mantle beneath the eastern inner Betics. This area had a complex pre-Cenozoic and Tertiary tectonic history astride the edges of the Iberian plate and the Alboran domain. The absence of suitable geochronological methods for precise dating ductile deformation in shallow peridotite minerals, along with the lack of macro-structural observations in small-sized xenoliths, makes it difficult to constrain the age of deformational events recorded in eastern Betic mantle xenoliths. As a consequence, differing hypotheses have been put forward about the geodynamic significance and age of the metamorphic, magmatic and deformation record of eastern Betics mantle xenoliths. Bianchini and co-authors (Beccaluva et al., 2004; Bianchini et al., 2011) have proposed that xenoliths mostly record pre-Cenozoic tectono-magmatic processes related to opening of the central Atlantic, and the westward propagation of Neotethys rifting and oceanization at the margins of the Iberian plate. As testified by plagioclase \pm quartz and orthopyroxene (\pm amphibole \pm phlogopite) veins in composite xenoliths (Arai et al., 2003; Shimizu et al., 2004; Rampone et al., 2010; Bianchini et al., 2011), Bianchini et al. (2011) argued that the only Alpine event recorded in this xenolith suite was silica-rich fluid/melts metasomatism related to Tertiary subduction and collisional processes that formed the Betic-Rif Cordillera. These authors further claim that this geodynamic interpretation is consistent with earlier proposal of Mesozoic formation of the Ronda orogenic peridotite (Van der Wal and Vissers, 1993, 1996) that, along with eastern Betics xenoliths, consider to be portions of the paleo-margin of southern Iberia. On the other hand, Rampone et al. (2010) suggested that the tectono-magmatic record of eastern Betics xenoliths is similar to that of the Ronda peridotite (Van der Wal and Vissers, 1993) and ascribed both to the Tertiary Alpine evolution of the Alboran lithospheric mantle. This interpretation implies a common mantle provenance for eastern Betics xenoliths and Western Betics Alpujarrides orogenic peridotites. Because the intracrustal emplacement of the Ronda occurred in the early Miocene (Esteban et al., 2011), this hypothesis also entails that eastern Betics xenoliths mostly record pre-Miocene Alpine tectono-magmatic events, which were only overprinted in the Neogene by slab-derived melt metasomatism (Rampone et al., 2010; Bianchini et al., 2011).

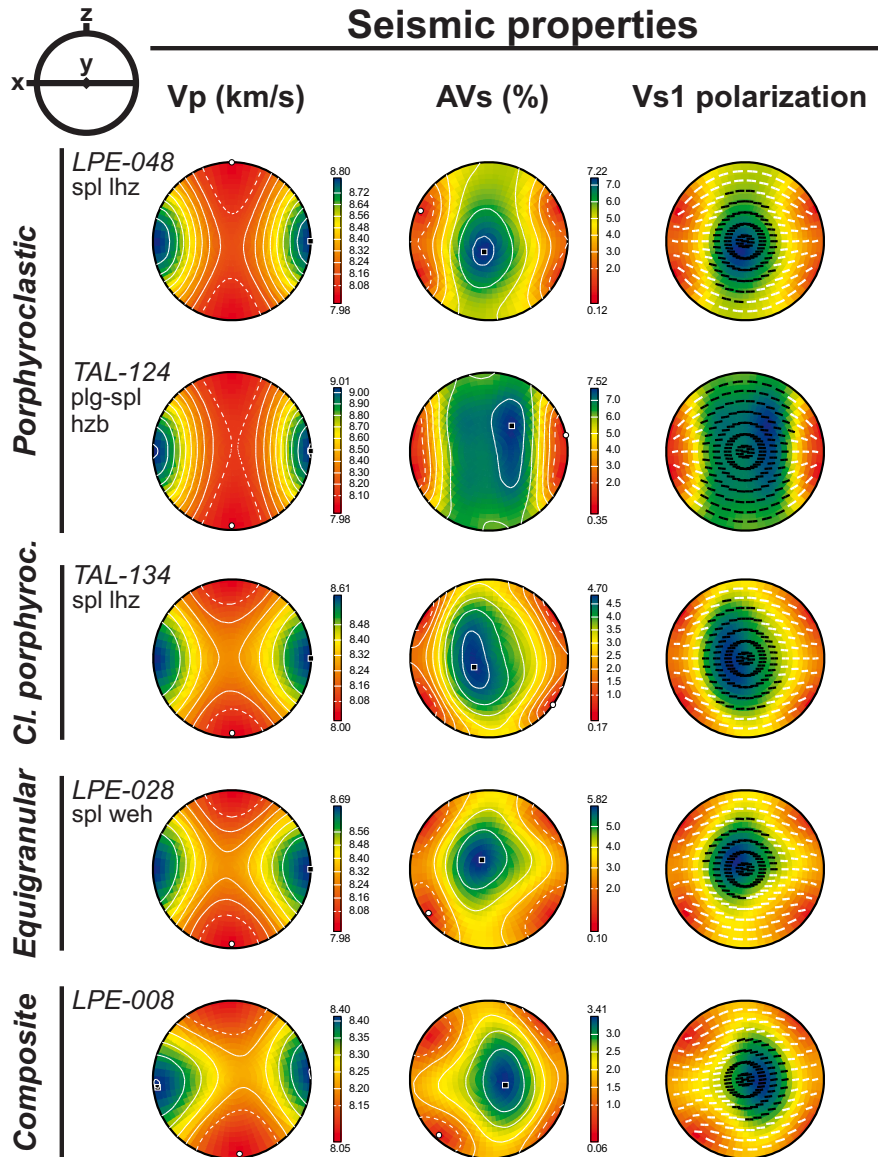


Fig. 45 Calculated seismic properties in selected eastern Betic xenoliths plotted on a lower hemisphere equal area net. V_p is the 3D distribution of P -wave velocity (**1st column**), AV_s is 3D distribution of the polarization anisotropy of S -waves owing to S -wave splitting (**2nd column**). V_{s1} polarization is a polarization plane of the fast split S -wave as a function of orientation of the incoming wave relative to the structural framework of the sample; V_{s1} polarization is presented as superimposed on AV_s (**3rd column**).

We have shown that Re-depletion model ages (TRD) of sulfides in eastern Betics xenoliths are as old as 2.6 Ga (Neoproterozoic) (González-Jiménez et al., 2013a). Inherited zircons in late Miocene anatectic dacite of the nearby El Hozayo volcano also yields U-Pb maximum ages of 2.8-2.5 Ga (Zack and Williams, 2001), indicating that subcrustal peridotites and lower crust in the eastern inner Betics form part of the same lithospheric domain recording a protracted tectono-magmatic history back to the Neoproterozoic. Neoproterozoic events are also recorded in

maximum TRD ages of the Betic-Rif orogenic peridotites (see compilation in Pearson and Nowell, 2004; Marchesi et al., 2010; González-Jiménez et al., 2013a, 2013b), and in U-Pb ages (2.7 Ga) of inherited zircons of the Central Betic Alpujárride gneisses overlying Western Betic orogenic peridotites (Zeck and Whitehouse, 1999; Zeck and Williams, 2001). Neoproterozoic TRD ages are not preserved in Iberian mantle samples (González-Jiménez et al., 2013a), which typically show a Paleoproterozoic maximum TRD age of ca. 1.8 Ga. Similar Paleoproterozoic maximum ages are widespread in European and African subcontinental mantle outboard from the Betics-Maghrebides-Liguria's chains, and are common ages zircons in the Central Iberian zone (González-Jiménez et al., 2013a and references therein). Re-depletion model ages of peridotite hence indicates that eastern Betics mantle xenoliths and Betic-Rif orogenic peridotites have a common provenance other than Iberian, and represent separated Archean subcontinental lithospheric mantle domain that played an important role in the development of the present architecture of the circum-Mediterranean lithosphere (González-Jiménez et al., 2013a; *qv.* Sec. 7). This result is line with geodynamic models proposing before the Neogene a more easterly – relative to the present Betic-Rif arc – paleogeographical position in the Mediterranean of the Betic-Rifean Alpujárrides-Septides metamorphic units hosting orogenic peridotites (Booth-Rea et al., 2007 and references therein), and the surrounding allochthonous sedimentary rocks from the Flysch imbricate thrust imbricate (Luján et al., 2006; Guerrero et al., 2012 and references therein). It must be noted, however, that eastern Betics Plio-Pleistocene alkali basalts erupted on Nevado-Filabride metamorphic units (Álvarez et al., 1989; Díaz de Federico et al., 1990) that constituted the exhumed paleo-Iberian margin as confirmed by inherited zircons recording maximum Paleoproterozoic U-Pb ages (Gómez-Pugnaire et al., 2012). These observations indicate a complex structural setting in the eastern Betics with upper crustal units having a different provenance than the lower crust and lithospheric mantle.

The non-Iberian provenance of Alpujárride orogenic peridotites and eastern Betic mantle xenoliths makes it difficult to correlate their tectono-magmatic record with Neotethys rifting and oceanization at the margins of the Iberian plate (Beccaluva et al., 2004; Bianchini et al., 2011). These correlations are mostly based on geochemical and geochronological data of (meta)igneous rocks of the Betic Nevado-Filábride metamorphic complex and Subbetic units (Bianchini et al., 2011) that constituted, respectively, the Palaeozoic continental crust of Iberian passive margin subducted below the Alboran wedge (López Sánchez-Vizcaíno et al., 2001; Booth-Rea et al., 2005; Martínez-Martínez et al., 2006; Platt et al., 2006; Gómez-Pugnaire et al., 2012; Behr and Platt, 2012), and its Jurassic to Tertiary sedimentary cover detached by

thin-skin tectonics during middle-Miocene westward collision of the Iberian margin with the allochthonous Alboran lithospheric wedge (Booth-Rea et al., 2007).

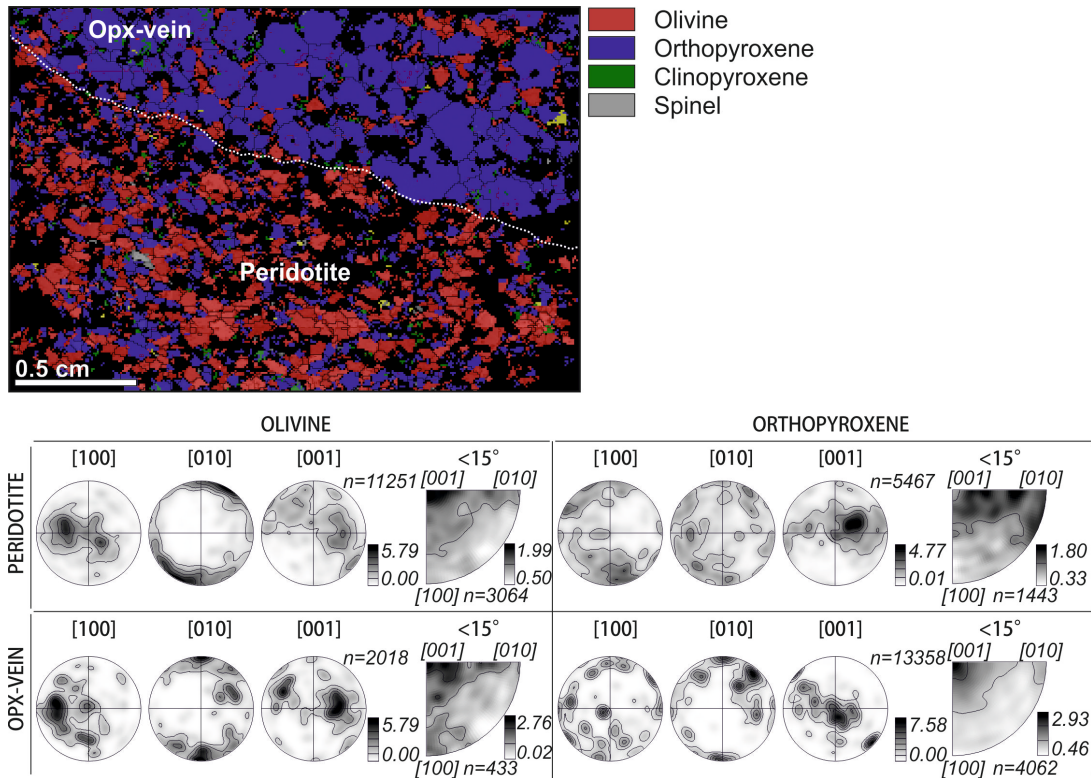


Fig. 46 EBSD phase map of the composite xenolith (LPE-008) with the olivine and orthopyroxene (Opx) CPOs and rotation axes. (The structural frame and abbreviations are the same as in Fig. 42.)

Despite their common provenance, several features indicate that eastern Betics mantle xenoliths sampled a more fertile mantle lithosphere with a distinct and younger deformation record than that sampled by the western Betics Ronda peridotite. In situ U-Pb ages of zircons in intrusive felsic veins in eastern Betics xenoliths yield crystallization ages of 4.4 and 2.2 Ma (Bianchini et al., 2011). Felsic and orthopyroxenite veins were formed by silica-rich metasomatism (Arai et al., 2003; Shimizu et al., 2004; Rampone et al., 2010; Bianchini et al., 2011), likely derived from subduction and/or edge delamination of the paleo-Iberian continental margin (Duggen et al., 2005). EBSD mapping of the composite xenolith LPE-008—made up of metasomatic orthopyroxenite veins enclosed in porphyroclastic lherzolite (Fig. 39e)—shows that in wall-rock porphyroclastic peridotite the [001]-axes of orthopyroxene are subparallel to the olivine [100]-axes and subparallel to lineation, while the [100]- and [010]-axes subnormal to the foliation (Fig. 46). This feature is characteristic of synkinematic deformation of orthopyroxene during dislocation high-T dislocation creep flow of mantle peridotite (Vauchez et al., 2012 and references therein). Interestingly, The [001]-axes of orthopyroxene in metasomatic veins are also parallel to the olivine [100]- and

orthopyroxene [001]-axes of wall-rock peridotite (Fig. 46), demonstrating that formation of metasomatic orthopyroxene at expenses of olivine during reactive percolation of Si-rich melt/fluids was coeval with high-temperature dislocation creep flow of host peridotite. Soustelle et al. (2010) have reported similar CPO features in sub-arc xenoliths where orthopyroxene formed by synkinematic percolation reaction of slab-derived silica-rich melts in mantle wedge peridotites. The similarity of CPO patterns in eastern Betic peridotite xenoliths regardless their texture, composition and metamorphic facies implies that eastern Betic xenoliths were coevally deformed under the same tectonic regime. In the eastern Betic xenoliths synkinematic silica-rich metasomatism leading to formation of orthopyroxene and orthopyroxenite veins (Rampone et al., 2010) hence indicates that deformation of eastern Betics xenoliths record mantle flow in the late Miocene. This contrast with the minimum Late Oligocene-Early Miocene Lu-Hf cooling ages (*ca.* 24 Ma) of ductile deformation recorded in western Betic-Rif orogenic peridotites (Garrido et al., 2011). These age differences show that while Ronda peridotite record ductile deformation shortly before the westward migration of the Alboran wedge before its collision with the paleo-Iberian and African Margin (Precigout et al., 2007; Garrido et al., 2011; Hidas et al., 2013), whereas the eastern Betic xenoliths record ductile mantle deformation coeval with late Neogene slab subduction and/or delamination of the subducted paleo-Iberian margin.

The olivine and orthopyroxene CPOs of eastern Betic xenolith also differ from those of Ronda and indicate ductile deformation under a different tectonic regime. Ronda peridotite record ductile deformation dominated by dislocation creep with dominant activation of the high-T, low-stress (010)[100] and (100)[001] slip systems of olivine and orthopyroxene, respectively (Vauchez and Garrido, 2001; Soustelle et al., 2009). Together with dispersion of olivine [100]- and orthopyroxene [001]-axes within the foliation and small obliquity between olivine [100] and orthopyroxene [001] maxima and the lineation, these CPOs are consistent with transpressional deformation (Tommasi et al., 1999, 2000; Soustelle et al., 2009). The CPOs of eastern Betic xenoliths show an distinct olivine axial-[100] pattern resulting from slip on two or more of the {0kl}[100] systems that is characteristics of deformation under simple shear—or mixture of simple and pure shear—with a variable imprint of a transtensional tectonic regime (Tommasi et al., 1999, 2000).

In addition of registering a younger, transtensional ductile deformation event, eastern Betic peridotite xenoliths are predominantly more fertile than common Ronda peridotite (Fig. 38). Most eastern Betics xenoliths are lherzolite with subordinate wehrlite and rare harzburgite (Fig. 38). In Ronda, lherzolite is rare in porphyroclastic peridotite of the tectonite

domain (Fig. 38); it mostly occur in Ronda as secondary lherzolite with transitional textures at the recrystallization front (Lenoir et al., 2001; Soustelle et al., 2009), and in the plagioclase tectonite domain as porphyroclastic plagioclase lherzolite formed by synkinematic, subsolidus breakdown of granular spinel lherzolite (Obata, 1980; Van der Wal and Vissers, 1996; Bodinier et al., 2008; Hidas et al., 2013) (Fig. 38). In eastern Betics xenoliths lherzolite is predominant in all textural types what points toward they sampling a more fertile Alboran lithospheric domain and/or that refertilization reactions forming secondary lherzolite were pervasive in the Neogene. The CPO of clinopyroxene in Ronda lherzolite is poorly developed in line with their secondary, late syn- to post-kinematic magmatic origin (Lenoir et al., 2001; Soustelle et al., 2009); however, eastern Betics porphyroclastic and transitional lherzolites display well-developed clinopyroxene {110}[001] CPO patterns parallel to peridotite lineation and olivine [100]-axis showing that clinopyroxene addition was magmatic was pre- to synkinematic. In Ronda lherzolite, plagioclase is produced by subsolidus breakdown (Obata, 1980; Van der Wal and Vissers, 1996; Bodinier et al., 2008) and associated to buckling and shearing of a highly attenuated lithospheric mantle section in the early Miocene (Hidas et al., 2013); plagioclase in eastern Betics plagioclase-spinel lherzolite occurs in all textural types including magmatic origin by melt metasomatism in the late Neogene (Arai et al., 2003; Shimizu et al., 2004, 2008; Rampone et al., 2010; Bianchini et al., 2011). This indicates that eastern Betic xenoliths record a lower pressure magmatic refertilization event in thinner, plagioclase facies lithosphere that is rare in Ronda peridotite where refertilization mostly occurred in thicker, spinel facies lithospheric mantle (Garrido and Bodinier, 1999; Lenoir et al., 2001; Soustelle et al., 2009).

5.8.2. Depth of Provenance and Ductil P-T Evolution of Eastern Betic Mantle Xenoliths

Mantle xenoliths in alkali basalts provide additional constraints about the thermal structure and deep tectonic processes operating in the deep uppermost mantle in the late Neogene. Eastern Betics xenoliths were equilibrated at the spinel to plagioclase lherzolite facies where the lack of accurate geobarometric formulations (Taylor, 1998; Nimis and Grütter, 2010 and references therein) prevents a detailed analysis of their P-T-t evolution. Textures and mineral compositions of xenoliths provide however clear evidence for decompression from garnet to plagioclase lherzolite facies depths (Kogarko et al., 2001; Shimizu et al., 2008; Rampone et al., 2010; this work). The presence in cluster porphyroclastic of coarse spinel-pyroxene clusters from garnet breakdown (Fig. 39b) (Shimizu et al., 2008; Rampone et al., 2010), together with extremely high $^{176}\text{Hf}/^{177}\text{Hf}$ and high Lu/Hf ratios in clinopyroxene and whole rock (Bianchini et al., 2011) with high Lu/Hf of both clinopyroxene and whole rock, demonstrates

an early equilibration in the garnet lherzolite stability field. Application of geobarometric formulations based on the maximum stability of spinel lherzolite in the Cr-FCMAS system (O'Neill, 1981; Webb and Wood, 1986) using the average spinel composition of cluster porphyroclastic peridotites constrains the minimum pressure of stability in the spinel-garnet transition at pressures of 1.83-1.91 GPa and depths of ca. 55-60 km (Fig. 47).

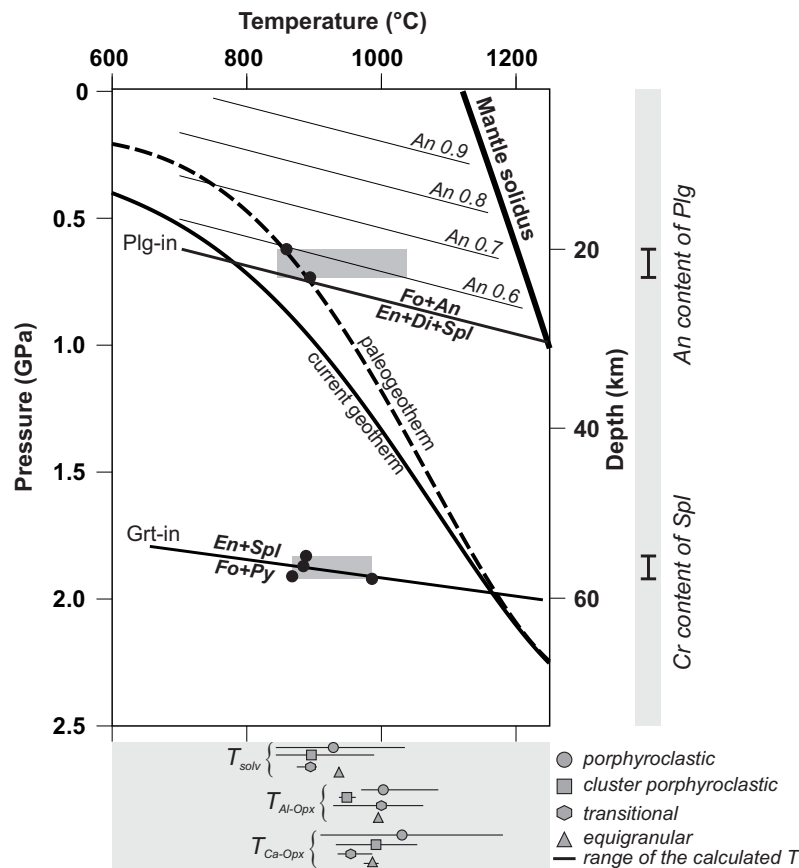


Fig. 47 Pressure-Temperature plot showing the range of temperatures and depth of equilibration of eastern Betics mantle xenoliths (see text for further details). The solid black curve is the current geotherm calculated from geophysical data near the Cartagena area (see text), and the dashed black line is the paleogeotherm at the time of entrainment of mantle xenoliths by Plio-Pleistocene alkali basalts. The spinel-garnet peridotite transition (Grt-in solid line) in the Cr-CMAS system is calculated from the spinel composition (O'Neill, 1981; Webb and Wood, 1986) of cluster porphyroclastic peridotite xenoliths. The spinel-plagioclase lherzolite transition is shown for the CMAS system (Plg-in solid line) and in the Ti,Cr-NCFMAS system for different An-contents of plagioclase (An - labeled thin lines) (Borghini et al., 2010, 2011). Mantle solidus is after Bucher and Frey, 1994. Brackets in the right side of the plots are the estimated initial minimum depth of equilibration in the spinel-garnet facies transition, and the final equilibration depth of xenoliths in the plagioclase-spinel facies as deduced from spinel and plagioclase composition, respectively. Estimated ranges and average equilibrium temperature (T_{solv} , $T_{\text{Al-Opx}}$, $T_{\text{Ca-Opx}}$) of different textural groups of xenoliths calculated using different geothermometric formulations (Taylor, 1998; Brey and Köhler, 1990; Witt-Eickschen and Seck, 1991; Nimis and Gutter, 2010) are shown at the bottom of the figure.

Rampone et al. (2010) proposed that eastern Betic cluster porphyroclastic xenoliths recorded early thinning and decompression of the lithospheric mantle from garnet- to spinel-lherzolite facies conditions (see also Shimizu et al., 2008). This event was followed by ductile shear flow in the spinel facies at increasing stresses at lithospheric conditions (<1100 °C) leading to the formation of porphyroclastic xenoliths. Although they argued that this tectono-magmatic evolution was similar to that documented in the Ronda peridotites of the western Betics, there are crucial differences on the age and style of deformation that preclude comparison of the relative sequence of formation of textural groups between Eastern Betics xenoliths and Ronda peridotites. Similar CPO patterns of cluster porphyroclastic and porphyroclastic xenoliths do not support synkinematic deformation, suggesting syn- to post-kinematic garnet breakdown. This interpretation is further supported by the coarse-granular grain size nature of cluster minerals mimicking garnet shapes within a fine-grained recrystallized matrix of olivine, pyroxene and elongated spinel neoblast (Fig. 39b), and the absence of any textural evidence of plastic deformation in pyroxene-spinel grains in clusters (*e.g.* the lack of undulose extinction recrystallized subgrains in pyroxenes, and non-elongated, coarse subhedral spinel; Fig. 39b), that are more consistent with syn- to post-kinematic breakdown of metastable garnet in the spinel to plagioclase facies. Rampone et al. (2010) argued for a pre-kinematic nature of clusters on the basis of systematic orientation of orthopyroxene exsolution cleavages; however, systematic orientation between orthopyroxene and precursor garnet are most likely due to topotactic growth during synkinematic decompressional breakdown of garnet (see also Padrón-Navarta et al., 2008; Frets et al., 2012).

Strong CPOs patterns of transitional and equigranular xenoliths and their similarity with those of porphyroclastic xenoliths point to a common synkinematic origin during high-temperature dislocation creep flow. Rampone et al. (2010) proposed that transitional and equigranular xenoliths were produced by static annealing of porphyroclastic xenoliths. Although mineral CPOs in ductile deformed peridotites can be preserved during heating and mineral coarsening (Vauchez and Garrido, 2001), this process leads to substantial grain growth, abnormal olivine grain growth, weakening of the pre-existing olivine CPO patterns, and increasing J-index of orthopyroxene CPOs (Vauchez and Garrido, 2001). Eastern Betics equigranular and transitional xenoliths show very well-developed olivine CPOs with similar or stronger olivine J-indexes than those in olivine from porphyroclastic xenoliths (Fig. 40, Table 6). These features, together with similar olivine grain size of the recrystallized matrix, preclude substantial post-kinematic grain growth and are inconsistent with the equigranular and transitional peridotites being produced by progressive obliteration of porphyroclastic

peridotites by static annealing recrystallization (Rampone et al., 2010). Textures and CPOs patterns of eastern Betics are more consistent with variable imprint of dynamic recrystallization and high-temperature dislocation creep during synkinematic decompression from spinel-garnet to plagioclase lherzolite facies.

Subsolidus breakdown of spinel to plagioclase and *in situ* growth of metasomatic plagioclase in eastern Betic xenoliths record decompression to plagioclase lherzolite facies depths coeval with shallow mantle metasomatism (Fig. 47) (Kogarko et al., 2001; Shimizu et al., 2004; Rampone et al., 2010; Bianchini et al., 2011). Using the anorthite content (An) of plagioclase in equilibrium with lherzolite assemblages as a geobarometer (Borghini et al., 2010, 2011), we obtain equilibration pressures of plagioclase-bearing xenoliths up to 0.62–0.73 (± 0.09) GPa at 860–895 °C, implying final equilibration depths between 19 to 22 km (Fig. 47). This range of shallow equilibration pressures is in good agreement with independent geobarometric estimates—and crystallization order—of intrusive pyroxenite and gabbroite veins (Rampone et al., 2010), and Al, Cr, and Ti zoning in pyroxenes indicating continued mantle uplift up to pressures of 0.7–0.9 GPa (Kogarko et al., 2001) (Fig. 47). This final shallow depth and high temperatures indicate equilibration under a high geothermal gradient with heat fluxes in excess of 110 mW·m⁻² (Fig. 47). The presence of plagioclase and spinel in virtually all textural types of xenoliths (Table 5) indicates that at the time of their entrainment by Plio-Pleistocene alkali basalts eastern Betics xenoliths were part of a highly attenuated mantle lithospheric section mostly equilibrated at spinel-plagioclase facies depths (Kogarko et al., 2001).

Eastern Betics mantle xenoliths hence preserve textural and compositional evidence for synkinematic decompression of the lithospheric mantle from minimum depths of 55–60 km (1 GPa) to depths of 19–22 km (0.62–0.73 GPa) under a transtensional deformation regime. The overprinting of synkinematic mineral assemblages from garnet-spinel to plagioclase facies and their CPO patterns demonstrates that 36–40 km uplift was continuously accommodated by thinning of the lithospheric mantle by high-temperature dislocation creep ductile flow. Uplift accommodated by diapiric asthenospheric flow (Kogarko et al., 2001; Shimizu et al., 2008) is inconsistent with the fine-grained size of peridotite xenoliths, their CPO patterns, deformation mechanisms, and the similarities of inherited maximum ages of mantle and lower crust xenoliths implying a common lithospheric provenance since the Neoproterozoic.

On the basis of mineral geothermobarometry and modeling of diffusion profiles in pyroxenes, Kogarko et al. (2001) suggested nearly adiabatic ascent of relatively hot mantle through the depth range of spinel lherzolites stability with a velocity $\leq 10 \text{ mm}\cdot\text{yr}^{-1}$ over 3-4 Myr, followed by a 1 Myr thermal relaxation event from 1200 °C to 850-900 °C. The inferred thinning and time span implies a lithospheric beta stretching factor of ca. 1.5 and high long-term strain rates of *ca.* $9\cdot 7\cdot 10\cdot 13 \text{ s}^{-1}$, which are values characteristics of rapidly extending continental lithosphere with high geothermal gradient of ca. $100 \text{ mW}\cdot\text{m}^{-2}$ (Kusznir and Park, 1987). Assuming that the 2.2-4.4 Ma age of metasomatic silica metasomatism (Bianchini et al., 2011) records the ending stages of ductile deformation in the plagioclase lherzolite facies, initiation of ductile thinning of thick subcontinental mantle must have been occurred between 6.2-9.4 Ma. This time span broadly overlaps with deep processes events in the eastern Betics such initiation of lower crust anatexis (*ca.* 9 Ma) (Cesare et al., 2003), and the change from subduction-related to intraplate-type volcanism (6.3-4.8 Myr) that was largely synchronous with uplift associated with the Messinian salinity crisis and ascribed by some authors to asthenospheric upwelling and lithospheric edge delamination during westward rollback of subducted Tethys oceanic lithosphere (Duggen et al., 2003, 2004 and references therein).

5.8.3. Seismic Anisotropy and Mantle Flow Beneath the Eastern Betics

Further inferences on the geodynamic significance of the decompressional ductile thinning recorded in eastern Betics xenoliths require independent constrains on the geometry of mantle flow beneath this region. Flow directions in the mantle can be mapped by the directional dependence of the properties of seismic waves travelling thorough elastically anisotropic rocks. Teleseismic S-waves traveling through an anisotropic upper mantle split in two perpendicularly polarized waves that travel at different velocities. The two parameters most often measured to quantify anisotropy from three-component seismic records are the azimuth, Φ , of polarization plane of the fast split polarized S-wave (S1) that is related to the fabric and the structural orientation of the anisotropic structure, and the delay time, δt , that is the difference in arrival time between the two split waves and depends on thickness and degree of intrinsic anisotropy of the medium. Seismic anisotropy in the upper mantle results primarily from the elastic anisotropy of olivine that develops CPOs during mantle flow upon stress (*e.g.* Nicolas and Christensen, 1987; Mainprice et al., 2000). Measurement of teleseismic shear-wave splitting therefore provides information on active and/or fossil upper mantle deformation and flow beneath a seismic station, with lateral resolution of tens of kilometers (Silver, 1996; Long and Silver, 2009; Long and Becker, 2010). Several research groups have used S-wave splitting of SKS phases to investigate the

structure and flow direction of the upper mantle beneath the westernmost Mediterranean around the Gibraltar Arc (Buontempo et al., 2008; Diaz et al., 2010; Bokelmann et al., 2011). These studies provide comparable results so that the orientation of the fast split polarized wave S1 is more or less tangential to the Alboran Sea and rotates around the Gibraltar Arc. In the eastern Betics, broad band seismic stations measure orientations of the plane of S1 are generally NE-SW trending and parallel to the crustal large-scale tectonic structures (Buontempo et al., 2008; Diaz et al., 2010; Bokelmann et al., 2011).

The calculated seismic properties of eastern Betics mantle xenoliths (Fig. 45) can be used to assess the contribution of the uppermost lithospheric upper mantle to S-wave SKS phase anisotropy measured at the nearby CART seismic station (Cartagena, Murcia). Seismic anisotropy due to anisotropic fabric in mantle peridotite depends on the type and strength of their mineral CPOs, dominant symmetry of the seismic properties, and orientation of mantle flow direction and plane. As S-waves sample mantle anisotropy at length scales ranging from a few to a thousand of kilometers, we calculated seismic properties for an average CPO of peridotite xenoliths of each volcanic center obtained by summation of the CPO of individual xenoliths (Fig. 48). For these calculations individual CPO are rotated as to have the lineation and the pole of the foliation in the E-W and N-S directions, respectively (Fig. 48). The determination of the dominant deformation mechanisms in olivine is fundamental to deduce flow patterns in the mantle from S-waves anisotropy data (Mainprice and Silver, 1993; Tommasi et al., 1999; Long and Becker, 2010). The average olivine CPOs of eastern Betic mantle xenoliths is—regardless volcanic center—typical of axial-[100] and orthorhombic peridotite fabric characterized by olivine [100]-axes strongly aligned along lineation, [010]-axes distributed in girdle normal to [100]-axes and foliation, and [001]-axes dispersed near the peridotite foliation plane (Fig. 48). This fabric is characteristic of olivine deformation accommodated by [100]-slip dislocation creep assisted by diffusional processes, which result in an alignment of olivine [100]-axes parallel to mantle flow in the direction of maximum shear (Mainprice and Silver, 1993; Tommasi et al., 1999; Long and Becker, 2010). The resulting axial-[100] olivine patterns in eastern Betic xenoliths implies that for all propagation directions the fast split S-wave is polarized parallel to the lineation (Fig. 48; lower panel) in the same direction as active or frozen mantle flow. The fastest S1 split propagates parallel to the lineation and the highest delay times are obtained for S1 propagating within the foliation and normal to the lineation (Fig. 48). The P-wave velocity displays a maximum parallel to the maximum alignment of olivine [100]-axis (8.6-8.62 km·s⁻¹), and a minimum perpendicular to it (7.98-7.99 km·s⁻¹). The S-wave maximum birefringence

($4.76 < AV_{S_{max}} < 4.77$ %) is correlated with the Y structural axes, and the fast split S-wave is polarized in a plane containing the propagation direction and the maximum alignment of olivine [100]-axes.

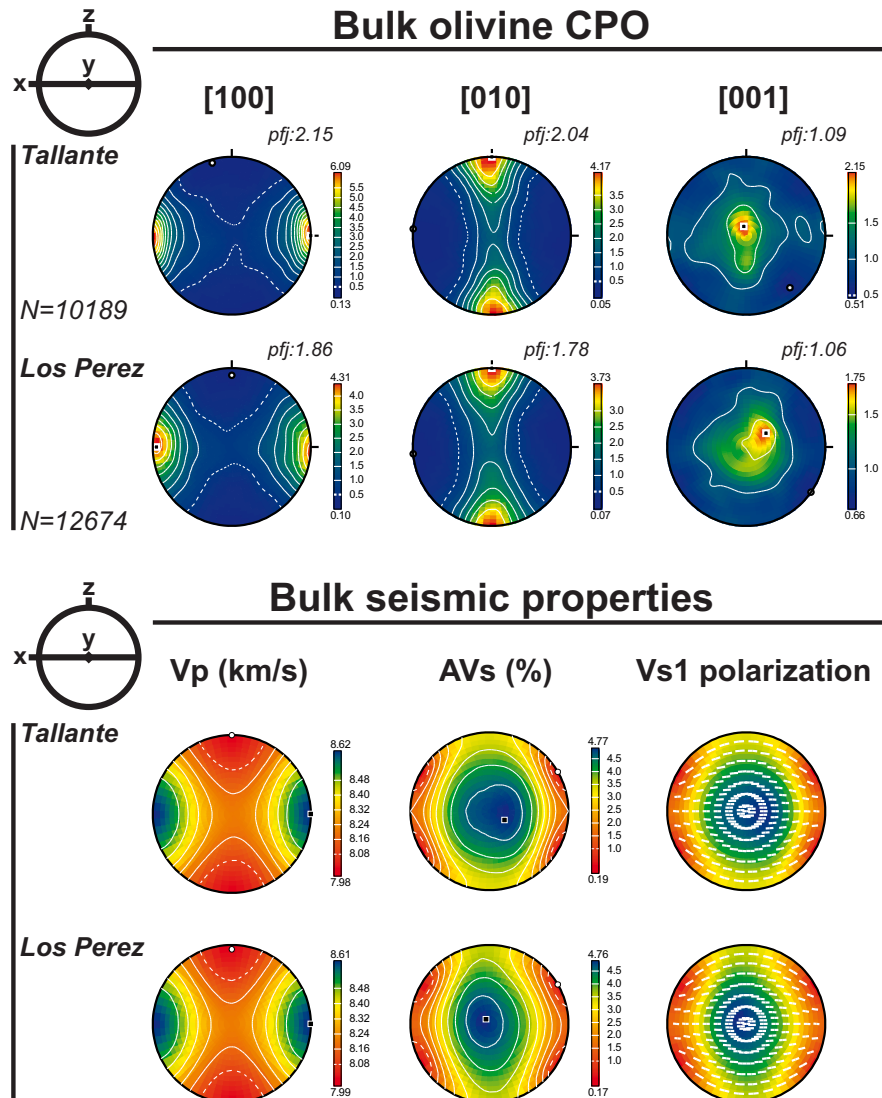


Fig. 48 The bulk olivine CPO and bulk seismic properties of Tallante (12 samples) and Los Perez (13 sample) xenoliths in lower hemisphere equal area stereographic projections. The average mantle rock composition of Tallante and Los Perez corresponds to 61.8 and 58.8% olivine, 20.2 and 25.6% orthopyroxene, and 18.0 and 15.6% clinopyroxene for, respectively. J^{ol} is 4.14 and 3.32 for Tallante and Los Perez, respectively.

Despite evidence for hydrous supra-subduction metasomatism in mantle xenoliths (Arai et al., 2003; Shimizu et al., 2004; Rampone et al., 2010; Bianchini et al., 2011) and arc-like volcanism predating the entrainment of xenoliths to the surface (Benito et al., 1999; Duggen et al., 2005), eastern Betics mantle xenoliths lack any evidence of olivine [010]-axial or B-type fabrics (Jung and Karato, 2001). Some authors have proposed that [010]-axial fabrics are

widespread in supra-subduction mantle where olivine is deformed at high stresses and low temperatures in the presence of water (Jung and Karato, 2001). Olivine [100]-axes in [010]-axial fabrics align in the shear plane (*i.e.* foliation) perpendicular to the maximum shear direction (*i.e.* lineation) and hence the azimuth of the fast split S1 wave is perpendicular to mantle flow (Mainprice and Silver, 1993; Jung and Karato, 2001; Long and Becker, 2010). The lack of [010]-axial fabric in eastern Betic xenoliths is in line with observations in sub-arc mantle xenoliths point to hydrous melts/fluids having few impact on fast S-wave splitting in the shallow mantle wedge of supra-subduction zones (Soustelle et al., 2010).

If mantle anisotropy is due to CPO anisotropy in eastern Betics mantle xenoliths, the predominance of axial-[100] fabrics in unambiguously constrain that the direction (*i.e.* lineation) of active or frozen mantle flow in the upper mantle is parallel to polarization plane of the fast S1 split polarized SKS wave (Fig. 49). Measurement of splitting of SKS phases in the CART seismic station—nearby the studied volcanic centers—(Fig. 49) yields average azimuths (Φ) of $N69 \pm 8^\circ$ (Buontempo et al., 2008; Diaz et al., 2010). SKS phases propagate nearly vertically through the upper mantle and their Φ is approximately the azimuth of polarized S1 wave in the horizontal plane (*i.e.* azimuthal anisotropy) (Silver, 1996; Long and Silver, 2009, 2009). As constrained by mantle xenoliths, the fast split polarized S-wave azimuth of $N69^\circ$ measured at CART station indicates active or frozen mantle flow parallel to this direction and a subhorizontal flow with olivine [100]-axes parallel to this lineation (Fig. 49). In good accord with our previous inferences, subhorizontal mantle flow derived from the combination of SKS data and xenolith fabrics invalidates vertical asthenospheric upwelling (De Larouzière et al., 1988; Kogarko et al., 2001; Shimizu et al., 2004, 2008; Julià et al., 2005) as the cause of SKS anisotropy and mantle flow in the eastern Betics.

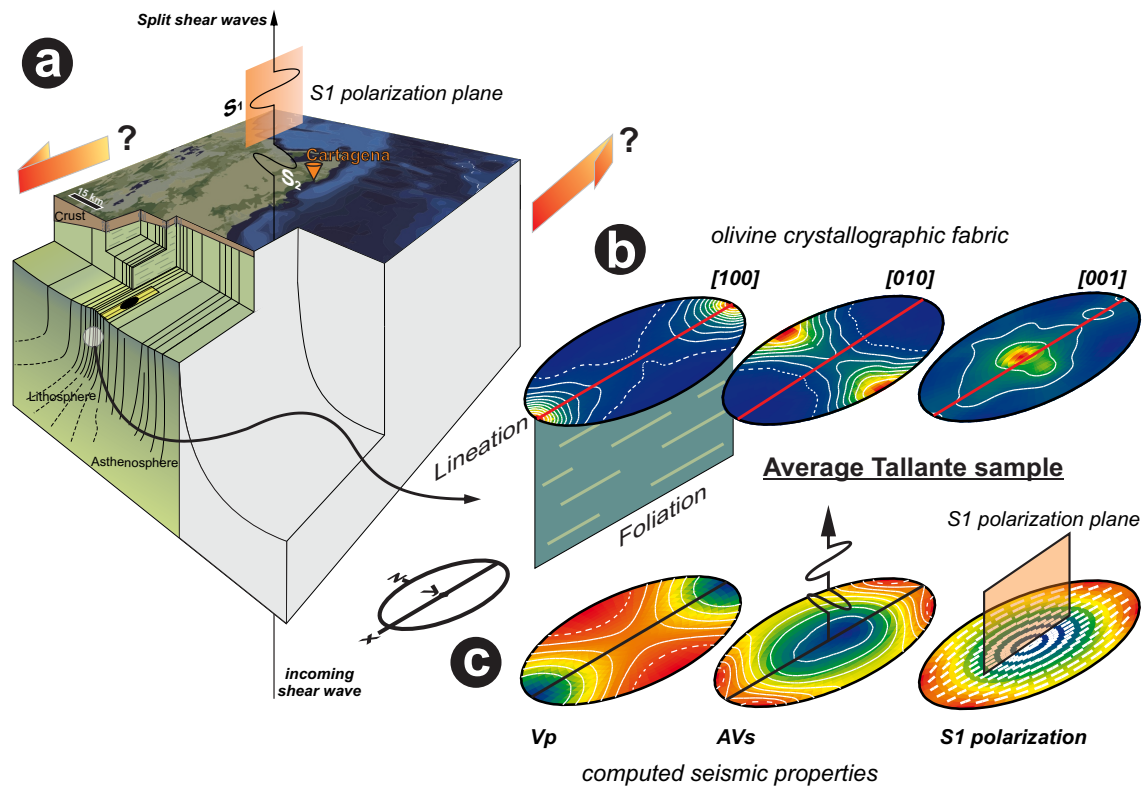


Fig. 49 Cartoon of a conceptual model for the continental lithospheric mantle beneath the eastern inner Betics (modified after Vauchez et al., 2012) (a) showing the assumed orientation of xenoliths (shown by Average Tallante sample, open circle) and a vertically incident polarized SKS wave that propagates through the studied vertically foliated and horizontally lineated subcontinental lithospheric mantle section (see text for details). Transpressive deformation regime (orange arrows) causes the development of an olivine CPO (b) with [100] close to the lineation, [010] close to the normal to the foliation plane, and [001] orthogonal to the lineation in the foliation plane. Panel (c) shows 3D seismic properties computed for this olivine CPO in the same structural reference frame. The V_p diagram shows the highest P-wave velocity parallel to [100]-axis; the AVs (δV_s) diagram shows the velocity difference between the fast and slow split S-waves for all propagation directions; the maximum birefringence is for S-waves propagating in a direction normal to the lineation, i.e., with a subvertical incidence in the case shown in (a). The S1 polarization diagram shows the orientation of the plane in which the fast S-wave is polarized; this plane is consistently defined by the fast S-wave propagation direction.

Pn—doubly refracted primary (head) wave that traveled partly in the upper mantle—tomography reveals as ENE trending low Pn-velocity with normal upper mantle velocities (V_{Pn} c. $8.1 \text{ km}\cdot\text{s}^{-1}$) (Serrano et al., 2005). As elsewhere in the Betic-Rif cordillera, an important observation in the study area is that SKS anisotropy pattern is broadly parallel to Pn anisotropy and both follow the arched-structure of the belt (Serrano et al., 2005; Buontempo et al., 2008; Diaz et al., 2010; Bokelmann et al., 2011). The fast propagation of P waves are parallel to the maximum concentration of olivine [100]-axis and parallel to mantle flow in the same azimuth as the fast-split S-wave, in good agreement with the calculated seismic properties of Eastern Betics xenoliths (Fig. 45, 48 & 49). Because Pn waves only propagate and sample anisotropy of in the uppermost lithospheric mantle this correlation indicates that Pn and SKS anisotropy comes mostly from the uppermost lithospheric mantle and reflects the orientation of the mantle olivine fabric in the eastern Betics (Buontempo et al., 2008).

The fast split S-waves might be polarized in any plane containing the direction of maximum alignment of olivine [100]-axes; therefore, its azimuth alone does not constrain the dip of the plane of maximum shear that corresponds to the tectonic foliation of upper mantle peridotite (Nicolas and Christensen, 1987; Mainprice and Silver, 1993; Silver, 1996; Tommasi et al., 1999; Long and Becker, 2010; Vauchez et al., 2012 and references therein). As long as the olivine [100]-axis is parallel to Φ of the fast split S-wave, foliation in the lithospheric mantle might be flat, steeply dipping or has variable dip with depth. The S-wave birefringence of Eastern Betic xenoliths (Fig. 48 & 49) implies that different foliation dips would result in different delays between polarized SKS waves. Buontempo et al. (2008) reported at the CART seismic stations dt of 1.52 ± 0.31 s that is within error similar to those obtained in later studies at this station (Diaz et al., 2010) (dt of 1.75 s; no error reported in this study). Assuming that the 22-25 km thick crust composed of sediment and igneous rocks in the eastern Betics (Banda and Ansorge, 1980; Banda et al., 1993; Julià et al., 2005; Pedrera et al., 2010) contributes a maximum of 0.3-0.5 s to this delay (Mainprice and Silver, 1993; Silver, 1996; Long and Becker, 2010), the subcrustal lithospheric contribution ranges between $1.0-1.2 \pm 0.3$ s. Three-dimensional gravity modeling combined with integrated heat flow and topography map out the base of lithospheric mantle in the Cartagena area at depth ranges of 60-70 km (Torre et al., 2000; their Fig. 9a) or of 90-100 km (Fullea et al., 2010). Analysis of teleseismic P-residuals places the lithosphere-asthenosphere boundary (LAB) in easternmost inner Betics at depths of ca. 80 km (Plomerová et al., 1993). Considering the 20-25 km crust in the area (Banda and Ansorge, 1980; Banda et al., 1993; Julià et al., 2005; Pedrera et al., 2010), these observations indicate that the current thickness of mantle lithosphere in the study area ranges between 40 and 80 km.

In order to constrain how the flat and vertical foliation end-member scenarios account for measured subcrustal delays, we calculate theoretical delay times for a mantle lithosphere with S-wave birefringence similar to that of average xenoliths (*avg-AVS*) (Fig. 48), and for that birefringence similar to porphyroclastic xenoliths (*por-AVs*) (Fig. 45; samples LPE-48 and TA-124). This latter case would reflect increasing preponderance of high-T porphyroclastic textures with depth. For a geometry with shallow dipping foliation and subhorizontal lineation parallel to the alignment of olivine [100]-axis—implying subcrustal asthenospheric flow parallel to the Moho—the measured subcrustal dt requires an anisotropic upper mantle layer of $147-176 \pm 63$ km with *avg-AVs* of 3.3 %, or a $96-81 \pm 35$ km layer with *por-AVs* of 6 %. For the case steeply dipping foliation and a subhorizontal lineation parallel to the alignment of olivine [100]-axis—implying mantle flow with strike-

slip component subparallel to Iberia margin—delays in CART station requires a anisotropic mantle layer of $103\text{-}123 \pm 44$ km with an *avg*-AVs of 4.8 %, or a $65\text{-}78 \pm 28$ km layer with *por*-AVs of 7.5 %. The estimates thicknesses of the mantle lithosphere of 40 and 80 km are within error in better accord with an anisotropic lithospheric mantle with a steeply dipping foliation and a subhorizontal lineation implying mantle flow with strike-slip component subparallel to Iberia margin as depicted in Fig. 49. A strike-slip mantle flow with a strong mechanical coupling with the continental crust is consistent with the observation that the polarization plane of the fast SKS-wave is parallel to the trend of the crustal geology (Buontempo et al., 2008; Diaz et al., 2010), a feature that is also observed in other mountain belts (Vauchez and Nicolas, 1991; Silver, 1996; Vauchez et al., 2012).

It is possible that a small contribution to anisotropy comes from the sublithospheric mantle just below the LAB (Fig. 49). Waveform modeling of receiver functions identifies pervasive low velocity zones (LVZ) in the uppermost mantle at depths of *ca.* 70-80 km in the eastern Betics (Calvert et al., 2000; Julià et al., 2005; Serrano et al., 2005), as well as low velocities in seismic tomography (Spakman and Wortel, 2004), that might reflect partial melting at the base of the lithospheric mantle. Studies of mantle peridotites indicate that heating and partial melting of the lithospheric mantle do not necessarily obliterate the minerals CPO inherited from the lithospheric mantle (Vauchez and Garrido, 2001). Anisotropy in LAB zones with LVZ may be an asthenospherized ghost lithosphere preserving an inherited lithospheric anisotropy but with asthenospheric properties regarding attenuation of seismic waves velocities (Vauchez and Garrido, 2001). The structural memory of the lithosphere may therefore be preserved in a region of asthenosphere-lithosphere interaction, where tomography studies would indicate a largely attenuated lithosphere from the presence of a shallow low-velocity anomaly while S-wave splitting measurement yields delays between arrivals of the fast and slow split waves requiring a larger lithosphere thickness (Vauchez and Garrido, 2001). This would indicate that the flow pattern is inherited since upper mantle heating and melting largely recorded by Plio-Pleistocene alkali volcanism.

5.8.4. Implication for the Deep Structure and Late Tertiary Geodynamics of the Eastern Betics

Despite large number of geophysical studies, there still are important discrepancies and unknowns about the structure and thermal state of the mantle lithosphere in the eastern Betics. The eastern Betics is characterized by increasing off-shore high heat-flow fluctuating from 60 to 120 mWm⁻² (De Larouzière et al., 1988; Pasquale et al., 1996; Torne et al., 2000;

Negredo et al., 2002), as well as by widespread Middle Miocene to Pleistocene subplutonic and volcanic rocks cropping out in a roughly NE-SW trending band extending through the eastern Alboran Sea into northeastern Morocco (Hernandez et al., 1987; Fernández-Soler, 1996; Duggen et al., 2008). Deep seismic refraction profiles in the Eastern Betic reveal different crustal types at both side of a strike-slip fault system (Banda and Ansorge, 1980; Banda et al., 1993; Julià et al., 2005). East of the fault system – where mantle xenolith-bearing alkali basalt occurs – the Moho is flat and shallower (23 km deep with V_p of 6.3 km·s⁻¹) than at the west (30 km deep and V_p of 6.1 km·s⁻¹). Using geophysical estimates of temperature at Moho of 700 °C and that of the lithospheric mantle at 45 km depth of 1100 °C (Torne et al., 2000; Soto et al., 2008), we estimate a current geotherm (Fig. 47) that results in a high surface heat flow of 105 mW·m⁻¹, which is in line with results published in the area (e.g. De Larouzière et al., 1988; Pasquale et al., 1996; Negredo et al., 2002).

The current geotherm is colder than the paleogeotherm inferred from Eastern Betics mantle xenoliths in (Fig. 47), suggesting a hotter thermal regime in the latest stages of ductile deformation at shallow depth. The paleogeotherm not only implies a hotter subcrustal mantle during ductile thinning to plagioclase facies, but also Moho temperatures in excess of 850 °C at 4.4 Ma, followed by the 1 Ma thermal relaxation (Kogarko et al., 2001) before the entrainment of mantle xenoliths in the Plio-Pleistocene. This high thermal gradient is also documented in lower crust xenoliths entrained together with mantle xenoliths in alkali basalts (Vielzeuf, 1983). As deduced previously, initiation of ductile thinning of thick subcontinental mantle lithosphere might have occurred between 6.2-9.4 Ma. This time span broadly overlaps with the initiation of lower-crust anatexis in the Eastern Betics profusely recorded in crustal xenoliths in lower Miocene calc-alkaline volcanoes (Cesare and Gómez-Pugnaire, 2001; Cesare et al., 2003; Álvarez-Valero and Kriegsman, 2007; Acosta-Vigil et al., 2007, 2010) and dated between 9.7-8.1 Ma (Zeck and Williams, 2001; Cesare et al., 2003). Álvarez-Valero and Kriegsman (2007) have argued that crustal anatexis – triggered by basaltic underplating – was concomitant in the late Miocene. The age of ductile thinning and decompression in the eastern Betics mantle xenoliths is in good line with lithospheric thinning that could itself be the source of heating (Torne et al., 2000). This time span also coincides with the change from subduction-related to intraplate-type volcanism (6.3-4.8 Myr), which is largely synchronous with uplift associated with the Messinian salinity crisis (Duggen et al., 2003, 2004 and references therein), and the end of the process coincides with Pliocene uplift in the Eastern Betics and the eastern Iberian margin (Bartrina et al., 1992; Janssen et al., 1993) that could have been driven by a late heating event during the post-

Miocene (Janssen et al., 1993). Widespread magmatic activity during the middle Miocene to Pliocene in the eastern Betics coincides with areas where the base of the lithosphere is shallow (<60 km, Torne et al., 2000). These multidisciplinary observations indicate close relationships between thin lithosphere, heating, crustal anatexis, magmatism and uplift in the late Miocene and Pliocene in the Eastern Betics.

Eastern Betics mantle xenolith data combined with seismic anisotropy data require mantle lithospheric thinning accommodated by ductile deformation in a transtensive regime with a dominant strike-slip component (Fig. 49) sometime in the late Neogene. This tectonic regime is consistent with late-Miocene crustal extension and associated subsidence in the Eastern Betics (Lonergan and Schreibers, 1993; Booth-Rea et al., 2004a, 2007; Meijninger and Vissers, 2006 and references therein). However in the crust, compressional Late-most Miocene to present-day structures, including large-scale open folds and both reverse and transcurrent faults are predominant in the eastern Betics (*e.g.* Montenat and Ott d'Estevou, 1990; Comas et al., 1999; Booth-Rea et al., 2004b, 2007; Giaconia et al., 2013) and in a great part of the Alboran Sea in agreement with the current tectonic setting of NW-SE plate convergence between Nubia and Eurasia. The NW-SE convergence of Nubian and Europe in the Eastern most is partly localized along a number of large strike-slip and reverse faults developed since the latest Miocene, some of which have inverted previous extensional faults (Meijninger and Vissers, 2006).

Seismic observations indicate the existence of an east to southeast dipping high-velocity body in the upper mantle below the Gibraltar arc, interpreted as subducted oceanic and/or delaminated continental lithospheres (Calvert et al., 2000; Gutscher et al., 2002; Spakman and Wortel, 2004 and references therein). A growing body of evidence supports the hypothesis that both subduction rollback and continental edge delamination beneath the continental margins may have contributed to the formation and development of the Gibraltar arc (Duggen et al., 2005; Booth-Rea et al., 2007 and references therein). Geochemical evidence derived from Neogene volcanisms suggest that it could be a combination of both, oceanic lithosphere under the central areas of the Alboran basin, coupled to delaminated Iberian continental lithospheric mantle under the eastern Betic-Rif margins (Duggen et al., 2003, 2004, 2005). The combination of Miocene westward slab retreat forming the Alboran Basin and late Miocene edge delamination of the subducted Iberian margins may account for some features observed in the eastern inner Betic mantle xenoliths. Vauchez and Nicolas (1991) suggested that in many collisional belts the dominant motion is strike-slip parallel to the main trend of compression and the entire lithosphere develops a fabric and becomes

anisotropic. They attribute this anisotropy to a dominant mantle flow parallel to the mountain belt during orogeny; however, in the eastern Betics it is unlikely that mantle flow reflects the NW-SE convergence of Nubia and Iberian since the late Tortonian. An alternative is the controlling role of a mantle fabric derived from Miocene slab rollback processes. Miocene W-SW slab retreat may have induced a large strike-slip deformation in the mantle at the edge of the Iberian margin and alignment of olivine (100) axis in the overriding Alboran plate. This process generated strong mantle anisotropy parallel to the Iberian-African margin. Edge delamination of the Iberian margin mantle may have caused lateral westward inflow of hot and extended lithospheric mantle of Alboran provenance under the detached margins flowing parallel to Iberia. This process would produce strong lateral decompression of lithospheric mantle and lower crust to fill the detached cold lithosphere that might explain the flat Moho, thin lithosphere, heating, crustal anatexis, shift of magmatism, and uplift in the late Miocene and Pliocene in the Eastern Betics. This process was coeval to middle to late Miocene east-west opening and oceanic magmatic accretion of the Algero-Balearic basin (Acosta et al., 2001; Mauffret et al., 2004; Booth-Rea et al., 2007).

The presence of inherited Middle to Late Miocene deep mantle fabrics may continue governing some tectonic processes. Earthquake moment tensors indicate deep strike slip faulting in the eastern Betics coherent with motion in a NE-SW-trending left-lateral shear zone (Stich et al., 2006), processes that are in principle incompatible with the general NW-SE plate convergence between Africa and Iberia.

This scenario of mantle and crustal xenoliths points towards an allochthonous Alboran-Alpujarride provenance of the lower crust and subcrustal lithospheric mantle, whereas calc-alkaline and alkaline volcanoes extrude in Nevado-Filábride upper crust of paleo-Iberian provenance (Booth-Rea et al., 2005; Platt et al., 2006). Nevado-Filábride units exposed in the easternmost Betics underwent eclogite facies followed by amphibolite metamorphism in a collisional context (Booth-Rea et al., 2005) in the early to middle Miocene (*e.g.* López Sánchez-Vizcaíno et al., 2001; Platt et al., 2006) just before subduction-related arc magmatism. During its westward migration, the Alboran orogenic wedge encountered the South Iberian and North Maghrebian margins, producing oblique collision fold-and-thrust belts at the margins allied with subduction and eclogite facies HP/LT metamorphism of the Iberian paleo-margin basement (Booth-Rea et al., 2007 and references therein) in the early middle Miocene (López Sánchez-Vizcaíno et al., 2001; Platt et al., 2006) contemporaneous with opening of the Algero-Balearic and Alboran Basins and just before the subduction-related arc magmatism in the eastern Betics. The lack of HP/LT in the lower crust and

mantle xenoliths seems in accordance with their differing provenance. Detachment of the subducted lithospheric mantle and westward replacement by Alboran-type lower lithosphere and mantle would account for the different provenance of mantle and crustal xenoliths.

5.9. Conclusion

Mantle xenoliths in Plio-Pleistocene alkali basalts in the easternmost inner Betic provide a snapshot of the structure and composition of the lithospheric mantle beneath the NE termination of the Alboran arc system in the western Mediterranean. Re-depletion model ages of sulfides in peridotite xenoliths and U-Pb ages in lower crust xenoliths and anatectic melts yield inherited Neoproterozoic ages similar to those reported in the Ronda orogenic peridotite and lower crust in the western Betics Alpujarrides. These ages indicate a non-Iberian provenance of the lower crust and subcrustal lithosphere in the eastern Betic. Despite their common Alboran provenance, eastern Betic mantle xenoliths sampled a more fertile mantle lithosphere recording a younger and distinct deformation regime than that preserved in the Ronda peridotite. CPOs of orthopyroxene in orthopyroxenite veins of composite xenoliths formed at 2.2-4.4 Ma by silica-rich fluid/melt reaction with mantle peridotite indicates that metasomatism was synkinematic with high-T ductile dislocation creep flow of mantle peridotite, demonstrating that ductile fabrics were developed sometime in the late Neogene.

Peridotite xenoliths show a distinct olivine axial-[100] pattern that is characteristic of deformation under simple shear in a transtensional tectonic regime. Texture and composition of xenoliths record decompression from depths of at least 55-60 km up to shallow subcrustal depths of 19-20 km. Synkinematic overprinting of mineral assemblages from the garnet-spinel to the plagioclase facies demonstrates that this 36-40 km uplift was continuously accommodated by ductile shear thinning of the lithospheric mantle. Lithospheric thinning had minimum stretching beta factors of *ca.* 1.5 and long-term high strain rates of *ca.* $9\cdot 7\cdot 10^{-13}$ s⁻¹, values that are characteristic of rapidly extending continental lithosphere with geothermal gradient in excess of 100 mW·m⁻².

As constrained by mantle xenoliths, the N 69° strike of SKS and Pn seismic anisotropy in the eastern Betics can be explained by a shallow lithospheric mantle fabric with olivine [100]-axes subhorizontal and subparallel to the mantle flow direction. A shallow mantle lithosphere thickness (40-80 km) and delays of SKS waves in the eastern Betics can only be accounted for by a steeply dipping mantle foliation and subhorizontal lineation; this

geometry of the lithospheric mantle peridotite fabric implies active or frozen mantle flow with a dominantly strike-slip component subparallel to the paleo-Iberian margin. This configuration may reflect strike-slip deformation in the early Miocene during W-SW slab retreat of the Alboran lithosphere at the edge of the Iberian margin. Compositional profiles in xenoliths indicate that initiation of ductile thinning of the subcontinental mantle may have occurred sometime between 6.2 and 9.4 Ma. This time span broadly overlaps with deep processes events in the eastern Betics such as onset of lower crust anatexis (*ca.* 9 Ma) and the change from subduction-related to intraplate-type volcanism (6.3-4.8 Ma). These magmatic events are synchronous with uplift associated with the Messinian salinity crisis that some authors ascribe to asthenospheric upwelling and lithospheric edge delamination of the Iberian margin during westward rollback of subducted Tethys oceanic lithosphere. Edge delamination of the Iberian margin mantle thinning and decompression of hot extended lithospheric of Alboran provenance and its lateral westward inflow under the detached margins to fill the detached cold lithosphere following the inherited S-SW lithospheric anisotropy. This process would explain flat Moho, thin lithosphere, heating, crustal anatexis, shift of magmatism, and uplift in the late Miocene and Pliocene in the Eastern Betics. Detachment of the subducted lithospheric mantle and westward replacement by Alboran-type hot lower lithosphere would account for Alboran provenance of mantle and lower crustal in the Eastern Betics. This geological paroxysm was coeval to middle to late Miocene E-W opening and oceanic magmatic accretion of the Algero-Balearic basin. The existence of strike-slip inherited mantle fabrics may continue governing some deep processes in the Eastern Betics.

6. Isotopic and geochemical composition of the subcontinental lithospheric mantle in the westernmost Mediterranean: Constrains from peridotite xenoliths in Plio-Pleistocene alkali basalts (eastern Betic Cordillera, SE Spain)

Z. Konc^a, C.J. Garrido^a, D. Bosch^b, C. Marchesi^a, K. Hidas^a, M.I. Varas-Reus^a & A. Acosta-Vigil^a

Abstract

Peridotite xenoliths in Plio-Pleistocene alkali basalts from the eastern Betic Cordillera (Murcia, SE Spain) provide key information on the Alpine tectono-magmatic processes that have affected the westernmost Mediterranean from a subcontinental lithospheric mantle. Here we present a detailed geochemical study comprising whole rock and mineral major- and trace element, as well as Nd-Sr-Pb isotopic composition data of spinel \pm plagioclase lherzolite, spinel \pm plagioclase harzburgite and spinel wehrlite xenoliths from Tallante and Los Perez volcanic centers. The whole rock major element compositional array of the studied set of xenoliths, supported by their mineral chemistry, reflects increasing fertility from clinopyroxene-poor peridotites (Group I; Mg# up to 0.915), common lherzolites (Group II; Mg# up to 0.906) and fertile lherzolites (Group III; Mg# of 0.868-0.889) to wehrlites (Mg# of 0.867-0.874), respectively. The mineral major element chemistry records the geochemical imprint of maximum 10-12 % partial melting in the most depleted Group-I peridotites. However, trace element and isotopic data attest for various degrees of metasomatic enrichment that overprinted the previously depleted lithospheric mantle. Interaction with melts produced enrichment of LREE in Group II and Group II peridotites, as well as wehrlites. In contrast to major and trace elements, Nd-Sr-Pb radiogenic isotope systematic is unrelated to compositional groups and shows isotopic variations between DMM to EM2 end-member and contribution of an Atlantic sediment-like component. Heterogeneous mantle lithology and major element chemistry coupled to overlapping isotopic composition also indicates the metasomatism of the studied set of peridotites by external melt(s) of a common source. These geochemical evidences attest for the percolation of slab-derived, SiO₂-undersaturated melts (and hydrous fluids) with carbonate sediment affinity in the pre-Miocene supra-subduction continental lithospheric mantle beneath the Alborán Basin, possibly released from the subducted Tethys oceanic lithosphere.

^a *Instituto Andaluz de Ciencias de la Tierra (IACT), CSIC & UGR, Avenida de las Palmeras 4, 18100 Armilla, Granada, Spain.*

^b *Géosciences Montpellier, Université Montpellier II & CNRS, Place E. Bataillon, 34095 Montpellier, France.*

6.1. Introduction

Mantle xenoliths in basalts and tectonically emplaced orogenic peridotite massifs provide key information for understanding the structure, composition and magmatic record of the Subcontinental Lithospheric Mantle (SCLM) (*e.g.* Downes, 2001; Bodinier and Godard, 2006; and references therein). In orogens with a protracted complex geodynamic evolution, post-orogenic alkali basalts commonly entrain upper mantle xenoliths—mostly spinel peridotites—that provide a unique window to investigate the isotopic and geochemical composition of deep lithospheric mantle orogenic roots. In the Alpine Betic-Rif arched orogenic belt in the westernmost Mediterranean, post-orogenic Plio-Pleistocene alkali basalts in the eastern Betic Cordillera have entrained numerous mantle xenoliths after a complex geodynamic evolution in the Tertiary that lead to the formation of the Gibraltar arc (Duggen et al., 2004; 2005; Doblas et al., 2007; Lustrino et al., 2011; Shimizu et al., 2008; Rampone et al., 2010; Bianchini et al., 2011; Konc et al., submitted). Since the latest Oligocene, the Betic-Rif orogen underwent different tectonic-magmatic stages encompassing subduction related and anorogenic magmatism; alkali basalt in the Southeastern Iberian Volcanic province reflect the last magmatic event (*e.g.* Fernández-Soler, 1996; Benito et al., 1999; Duggen et al., 2004, 2005, 2008; Cebriá et al., 2009). These basalts have entrained peridotite mantle xenoliths of the lithospheric mantle after tectono-magmatic processes associated with the Tertiary geodynamic evolution that shaped the Gibraltar arc (Faccenna et al., 2000; Spakman and Wortel, 2004; Booth-Rea et al., 2007; and references therein). These mantle xenoliths therefore provide key information on how these tectono-magmatic processes disturbed the isotopic and geochemical composition of the subcontinental lithospheric mantle reservoir in the westernmost Mediterranean during the Alpine orogeny.

In this paper we present a comprehensive study of the major, trace and Nd-Sr-Pb isotopic composition in whole rock and minerals from peridotite xenoliths hosted in Plio-Pleistocene alkali basalts from the eastern Betic Cordillera. This dataset allows us to investigate the nature and geochemical composition of the SCLM in the eastern Betic Cordillera and its relationship with Alpine and prior tectono-magmatic processes that have affected this orogen.

6.2. Sampling, Lithology and Texture of Eastern Betics Xenoliths

Mantle xenoliths for this study (Table 7) come from the Plio-Pleistocene (2.3-2.9 Ma) alkali basalt volcanic centers of Tallante and Los Perez near Cartagena (SE Spain) (Boivin, 1981; Vielzeuf, 1983; Dupuy et al., 1986; Capedri et al., 1989; Arai et al., 2003; Beccaluva et al., 2004;

Shimizu et al., 2008; Rampone et al., 2010; Bianchini et al., 2011). Konc et al. (submitted) have provided a detail description of the sampling, petrography, microstructure and mineral Crystal Preferred Orientation (CPO) of mantle xenoliths selected for the present geochemical study (Table 7). Xenoliths are anhydrous spinel and spinel-plagioclase lherzolite, and subordinate spinel (\pm plagioclase) harzburgites and spinel wehrlites (Fig. 50) with porphyroclastic (Fig. 51f), cluster porphyroclastic (Fig. 51e), equigranular, and transitional textures (Fig. 51c-f) (Konc et al., submitted). Tallante xenoliths are clinopyroxene-poor lherzolites and harzburgites (Fig. 50) (see also, Rampone et al., 2010; Bianchini et al., 2011). Los Perez xenoliths are mostly lherzolites with variable clinopyroxene content including clinopyroxene-rich lherzolites with modal compositions near that of the primitive mantle, and rare wehrlites (Konc et al., submitted; Fig. 50). As confirmed by detailed EBSD mapping, the selected xenoliths for this study contain no amphibole or hydrous phases. Neither composite xenoliths—*i.e.* plagioclase-quartz veins or orthopyroxenite veins (Arai et al., 2003; Shimizu et al., 2004, 2008; Rampone et al., 2010; Bianchini et al., 2011)—has been selected for the present study. Detailed Scanning Electron Microscopy inspection has revealed apatite inclusions (10-20 μ m) in clinopyroxene of spinel-plagioclase lherzolite sample TAL-014 (Fig. 51a,b). Interstitial and inclusions of sulfides are common in all peridotite xenoliths.

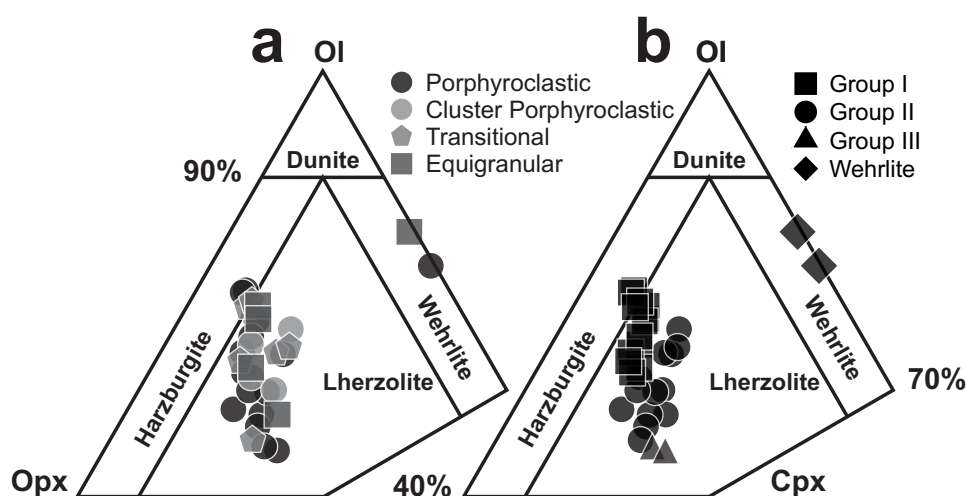


Fig. 50 Streckeisen diagrams (*c.f.* Streckeisen, 1974) showing the lithology of the studied SE IVP xenoliths in terms of their texture (a) and groups of their fertility character (b).

Application of two-pyroxene solvus (T_{solv} , Taylor, 1998), Ca-in-orthopyroxene ($T_{\text{Ca-opx}}$, Brey and Köhler, 1990; $T^*_{\text{Ca-opx}}$, Nimis and Grütter, 2010), and Al-in-orthopyroxene ($T_{\text{Al-opx}}$, Witt-Eickschen and Seck, 1991) geothermometry, indicates that there is no correlation between textural types, lithology and equilibration temperature (Konc et al., submitted).

Porphyroclastic peridotites tend to yield higher average temperatures (T_{Ca-opx} & $T^*_{Ca-opx}=1032\pm92$; $T_{Al-opx}= 1008\pm47$ °C) than cluster porphyroclastic (T_{Ca-opx} & $T^*_{Ca-opx}= 987\pm44$ °C; $T_{Al-opx}= 948\pm11$ °C) and transitional peridotites (T_{Ca-opx} & $T^*_{Ca-opx}= 959\pm66$ °C; $T_{Al-opx}= 1000\pm66$ °C), and the equigranular lherzolite (T_{Ca-opx} & $T^*_{Ca-opx}= 980\pm10$ °C; $T_{Al-opx}= 988$ °C) (Konc et al., submitted). These temperature estimates are similar to those reported in previous studies of Tallante xenoliths (920-1020°C, Seghedi et al., 2002; 830-930°C for porphyroclastic peridotites, Beccaluva et al., 2004; 950-1020°C for cluster porphyroclastic peridotites, Shimizu et al., 2008; and 960-1020°C for all textural groups, Rampone et al., 2010).

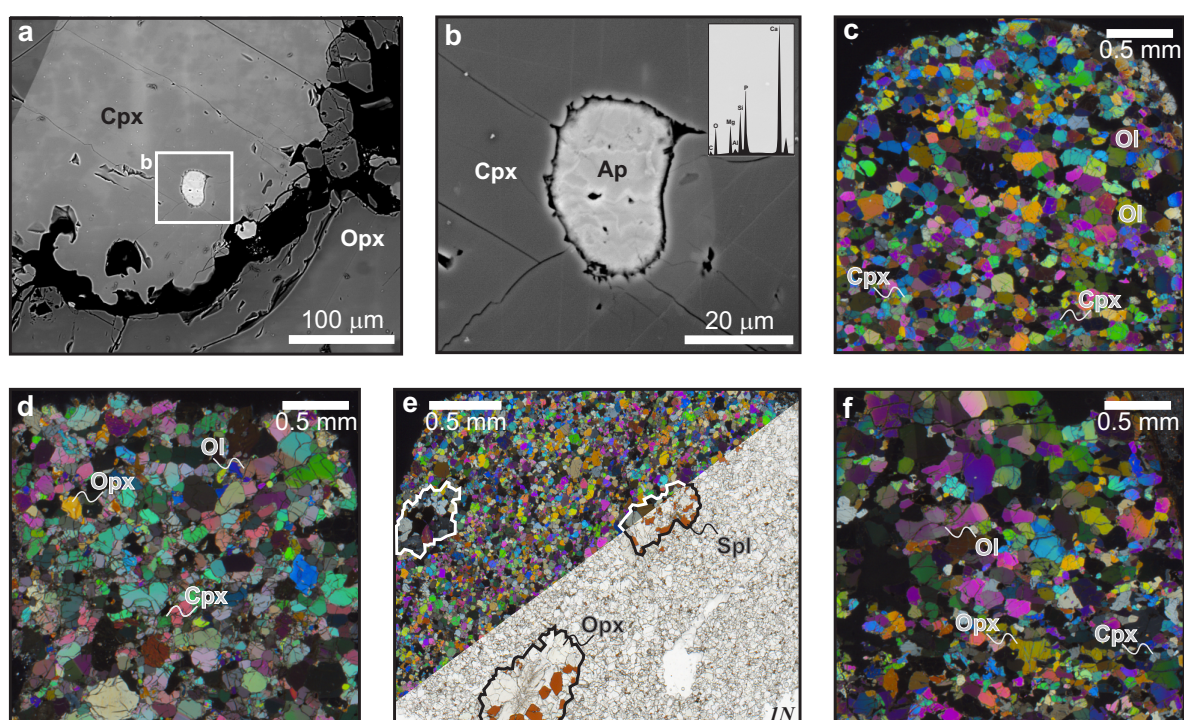


Fig. 51 Photo table displays apatite-bearing clinopyroxene (Cpx) surrounding by orthopyroxenes (Opx) in sample TAL-014 (a), tiny apatite (Ap) inclusion with its WDS spectrum (b) and the different representative textures (c-f) of the studied SE IVP xenoliths. c) Equigranular spinel wehrlite (Ol: olivine), d) transitional texture spinel lherzolite, e) cluster porphyroclastic spinel lherzolite with pyroxene-spinel (Spl) clusters marked black/white lines, and f) Porphyroclastic spinel-plagioclase peridotite. (Photomicrograph c, d and f are taken by cross-polarized setup, while e is a montage made by cross-polarized and only plain polarized (1N) setup.)

6.3. Results

6.3.1. Whole Rock Major and Minor Elements: Compositional Groups

The whole rock major and minor element of xenoliths are given in Table 8 and illustrated in Fig. 52. On the basis of their major element composition, we have differentiated four main compositional groups of xenoliths. The main lithological and compositional features of each group are as follow:

(i.) Group I (n=13) are clinopyroxene-poor peridotites (<8 vol%) ranging in modal composition from harzburgite to depleted lherzolite (Fig. 50b; Table 7) with Mg# of 0.902-0.915 (Mg# is Mg/(Mg+Fe) in mol%). This group contains the most depleted peridotite samples among studied xenoliths. They are characterized by high MgO (43.0-45.3 wt%) and low FeO (7.3-8.3 wt%) contents, and by barren composition in terms of basaltic components (Al_2O_3 = 1.4-2.3 wt%, CaO= 1.0-1.9 wt% and TiO_2 = 0.06-0.2).

(ii.) Group II (n=13) is composed of common lherzolites with clinopyroxene contents ranging from 8 to 12 vol% (Fig. 50b; Table 7) with Mg# between 0.892-0.906. They are moderately depleted and have 2.2-3.2 wt% of Al_2O_3 , 1.9-2.7 wt% of CaO, 7.6-8.8 wt%, of Fe, and of 39.8-42.6 wt% of MgO.

(iii.) Group III (n=2) is rather fertile lherzolites (8-12 vol% of clinopyroxene; Fig. 50b) with low Mg# (0.868-0.889). They are enriched in basaltic components (Al_2O_3 = 3.7-4.6 wt%, CaO= 3.3-3.4 wt% and TiO_2 = 0.28-0.51) and FeO (8.1-10.0 wt%), and poor in MgO (36.4-37.1 wt%).

(iv.) Wehrlites (n=2) contain 15-18% of clinopyroxene (Fig. 50; Table 7) with very low Mg# (0.867-0.874). The high CaO (3.5-3.9 wt%) and FeO (10.7-11.0 wt%) contents and moderate MgO (40.4-41.6 wt%) contents, whereas their Mg# are low (0.867-0.874).

In the MgO/SiO₂ vs. Al₂O₃/SiO₂ diagram (Fig. 52a), the majority of xenoliths plots in the terrestrial mantle array (e.g. Jagoutz et al., 1979; Hart and Zindler, 1986), except for two depleted samples (LP08-12, TAL-102), some moderately depleted, Group III and wehrlite peridotites. Overall, eastern Betics xenoliths show a clear trend from fertile (low MgO/SiO₂, high Al₂O₃/SiO₂) to depleted and wehrlite peridotites (high MgO/SiO₂, low Al₂O₃/SiO₂). This trend is ordinarily interpreted as a melting trend defined by residues of variable partial melting and extraction from a common source similar to fertile primitive upper mantle lherzolite. As other mantle peridotites (Bodinier and Godard, 2006), Eastern Betic mantle xenoliths show positive correlations in CaO vs. Al₂O₃ plot (Fig. 52b), which is interpreted as a melting or refertilization trend. In this plot, Group III peridotites constitute the most fertile end member with high CaO wt% and high Al₂O₃ wt% similar or greater than Primitive Mantle (PM), whereas Group I plots toward the most depleted end of the trend. Wehrlites plot off the trend and have high CaO wt% and low Al₂O₃ wt%. Different groups of Eastern Betics xenolith can be differentiated in FeO wt% vs. MgO wt% diagram (Fig. 52c); most depleted peridotites have high Mg# (>90) and fertile lherzolite and wehrlite have the lowest values (<89).

In terms of minor and transition elements (Table 8), the V and Zn contents increase from Group I to Group III xenolith. Cr, Co and Ni tend to increase from Group III to Group I (Fig. 52d), although there is no clear trend. Wehrlites have minor element compositions that largely overlap those of Group II xenoliths.

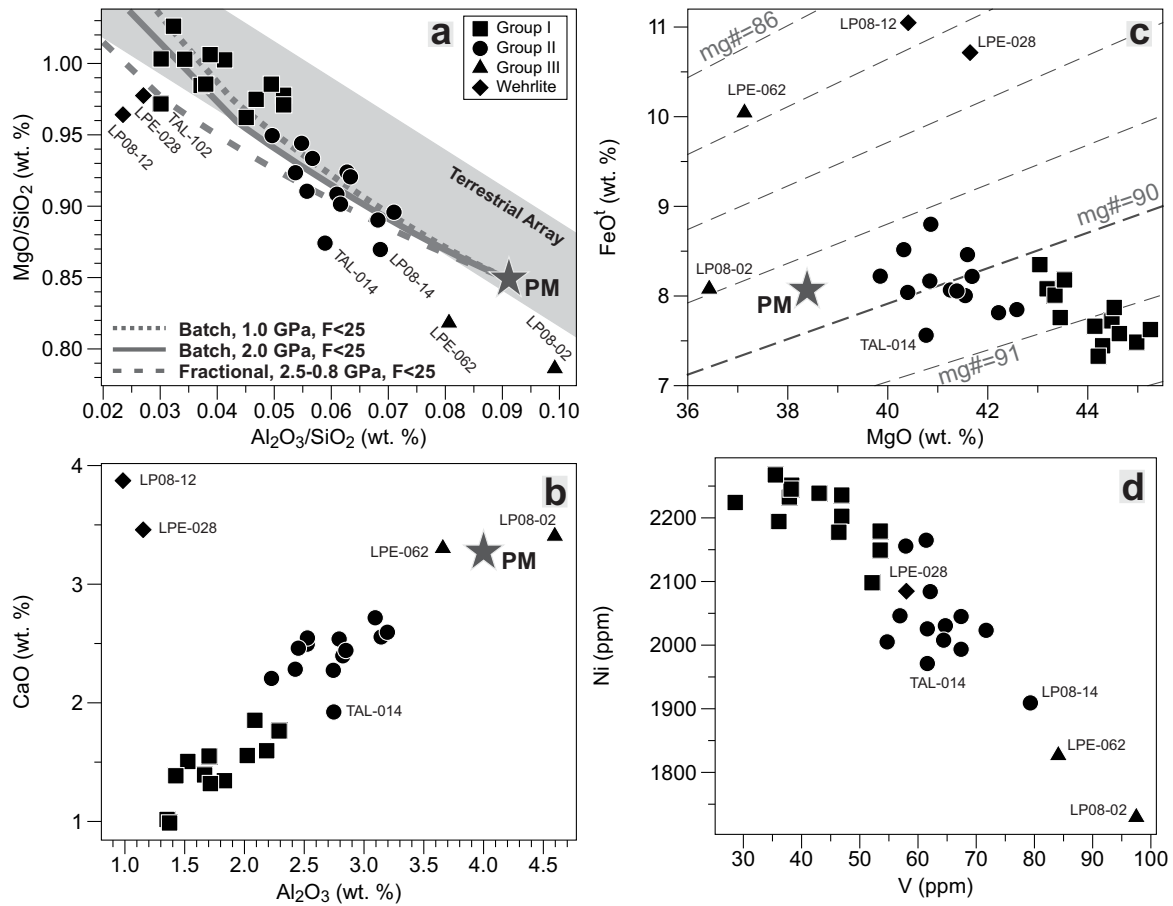


Fig. 52 Whole rock major and minor element composition of SE IVP xenoliths by Al_2O_3/SiO_2 vs. MgO/SiO_2 (a), CaO vs. Al_2O_3 (b), FeO vs. MgO with Mg-numbers tie-lines (c), and Ni vs. V (d). Data plotted on an anhydrous basis in wt.% for major elements, and in ppm for minor elements. Terrestrial array in plot of Al_2O_3/SiO_2 vs. MgO/SiO_2 (a) from Jagoutz et al. (1976) and Hart and Zindler (1986); curves of polybaric near-fractional and isobaric batch melting redrawn from Niu (1997).

6.3.2. Whole Rock Trace Elements

The whole rock trace element abundances of eastern Betic xenoliths are given in the Table 9. The whole rock patterns of Rare Earth Element (REE) normalized to C1 chondrite and of trace elements normalized to primitive mantle (PM) are shown in Fig. 53 (solid symbols) (normalizing values after Sun and McDonough, 1989).

Overall, the REE concentration decreases from Group III and wehrlite to Group I. Group I have REE content below C1 chondrite values. They flat REE patterns slightly depleted in Light REE (LREE), with a relative enrichment in La to Ce relative to other LREE

(Fig. 53a). Harzburgite TAL-102 has markedly different U-shape pattern characterized by low MREE-HREE and an increase LREE segment (Fig. 53a). Group II xenoliths have higher REE content—1-10 times C1 Chondrites (Fig. 53b). The more REE depleted samples of this group show flat REE patterns slightly enriched in LREE that are similar to those of Group I xenoliths (Fig. 53b). The more REE enriched samples of Group II show distinct REE patterns: apatite-bearing lherzolite TAL-014 displays a REE pattern characterized by a flat MREE-HREE segment similar to Group II patterns, but it has a distinct convex-upward LREE segment with Nd and Sm maxima (Fig. 53b) that might be symptomatic of apatite crystallization in an open system; lherzolite LP08-14 has a LREE-enriched flat REE pattern with a pronounced Eu negative anomaly (Fig. 53b). The Group III lherzolite has the highest REE contents among the studied lherzolites, and a flat REE pattern enriched in LREE (Fig. 53b). Wehrlite LPE-028 displays high REE contents and REE pattern are LREE-enriched and characterized by a straight HREE segment, a progressive enrichment of MREE, and a flat LREE segment (Fig. 54).

The trace element patterns (right panel of Fig. 53 & 54; patterns with closed symbols) of Group I xenoliths show lower concentrations ($< PM$) than those of Group II xenoliths; the normalized patterns of both groups show Pb and Ta positive spikes, and are enriched in highly incompatible trace elements (Rb, Th, and U) relative to more compatible REE (Fig. 53a,b). The pattern of the Group III xenolith is similar to that of other xenoliths groups, but shows less pronounced negative anomalies of Nb-Ta and Zr-Hf (Fig. 53c). The normalized pattern of wehrlite LP-028 is enriched in all trace elements; it lacks Pb spikes, has negative Nb-Ta, Sr, and Zr-Hf anomalies—relative to MREE—and shows depletion of Th and U relative to more compatible trace elements (Fig. 54).

6.3.3. Mineral Major Elements

The average olivine Mg# [$Mg/(Mg+Fe)$] in the Group I varies between 0.903-0.905, and decreases progressively from Group II (0.886-0.900) to Group III (~ 0.897) olivine; wehrlites have the lowest Mg# ranging between 0.866-0.869. The average the lowest olivine FeO content is found in Group I xenoliths (9.07-9.46 wt%) and the highest in wehrlites (12.4-12.7 wt.%). The olivine FeO content of Group I and Group II xenoliths ranges between ~ 10.0 wt% and 9.54-11.0 wt%, respectively.

Table 7. Texture, modal abundances and calculated equilibrium temperatures of the studied SE IVP xenoliths

| Sample | Texture | OI | Opx | Cpx | T _{Cpx-Opx} (±31 C°) | T _{Ca-in-Opx} (±16 C°) | T* _{Ca-in-Opx} (±25-45 C°) | T _{Cr-Al-Opx} (±15 C°) |
|-------------------------|-------------------------------|------|------|------|----------------------------------|------------------------------------|--|------------------------------------|
| Group I | | | | | | | | |
| TAL-047 | Cluster porphyroclastic | 0.74 | 0.19 | 0.07 | | | | |
| TAL-052 | Porphyroclastic | 0.74 | 0.20 | 0.07 | | | | |
| TAL-056 | Porphyroclastic | 0.76 | 0.17 | 0.06 | | | | |
| TAL-077 | Porphyroclastic | 0.79 | 0.16 | 0.04 | | | | |
| TAL-084 | Transition | 0.78 | 0.17 | 0.05 | 892.3 | 955.5 | 934.6 | 1010.4 |
| TAL-094 | Transition | 0.78 | 0.17 | 0.05 | 904.5 | 969.9 | 951.9 | 1063.3 |
| TAL-099 | Porphyroclastic | 0.72 | 0.20 | 0.08 | | | | |
| TAL-102 | Porphyroclastic | 0.79 | 0.17 | 0.04 | | | | |
| TAL-110 | Equigranular | 0.77 | 0.17 | 0.06 | | | | |
| TAL-125 | Porphyroclastic | 0.73 | 0.20 | 0.07 | | | | |
| TAL-131 | Porphyroclastic | 0.72 | 0.21 | 0.08 | | | | |
| TAL-143 | Porphyroclastic | 0.78 | 0.16 | 0.06 | | | | |
| TAL-149 | Porphyroclastic | 0.75 | 0.18 | 0.07 | | | | |
| Group II | | | | | | | | |
| LP08-03 | Porphyroclastic | 0.68 | 0.21 | 0.11 | | | | |
| LP08-14 | Transition | 0.65 | 0.23 | 0.12 | | | | |
| LPE-029 | Cluster porphyroclastic | 0.71 | 0.20 | 0.09 | 985.9 | 1055.2 | 1050.2 | 935.3 |
| LPE-042 | Equigranular | 0.68 | 0.20 | 0.13 | | | | |
| LPE-046 | Porphyroclastic | 0.67 | 0.22 | 0.12 | | | | |
| LPE-048 | Porphyroclastic | 0.73 | 0.16 | 0.10 | 977.2 | 1047.1 | 1041.0 | 968.5 |
| LPE-061 | Porphyroclastic | 0.70 | 0.20 | 0.11 | 859.1 | 1124.1 | 1124.7 | 1083.2 |
| TAL-001 | Transition | 0.74 | 0.17 | 0.10 | 872.5 | 979.7 | 963.5 | 932.7 |
| TAL-014 | Porphyroclastic | 0.68 | 0.23 | 0.09 | 893.6 | 1175.0 | 1177.0 | 1069.8 |
| TAL-106 | Transition | 0.74 | 0.16 | 0.10 | | | | |
| TAL-112 | Cluster porphyroclastic | 0.76 | 0.15 | 0.10 | 884.1 | 955.5 | 934.7 | 944.9 |
| TAL-127 | Porphyroclastic | 0.70 | 0.21 | 0.09 | 1037.8 | 951.4 | 929.7 | 993.6 |
| TAL-134 | Cluster porphyroclastic | 0.70 | 0.19 | 0.11 | 887.9 | 956.0 | 935.2 | 946.6 |
| Group III | | | | | | | | |
| LP08-02 | Porphyroclastic | 0.64 | 0.21 | 0.14 | 843.6 | 931.9 | 906.0 | 981.9 |
| LPE-062 | Porphyroclastic | 0.65 | 0.22 | 0.13 | | | | |
| Wehrlite | | | | | | | | |
| LP08-12 | Porphyroclastic | 0.82 | — | 0.18 | | | | |
| LPE-028 | Equigranular | 0.85 | — | 0.15 | | | | |
| T _{Cpx-Opx} | Taylor, 1998 | | | | | | | |
| T _{Ca-in-Opx} | Brey and Köhler, 1990 | | | | | | | |
| T* _{Ca-in-Opx} | Nimis and Grütter, 2010 | | | | | | | |
| T _{Cr-Al-Opx} | Witt-Eickschen and Seck, 1991 | | | | | | | |

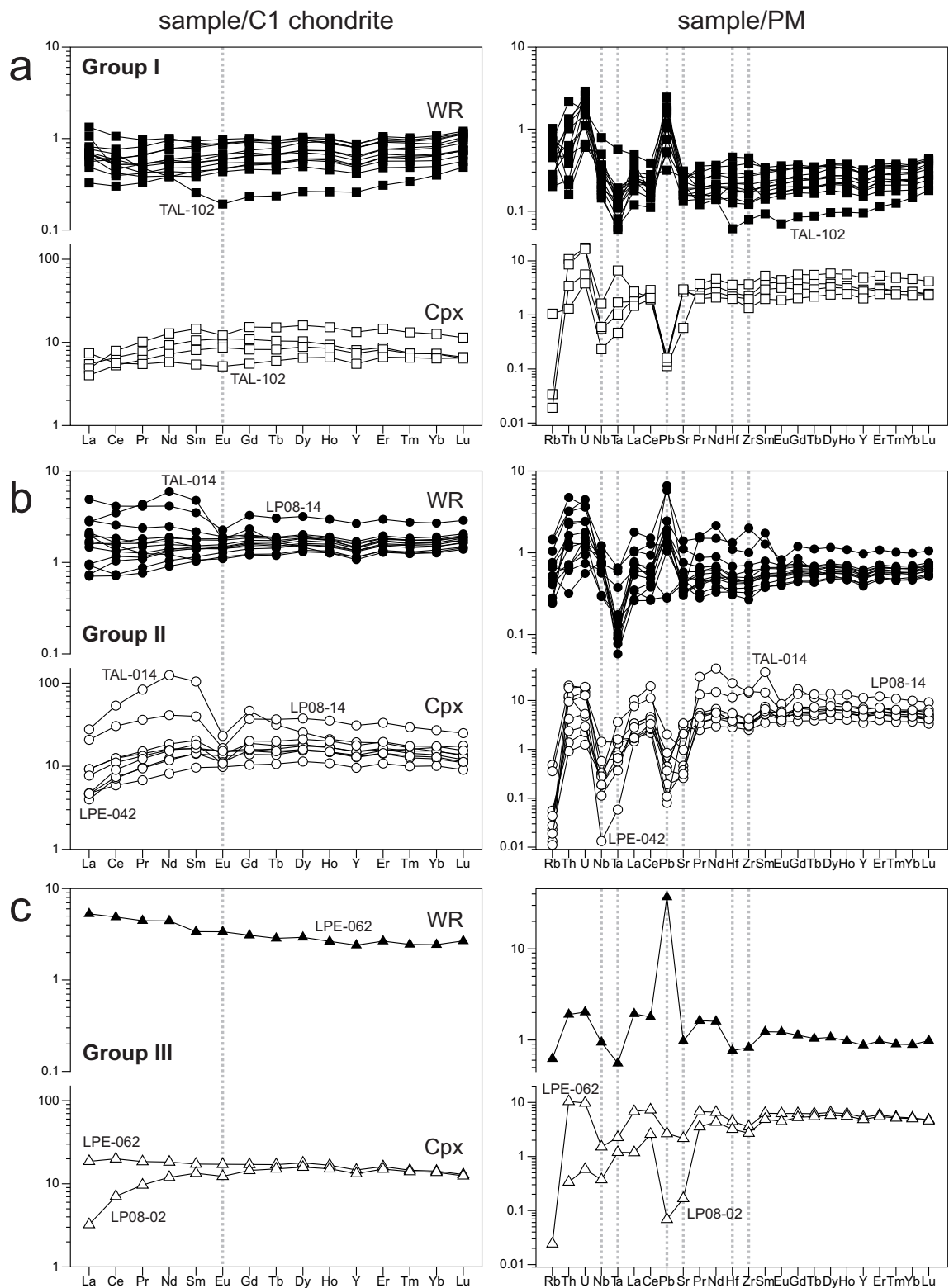


Fig. 53 C1 chondrite-normalized REE patterns (*left panel*) and Primitive Upper Mantle (PM) normalized trace element patterns (*right panel*) of whole rock (black symbols) and clinopyroxenes (open symbols) grouped by their geochemical classification (**a-c**). Normalizing values after Sun and McDonough (1989).

The variation of the orthopyroxene average Mg# in xenoliths follows the same trend as for olivine Mg#; Group I xenoliths have the highest Mg# value (0.906-0.910) and it slightly decreases in Group II (0.894-0.904) and Group III (~0.902). Average Al₂O₃ and CaO contents in orthopyroxene varies between 3.70-4.34 wt.% and 0.66-0.71 wt.% in Group I, 3.36-4.35 wt.% and 0.60-1.55 wt.% in Group II and ~3.76 wt.% and ~0.60 wt.% in Group III, respectively.

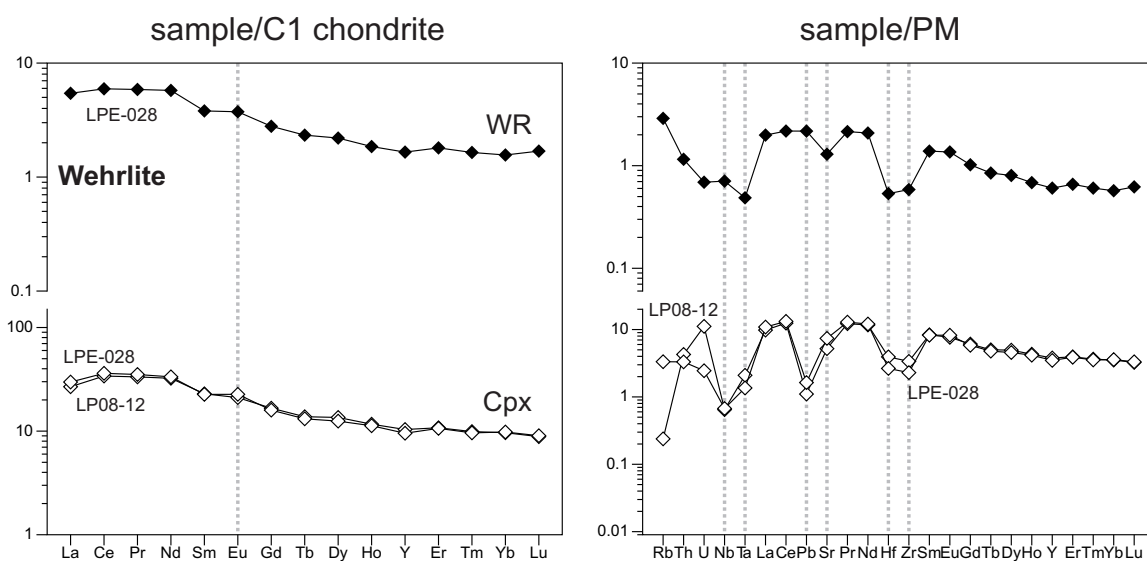


Fig. 54 C1 chondrite-normalized REE patterns (*left panel*) and Primitive Upper Mantle (PM) normalized trace element patterns (*right panel*) of whole rock (black symbols) and clinopyroxenes (open symbols) of SE IVP wehrlite xenoliths. Normalizing values after Sun and McDonough (1989).

Clinopyroxenes have average Mg# between 0.913-0.927, with minor differences among groups (Group I: 0.920-0.927, Group II: 0.913-0.923 and Group III: ~0.923); wehrlite clinopyroxenes have the lowest Mg# values (0.875-0.887). There are significant differences among xenolith groups in the Na₂O content of clinopyroxene. Group I clinopyroxenes have Na₂O contents of 0.82-0.93 wt.%, whereas the Na₂O content of clinopyroxene in more fertile groups is relatively lower (Group II: 0.53-0.83 wt.% and Group III: ~0.73 wt.%); whereas, Na₂O content of wehrlites ranges from 0.94-1.16 wt.%. The FeO and Al₂O₃ content of clinopyroxenes in all groups are constant, ranging between 2.19-2.71 wt.% and 4.81-5.98 wt.%, respectively.

Mg# and Cr# of spinel is highly variable (Mg# = 0.723-0.809; Cr# = 0.120-0.238) and there is large overlap among different groups except for wehrlite spinels that tend to have the lower Mg# (0.586-0.635) and the higher Cr# (0.302-0.329) values. In the olivine-spinel

mantle array diagram (OSMA, Fig. 55) of Arai (1994), the available depleted, moderate depleted and fertile mantle xenoliths lie within the OSMA field, and within the range of the abyssal peridotites (Johnson et al., 1990; Hellebrand et al., 2002; Bryndzia and Wood, 1990), whereas those of wehrlite samples plot outside the array and trend to that generally described as field of 'Fe-enrichment' (e.g. Beard et al., 2007). On the basis of Mg# and Cr# of spinel, the majority of eastern Betics xenoliths record around 10 % of partial melting (Fig. 55).

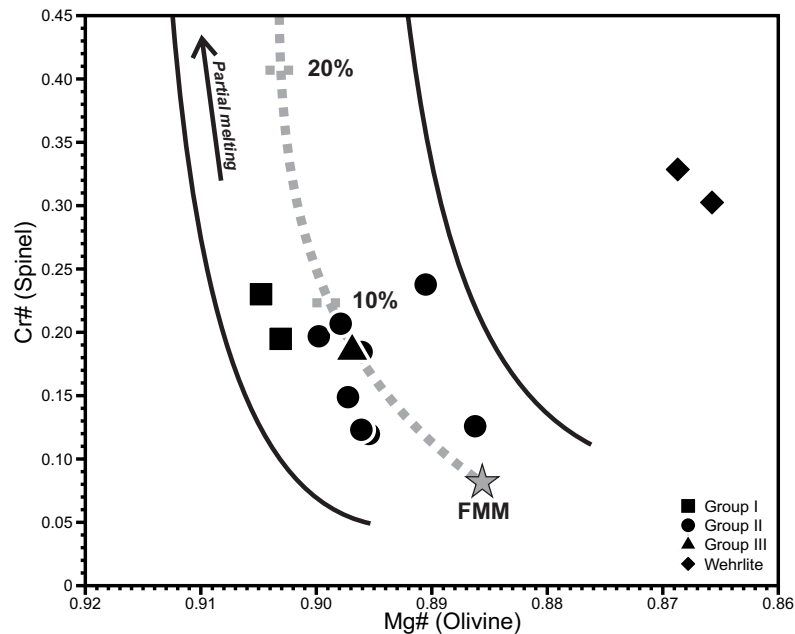


Fig. 55 Pot of spinel Cr# vs. olivine Mg# for SE IVP xenoliths. The Olivine-Spinel Mantle Array (OSMA) and degrees of partial melting are from Arai (1994); FMM (gray star) is the Fertile MORB Mantle after Pearce et al. (2000).

6.3.4. Trace Element Composition of Clinopyroxene

LA-ICP-MS results for clinopyroxene from the different groups are presented in Table 11. Chondrite-normalized (*c.f.* Sun and McDonough, 1989) REE pattern of clinopyroxenes (n=4) from Group I have a convex-upward shape (Fig. 53a) depleted in LREE with $0.33 \leq (La/Sm)_N \leq 0.52$ and $0.38 \leq (La/Yb)_N \leq 0.75$. Clinopyroxenes (n=7) of Group II have also convex-upward REE pattern (Fig. 53b) depleted in LREE—they overlap with those from Group I—with $0.26 \leq (La/Sm)_N \leq 0.57$ and $0.24 \leq (La/Yb)_N \leq 0.75$. Samples TAL-014 and LP08-14 have different patterns than those from Group II; they are enriched in LREE; particularly in Pr, Nd, and Sm, and have a negative Eu anomaly. Clinopyroxenes (n=2) from Group III peridotites have a flat (LPE-062, $(La/Sm)_N=1.08$ and $(La/Yb)_N=1.31$) and a convex-upward REE patterns (Fig. 53c) with strongly depletion in LEE (LP08-02, $(La/Sm)_N=0.24$ and $(La/Yb)_N=0.24$); while the

clinopyroxene REE patterns ($n=2$) of wehrlites are characterized by LREE-enriched patterns with $1.17 \leq (\text{La}/\text{Sm})_N \leq 1.32$ and $2.78 \leq (\text{La}/\text{Yb})_N \leq 3.04$ (Fig. 54).

Primitive upper mantle (PUM) normalized (*c.f.* Sun and McDonough, 1989) multi-element patterns of clinopyroxene (Fig. 53 & 54; right panel, open symbols) in Group I peridotites are characterized by variable abundance of incompatible trace elements. Their patterns show strong negative anomalies of Rb, Nb and Pb, positive Th and U spikes, and an approximately flat pattern for elements more compatible than Sr (Fig. 53a). Multi-element patterns of Group II clinopyroxenes are similar those from Group I, but show more pronounced Rb, Nb and Pb negative anomalies, and a mild negative Sr spike (Fig. 53b). Group III clinopyroxenes have highly variable incompatible trace element distribution; the pattern of lherzolite LPE-062 shows a strong Rb depletion and moderate negative anomalies on Nb, Pb and Sr; the normalized pattern of lherzolite LP08-02 has depleted trend for the most incompatible elements and negative Pb and Sr spikes (Fig. 53c). The pattern of both samples is characterized by moderate Zr-Hf negative anomalies. The pattern of wehrlite clinopyroxenes displays negative Nb-Ta, Pb and Zr-Hf anomalies (Fig. 54). A common feature of the normalized patterns of eastern Betics xenoliths is the opposite Pb spikes of the whole rock (positive anomalies) and clinopyroxenes (negative anomalies) from the same sample (Fig. 53 & 54).

6.3.5. Isotopic Composition

Whole rock and clinopyroxene Sr, Nd and Pb isotopic ratios of eastern Betics xenoliths are reported in Table 12, and illustrated in the usual isotope ratios bivariate diagrams (Fig. 56). For comparison, we also show in Fig. 56a the isotopic composition of the Ronda peridotite (Reisberg and Zindler, 1986; Reisberg et al., 1989), and the published isotopic data for Tallante (clinopyroxene-poor and clinopyroxene-rich) peridotite xenoliths (Beccaluva et al., 2004; Bianchini et al., 2011). Also shown in this figure, the hypothetical mantle isotopic reservoir end members (DM, HIMU, EM1 & EM2; Zindler and Hart, 1986; Hart, 1988). Tie-lines in Fig. 56 (dashed lines)—for those samples where is available—link the isotopic ratio of the whole rock and clinopyroxene analyses. Isotopic data on clinopyroxene separates are few due to the small size of the studied xenoliths and the large amount of separates required for multi-isotopic Sr-Nd-Pb analyses; particularly Pb isotopes (Table 12).

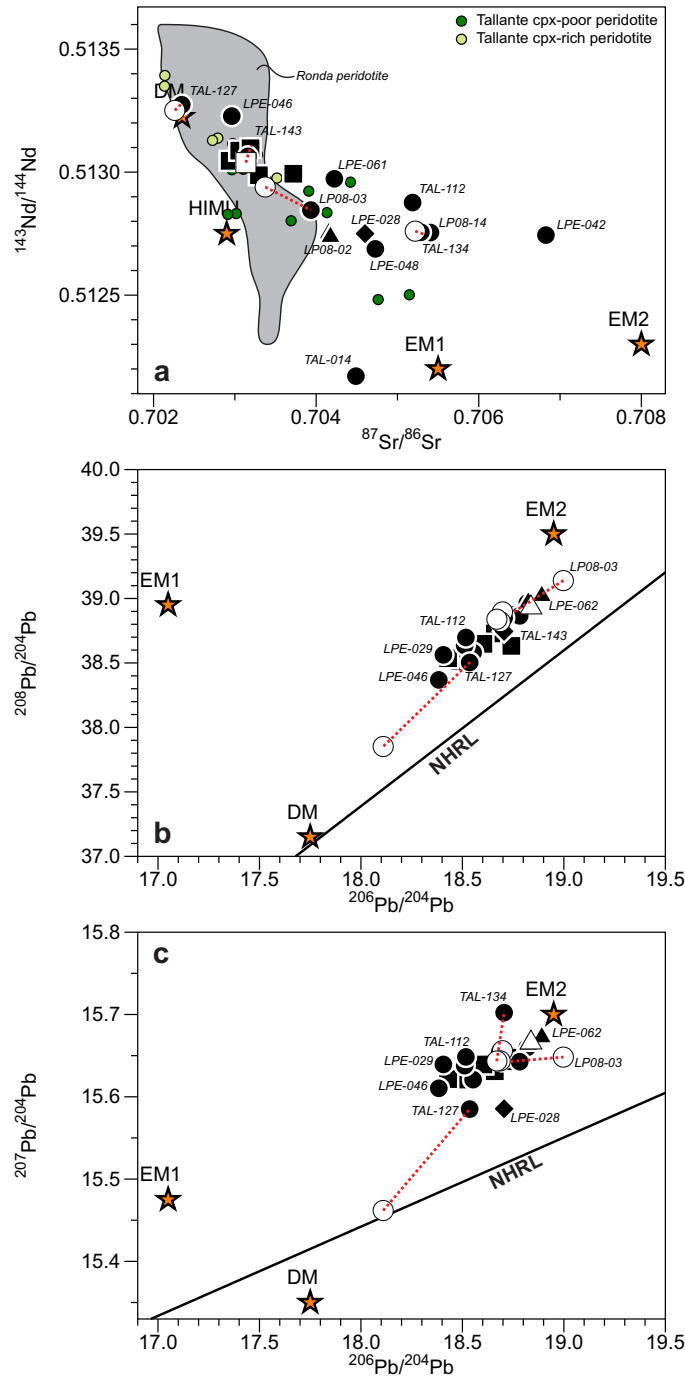


Fig. 56 Age corrected (3 Ma) Sr-Nd (a) and Pb (b, c) radiogenic isotope ratios of clinopyroxene separates (open symbols) and whole (black symbols) rock of SE IVP xenoliths. Legend of the studied peridotite groups is same as in Fig. 52. Characteristic SE IVP xenoliths are labeled with their sample codes and those xenoliths that have both clinopyroxene and whole rock isotopic data and show decoupling are marked with tie lines (red dashed lines). Data of Ronda peridotite (gray area), Tallante clinopyroxene (cpx)-poor peridotite (dark green circles) and Tallante cpx-rich peridotite (light green circles) are from Reisberg and Zindler (1986), Reisberg et al. (1989), Beccaluva et al. (2004) and Bianchini et al. (2011). Hypothetical mantle reservoirs are from Zindler and Hart (1986) and Hart (1988).

Whole rock Pb isotope ratios of Group I (n=5) peridotite range between 18.430-18.741 for $^{206}\text{Pb}/^{204}\text{Pb}$, 15.621-15.643 for $^{207}\text{Pb}/^{204}\text{Pb}$ and 38.513-38.729 for $^{208}\text{Pb}/^{204}\text{Pb}$ (Fig. 56). Whole rock $^{87}\text{Sr}/^{86}\text{Sr}$ (n=5) and $^{143}\text{Nd}/^{144}\text{Nd}$ (n=5) ratios vary from 0.7029 to 0.7037, and from 0.51298 to 0.51309, respectively. Whole rock Pb isotope ratios of Group II (n=12) peridotite range between 18.384-18.820 for $^{206}\text{Pb}/^{204}\text{Pb}$, 15.585-15.702 for $^{207}\text{Pb}/^{204}\text{Pb}$, and 38.368-38.965 for $^{208}\text{Pb}/^{204}\text{Pb}$. Whole rock $^{87}\text{Sr}/^{86}\text{Sr}$ (n=12) and $^{143}\text{Nd}/^{144}\text{Nd}$ (n=12) ratios range between 0.7023-0.7068 and 0.51217-0.51328, respectively. Whole rock Pb isotope ratios of Group III (n=2) peridotite range between 18.824-18.891 for $^{206}\text{Pb}/^{204}\text{Pb}$, 15.663-15.672 for $^{207}\text{Pb}/^{204}\text{Pb}$ and 38.968-39.020 for $^{208}\text{Pb}/^{204}\text{Pb}$ (Fig. 56), the whole rock $^{87}\text{Sr}/^{86}\text{Sr}$ ratio (n=2) is 0.7042 and the $^{143}\text{Nd}/^{144}\text{Nd}$ (n=2) ratio varies from 0.51273 to 0.51275. Whole rock Pb isotope ratios of wehrlite (n=1), 18.705 for $^{206}\text{Pb}/^{204}\text{Pb}$, 15.585 for $^{207}\text{Pb}/^{204}\text{Pb}$ and 38.743 for $^{208}\text{Pb}/^{204}\text{Pb}$. The whole rock $^{87}\text{Sr}/^{86}\text{Sr}$ and $^{143}\text{Nd}/^{144}\text{Nd}$ ratios are 0.7046 and 0.51275, respectively.

Group I clinopyroxene $^{87}\text{Sr}/^{86}\text{Sr}$ ratio is 0.7031 (TAL-143) and clinopyroxene from Group II (n=3) have variable Pb ratios ranging 18.110-18.997 for $^{206}\text{Pb}/^{204}\text{Pb}$, 15.643-15.656 for $^{207}\text{Pb}/^{204}\text{Pb}$, and 38.821-39.139 for $^{208}\text{Pb}/^{204}\text{Pb}$. Their $^{87}\text{Sr}/^{86}\text{Sr}$ (n=3) and $^{143}\text{Nd}/^{144}\text{Nd}$ (n=5) ratios vary from 0.7032 to 0.7052 and from 0.51274 to 0.51290, respectively. Group III clinopyroxene (LP08-02) a Pb isotopic ratios of 18.838 for $^{206}\text{Pb}/^{204}\text{Pb}$, 15.666 for $^{207}\text{Pb}/^{204}\text{Pb}$, and 38.929 for $^{208}\text{Pb}/^{204}\text{Pb}$, and its $^{143}\text{Nd}/^{144}\text{Nd}$ ratio is 0.51299.

In $^{87}\text{Sr}/^{86}\text{Sr}$ vs. $^{143}\text{Nd}/^{144}\text{Nd}$ plot (Fig. 56a) our data show a similar variation to those reported in previous studies of Tallante (Beccaluva et al., 2004; Bianchini et al., 2011); however, our data show a wider dispersion towards more radiogenic $^{87}\text{Sr}/^{86}\text{Sr}$ and $^{143}\text{Nd}/^{144}\text{Nd}$ values. Eastern Betics xenoliths near the DMM component overlap the field of Ronda peridotites (Reisberg and Zindler, 1986; Reisberg et al., 1989), at lower $^{87}\text{Sr}/^{86}\text{Sr}$ and higher $^{143}\text{Nd}/^{144}\text{Nd}$. In the $^{208}\text{Pb}/^{204}\text{Pb}$ vs. $^{206}\text{Pb}/^{204}\text{Pb}$ plot (Fig. 56b), eastern Betic xenoliths display trend between DMM and EM2 component, above northern hemisphere reference line (NHRL).

6.4. Discussion

6.4.1. Redox State of the Eastern Betics Lithospheric Mantle

Upper mantle spinel peridotite samples record oxygen fugacity ($f\text{O}_2$) in the array ± 2 log units of the Fayalite-Magnetite-Quartz (FMQ) oxygen buffer. Rocks with closer relations to the asthenosphere show more reduced end of this range, while samples with long histories in the lithosphere or from subduction zones appear more oxidized (Frost and McCammon,

2008). In mafic and ultramafic magmas, the crystal structures of most liquid phase prefer to integrate V^{3+} ; however, terrestrial fO_2 not only V^{3+} , but also V^{4+} and V^{5+} are expected to be present (Canil, 2002). The abundance of V^{4+} and V^{5+} is minor, and the fraction of V^{3+} decreases significantly with increasing fO_2 (Canil, 1999, 2002). On the other hand, experimental studies show that the number of valence states (including also V^{2+}) of V decreases with increasing fO_2 (Lindstrom, 1976). Accordingly, increased fO_2 during melting and/or crystallization will decrease the total compatibility of V. Metasomatism of the lithospheric mantle does not seem to play a main role in modifying the V content (Canil, 2002).

Fig. 57 shows the variation of whole rock V content with MgO and Al_2O_3 for the eastern Betics peridotite xenoliths. The majority of samples plot around the FMQ-1. In the plot of V versus MgO (Fig. 57b), Group III peridotites are characterized by high V and low MgO contents and do not fit experimentally determined fO_2 curves. Moderately depleted Group II xenoliths show deviations either towards FMQ-2 or FMQ values. In the V versus Al_2O_3 plot (Fig. 57c), one Group III fertile xenolith plots close FMQ-2, together with a moderately depleted Group II sample. Wehrlite displays different fO_2 values for MgO (ca. FMQ-1) and Al_2O_3 (> FMQ-3). Compare with mantle rocks from different tectonic settings, Eastern Betic xenoliths are less oxidized than supra-subduction mantle (Wood and Virgo, 1989; Canil et al., 1990; Brandon and Draper 1996; McInnes et al., 2001; Parkinson et al., 2003) and subcontinental continental xenoliths (Ionov and Wood, 1992). Eastern Betic xenoliths slightly overlap with subduction xenoliths from British Columbia at around FMQ-1, and fall within the less oxidized range of continental xenoliths from Central Asia. Eastern Betic xenoliths show better correlation with fO_2 s of peridotite massifs (Woodland et al., 1992, 1996, 2006), particularly with samples for Ronda (median value around FMQ-1; Frost and McCammon, 2008). Peridotite massif (such as Ronda) record similar levels of fO_2 with those from seafloor abyssal peridotites that support an asthenospheric character (Frost and McCammon, 2008). In Ronda, these data are consistent with asthenospherization of the subcontinental lithospheric mantle during extreme thinning of lithospheric mantle (Garrido and Bodinier, 1999; Lenoir et al., 2001; Vauchez and Garrido, 2001; Précigout et al., 2007; Bodinier et al., 2008; Soustelle et al., 2009). The whole fO_2 s (ca. FMQ-1) beneath eastern Betic mantle lithosphere indicates an asthenospherized thin mantle similar; this process can be inherited from the Oligocene thinning during back-arc roll-back of the proto-Alboran in the central Mediterranean (Précigout et al., 2007; Garrido et al., 2011; Hidas et al., 2013). Alternatively, it might have been acquired during middle to late Neogene extension

recorded associated to strike-slip flow upwelling of highly attenuated mantle (Konc et al., submitted).

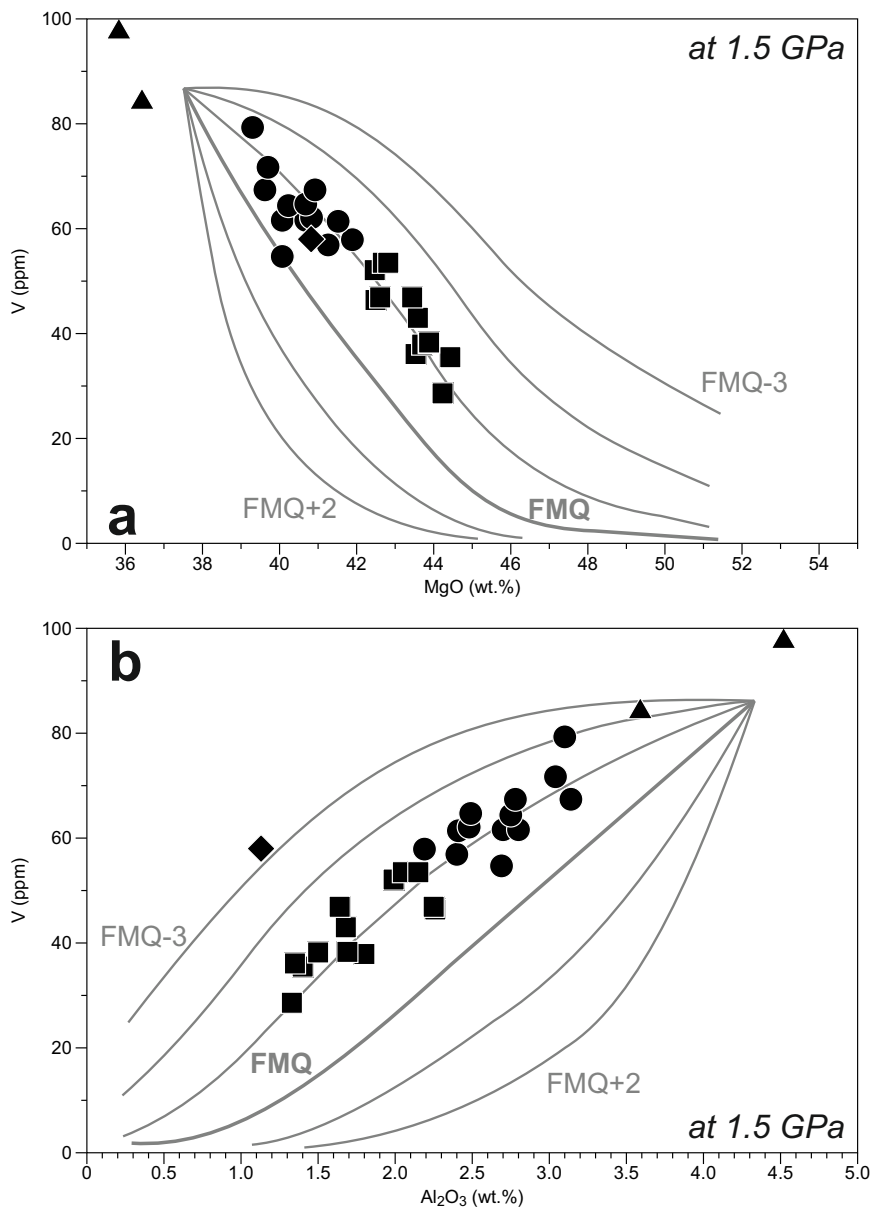


Fig. 57 Plots represent the oxygen fugacity of the studied samples in terms of their V, MgO and Al₂O₃ contents (**a,b**). Partial melting curves that are at 1 log unit intervals and spanning fO_2 's from FMQ-3 to FMQ+2 (solid lines) from Lee et al. (2003). Sample legend is same as in Fig. 52.

6.4.2. Whole Rock Compositional Record of Partial Melting and Refertilization

The eastern Betics peridotite xenoliths exhibit linear trends from fertile to depleted compositions in terms of whole rock major element contents, which are common place in mantle peridotites (Fig. 52) (Bodinier and Godard, 2006; and references therein); From Group III to I, with Group II having intermediate compositions, these trends are defined by

decreasing CaO, FeO^t, Al₂O₃ and increasing MgO contents, as well as increasing Mg#. This depletion trend fits with abyssal peridotites and theoretical mantle residua underwent progressive partial melting reported by Niu (1997). Eastern Betic xenoliths show maximum *ca.* 10-12% of partial melting (Fig. 55). The field of the studied xenoliths in the OSMA diagram, low Mg# of olivine and low to moderate Cr# of spinel, broadly coincides also with values of the most fertile abyssal peridotites in ocean ridge settings (Marchesi et al., 2011).

Fig. 58a shows the chondrite-normalized (*c.f.* Sun and McDonough, 1989) whole rock REE patterns of the selected eastern Betics xenoliths and the curves calculated for non-modal fractional melting of the depleted MORB mantle (WR_{model}) in the spinel lherzolite facies. Group III xenoliths show similar compositions to the MORB. MREE and particularly HREE variation peridotites display a maximum 5-6% and *ca.* 7% to 13% melt extraction for Group II and depleted Group I peridotites, respectively. Whole rock LREE – and in some instances MREE – abundances in obviously depart from the predictions of the melting model and are directed by different magmatic processes (see later). However, a similar fractionation melting model (starting with CPX_{modal}, Fig. 58b) in the spinel stability field does not reproduce the same melt extraction degree for clinopyroxenes from eastern Betics xenoliths. The available HREE and MREE depleted end-member of clinopyroxenes from Group I and Group II xenoliths show 1-2% and *ca.* 5% partial melting in maximum, respectively. However, the modal proportion of clinopyroxene in Group I harzburgites (*e.g.* TAL-127) ranges *ca.* 4-5%; and according to Niu (1997), these values could imply melting degrees of 18-23%. The less depleted clinopyroxenes form the different group either have higher concentration than the calculated initial clinopyroxene (CPX_{modal}) or overlap it in some elements (such as Lu, Eu, Ce in case of sample TAL-056). Metasomatic modification of LREE budget (in both whole rock and clinopyroxene) does not allow us that to distinguish between batch and fractional melting. Consequently, eastern Betics peridotite xenoliths underwent a moderate depletion related to previous melting event that could significantly affect the whole rock compositions. Alternatively, the observed REE abundance variations and depletion trends can be ascribed to trace element re-enrichment during metasomatism and it may reflect refertilization (Cpx-addition) from depleted compositions (Lenoir et al., 2001; Le Roux et al., 2007; Bodinier et al., 2008).

Re melting depletion ages in Os-bearing minerals from xenoliths and peridotite massifs from the inner Mediterranean region (Sicilian Hyblean Plateau, Kraubath ultramafic massif) show a common oldest TRD peak at ~2.3 Ga (González-Jiménez et al., 2013; Chap. 7). This age is similar to the oldest whole-rock TMA age of 2.2 Ga obtained by Pearson and Nowell

(2004) for pyroxenites of the Beni Bousera massif in northern Morocco and the 2.4 Ga peak in primary magmatic sulfides from peridotites of the internal Ligurides (Alard et al., 2005). We find a slightly older peak at 2.6 Ga in sulfides from Eastern Betics mantle xenoliths (González-Jiménez et al., 2013; Chap. 7). These ages clearly identify an older lithospheric mantle formed near the Archean/Paleo-Proterozoic boundary at ~2.2-2.6 Ga, sitting within the more recent Betics-Maghrebides-Apennines front generated during the Alpine-Betic orogeny. Therefore, If the observed compositional trends observed in Eastern Betics mantle xenoliths are due to different degrees of partial melting, they likely reflects multistage processes integrating a protracted history of melting of the Mediterranean lithospheric mantle since the Neoproterozoic. Without knowledge of the pre-Cenozoic composition of the Eastern Betics mantle, deconvolution of compositional variations due to Tertiary melting events is intractable.

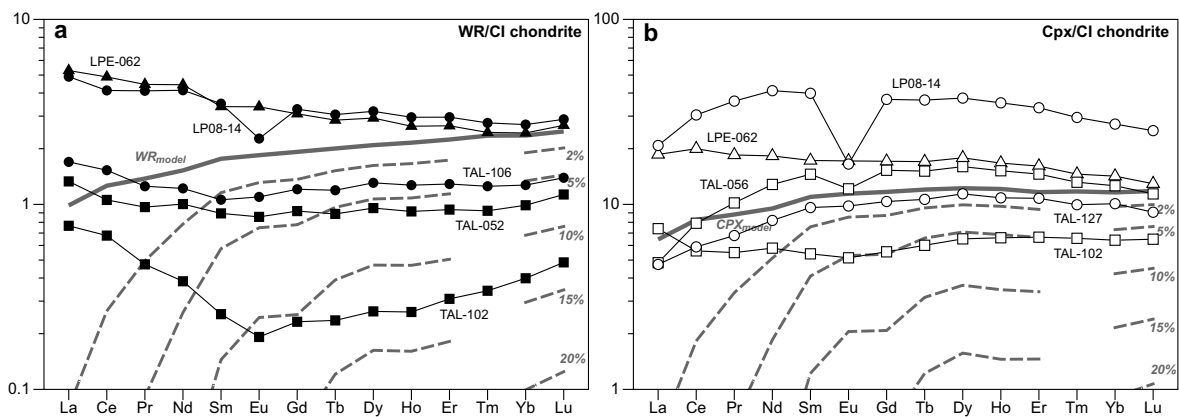


Fig. 58 C1 chondrite-normalized (Sun and McDonough, 1989) REE patterns of SE IVP mantle whole rocks (WR, **a**) and clinopyroxenes (Cpx, **b**) compared with non-modal fractional melting curves (dashed lines) of spinel lherzolite (source and melting ol:opx:cpx modal proportion 0.57:0.28:0.15 and - 0.03:0.50:0.53, respectively, by Niu, 1997 at 2 GPa). Symbols are same as in Fig. 52, and labels show the partial melting degrees. The source composition (solid lines) corresponds with the depleted MORB mantle (Salters and Stracke, 2004). Partition coefficients are from Bedini and Bodinier (1999), Su and Langmuir (2003) and Donnelly et al. (2004).

6.4.3. Metasomatism of Eastern Betics Lithospheric Mantle

Mantle metasomatism—modal or cryptic—induces variable degrees of post-melting enrichment of incompatible elements in continental lithospheric mantle peridotites (e.g. Hawkesworth et al., 1984; Lenoir et al., 2001; Downes, 2001; Pearson et al., 2003; Bodinier and Godard, 2006). These geochemical modifications—referred to as mantle metasomatism (Menzies and Hawkesworth, 1987)—occur by melt/rock interaction involving percolation of small fraction of volatile-rich silicate melts and/or carbonate melts of asthenospheric or lithospheric provenance (e.g. McKenzie, 1989; Bodinier et al., 1990; Dautria et al., 1992; Harte

et al., 1993; Garrido and Bodinier, 1999; Grégoire et al., 2001; Lenoir et al., 2001; Ionov et al., 2002b; Soustelle et al., 2009).

In terms of incompatible trace elements, many Eastern Betics peridotite xenoliths display variable degrees of metasomatic enrichment that overprints their depleted lithospheric mantle signature induced by partial melting. Fig. 59 shows normalized trace element patterns of melts in trace element exchange equilibrium with clinopyroxenes from eastern Betics xenoliths showing a strong metasomatic imprint; this imprint is generally revealed by enrichments of LREE and MREE in clinopyroxene. For these calculations we use $D_{\text{cpx}}/\text{melt}$ suitable for basaltic and mantle clinopyroxene compositions (Garrido et al., 2000; Su and Langmuir, 2003; Donnelly et al., 2004). Mantle wehrlites are often considered as proof of carbonatite mantle metasomatism in the (e.g. Yaxley et al., 1991; Dautria et al., 1992; Rudnick et al., 1993). Consequently, one of the potential metasomatic agents may have been carbonatitic or carbonate-rich melt. Alternatively, carbonatite-rich melt may derive from crystal fractionation of small melt fractions of volatile rich silicate melts, which usually have precursors with alkali basalt-like trace element signature (McKenzie, 1989; Bedini et al., 1997). Comparison of trace element and REE patterns of calculated melts with those of carbonatites (Balogh et al., 1999; Hoernle et al., 2002) and eastern Betics alkali basalts (Turner et al., 1999; Duggen et al., 2005) reveals that—in terms of trace element composition—the precursor metasomatic agent might be related to alkali-silicate melts (Fig. 59). Mismatches between calculated and putative metasomatic melts are found for Sr (Fig. 59a), Y, Eu, and, some cases, excess of LREE relative to calculated compositions (Fig. 59b). Silicate-carbonatitic melt metasomatism inducing similar enrichments in mantle lithospheric peridotites are common in the continental lithospheric mantle (Dautria et al., 1992; Beccaluva et al., 2007).

6.4.4. Isotopic Composition of Metasomatic Melts

Fig. 60 shows the whole rock isotope ratios versus $(\text{Nd}/\text{Yb})_{\text{N}}$ ratio in eastern Betic xenoliths in order to investigate potential causative effects between isotopic variation and MREE/HREE enrichments due to metasomatism. In Fig. 60a, whole rock $^{143}\text{Nd}/^{144}\text{Nd}$ displays a trend from more radiogenic $^{143}\text{Nd}/^{144}\text{Nd}$ and less $(\text{Nd}/\text{Yb})_{\text{N}}$ values (upper left corner) towards less radiogenic $^{143}\text{Nd}/^{144}\text{Nd}$ and higher $(\text{Nd}/\text{Yb})_{\text{N}}$ values. Group I and II xenoliths overlap in the upper left corner; particularly, two samples of moderate depleted xenoliths (e.g. TAL-127) that are more radiogenic in $^{143}\text{Nd}/^{144}\text{Nd}$ than peridotites from the depleted sample. Fertile sample LPE-062 represents the end of the trend characterized by the least radiogenic $^{143}\text{Nd}/^{144}\text{Nd}$ and higher $(\text{Nd}/\text{Yb})_{\text{N}}$ values. Only LPE-028 wehrlite and TAL-014 apatite-bearing lherzolite plots off the general trend defined by other eastern Betics

xenoliths; both samples shows highly metasomatized $(Nd/Yb)_N$ values (>3.5) with less radiogenic $^{143}Nd/^{144}Nd$ ratio, particularly TAL-014. The inversion of this tendency can be seen in $^{208}Pb/^{204}Pb$ and $^{207}Pb/^{204}Pb$ plots (Fig. 60c-d) In case of $^{87}Sr/^{86}Sr$ (Fig. 60b) there is a clear divergence of Group II xenoliths; particularly sample LPE-042. These discrepancies point to Sr-Nd isotopic decoupling in eastern Betics mantle xenoliths.

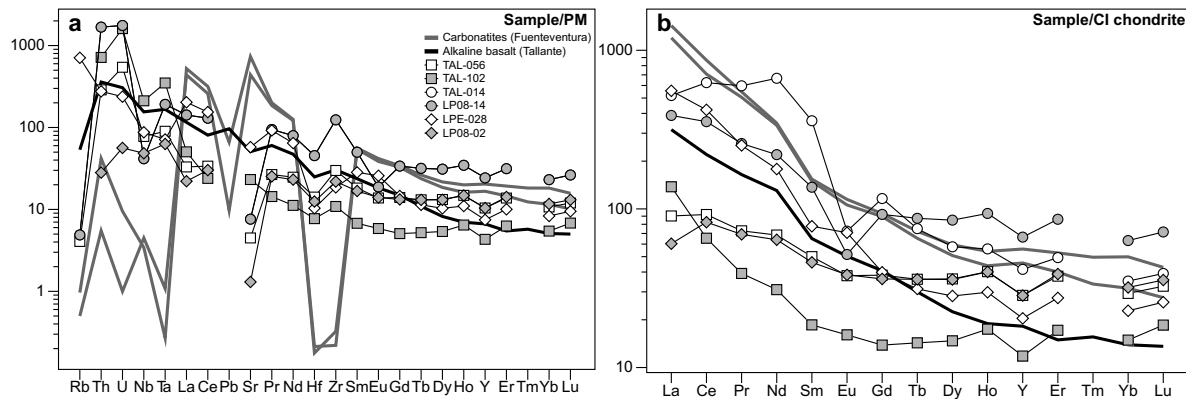


Fig. 59 PM normalizes trace element (a) and C1 chondrite-normalized REE (b) patterns of the calculated melt (partition coefficients from Bedini and Bodinier, 1990; Su and Langmuir, 2003; Donnelly et al., 2004) in exchange equilibrium with selected SE IVP xenoliths compared with the trace element and REE patterns of carbonatites from Fuerteventura (Hoernle et al., 2002) and alkaline basalt from Tallante (Turner et al., 1999). Normalizing values after Sun and McDonough (1989).

The trace element disequilibrium between whole rocks and clinopyroxene, particularly in Group II (Fig. 53b), also appears minor in their isotope ratios (Fig. 56, marked with tie lines). In Group II samples, isotopic ratios indicate also minor disequilibrium in samples TAL-134, TAL-127 and LP08-03, while in cases of Group I and Group III peridotites have isotopic composition with equilibrium between clinopyroxene and their whole rock. Clinopyroxene from sample TAL-127 have more DMM-like character than its whole rock in terms of their Pb isotopic composition; however this mismatch is not shown in their Nd-Sr isotope systematics (Fig. 56a). Decoupling between clinopyroxene and whole rock of LP08-03 appears in investigated isotopes Fig. 56.

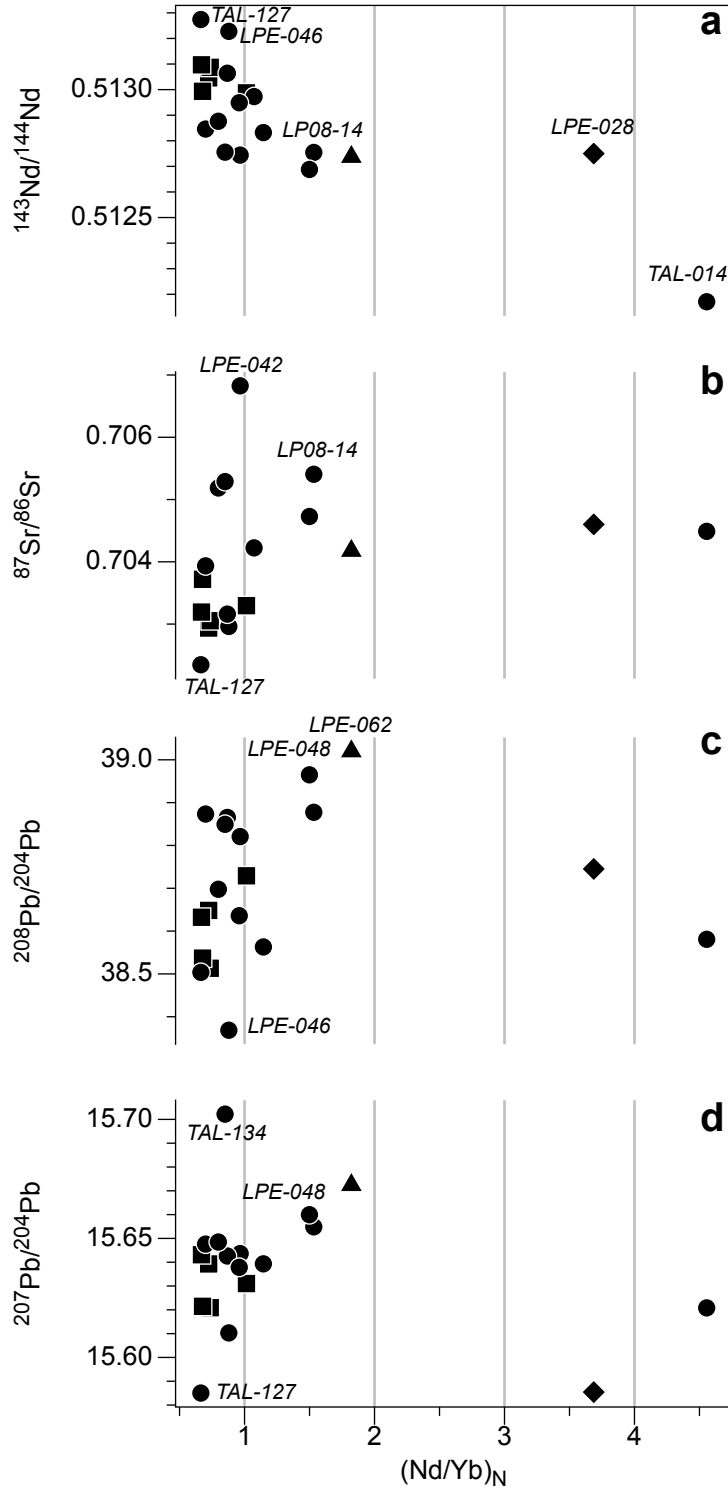


Fig. 60 $(Nd/Yb)_N$ content of the SE IVP whole rock samples in function of their $^{143}Nd/^{144}Nd$ (a), $^{87}Sr/^{86}Sr$ (b), $^{208}Pb/^{204}Pb$ (c) and $^{207}Pb/^{204}Pb$ (d) isotopic ratios. Sample legend is same as in Fig. 52 and the normalizing values after Sun and McDonough (1989).

Whole rock isotopes for Group II samples TAL-127 and LPE-046 show the most depleted isotopic signatures (Fig. 56) and have low REE abundances. In Fig. 61a, these two

xenoliths have $^{143}\text{Nd}/^{144}\text{Nd}$ ratios greater than Atlantic mid-ocean ridge basalt (MORB; Zindler and Hart, 1986; Hofmann, 1997), but fall within the DM range of Zindler and Hart (1986) and Hart (1988). All eastern Betics mantle xenoliths plots within European Lithospheric Mantle domain (*e.g.* Downes, 2001), as mantle xenoliths from the Massif Central (Downes and Dupuy, 1987; Zangana et al., 1997), Pannonian Basin (Rosenbaum et al., 1997), and Pyrenean peridotite massifs (*e.g.* Downes et al., 1991; Mukasa et al., 1991; Downes, 2001). Eastern Betic xenoliths plot to the right of the mantle array on the Nd *vs.* Sr isotope covariation diagram indicating two trends toward an EM I-like and EM II-like end-members (*c.f.* Zindler and Hart, 1986; Hart, 1988), respectively. Most Betics xenoliths overlap the isotopic composition of Tallante alkali basalts (Turner et al., 1999; Beccaluva et al., 2004) and partly the Beni Bousera pyroxenites (Hamelin and Allègre, 1988; Kumar et al., 1996). In the Nd-Sr isotopic ratio plots (Fig. 61a) overlap marginally the field of Alboran tholeiitic series basalts (Duggen et al., 2004, 2008; Gill et al., 2004). The $^{208}\text{Pb}/^{204}\text{Pb}$ *vs.* $^{206}\text{Pb}/^{204}\text{Pb}$ isotope plot (Fig. 56 & 61b) presents linear trend towards EM2 that is characteristic of subducted continental material, which is located the mixing lines of DM and marine sediments (Dickin, 2005). Although eastern alkali basalts are spatially associated to K-rich magmatism (Venturelli et al., 1984; Nelson et al., 1986; Toscani et al., 1990; Turner et al., 1999; Zeck et al., 1999; Schaefer et al., 2000; Beccaluva et al., 2004; Duggen et al., 2004; Cebria et al., 2009; Conticelli et al., 2009; Preleveic et al., 2008, 2010), they display the best fit with the Atlantic sediments (Ben Othman et al., 1989; Revel et al., 1996; Hoernle, 1998; Jolly et al., 2006) (Fig. 61b). In the $^{207}\text{Pb}/^{204}\text{Pb}$ - $^{206}\text{Pb}/^{204}\text{Pb}$ plot eastern Betic xenoliths show isotopic ratios close to EM2, and Atlantic sediments (Fig. 61c).

Most depleted Group II xenoliths (TAL-127, LPE-046 and LPE-127 clinopyroxenes) (Fig. 56 & 61) can be explained by different degrees of metasomatism of ancient LREE depleted lithospheric mantle (Ionov et al., 2002). Such tendency have been shown by the eastern Betics mantle xenoliths (whole rocks and clinopyroxenes) observed in Sr-Nd isotope relationships, might be explained either as product of metasomatic processes or from an unusual composition of the metasomatic agent. The host basalt (Turner et al., 1999; Beccaluva et al., 2004) shows some discrepancy with trends of the eastern Betics xenolith showing in Fig. 61, thus, the precursor of the enriched metasomatic source is clearly not the host alkali magma. Such variations can be due to mixing of components (Dickin, 2005), but and alternatively be produced by melt percolation (Ionov et al., 2002).

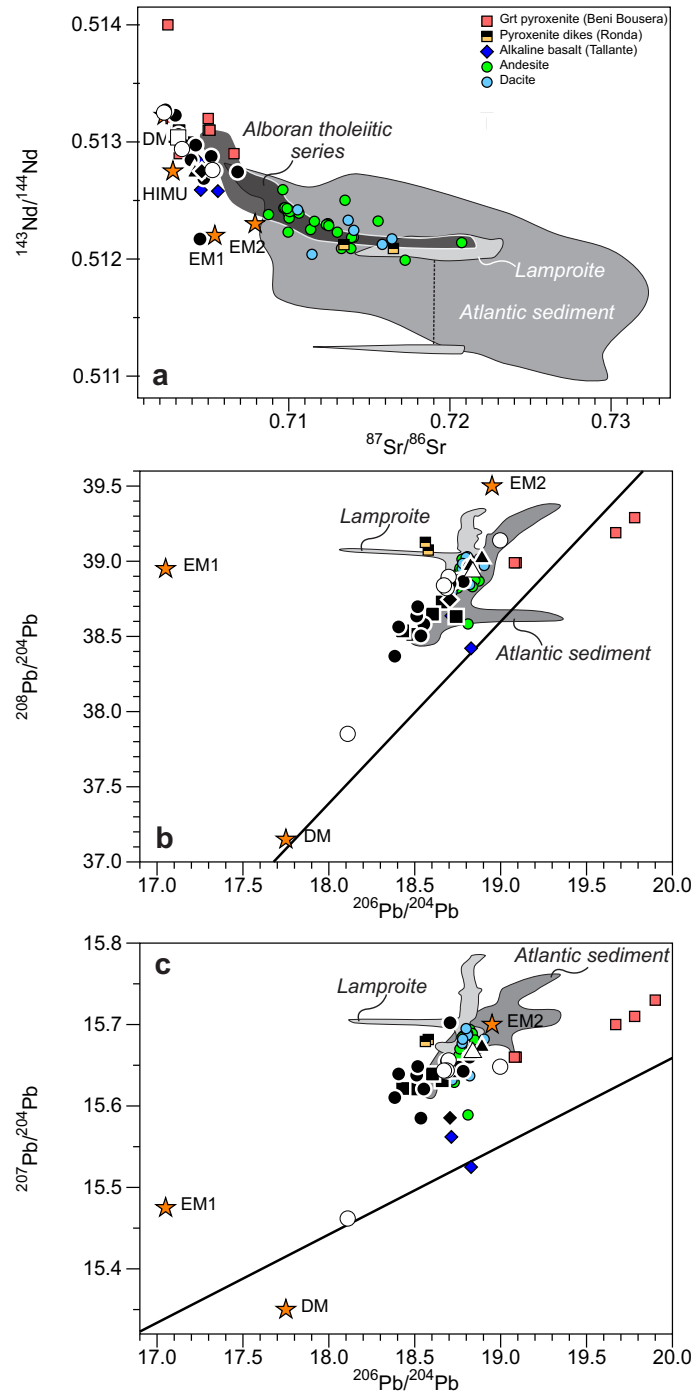


Fig. 61 Age corrected (3 Ma) Sr-Nd (a) and Pb (b, c) radiogenic isotope ratios of clinopyroxene separates (open symbols) and whole (black symbols) rock of SE IVP xenoliths. Legend of the studied peridotite groups is same as in Fig. 4. Field of Atlantic sediment (dark gray area), Lamproite (light gray area), Alboran tholeiitic series (black transparent area) and plots of Garnet (Grt) pyroxenite of Beni Bousera, Ronda pyroxenite dikes, Tallante alkaline basalt, Andesite and Dacite from the Alboran region are from Venturelli et al. (1984), Nelson et al. (1986), Hamelin and Allegre (1988), Ben Othman (1989), Toscani et al. (1990), Kumar et al. (1996), Revel et al. (1996), Hoernle (1998), Turner et al. (1999), Zeck et al. (1999), Schaefer et al. (2000), Beccaluva et al. (2004), Duggen et al. (2004, 2008), Gill et al. (2004), Jolly et al. (2006), Prevelic et al. (2008, 2010), Cebria et al. (2009), Conticelli et al. (2009). Hypothetical mantle reservoirs are from Zindler and Hart (1986) and Hart (1988).

The Pb isotopic data can be explained by two-component mixing of DM-type related eastern Betics proto-Alboran lithosphere and a component of melts enriched in $^{208}\text{Pb}/^{204}\text{Pb}$, $^{207}\text{Pb}/^{204}\text{Pb}$ and $^{206}\text{Pb}/^{204}\text{Pb}$ (Fig. 56 & 61). A possible candidate for such melt would be mixtures of EM2 component—likely fluids derived from Atlantic sediments—and a silicate melt (Fig. 61b-c). However, this mixing is not evident in terms of Sr-Nd isotopic compositions (Fig. 61a). Decoupling of Sr-Nd and Pb isotopes might be due to the greater mobility of Pb, which can be reproduced by chromatographic fractionation processes advised by Bodinier et al. (2004) and later presented by Beccaluva et al. (2007) within broader region of this study. If so, the best candidate as metasomatic agent are melts with carbonatitic affinity derived from melt/fluids containing an oceanic sediment signature. The radiogenic isotopic signatures of the different lavas of the studied region can confirm this affinity (Fig. 61) (Duggen et al., 2004).

Alkali basalts in the Eastern Betics and northwestern Africa are ascribed to decompression melting of the upwelling asthenosphere triggered by subcontinental delamination (Duggen et al., 2004). Eastern Betics mantle xenoliths recorded mantle metasomatism well before their host magma (3 Ma). Their Pb isotope systematics show imprint of subduction related metasomatism (EM2 close, Atlantic sediment-like) component. Thus, the studied eastern Betics mantle xenoliths might suffer metasomatism by subduction-related melt during the Early to Middle-Miocene before crustal thinning and asthenospheric upwelling, which are recorded in the fabric of xenoliths (Shimizu et al., 2008; Rampone et al., 2010; Konc et al., submitted) and their V systematic.

6.4.5. Formation of Wehrlites

Mantle wehrlites are considered traditionally as the cause of metasomatism by carbonate melts in the lithospheric mantle (*e.g.* Yaxley et al., 1991; Rudnick et al., 1993; Dautria et al., 1992; Coltorti et al., 1999 and references therein). Other authors ascribe mantle wehrlites to carbonate-rich silicate and/or SiO_2 -undersaturated alkali melt metasomatism (*e.g.* Zinngrebe and Foley, 1995; Ionov et al., 2005, Beard et al., 2007; Raffone et al., 2009 and reference therein). In eastern Betics wehrlites there is no unequivocal geochemical evidence for carbonate metasomatism. Their isotopic systematics (Fig. 56 & 61) and deformation pattern (Konc et al., submitted), strongly points to a common origin with other lherzolites from the same suite. Crystallization of wehrlite requires carbonate melts or carbonate or carbonate-rich silicate melts undersaturated in orthopyroxene at mantle lithospheric pressures. Percolation-reaction of these melts with lithospheric mantle peridotite would crystallize clinopyroxene after peridotite orthopyroxene and form wehrlite (*e.g.* Yaxley et al., 1991;

Dautria et al., 1992; Rudnick et al., 1993; Xu et al., 1998; Coltorti et al., 1999 and references therein). The existence of apatite inclusions in secondary clinopyroxenes in sample TAL-014 might be modal fingerprint of carbonate metasomatism in the Eastern Betics mantle.

Percolation-reaction modelling (Bedini et al., 1997; Xu et al., 1998; Ionov et al., 2002; Raffone et al., 2009; Soustelle et al., 2009) indicates that carbonate-rich melts reacting with depleted mantle peridotites—similar to most depleted Group I and II—may generate wehrlites with REE patterns to those of Eastern Betic wehrlites (Fig. 54). SiO₂-undersaturated melt metasomatism in the eastern Betic lithospheric mantle may account for the formation of most fertile peridotite (Group III) and wehrlite after depleted mantle lithosphere (Group I and Group II). Wehrlites may represent mantle sections closer to the melt-rock fertilization reaction fronts along channels. These geochemical evidences attest for the percolation of slab-derived, SiO₂-undersaturated melts (and hydrous fluids) with carbonate sediment affinity in the pre-Miocene supra-subduction continental lithospheric mantle beneath the Alborán Basin, possibly released from the subducted Tethys oceanic lithosphere.

6.5. Conclusion

According to our petrological and geochemical study of eastern Betics xenoliths, the following conclusions can be drawn. Eastern Betics spinel (\pm plagioclase) peridotite xenoliths present a snapshot taken from the young SLCM of the Alboran region that composed by mainly lherzolitic and subordinate wehrlite and harzburgitic modal composition with varied textural features. Their relatively high (*ca.* 935-1070 °C) equilibrium temperature with characteristic petrographic elements (appearance of plagioclase) proposed that they were sampled from thinned lithospheric mantle, which is corroborated with the values of the oxygen fugacity (FMQ-2) of the studied xenoliths. Based on the whole rock major element content of the xenoliths (Mg# 0.915-0.867), 4 different groups have been established concerning their fertility from depleted to fertile character and the wehrlite samples. The studied xenoliths show that the sampled eastern Betics mantle section have been suffered different degree of partial melting up to 20% before metasomatic interaction partially overprinting their geochemical properties.

Metasomatic events affected the studied eastern Betics mantle sections in different degree by percolating subduction-related carbonate bearing melt. This melt have been indicated by the Nd-Sr-Pb radiogenic isotopic composition, which show relation EM2 close, Atlantic sediment-like composition. However, Nd-Sr isotopic ratio is slightly separated from Pb isotopic ratios, and point samples toward more DM character. Subduction-related melt

can be derived from releasing of sedimentary melts (and hydrous fluids) from subducted Tethys oceanic lithosphere in the mantle wedge beneath the Alboran Basin starting from approximately Early/Middle Miocene. Progressive interaction of carbonate bearing can also be responsible for the formation of the underrepresented wehrlites and apatite-bearing clinopyroxenes in spinel lherzolite. That event was followed by the delamination of SLCM associated with upwelling asthenosphere (from Late Miocene), which is recorded in the equilibrium temperature and mineral association (cluster porphyroclasts) of the eastern Betics xenoliths before they were sampled by the alkali magmatism as a closing event of the magmatic evolution of the Alboran region.

Table 8 Major and minor element composition for whole-rock SE IVP peridotite xenoliths

| Sample | TAL-047 | TAL-052 | TAL-056 | TAL-077 | TAL-084 | TAL-094 | TAL-099 | TAL-102 | TAL-110 | TAL-125 | TAL-131 | TAL-143 | TAL-149 |
|--------------------------------|---------|---------|---------|---------|---------|---------|---------|---------|---------|---------|---------|---------|---------|
| SiO ₂ | 44.8 | 44.9 | 44.3 | 44.8 | 44.4 | 44.3 | 44.6 | 45.6 | 44.5 | 44.2 | 44.3 | 44.1 | 44.9 |
| Al ₂ O ₃ | 1.7 | 2.0 | 2.3 | 1.4 | 1.8 | 1.7 | 2.1 | 1.4 | 1.5 | 2.2 | 2.3 | 1.4 | 1.7 |
| FeO ⁱ | 7.7 | 8.1 | 8.0 | 7.5 | 7.7 | 7.9 | 7.8 | 7.4 | 7.6 | 8.2 | 8.3 | 7.6 | 7.3 |
| MnO | 0.13 | 0.14 | 0.14 | 0.13 | 0.13 | 0.13 | 0.14 | 0.13 | 0.13 | 0.14 | 0.14 | 0.13 | 0.13 |
| MgO | 44.1 | 43.2 | 43.3 | 45.0 | 44.5 | 44.5 | 43.4 | 44.3 | 44.6 | 43.5 | 43.0 | 45.3 | 44.2 |
| CaO | 1.4 | 1.6 | 1.8 | 1.0 | 1.3 | 1.3 | 1.9 | 1.0 | 1.5 | 1.6 | 1.8 | 1.4 | 1.6 |
| TiO ₂ | 0.16 | 0.11 | 0.11 | 0.18 | 0.10 | 0.16 | 0.13 | 0.16 | 0.11 | 0.17 | 0.07 | 0.06 | 0.20 |
| P ₂ O ₅ | 0.01 | 0.02 | 0.01 | 0.01 | 0.01 | 0.01 | 0.02 | 0.01 | 0.01 | 0.02 | 0.01 | 0.01 | 0.02 |
| Mg# | 0.911 | 0.905 | 0.906 | 0.915 | 0.911 | 0.910 | 0.909 | 0.914 | 0.913 | 0.905 | 0.902 | 0.914 | 0.915 |
| V (ppm) | 46.9 | 52.1 | 46.9 | 28.6 | 37.9 | 38.3 | 53.5 | 36.1 | 38.2 | 53.5 | 46.4 | 35.5 | 43.0 |
| Cr (ppm) | 3093.0 | 2512.5 | 2668.2 | 2668.0 | 2587.1 | 2299.1 | 2751.8 | 2554.7 | 2548.0 | 2330.3 | 2548.4 | 3059.1 | 2647.2 |
| Co (ppm) | 134.6 | 133.4 | 136.7 | 143.0 | 142.9 | 137.9 | 134.8 | 136.8 | 151.4 | 140.3 | 138.4 | 150.3 | 143.9 |
| Ni (ppm) | 2235.9 | 2098.1 | 2202.5 | 2224.2 | 2232.8 | 2251.4 | 2179.3 | 2194.3 | 2245.2 | 2149.4 | 2177.5 | 2267.5 | 2238.8 |
| Zn (ppm) | 53.0 | 50.1 | 53.6 | 47.5 | 49.1 | 51.9 | 50.5 | 49.5 | 47.3 | 50.9 | 55.8 | 48.8 | 48.6 |

| Group II | | | | | | | | | | | | | |
|--------------------------------|---------|---------|---------|---------|---------|---------|---------|---------|---------|---------|---------|---------|---------|
| Sample | LP08-03 | LP08-14 | LPE-029 | LPE-042 | LPE-046 | LPE-048 | LPE-061 | TAL-001 | TAL-014 | TAL-106 | TAL-112 | TAL-127 | TAL-134 |
| SiO ₂ | 45.3 | 45.8 | 45.0 | 45.4 | 45.3 | 44.6 | 45.0 | 45.0 | 46.6 | 44.8 | 45.0 | 44.7 | 45.1 |
| Al ₂ O ₃ | 2.5 | 3.1 | 2.7 | 3.1 | 2.8 | 2.5 | 3.2 | 2.8 | 2.7 | 2.2 | 2.8 | 2.5 | 2.4 |
| FeO ⁱ | 8.1 | 8.2 | 8.8 | 8.0 | 8.2 | 8.5 | 8.5 | 8.0 | 7.6 | 7.8 | 8.1 | 7.8 | 8.2 |
| MnO | 0.14 | 0.15 | 0.14 | 0.14 | 0.15 | 0.14 | 0.14 | 0.15 | 0.13 | 0.14 | 0.14 | 0.14 | 0.14 |
| MgO | 41.3 | 39.8 | 40.9 | 40.4 | 40.8 | 41.6 | 40.3 | 41.5 | 40.8 | 42.6 | 41.4 | 42.2 | 41.7 |
| CaO | 2.5 | 2.6 | 2.3 | 2.7 | 2.5 | 2.5 | 2.6 | 2.4 | 1.9 | 2.2 | 2.4 | 2.5 | 2.3 |
| TiO ₂ | 0.20 | 0.19 | 0.18 | 0.22 | 0.19 | 0.13 | 0.19 | 0.09 | 0.21 | 0.14 | 0.16 | 0.19 | 0.09 |
| P ₂ O ₅ | 0.01 | 0.04 | 0.02 | 0.01 | 0.02 | 0.02 | 0.02 | 0.02 | 0.02 | 0.01 | 0.01 | 0.01 | 0.01 |
| Mg# | 0.901 | 0.896 | 0.892 | 0.899 | 0.899 | 0.897 | 0.894 | 0.902 | 0.906 | 0.906 | 0.901 | 0.906 | 0.900 |
| V (ppm) | 64.7 | 79.3 | 54.7 | 71.7 | 64.4 | 62.1 | 67.4 | 67.4 | 61.6 | 57.9 | 61.6 | 61.4 | 56.9 |
| Cr (ppm) | 2399.1 | 2161.1 | 2383.1 | 2462.4 | 2261.6 | 2506.1 | 2436.6 | 2519.9 | 2326.2 | 2595.1 | 2385.6 | 2644.4 | 2029.3 |
| Co (ppm) | 134.8 | 135.2 | 131.9 | 143.4 | 142.8 | 133.5 | 124.8 | 131.8 | 132.1 | 142.0 | 136.5 | 130.6 | 131.7 |
| Ni (ppm) | 2030.5 | 1909.2 | 2005.1 | 2023.3 | 2007.8 | 2084.1 | 1993.5 | 2045.0 | 1971.1 | 2155.7 | 2025.6 | 2164.9 | 2046.1 |
| Zn (ppm) | 49.9 | 50.1 | 58.4 | 53.6 | 51.6 | 57.0 | 55.1 | 52.8 | 49.1 | 51.1 | 53.4 | 51.8 | 48.0 |

| Sample | Group III | | Wehrlite | |
|--------------------------------|-----------|---------|----------|----------|
| | LPE-062 | LP08-02 | LPE-028 | LP08-12* |
| SiO ₂ | 45.4 | 46.3 | 42.6 | 41.9 |
| Al ₂ O ₃ | 3.7 | 4.6 | 1.2 | 0.98 |
| FeO ⁱ | 10.0 | 8.1 | 10.7 | 11.0 |
| MnO | 0.18 | 0.14 | 0.20 | 0.19 |
| MgO | 37.1 | 36.4 | 41.6 | 40.4 |
| CaO | 3.3 | 3.4 | 3.5 | 3.9 |
| TiO ₂ | 0.28 | 0.51 | 0.19 | 0.13 |
| P ₂ O ₅ | 0.02 | 0.10 | 0.02 | - |
| Mg# | 0.868 | 0.889 | 0.874 | 0.867 |
| V (ppm) | 84.1 | 97.5 | 58.0 | - |
| Cr (ppm) | 2273.6 | 2013.8 | 2488.3 | - |
| Co (ppm) | 119.6 | 122.5 | 113.7 | - |
| Ni (ppm) | 1826.7 | 1729.5 | 2084.8 | - |
| Zn (ppm) | 71.1 | 54.0 | 81.1 | - |

* Whole rock composition by mass balance compilation

Table 9 Whole-rock trace element composition for the studied peridotite xenoliths

| Group I | | | | | | | | | | | | | |
|---------|---------|---------|---------|---------|---------|---------|---------|---------|---------|---------|---------|---------|---------|
| Sample | TAL-047 | TAL-052 | TAL-056 | TAL-077 | TAL-084 | TAL-094 | TAL-099 | TAL-102 | TAL-110 | TAL-125 | TAL-131 | TAL-143 | TAL-149 |
| Rb | 0.274 | 0.426 | 0.171 | 0.343 | 0.274 | 0.268 | 0.488 | 0.141 | 0.134 | 0.296 | 0.432 | 0.117 | 0.612 |
| Sr | 3.775 | 4.601 | 6.157 | 2.658 | 3.125 | 3.509 | 5.545 | 3.122 | 3.136 | 5.147 | 6.020 | 4.313 | 4.564 |
| Y | 0.905 | 1.247 | 1.357 | 0.654 | 0.800 | 0.971 | 1.369 | 0.406 | 0.786 | 1.250 | 1.234 | 0.759 | 1.010 |
| Zr | 2.215 | 4.682 | 2.922 | 2.323 | 1.806 | 1.878 | 2.804 | 0.834 | 1.269 | 4.022 | 1.700 | 1.319 | 1.874 |
| Nb | 0.229 | 0.519 | 0.120 | 0.164 | 0.130 | 0.195 | 0.140 | 0.180 | 0.105 | 0.324 | 0.242 | 0.095 | 0.238 |
| Cs | 0.015 | 0.033 | 0.021 | 0.024 | 0.013 | 0.015 | 0.027 | 0.013 | 0.011 | 0.031 | 0.027 | 0.010 | 0.033 |
| Ba | 3.611 | 4.856 | 1.972 | 2.243 | 2.081 | 2.003 | 2.814 | 2.476 | 2.220 | 2.412 | 4.522 | 3.943 | 4.295 |
| La | 0.161 | 0.315 | 0.142 | 0.153 | 0.115 | 0.163 | 0.133 | 0.181 | 0.161 | 0.193 | 0.167 | 0.078 | 0.250 |
| Ce | 0.318 | 0.648 | 0.374 | 0.258 | 0.241 | 0.330 | 0.363 | 0.416 | 0.312 | 0.468 | 0.360 | 0.185 | 0.281 |
| Pr | 0.048 | 0.090 | 0.060 | 0.036 | 0.039 | 0.049 | 0.062 | 0.044 | 0.039 | 0.076 | 0.046 | 0.030 | 0.049 |
| Nd | 0.268 | 0.454 | 0.350 | 0.176 | 0.215 | 0.251 | 0.348 | 0.174 | 0.197 | 0.432 | 0.244 | 0.173 | 0.264 |
| Sm | 0.094 | 0.132 | 0.123 | 0.057 | 0.071 | 0.081 | 0.117 | 0.038 | 0.063 | 0.139 | 0.085 | 0.065 | 0.080 |
| Eu | 0.038 | 0.048 | 0.050 | 0.024 | 0.030 | 0.033 | 0.049 | 0.011 | 0.027 | 0.055 | 0.037 | 0.026 | 0.033 |
| Gd | 0.139 | 0.183 | 0.186 | 0.092 | 0.109 | 0.129 | 0.189 | 0.046 | 0.102 | 0.200 | 0.149 | 0.104 | 0.128 |
| Tb | 0.024 | 0.032 | 0.034 | 0.016 | 0.020 | 0.024 | 0.034 | 0.008 | 0.019 | 0.034 | 0.028 | 0.019 | 0.024 |
| Dy | 0.173 | 0.235 | 0.254 | 0.121 | 0.147 | 0.183 | 0.249 | 0.065 | 0.148 | 0.240 | 0.222 | 0.143 | 0.181 |
| Ho | 0.037 | 0.050 | 0.056 | 0.025 | 0.033 | 0.040 | 0.054 | 0.014 | 0.032 | 0.048 | 0.051 | 0.031 | 0.040 |
| Er | 0.108 | 0.150 | 0.168 | 0.077 | 0.100 | 0.122 | 0.161 | 0.049 | 0.099 | 0.146 | 0.152 | 0.091 | 0.122 |
| Tm | 0.016 | 0.023 | 0.025 | 0.012 | 0.015 | 0.020 | 0.024 | 0.009 | 0.016 | 0.022 | 0.024 | 0.014 | 0.019 |
| Yb | 0.108 | 0.159 | 0.172 | 0.080 | 0.104 | 0.132 | 0.156 | 0.064 | 0.105 | 0.140 | 0.166 | 0.092 | 0.127 |
| Lu | 0.019 | 0.028 | 0.030 | 0.014 | 0.019 | 0.024 | 0.028 | 0.012 | 0.018 | 0.026 | 0.029 | 0.016 | 0.022 |
| Hf | 0.062 | 0.129 | 0.084 | 0.061 | 0.048 | 0.056 | 0.072 | 0.017 | 0.036 | 0.101 | 0.053 | 0.041 | 0.049 |
| Ta | 0.006 | 0.021 | 0.005 | 0.004 | 0.003 | 0.005 | 0.004 | 0.006 | 0.002 | 0.004 | 0.007 | 0.002 | 0.005 |
| Pb | 0.156 | 0.248 | 0.257 | 0.078 | 0.166 | 0.279 | 0.256 | 0.368 | 0.236 | 0.047 | 0.178 | 0.113 | 0.080 |
| Th | 0.096 | 0.175 | 0.046 | 0.081 | 0.050 | 0.038 | 0.031 | 0.097 | 0.108 | 0.013 | 0.043 | 0.020 | 0.016 |
| U | 0.038 | 0.034 | 0.058 | 0.030 | 0.022 | 0.013 | 0.041 | 0.052 | 0.044 | 0.012 | 0.022 | 0.031 | 0.013 |

| Group II | | | | | | | | | | | | | |
|----------|---------|---------|---------|---------|---------|---------|---------|---------|---------|---------|---------|---------|---------|
| Sample | LP08-03 | LP08-14 | LPE-029 | LPE-042 | LPE-046 | LPE-048 | LPE-061 | TAL-001 | TAL-014 | TAL-106 | TAL-112 | TAL-127 | TAL-134 |
| Rb | 0.395 | 0.866 | 0.415 | 0.169 | 0.308 | 0.882 | 0.453 | 0.316 | 0.267 | 0.632 | 0.151 | 0.248 | 0.141 |
| Sr | 9.300 | 27.771 | 11.618 | 8.507 | 8.382 | 22.148 | 15.106 | 10.083 | 7.151 | 5.968 | 6.771 | 8.025 | 6.524 |
| Y | 2.110 | 4.178 | 2.059 | 2.662 | 2.471 | 2.299 | 2.557 | 2.236 | 1.808 | 1.687 | 2.288 | 1.780 | 2.109 |
| Zr | 3.904 | 21.054 | 5.041 | 5.203 | 4.747 | 7.379 | 6.310 | 4.518 | 10.534 | 2.811 | 4.509 | 3.399 | 4.446 |
| Nb | 0.403 | 0.485 | 0.686 | 0.458 | 0.514 | 0.804 | 0.497 | 0.198 | 0.482 | 0.372 | 0.493 | 0.192 | 0.589 |
| Cs | 0.042 | 0.064 | 0.043 | 0.019 | 0.027 | 0.055 | 0.029 | 0.012 | 0.011 | 0.037 | 0.024 | 0.012 | 0.020 |
| Ba | 3.956 | 12.991 | 4.361 | 3.555 | 7.125 | 7.767 | 6.907 | 7.267 | 4.458 | 4.607 | 2.045 | 3.469 | 1.495 |
| La | 0.220 | 1.162 | 0.468 | 0.382 | 0.474 | 0.686 | 0.504 | 0.348 | 0.658 | 0.402 | 0.228 | 0.168 | 0.174 |
| Ce | 0.452 | 2.531 | 1.127 | 0.988 | 0.824 | 1.571 | 1.005 | 0.806 | 2.133 | 0.938 | 0.716 | 0.438 | 0.637 |
| Pr | 0.082 | 0.382 | 0.150 | 0.150 | 0.139 | 0.222 | 0.169 | 0.117 | 0.404 | 0.117 | 0.106 | 0.071 | 0.101 |
| Nd | 0.472 | 1.871 | 0.771 | 0.831 | 0.710 | 1.119 | 0.854 | 0.642 | 2.689 | 0.551 | 0.625 | 0.411 | 0.602 |
| Sm | 0.170 | 0.518 | 0.221 | 0.268 | 0.225 | 0.321 | 0.261 | 0.206 | 0.705 | 0.157 | 0.219 | 0.153 | 0.210 |
| Eu | 0.072 | 0.127 | 0.080 | 0.102 | 0.088 | 0.107 | 0.098 | 0.082 | 0.100 | 0.061 | 0.083 | 0.064 | 0.079 |
| Gd | 0.281 | 0.651 | 0.298 | 0.390 | 0.347 | 0.400 | 0.370 | 0.322 | 0.464 | 0.240 | 0.331 | 0.244 | 0.313 |
| Tb | 0.052 | 0.110 | 0.053 | 0.068 | 0.062 | 0.067 | 0.066 | 0.057 | 0.060 | 0.043 | 0.060 | 0.045 | 0.054 |
| Dy | 0.385 | 0.783 | 0.383 | 0.496 | 0.456 | 0.469 | 0.482 | 0.425 | 0.360 | 0.322 | 0.450 | 0.333 | 0.397 |
| Ho | 0.083 | 0.163 | 0.081 | 0.105 | 0.098 | 0.096 | 0.099 | 0.091 | 0.070 | 0.070 | 0.096 | 0.074 | 0.087 |
| Er | 0.248 | 0.474 | 0.244 | 0.313 | 0.293 | 0.277 | 0.296 | 0.272 | 0.213 | 0.206 | 0.285 | 0.217 | 0.256 |
| Tm | 0.038 | 0.069 | 0.036 | 0.046 | 0.043 | 0.041 | 0.044 | 0.040 | 0.031 | 0.031 | 0.044 | 0.032 | 0.039 |
| Yb | 0.240 | 0.435 | 0.240 | 0.306 | 0.288 | 0.266 | 0.283 | 0.264 | 0.210 | 0.205 | 0.279 | 0.221 | 0.252 |
| Lu | 0.041 | 0.072 | 0.041 | 0.051 | 0.049 | 0.043 | 0.047 | 0.046 | 0.036 | 0.035 | 0.047 | 0.037 | 0.044 |
| Hf | 0.103 | 0.375 | 0.122 | 0.143 | 0.130 | 0.193 | 0.151 | 0.126 | 0.310 | 0.087 | 0.142 | 0.094 | 0.118 |
| Ta | 0.003 | 0.022 | 0.005 | 0.004 | 0.003 | 0.024 | 0.004 | 0.006 | 0.005 | 0.014 | 0.003 | 0.006 | 0.002 |
| Pb | 0.043 | 0.871 | 0.255 | 0.234 | 0.042 | 0.366 | 0.274 | 0.993 | 0.185 | 0.367 | 0.285 | 0.158 | 0.200 |
| Th | 0.049 | 0.256 | 0.105 | 0.190 | 0.025 | 0.380 | 0.130 | 0.057 | 0.094 | 0.259 | 0.177 | 0.054 | 0.055 |
| U | 0.015 | 0.072 | 0.025 | 0.049 | 0.011 | 0.075 | 0.036 | 0.019 | 0.027 | 0.089 | 0.048 | 0.030 | 0.023 |

Table 9 cont.

| Sample | Group III | | Wehrlite | | BIR-1 (basalt powder) | | UB-N (serpentinite powder) | | JP-1 (peridotite powder) | | |
|--------|-----------|---------|---------------|--------------|-----------------------|--------------|----------------------------|--------------|--------------------------|-----------------------|----------|
| | LPE-062 | LPE-028 | measured | | measured | | measured | | Deschamps et al. (2010) | Paulick et al. (2006) | measured |
| | | | average (n=2) | st. dev. (%) | average (n=2) | st. dev. (%) | average (n=2) | st. dev. (%) | | | |
| Rb | 0.374 | 1.735 | 0.186 | 1.0 | 3.273 | 0.7 | 0.303 | 0.308 | 0.319 | | |
| Sr | 19.345 | 25.741 | 103.236 | 0.0 | 7.558 | 0.5 | 0.693 | 0.662 | 0.656 | | |
| Y | 3.771 | 2.600 | 14.190 | 0.8 | 2.450 | 0.3 | 0.105 | 0.098 | 0.095 | | |
| Zr | 8.652 | 6.145 | 12.840 | 5.7 | 3.578 | 1.0 | 6.107 | 6.039 | 6.010 | | |
| Nb | 0.620 | 0.465 | 0.454 | 18.4 | 0.058 | 1.4 | 0.044 | 0.049 | 0.044 | | |
| Cs | 0.015 | 0.046 | 0.008 | 30.5 | 11.401 | 0.6 | 0.040 | 0.040 | 0.043 | | |
| Ba | 8.064 | 16.865 | 6.871 | 3.0 | 26.165 | 3.3 | 9.830 | 11.514 | 11.050 | | |
| La | 1.254 | 1.287 | 0.584 | 1.3 | 0.326 | 8.6 | 0.028 | 0.038 | 0.030 | | |
| Ce | 2.995 | 3.644 | 1.799 | 0.6 | 0.805 | 7.5 | 0.062 | 0.076 | 0.063 | | |
| Pr | 0.414 | 0.546 | 0.342 | 0.0 | 0.115 | 3.8 | 0.007 | 0.010 | 0.008 | | |
| Nd | 2.003 | 2.602 | 2.296 | 0.3 | 0.613 | 4.2 | 0.031 | 0.038 | 0.033 | | |
| Sm | 0.500 | 0.563 | 1.016 | 0.5 | 0.203 | 2.3 | 0.008 | 0.011 | 0.008 | | |
| Eu | 0.189 | 0.209 | 0.514 | 0.8 | 0.081 | 1.1 | 0.003 | 0.002 | 0.002 | | |
| Gd | 0.614 | 0.555 | 1.846 | 1.7 | 0.327 | 1.6 | 0.012 | 0.010 | 0.010 | | |
| Tb | 0.103 | 0.084 | 0.346 | 1.3 | 0.059 | 0.8 | 0.002 | 0.002 | 0.002 | | |
| Dy | 0.720 | 0.541 | 2.626 | 1.4 | 0.446 | 0.4 | 0.016 | 0.018 | 0.015 | | |
| Ho | 0.146 | 0.102 | 0.566 | 2.3 | 0.095 | 0.0 | 0.004 | 0.004 | 0.004 | | |
| Er | 0.426 | 0.288 | 1.661 | 0.9 | 0.286 | 1.0 | 0.013 | 0.014 | 0.012 | | |
| Tm | 0.061 | 0.041 | 0.244 | 0.1 | 0.044 | 0.3 | 0.002 | 0.003 | 0.003 | | |
| Yb | 0.392 | 0.251 | 1.549 | 0.7 | 0.283 | 1.5 | 0.020 | 0.022 | 0.021 | | |
| Lu | 0.067 | 0.042 | 0.253 | 0.6 | 0.049 | 0.8 | 0.004 | 0.005 | 0.004 | | |
| Hf | 0.216 | 0.151 | 0.481 | 4.3 | 0.111 | 0.7 | 0.113 | 0.143 | 0.121 | | |
| Ta | 0.021 | 0.018 | 0.024 | 8.9 | 0.014 | 0.6 | 0.004 | 0.004 | 0.004 | | |
| Pb | 5.556 | 0.326 | 2.939 | 3.3 | 13.035 | 4.5 | 0.101 | 0.078 | 0.242 | | |
| Th | 0.152 | 0.092 | 0.032 | 3.8 | 0.065 | 26.6 | 0.014 | 0.014 | 0.014 | | |
| U | 0.040 | 0.014 | 0.009 | 7.5 | 0.047 | 0.2 | 0.014 | 0.013 | 0.012 | | |

Table 10 Average major element compositions (wt.%) of minerals of the studied SE IVP xenoliths

| Sample | Group I | | | | Group II | | | | | | | | | | | |
|--------------------------------|---------|--------|--------|--------|----------|--------|--------|--------|---------|--------|--------|--------|---------|--------|--------|--------|
| | TAL-084 | | | | TAL-094 | | | | LPE-029 | | | | LPE-048 | | | |
| | Ol | Opx | Cpx | Spl | Ol | Opx | Cpx | Spl | Ol | Opx | Cpx | Spl | Ol | Opx | Cpx | Spl |
| SiO ₂ | 41.1 | 55.8 | 52.4 | 0.09 | 41.2 | 55.4 | 51.8 | 0.01 | 41.1 | 56.1 | 52.0 | 0.01 | 40.8 | 55.3 | 51.3 | 0.08 |
| Al ₂ O ₃ | b.d.l. | 3.70 | 4.81 | 48.8 | b.d.l. | 4.34 | 5.70 | 50.1 | b.d.l. | 3.64 | 5.49 | 56.3 | b.d.l. | 3.70 | 5.06 | 48.7 |
| Cr ₂ O ₃ | b.d.l. | 0.59 | 1.17 | 21.7 | b.d.l. | 0.67 | 1.20 | 18.1 | b.d.l. | 0.34 | 0.79 | 12.1 | b.d.l. | 0.48 | 0.96 | 17.8 |
| TiO ₂ | b.d.l. | 0.07 | 0.26 | 0.07 | b.d.l. | 0.09 | 0.39 | b.d.l. | b.d.l. | 0.12 | 0.52 | 0.08 | b.d.l. | 0.16 | 0.63 | 0.14 |
| Na ₂ O | b.d.l. | b.d.l. | 0.82 | b.d.l. | b.d.l. | b.d.l. | 0.93 | b.d.l. | b.d.l. | b.d.l. | 0.53 | b.d.l. | b.d.l. | 0.06 | 0.74 | b.d.l. |
| MgO | 48.4 | 32.7 | 15.7 | 19.7 | 49.4 | 33.1 | 15.7 | 19.5 | 48.1 | 32.8 | 16.2 | 19.8 | 48.0 | 32.1 | 16.0 | 18.9 |
| MnO | 0.13 | 0.13 | 0.09 | 0.15 | 0.14 | 0.14 | 0.09 | 0.16 | 0.14 | 0.15 | 0.08 | 0.12 | 0.13 | 0.14 | 0.09 | 0.17 |
| FeO ⁱ | 9.07 | 5.77 | 2.19 | 8.32 | 9.46 | 6.14 | 2.44 | 11.5 | 11.0 | 6.95 | 2.63 | 10.7 | 9.54 | 6.09 | 2.71 | 12.2 |
| K ₂ O | b.d.l. | b.d.l. | b.d.l. | b.d.l. | b.d.l. | b.d.l. | b.d.l. | b.d.l. | b.d.l. | b.d.l. | b.d.l. | b.d.l. | b.d.l. | b.d.l. | b.d.l. | b.d.l. |
| CaO | 0.05 | 0.66 | 22.1 | b.d.l. | 0.05 | 0.71 | 21.9 | b.d.l. | b.d.l. | 0.60 | 21.8 | b.d.l. | 0.06 | 0.96 | 21.1 | b.d.l. |
| NiO | 0.38 | 0.07 | 0.05 | 0.26 | 0.40 | 0.07 | b.d.l. | 0.33 | 0.38 | 0.09 | 0.06 | 0.36 | 0.38 | 0.10 | 0.07 | 0.32 |
| Σ | 99.2 | 99.5 | 99.5 | 99.2 | 100.7 | 100.7 | 100.2 | 99.7 | 100.7 | 100.8 | 100.1 | 99.4 | 99.0 | 99.1 | 98.6 | 98.2 |
| mg# | 0.905 | 0.910 | 0.927 | 0.809 | 0.903 | 0.906 | 0.920 | 0.752 | 0.886 | 0.894 | 0.917 | 0.768 | 0.900 | 0.904 | 0.913 | 0.735 |
| cr# | 0.230 | 0.230 | 0.230 | 0.230 | 0.195 | 0.195 | 0.195 | 0.195 | 0.126 | 0.126 | 0.126 | 0.126 | 0.197 | 0.197 | 0.197 | 0.197 |

| Sample | Group II | | | | TAL-001 | | | | TAL-014 | | | | TAL-112 | | | |
|--------------------------------|----------|--------|--------|--------|---------|--------|--------|--------|---------|--------|--------|--------|---------|--------|--------|--------|
| | LPE-061 | | | | TAL-001 | | | | TAL-014 | | | | TAL-112 | | | |
| | Ol | Opx | Cpx | Spl | Ol | Opx | Cpx | Spl | Ol | Opx | Cpx | Spl | Ol | Opx | Cpx | Spl |
| SiO ₂ | 41.0 | 55.4 | 51.79 | 0.079 | 40.8 | 55.4 | 51.2 | 0.10 | 41.3 | 55.4 | 51.8 | 0.01 | 41.3 | 55.9 | 52.1 | 0.02 |
| Al ₂ O ₃ | b.d.l. | 4.53 | 4.806 | 47.72 | b.d.l. | 3.36 | 5.14 | 51.0 | b.d.l. | 4.35 | 5.22 | 49.3 | b.d.l. | 4.01 | 5.72 | 57.3 |
| Cr ₂ O ₃ | b.d.l. | 0.70 | 1.02 | 22.18 | b.d.l. | 0.43 | 1.04 | 17.2 | b.d.l. | 0.70 | 1.20 | 19.2 | b.d.l. | 0.39 | 0.78 | 11.6 |
| TiO ₂ | b.d.l. | b.d.l. | 0.80 | 0.06 | b.d.l. | 0.14 | 0.65 | 0.05 | b.d.l. | 0.21 | 0.81 | 0.11 | b.d.l. | 0.11 | 0.57 | 0.06 |
| Na ₂ O | b.d.l. | b.d.l. | 0.611 | b.d.l. | b.d.l. | b.d.l. | 0.74 | b.d.l. | b.d.l. | 0.08 | 0.83 | b.d.l. | b.d.l. | b.d.l. | 0.78 | b.d.l. |
| MgO | 47.63 | 32.3 | 15.65 | 17.51 | 48.0 | 32.6 | 15.5 | 18.9 | 49.1 | 32.3 | 15.7 | 19.2 | 48.8 | 32.9 | 15.7 | 20.4 |
| MnO | 0.155 | 0.14 | 0.088 | 0.155 | 0.13 | 0.15 | 0.09 | 0.16 | 0.14 | 0.15 | 0.07 | 0.17 | 0.13 | 0.14 | 0.08 | 0.13 |
| FeO ⁱ | 10.44 | 6.29 | 2.338 | 12.0 | 9.92 | 6.22 | 2.39 | 10.0 | 9.95 | 6.30 | 2.36 | 11.3 | 10.1 | 6.43 | 2.37 | 9.80 |
| K ₂ O | b.d.l. | b.d.l. | b.d.l. | b.d.l. | b.d.l. | b.d.l. | b.d.l. | b.d.l. | b.d.l. | b.d.l. | b.d.l. | b.d.l. | b.d.l. | b.d.l. | b.d.l. | b.d.l. |
| CaO | b.d.l. | 1.30 | 22.71 | b.d.l. | 0.05 | 0.73 | 21.95 | b.d.l. | 0.05 | 1.55 | 22.11 | b.d.l. | 0.05 | 0.67 | 22.27 | b.d.l. |
| NiO | 0.355 | 0.07 | 0.054 | 0.25 | 0.37 | 0.08 | b.d.l. | 0.34 | 0.41 | 0.08 | b.d.l. | 0.33 | 0.38 | 0.10 | 0.05 | 0.34 |
| Σ | 99.64 | 100.7 | 99.87 | 99.93 | 99.3 | 99.1 | 98.8 | 97.7 | 100.9 | 101.1 | 100.1 | 99.7 | 100.7 | 100.8 | 100.4 | 99.6 |
| mg# | 0.891 | 0.901 | 0.923 | 0.723 | 0.896 | 0.903 | 0.920 | 0.771 | 0.898 | 0.901 | 0.922 | 0.753 | 0.895 | 0.901 | 0.922 | 0.788 |
| cr# | 0.238 | 0.238 | 0.238 | 0.238 | 0.184 | 0.184 | 0.184 | 0.184 | 0.207 | 0.207 | 0.207 | 0.207 | 0.120 | 0.120 | 0.120 | 0.120 |

Ol – olivine; Opx – orthopyroxene; Cpx – clinopyroxene; Spl – spinel; b.d.l. – below detection limit

Table 10 cont.

| Sample | Group II | | | | | | | | Group III | | | |
|--------------------------------|----------|--------|--------|--------|---------|--------|--------|--------|-----------|--------|--------|--------|
| | TAL-127 | | | | TAL-134 | | | | LP08-02 | | | |
| | Ol | Opx | Cpx | Spl | Ol | Opx | Cpx | Spl | Ol | Opx | Cpx | Spl |
| SiO ₂ | 41.2 | 55.4 | 51.77 | 0.09 | 40.7 | 55.9 | 51.2 | 0.08 | 41.1 | 55.8 | 51.3 | 0.01 |
| Al ₂ O ₃ | b.d.l. | 4.21 | 5.22 | 55.4 | b.d.l. | 4.03 | 5.89 | 56.0 | 0.01 | 3.76 | 5.98 | 51.2 |
| Cr ₂ O ₃ | b.d.l. | 0.49 | 1.20 | 14.4 | b.d.l. | 0.38 | 0.81 | 11.7 | b.d.l. | 0.53 | 1.00 | 17.5 |
| TiO ₂ | b.d.l. | 0.11 | 0.80 | b.d.l. | b.d.l. | 0.12 | 0.54 | 0.06 | b.d.l. | 0.15 | 0.71 | 0.08 |
| Na ₂ O | b.d.l. | b.d.l. | 0.53 | b.d.l. | b.d.l. | b.d.l. | 0.82 | b.d.l. | b.d.l. | b.d.l. | 0.73 | b.d.l. |
| MgO | 48.0 | 32.3 | 15.68 | 19.6 | 48.3 | 32.9 | 15.4 | 20.2 | 49.0 | 33.1 | 15.4 | 19.1 |
| MnO | 0.15 | 0.14 | 0.07 | 0.13 | 0.14 | 0.15 | 0.08 | 0.14 | 0.16 | 0.15 | 0.09 | 0.17 |
| FeO ^t | 9.81 | 6.24 | 2.355 | 10.2 | 9.98 | 6.43 | 2.38 | 9.55 | 10.0 | 6.44 | 2.26 | 11.0 |
| K ₂ O | b.d.l. | b.d.l. | b.d.l. | b.d.l. | b.d.l. | b.d.l. | b.d.l. | b.d.l. | b.d.l. | b.d.l. | b.d.l. | b.d.l. |
| CaO | 0.05 | 0.65 | 22.11 | b.d.l. | 0.05 | 0.67 | 21.81 | b.d.l. | 0.05 | 0.60 | 22.45 | b.d.l. |
| NiO | 0.38 | 0.09 | b.d.l. | 0.31 | 0.36 | 0.09 | 0.08 | 0.33 | 0.38 | 0.09 | b.d.l. | 0.29 |
| Σ | 99.7 | 99.7 | 99.7 | 100.3 | 99.5 | 100.8 | 99.1 | 98.0 | 100.8 | 100.6 | 100.0 | 99.4 |
| mg# | 0.897 | 0.902 | 0.922 | 0.775 | 0.896 | 0.901 | 0.920 | 0.790 | 0.897 | 0.902 | 0.924 | 0.756 |
| cr# | 0.149 | | | | 0.123 | | | | 0.186 | | | |

| Sample | Wehrlite | | | | | | | |
|--------------------------------|----------|-----|--------|--------|---------|-----|--------|--------|
| | LP08-12 | | | | LPE-028 | | | |
| | Ol | Opx | Cpx | Spl | Ol | Opx | Cpx | Spl |
| SiO ₂ | 40.1 | - | 50.9 | 0.05 | 40.7 | - | 52.0 | 0.11 |
| Al ₂ O ₃ | b.d.l. | - | 5.14 | 38.8 | b.d.l. | - | 4.78 | 37.5 |
| Cr ₂ O ₃ | b.d.l. | - | 1.22 | 25.1 | b.d.l. | - | 1.33 | 27.3 |
| TiO ₂ | b.d.l. | - | 0.69 | 0.66 | b.d.l. | - | 0.47 | 0.50 |
| Na ₂ O | b.d.l. | - | 0.94 | b.d.l. | b.d.l. | - | 1.16 | b.d.l. |
| MgO | 46.0 | - | 15.4 | 16.6 | 45.9 | - | 15.5 | 15.3 |
| MnO | 0.21 | - | 0.11 | 0.23 | 0.21 | - | 0.13 | 0.22 |
| FeO ^t | 12.7 | - | 3.50 | 17.1 | 12.4 | - | 3.9 | 19.3 |
| K ₂ O | b.d.l. | - | b.d.l. | b.d.l. | b.d.l. | - | b.d.l. | b.d.l. |
| CaO | 0.14 | - | 20.8 | b.d.l. | 0.12 | - | 20.2 | b.d.l. |
| NiO | 0.29 | - | 0.05 | 0.26 | 0.31 | - | 0.05 | 0.25 |
| Σ | 99.5 | - | 98.8 | 98.7 | 99.7 | - | 99.6 | 100.5 |
| mg# | 0.866 | | 0.887 | 0.635 | 0.869 | | 0.875 | 0.586 |
| cr# | 0.302 | | | | 0.329 | | | |

Table 11 Clinopyroxene trace element composition for the studied peridotite xenoliths

| Sample | Group I | | | Group II | | | | | | | | |
|--------|---------|---------|---------|----------|---------|---------|---------|---------|---------|---------|---------|---------|
| | TAL-047 | TAL-056 | TAL-084 | LP08-14 | LPE-029 | LPE-042 | LPE-048 | LPE-061 | TAL-001 | TAL-127 | TAL-134 | TAL-014 |
| Li | 6.652 | 5.037 | 4.078 | - | 10.673 | 21.331 | 3.092 | 10.433 | 5.756 | 5.856 | 14.673 | - |
| Rb | 0.021 | 0.011 | 0.632 | 0.014 | 0.008 | 0.017 | 0.289 | 0.214 | 0.011 | 0.033 | 0.026 | 0.007 |
| Sr | 56.513 | 11.448 | 53.707 | 19.420 | 64.703 | 41.227 | 9.175 | 6.197 | 7.458 | 57.283 | 67.582 | 5.167 |
| Y | 12.637 | 20.897 | 11.560 | 48.683 | 20.117 | 21.310 | 23.422 | 27.908 | 23.658 | 15.030 | 20.427 | 30.490 |
| Zr | 23.310 | 38.720 | 20.662 | 160.540 | 34.513 | 31.514 | 41.762 | 44.215 | 33.862 | 26.354 | 32.620 | 152.083 |
| Nb | 0.363 | 0.394 | 0.153 | 0.210 | 0.940 | 0.009 | 0.075 | 0.379 | 0.183 | 0.213 | 0.124 | 0.122 |
| La | 1.296 | 1.147 | 0.954 | 4.933 | 2.183 | 0.946 | 2.193 | 1.112 | 1.096 | 1.122 | 1.830 | 6.590 |
| Ce | 4.035 | 4.848 | 3.247 | 18.660 | 7.637 | 4.376 | 7.690 | 5.552 | 4.552 | 3.611 | 6.785 | 32.887 |
| Pr | 0.711 | 0.947 | 0.572 | 3.363 | 1.320 | 0.896 | 1.407 | 1.141 | 0.878 | 0.631 | 1.237 | 7.773 |
| Nd | 4.180 | 5.793 | 3.276 | 18.613 | 7.343 | 5.553 | 8.380 | 6.975 | 5.348 | 3.701 | 7.127 | 56.390 |
| Sm | 1.564 | 2.154 | 1.198 | 5.900 | 2.398 | 2.088 | 3.025 | 2.702 | 2.119 | 1.423 | 2.437 | 15.480 |
| Eu | 0.619 | 0.680 | 0.485 | 0.925 | 0.838 | 0.745 | 0.778 | 0.607 | 0.626 | 0.549 | 0.855 | 1.297 |
| Gd | 2.161 | 3.043 | 1.635 | 7.350 | 3.040 | 2.760 | 3.757 | 4.002 | 3.116 | 2.063 | 3.192 | 9.253 |
| Tb | 0.374 | 0.545 | 0.295 | 1.319 | 0.527 | 0.494 | 0.638 | 0.719 | 0.582 | 0.383 | 0.546 | 1.136 |
| Ti | 2625.2 | 3442.7 | 1980.3 | 13662.1 | 3267.7 | 6579.1 | 4501.4 | 5418.3 | 3910.9 | 2640.4 | 3560.3 | 11019.6 |
| Dy | 2.530 | 3.935 | 2.173 | 9.237 | 3.803 | 3.800 | 4.493 | 5.187 | 4.322 | 2.804 | 3.910 | 6.273 |
| Ho | 0.514 | 0.836 | 0.464 | 1.947 | 0.814 | 0.818 | 0.927 | 1.107 | 0.925 | 0.597 | 0.826 | 1.164 |
| Er | 1.381 | 2.333 | 1.312 | 5.327 | 2.267 | 2.472 | 2.551 | 3.139 | 2.630 | 1.726 | 2.302 | 3.053 |
| Tm | 0.187 | 0.329 | 0.184 | 0.738 | 0.315 | 0.401 | 0.358 | 0.437 | 0.382 | 0.249 | 0.331 | 0.414 |
| Yb | 1.166 | 2.031 | 1.174 | 4.373 | 1.973 | 2.710 | 2.202 | 2.793 | 2.455 | 1.624 | 2.074 | 2.428 |
| Lu | 0.160 | 0.285 | 0.166 | 0.626 | 0.275 | 0.441 | 0.300 | 0.386 | 0.335 | 0.227 | 0.282 | 0.343 |
| Hf | 0.728 | 1.024 | 0.616 | 3.285 | 1.066 | 1.148 | 1.442 | 1.538 | 1.008 | 0.798 | 1.086 | 6.437 |
| Ta | 0.038 | 0.063 | 0.017 | 0.135 | 0.052 | 0.002 | 0.014 | 0.025 | 0.059 | 0.049 | 0.021 | 0.028 |
| Pb | 0.024 | 0.017 | 0.021 | 0.303 | 0.067 | 0.113 | 0.128 | 0.055 | 0.016 | 0.012 | 0.067 | 0.029 |
| Th | 0.863 | 0.276 | 0.104 | 1.612 | 0.906 | 0.335 | 1.449 | 0.758 | 0.073 | 0.110 | 0.190 | 0.989 |
| U | 0.350 | 0.112 | 0.077 | 0.362 | 0.296 | 0.106 | 0.380 | 0.254 | 0.025 | 0.045 | 0.059 | 0.095 |

Table 11 cont.

| Sample | Group III | | Wehrlite | | BIR-1G (basalt glass) | |
|--------|-----------|---------|----------|---------|-------------------------|--------------|
| | LP08-02 | LPE-062 | LP08-12 | LPE-028 | measured average (n=17) | st. dev. (%) |
| Li | 4.663 | 4.100 | 35.844 | 25.431 | 3.167 | 12.8 |
| Rb | - | 0.015 | 0.143 | 1.999 | 0.190 | 18.2 |
| Sr | 3.323 | 43.168 | 103.48 | 147.10 | 100.87 | 4.6 |
| Y | 20.840 | 23.024 | 16.278 | 14.977 | 12.709 | 5.3 |
| Zr | 28.333 | 37.274 | 35.391 | 24.077 | 11.872 | 5.7 |
| Nb | 0.246 | 0.993 | 0.426 | 0.443 | 0.496 | 7.4 |
| La | 0.767 | 4.414 | 6.355 | 7.054 | 0.589 | 10.0 |
| Ce | 4.337 | 12.252 | 20.849 | 22.154 | 1.923 | 7.2 |
| Pr | 0.900 | 1.721 | 3.103 | 3.274 | 0.363 | 7.8 |
| Nd | 5.408 | 8.262 | 14.621 | 15.100 | 2.275 | 5.5 |
| Sm | 1.983 | 2.557 | 3.391 | 3.349 | 1.004 | 8.9 |
| Eu | 0.688 | 0.962 | 1.179 | 1.269 | 0.492 | 5.6 |
| Gd | 2.880 | 3.404 | 3.314 | 3.173 | 1.662 | 8.2 |
| Tb | 0.544 | 0.613 | 0.496 | 0.473 | 0.321 | 9.0 |
| Ti | 4034.5 | 5048.5 | 5422.1 | 3269.7 | 6150.6 | 11.3 |
| Dy | 3.902 | 4.392 | 3.334 | 3.072 | 2.474 | 7.3 |
| Ho | 0.833 | 0.920 | 0.642 | 0.620 | 0.542 | 5.6 |
| Er | 2.405 | 2.576 | 1.724 | 1.701 | 1.568 | 6.4 |
| Tm | 0.351 | 0.364 | 0.248 | 0.240 | 0.241 | 9.5 |
| Yb | 2.213 | 2.288 | 1.554 | 1.578 | 1.618 | 10.5 |
| Lu | 0.312 | 0.323 | 0.221 | 0.226 | 0.241 | 10.4 |
| Hf | 0.904 | 1.265 | 1.111 | 0.749 | 0.505 | 13.5 |
| Ta | 0.044 | 0.083 | 0.077 | 0.050 | 0.039 | 32.8 |
| Pb | 0.010 | 0.399 | 0.165 | 0.245 | 4.233 | 7.9 |
| Th | 0.027 | 0.837 | 0.342 | 0.265 | 0.028 | 20.6 |
| U | 0.012 | 0.195 | 0.223 | 0.049 | 0.019 | 37.0 |

Table 12 Pb, Sr and Nd isotope ratios for SE IVP mantle xenoliths

| Sample | ²⁰⁶ Pb / ²⁰⁴ Pb | | ²⁰⁷ Pb / ²⁰⁴ Pb | | ²⁰⁸ Pb / ²⁰⁴ Pb | | ⁸⁷ Sr / ⁸⁶ Sr | | ¹⁴³ Nd / ¹⁴⁴ Nd | |
|------------------|---------------------------------------|--------|---------------------------------------|--------|---------------------------------------|--------|-------------------------------------|---------|---------------------------------------|----------|
| | WR | Cpx | WR | Cpx | WR | Cpx | WR | Cpx | WR | Cpx |
| <i>Group I</i> | | | | | | | | | | |
| TAL-052 | 18.660 | - | 15.631 | - | 38.729 | - | 0.70330 | - | 0.512987 | - |
| TAL-056 | 18.603 | - | 15.639 | - | 38.648 | - | 0.70294 | - | 0.513046 | - |
| TAL-084 | 18.488 | - | 15.621 | - | 38.513 | - | 0.70305 | - | 0.513087 | - |
| TAL-094 | 18.430 | - | 15.621 | - | 38.537 | - | 0.70372 | - | 0.512993 | - |
| TAL-143 | 18.741 | - | 15.643 | - | 38.632 | - | 0.70319 | 0.70314 | 0.513097 | 0.513039 |
| <i>Group II</i> | | | | | | | | | | |
| LP08-03 | 18.756 | 18.997 | 15.648 | 15.648 | 38.873 | 39.139 | 0.70393 | 0.70337 | 0.512846 | 0.512940 |
| LP08-14 | 18.685 | 18.697 | 15.655 | 15.656 | 38.877 | 38.896 | 0.70541 | - | 0.512754 | 0.512743 |
| LPE-029 | 18.406 | - | 15.639 | - | 38.563 | - | - | - | 0.512832 | - |
| LPE-042 | 18.686 | 18.686 | 15.644 | 15.644 | 38.821 | 38.821 | 0.70683 | - | 0.512744 | - |
| LPE-046 | 18.384 | - | 15.610 | - | 38.368 | - | 0.70296 | - | 0.513228 | - |
| LPE-048 | 18.820 | - | 15.660 | - | 38.965 | - | 0.70473 | - | 0.512688 | - |
| LPE-061 | - | - | - | - | - | - | 0.70422 | - | 0.512973 | 0.51290 |
| TAL-001 | 18.782 | - | 15.643 | - | 38.865 | - | 0.70316 | - | 0.513064 | - |
| TAL-014 | 18.553 | - | 15.621 | - | 38.581 | - | 0.70449 | - | 0.512171 | - |
| TAL-106 | 18.511 | - | 15.638 | - | 38.636 | - | - | 0.70320 | 0.512949 | - |
| TAL-112 | 18.517 | - | 15.648 | - | 38.698 | - | 0.70519 | - | 0.512876 | - |
| TAL-127 | 18.536 | 18.110 | 15.585 | 15.462 | 38.504 | 37.852 | 0.70235 | 0.70226 | 0.513274 | 0.513251 |
| TAL-134 | 18.706 | 18.670 | 15.702 | 15.643 | 38.849 | 38.839 | 0.70529 | 0.70526 | 0.512756 | 0.512760 |
| <i>Group III</i> | | | | | | | | | | |
| LP08-02 | 18.824 | 18.838 | 15.663 | 15.666 | 38.968 | 38.929 | 0.70416 | - | 0.512753 | 0.512995 |
| LPE-062 | 18.891 | - | 15.672 | - | 39.020 | - | 0.70418 | - | 0.512737 | - |
| <i>Wehrlite</i> | | | | | | | | | | |
| LPE-028 | 18.705 | - | 15.585 | - | 38.745 | - | 0.70460 | - | 0.512750 | - |

WR – whole rock; Cpx – clinopyroxene

7. The architecture of the European-Mediterranean Lithosphere: a synthesis of the Re-Os evidence

J.M. González-Jimenez^a, C. Villaseca^b, W.L. Griffin^a, E. Belousova^a, Z. Konc^c, E. Ancochea^b, S.Y. O'Reilly^a, N. Pearson^a, C.J. Garrido^c & F. Gervilla^d

Abstract

Re-depletion model ages (TRD) of sulfides in peridotite xenoliths from the subcontinental mantle beneath Central Spain (Calatrava Volcanic Field), reveal that episodes of mantle magmatism/metasomatism in the Iberia microplate were linked to crustal growth events, mainly during supercontinent assembly/breakup at around ~1.8, 1.1, 0.9, 0.6 and 0.3 Ga. A synthesis of available in situ and whole-rock Os-isotope data on mantle-derived peridotites shows that this type of mantle (maximum TRD ca. 1.8 Ga) is widespread in the subcontinental mantle of Europe and Africa outboard from the Betics-Maghrebides-Appenines front. In contrast, the mantle enclosed within the Alpine domain records TRD as old as 2.6 Ga, revealing a previously unrecognized Archean domain or domains in the Central/Western Mediterranean. Our observations indicate that ancient fragments of subcontinental lithospheric mantle have played an important role in the development of the present architecture of the Mediterranean lithosphere.

^a ARC Centre of Excellence for Core to Crust Fluid Systems (CCFS) and GEMOC, Department of Earth and Planetary Sciences, Macquarie University, Sydney, NSW 2109, Australia.

^b Departamento de Petrología y Geoquímica and Instituto de Geociencias (UCM-CSIC), 28040, Madrid, Spain.

^c Instituto Andaluz de Ciencias de la Tierra (IACT), Consejo Superior de Investigaciones Científicas & Universidad de Granada (CSIC & UGR), Avenida de las Palmeras, 418100-Armilla (Granada), Spain

^d Departamento de Mineralogía y Petrología and Instituto Andaluz de Ciencias de la Tierra (IACT), UGR-CSIC, Facultad de Ciencias, 18002, Granada, Spain.

7.1. Introduction

Until now, the timing of formation and the evolution of the Iberian microplate has been constrained mainly from U-Pb ages of magmatic zircons, Hf model ages of inherited zircons and whole-rock Nd model ages of crustal igneous and metamorphic rocks. However, there has been little robust information on the age of the lithospheric mantle beneath this continental crust; it is the missing key for a full understanding of the geological framework of the Iberian microplate. This gap has now been filled by determining the Re-Os systematics of sulfides in peridotite xenoliths that represent samples of this mantle. Since Re and Os preferentially concentrate in mantle minerals, unlike those lithophile elements commonly used in other isotopic systems in the earth sciences, their isotopes are uniquely useful in tracking events of mantle melt depletion and refertilisation.

In this work we use in situ laser ablation analysis by multi-collector inductively coupled mass spectrometry (LA-MC-ICPMS) to study the Re-Os isotopic composition of sulfides in xenoliths from the Calatrava Volcanic Field (CFV) in central Spain. The CVF contains a suite of peridotite xenoliths from the lithospheric mantle underlying the crust of the Iberian microplate. Our results suggest that the mantle and crust constituting the Iberian microplate have coexisted since at least Paleo-Proterozoic time. The comparison of our data with Os-isotopic data from mantle-derived materials from other localities in Central/Western Europe and Africa allows us to examine the evolution and architecture of the European - Mediterranean mantle, revealing a heterogeneous mantle structure across the region and indicating the presence of a previously unrecognised Archean domain.

7.2. Geological Setting and Sample Background

The Calatrava Volcanic Field (CVF) is an intracontinental zone within the Central Iberia Zone of Central Spain where upper crust only from Neo-Proterozoic time has been preserved. The CVF comprises around 200 small monogenetic volcanic centers. An initial minor ultrapotassic event at around 8.7-6.4 Ma was followed by the eruption of alkali basalts, basanites, and olivine nephelinites and melilitites from 3.7 to ca. 0.7 Ma, that entrained abundant deep-seated xenoliths, dominantly spinel lherzolites of the Cr-diopside suite (after Wilshire and Shervais, 1975), and wehrlites and phlogopite-rich clinopyroxenites of the Al-augite series (Ancochea, 2004). These xenoliths record different types of metasomatism including carbonatitic, silica-undersaturated alkaline, and subduction-related styles (Villaseca et al., 2010; Bianchini et al. 2010; O'Reilly and Griffin, 2012).

The xenoliths studied here come from the El Aprisco olivine melilite maar (Villaseca et al., 2010). They are nine coarse-grained lherzolites and two wehrlites that equilibrated in the spinel facies (1.5-0.7 GPa) at temperatures of 1120-940 °C and contain accessory metasomatic minerals (amphibole, apatite, calcite). Interstitial glass commonly surrounds these metasomatic minerals and contains relics of them as well as incompletely-reacted primary silicates and newly-formed clinopyroxene, olivine and spinel (Villaseca et al., 2010).

Sulfides (1-500µm) were identified in polished thin sections; they are enclosed in olivine and pyroxenes, rarely at the triple junctions between the main silicates, and more commonly in the interstitial glass. Major-element analysis by electron microprobe shows that all the sulfides are Fe-rich monosulfide solid solution, with Fe > 38.9 wt% and Ni contents > 9.93 wt%. There is no difference in composition between included and interstitial sulfides.

7.3. Results and Interpretation

7.3.1. *In Situ Re-Os Model Ages on Mantle Sulfides*

The Os-isotope compositions of over 800 individual sulfides $\geq 50 \mu\text{m}$ were measured in situ using LA-MC-ICPMS at CCFS/GEMOC (Macquarie University, Australia) following the procedures described by Pearson et al. (2002). In our dataset, only grains with $^{187}\text{Re}/^{188}\text{Os} < 1.2$ were selected, thus ensuring an accurate correction of the isobaric overlap of ^{187}Re on ^{188}Os . In our analysis we disregarded grains with superchondritic $^{187}\text{Os}/^{188}\text{Os}$ (> 0.1281 ; Walker et al. 2002) unsupported by their low Re/Os, which yielded geologically unreasonable future Re-Os model ages. Additionally, to ensure high-precision model-age constraints, we used grains only with propagated 2SE analytical uncertainties on $^{187}\text{Os}/^{188}\text{Os} < 0.2 \text{ Ga}$ (Table DR1).

The 68 sulfides from El Aprisco that meet these criteria have subchondritic $^{187}\text{Os}/^{188}\text{Os}$ (0.1147 to 0.1265) with $^{187}\text{Re}/^{188}\text{Os}$ varying from subchondritic (< 0.358) to suprachondritic (0.432-0.572) (Fig. DR1 & Table DR1). Only those sulfides with $^{187}\text{Re}/^{188}\text{Os} < 0.07$ -0.08 may preserve undisturbed isotopic signatures representative of mantle melting/refertilisation events (Griffin et al., 2004). Only 12 of our sulfides display $^{187}\text{Re}/^{188}\text{Os} < 0.08$ (italic font in Table RD1). A screening of the other 56 sulfides with $^{187}\text{Re}/^{188}\text{Os} > 0.08$ in Re-Os isotope plots reveals that many of the sulfide grains show the effects of recent Re-addition, probably associated with the magmatic activity that brought the xenoliths to the surface at $\sim 2 \text{ Ma}$. As little or no ^{187}Os ingrowth has occurred since this recent Re-enrichment, the TRD of these sulfides (calculated assuming Re = 0 ppm) still provide useful minimum estimates of the

timing of mantle events. For grains with $^{187}\text{Re}/^{188}\text{Os} > 0.08$ but uncorrelated Re-Os, we have constructed two cumulative plots of Re-depletion model ages: one uses TRD ages of sulfides with “undisturbed” $^{187}\text{Os}/^{188}\text{Os}$ (grains with $^{187}\text{Re}/^{188}\text{Os} < 0.08$ as well as with $^{187}\text{Re}/^{188}\text{Os} > 0.08$ lying on horizontal trends in Re-Os plots); the other uses only those grains with $^{187}\text{Re}/^{188}\text{Os} > 0.08$ and uncorrelated Re-Os (Table DR1). The two plots produce identical distributions of age peaks. Therefore the TRD obtained from all the 68 sulfide grains selected here can be used to unravel the evolution of the lithospheric mantle beneath Iberia.

7.3.2. Origin and Evolution of the Iberian Lithosphere: a 1.8 Ga-history of Mantle-Crust Interaction and Supercontinent Assemblies

Fig. 62 shows a strong coincidence between the five peaks (at 1.8, 1.1, 0.9, 0.6 and 0.33 Ga) in the distribution of TRD model ages of the El Aprisco sulfides and the timing of well-constrained magmatic events recorded in the overlying crust of Iberia. Most of the ages are older than the exposed crust in the immediate area, implying the possible existence of older crust at depth. Interestingly, the three main peaks in the El Aprisco sulfides at 1.8, 0.5 and 0.3 are consistent with TRD ages obtained for mantle-derived materials of comparable mantle suites on both sides of the Mediterranean realm (Central/Western Europe and North Africa). The smoother curve for the synthesised European-African mantle data largely reflects the number of intermediate model ages produced by the mixing of sulfide populations in individual whole-rock samples (Fig. 62).

The oldest Paleoproterozoic event (1.8 Ga) seen in the TRD model ages of the El Aprisco sulfides (Fig. 62) correlates with whole-rock Nd model ages (1.7-2.0 Ga) of Neo-Proterozoic sediments (~ 560 Ma) of the Central Iberian Zone (Villasca et al., 1998) and Hf model ages (1.6-1.8 Ga) of inherited zircons from Hercynian granulites (which have lower Paleozoic to Neo-Proterozoic metaigneous and metasedimentary protoliths) sampled in migmatite terranes and lower crustal xenoliths from the Central Iberia Zone (Villasca et al., 2011a). The correspondence of mantle and crustal ages supports the suggestion that primary mantle differentiation and crustal growth in the Iberian lithosphere took place ~ 1.6-2.0 Ga ago.

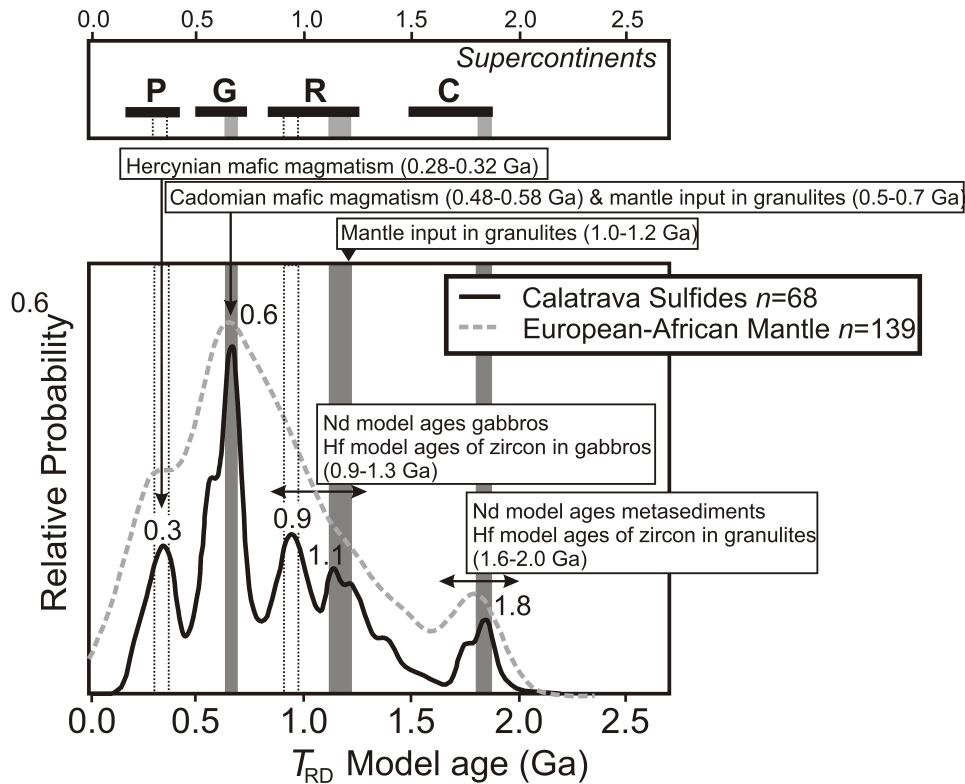


Fig. 62 Cumulative-probability plots of T_{RD} model ages for the El Aprisco mantle sulfides (black solid line) compared with the age intervals corresponding to events recorded in the crust of Central Iberia (see references in the text) and major events of supercontinent growth (**P** = Pangea, **G** = Gondwana, **R** = Rodinia and **C** = Columbia; see references in the Table DR1). The events of amalgamation or breakup of supercontinents recorded in the Iberian lithosphere are shown as grey or white dotted columns respectively. A cumulative-probability curve of T_{RD} model ages for mantle-derived materials from both sides of the Mediterranean realm in Central/Western Europe and North Africa (grey dashed line) has also been included for comparison (see details in the text and Table DR1 for localities and references). Note that only positive T_{RD} are plotted, and in the case of whole-rock (or mineral concentrate) results only data compared against Al_2O_3 or other melt depletion indicators (e.g. Rudnick and Walker, 2009) were considered. To ensure comparison among all the localities the T_{RD} were calculated with reference to ECR (Walker et al., 2002) and an uncertainty of 0.1 Ga was assumed for all single data points.

Reworking of this ancient lithosphere in the Neo-Proterozoic and Paleozoic may explain the four younger peaks in the sulfide TRD model ages. Thus, the mantle event at ca 0.6 Ga correlates with the 0.48-0.58 Ga mafic to silicic magmatism in the Central Iberian zone associated with the Cadomian orogeny (Pereira et al., 2010; Bandrés et al., 2004). The involvement of the mantle is evidenced by juvenile Hf isotopic signatures (ϵHf_t up to +9.7) of inherited zircons (U-Pb age 0.5-0.7 Ga) in the Hercynian granulites. Extensional decompression associated with delamination of lower-crustal rocks may have promoted upwelling and melting of the mantle following the Hercynian collision (Orejana et al., 2009). This would explain the correlation between the magmatic event at 0.3 Ga recorded in mantle

sulfides and the silicic and mafic magmatism of both crustal and mantle origin recognized in the Central Iberian Zone at 0.28-0.32 Ga (Fernández-Suárez et al., 2000). Melt production in the mantle beneath Iberia at 0.9-1.3 Ga is reflected in TRD model ages of 0.9-1.1 Ga in mantle sulfides, positive ϵ_{Hf} signatures (up to +12.8) of 1.0-1.2 Ga inherited zircon in Hercynian granulites (Villaseca et al., 2011a), Hf model ages of 0.9-1.2 Ga in magmatic zircons and the Nd whole-rock model ages of 1.0-1.3 Ga in the Hercynian gabbros (297-306 Ma) that intruded the Central Iberian Zone (Fig. 63; Orejana et al., 2009; Villaseca et al., 2011b).

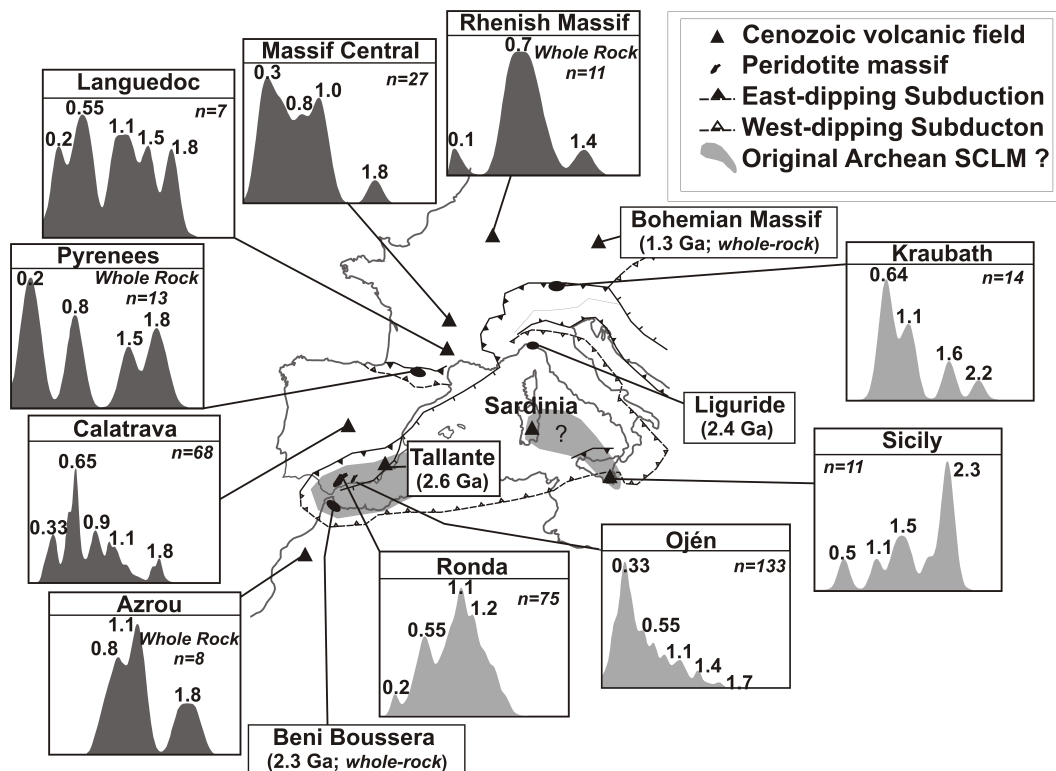


Fig. 63 Cumulative-probability plots for Re-Os model ages of sulfides, platinum-group minerals, mineral concentrates and whole-rock samples of xenoliths from Cenozoic volcanic fields and massifs in the Central-Western Mediterranean region (age peaks are in Ga; whole-rock ages are minimum ages). Grey fields refer to inferred original Archean subcontinental lithospheric mantle (details in the text). Note that in all cases only positive T_{RD} are shown, except for Beni Boussera, for which the Re-Os model age presented is T_{MA} . Whole-rock and mineral-separate Os data were screened following the same criteria as in Fig. 62. References for each locality are given in Table DR1.

The alkaline (silicate to carbonatite) metasomatism observed in some xenoliths of the CVF in the Tertiary may be responsible for the negative model ages of sulfides with highly radiogenic $^{187}\text{Os}/^{188}\text{Os}$ unsupported by low Re/Os ratios; these were excluded from this analysis.

Fig. 62 shows that the formation of the Iberian lithosphere at ~1.6-2.0 Ga coincides with the first-order event of mantle-crust differentiation that occurred during the assembly of the

supercontinent Columbia at 1.8-1.5. The 1.3-0.9 Ga timing of magmatic events recorded for both crustal and mantle materials in Iberia coincide with the amalgamation of Rodinia at ~ 1.25 Ga and its breakup at ~ 0.75 Ga. The peak in TRD at 0.6 Ga correlates with the beginning of continental collisions to form Gondwana (~ 0.65 Ga), whereas the TRD age peak at 0.3 Ga may be correlated with post-tectonic stages and the initiation of the breakup of Pangaea recorded in the Central Iberia Zone at ~ 0.26 Ga (Orejana et al., 2008).

7.3.3. Implication for the Architecture of the European-Mediterranean Lithosphere

Fig. 63 shows that mantle-derived rocks on both sides of the Mediterranean realm (Central/Western Europe and North Africa) yield maximum TRD \leq 1.8 Ga, whereas those from the inner Mediterranean region show both younger and older (up to 2.6 Ga) ages. Many sulfides in xenoliths from the mantle beneath Western Europe (Calatrava, Languedoc and Massif Central) show a common oldest peak at 1.8 Ga. This peak is also recognised in whole-rock samples from the Pyrenees (France) and Azrou (North Africa) but is slightly older than the oldest peaks at < 1.4-1.3 Ga found in whole rock samples from Central Europe (Bohemian and Rhenish Massifs). Nevertheless, although these whole-rock ages were screened against indices of melt depletion in the rock (*e.g.* Al_2O_3 ; Rudnick and Walker, 2009), they must be seen as a guide and can only be regarded as minimum values as they may integrate multiple generations of sulfides (*e.g.* Alard et al., 2002; Griffin et al. 2004). All these data are consistent with the existence of a common Paleo-Proterozoic mantle on both sides of the Mediterranean realm, formed ~ 1.8 Ga ago as recorded in the other parts of the European basement.

In contrast, Os-bearing minerals from xenoliths and peridotite massifs from the inner Mediterranean region (Sicilian Hyblean Plateau, Kraubath ultramafic massif) show a common oldest TRD peak at ~ 2.3, identical to the oldest whole-rock TMA age of 2.2 Ga obtained by Pearson and Nowell (2004) for pyroxenites of the Beni Bousera massif in northern Morocco and the 2.4 Ga peak in primary magmatic sulfides from peridotites of the internal Ligurides (Alard et al., 2005). A slightly older peak at 2.6 Ga has recently been reported by Konc et al. (2012) in sulfides from mantle xenoliths from the Tallante volcanic Field in southern Spain. These ages clearly identify an older lithospheric mantle formed near the Archean/Paleo-Proterozoic boundary at ~ 2.2-2.6 Ga, sitting within the more recent Betics-Maghrebides-Appenines front (Fig. 63) generated during the Alpine-Betic orogeny.

Seismic, gravity and heat-flow data suggest that the structure to 70 km beneath the Mediterranean Sea consists of ribbons of continental lithosphere (Valencia through the

Balearic promontory, the Sardinia-Corsica block, and the Hyblean Plateau beneath Sicily) separated by areas of thinned subcontinental lithosphere or new oceanic crust (Alboran, Liguro-Provençal, Vavilov, Marsili Tyrrenian sea basins) (*e.g.* Guegen et al., 1997; Booth-Rea et al., 2007). In the ribbon beneath Sicily, xenolith data suggest that thinned Archean continental crust overlies subcontinental mantle of the same age (Sapienza et al., 2007). Thus all of these continental ribbons and the subcontinental Archean/Paleo-Proterozoic mantle widespread through the Betics-Maghrebides-Apennines front may be the fragmented remnants of an Archean microcontinent within the inner Mediterranean area. The repetition of model age peaks at ~ 0.9 -1.2, ~ 0.4 -0.7, and ~ 0.3 Ga in the mantle both within and outside the Central-Western Mediterranean realm (Fig. 63) suggests that this microplate was strongly modified and fragmented (but survived) during supercontinent assembly-disruption cycles since Paleo-Proterozoic times.

In the context of convergence of Africa and Europe during the Tertiary, dismembered blocks of this ancient microplate could spread, colliding with passive margins (Iberia, Magrhebide, Adria), thus contributing to the development of subduction-related volcanic arcs within the inner Mediterranean (Faccena et al., 2004, Booth-Rea et al. 2007; Garrido et al., 2011; Carminati et al., in press). We suggest that these major tectonic events have stripped off most of the old continental crust, leaving behind residues of ancient subcontinental mantle. This mantle, buoyant relative to the asthenosphere, would continue to ride over the small-scale convective cells detected by seismic tomography at depths > 200 km (O'Reilly et al., 2009; Faccenna and Becker, 2010), then become part of the oceanic basin and serve as the basement for the accumulation of oceanic basalts and sediments. An analogous process has been described in detail from the Internal Ligurides, where a typical Mesozoic oceanic volcanic-sedimentary section overlies the Archean mantle peridotites (Rampone et al., 2005). It is important to note that some portions of the Archean SCLM within the inner Mediterranean were refertilised ($Mg\# = 89$ -90 of olivine in peridotite) by the passage of subduction-related fluids in the Cenozoic. However, these fluids were not able to erase the old Archean Re-Os signatures preserved in some sulfides (Marchesi et al. 2010).

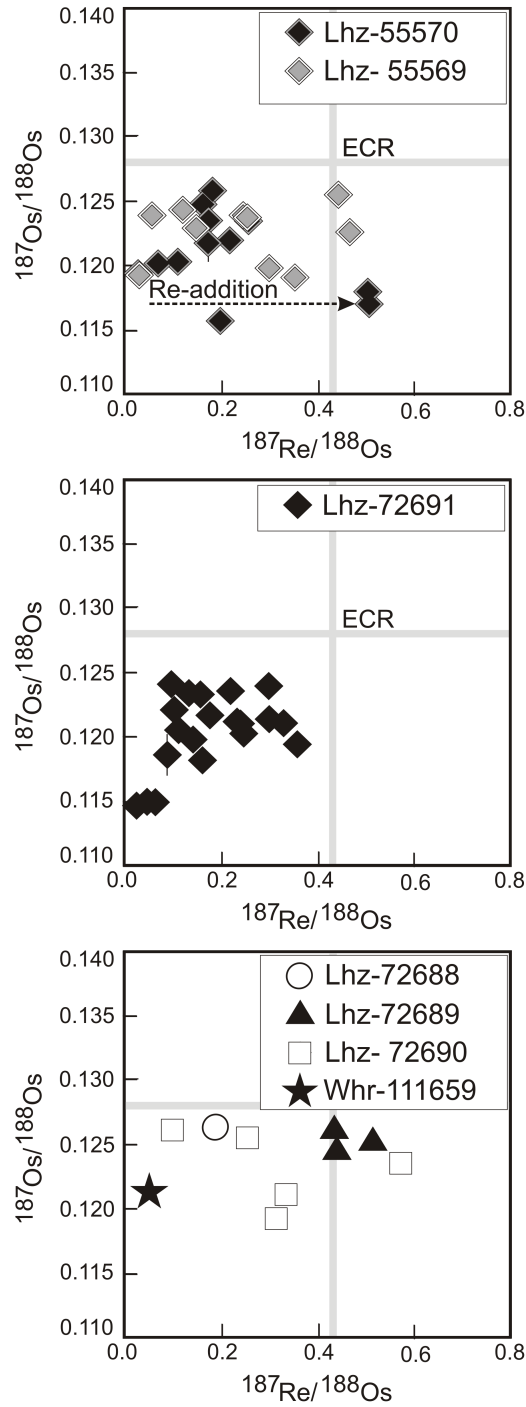


Figure DR1 Plots of $^{187}\text{Re}/^{188}\text{Os}$ versus $^{187}\text{Os}/^{188}\text{Os}$ for sulfides of the El Aprisco peridotite xenoliths. Note that uncertainties (2SE) are presented as bars but in most cases they are smaller than symbols sizes. ECR correspond to values of the Enstatitic Chondritic Reservoir (Walker et al., 2002). Legend inset; **Lhz**: lherzolite; **Whr**: wehrlite, numbers refer to the sample labeling of Villaseca et al. (2010)

Part III

Conclusions

8. Conclusions

The main goal of this Thesis has been to investigate the structure and geochemical composition and evolution of the subcontinental lithospheric mantle (SCLM) beneath convergent settings and that are recorded in mantle xenoliths hosted in postorogenic alkaline magmatism. The Thesis investigates two cases of study: (i.) SCLM involving circumcratonic in collisional orogens around cratons (Sangilen Plateau, Tuva, Russia); and (ii.) SCLM recording supra-subduction and continental delamination tectonomagmatic processes related to the Tertiary Alpine evolution of the Betic-Rif Cordillera (SE Iberian Volcanic Province, Murcia, SE Spain).

8.1. SCLM Involving Circumcratonic Mantle in Collisional Orogens

We have studied spinel peridotite xenoliths hosted in Early Ordovician alkaline lamprophyres from the Sangilen Plateau (Tuva, Russia) in the accretionary Central Asian orogenic belt (southern Siberia). These lamprophyre-hosted spinel peridotite xenoliths allowed us to investigate the composition and thermal structure of the circumcratonic subcontinental lithospheric mantle of the Tuva-Mongolian micro-continent. Sangilen mantle xenoliths therefore offer complementary information on the Central Asia subcontinental mantle lithosphere to that provided by mantle xenoliths in younger Neogene basalts that sample the subcontinental mantle.

On the basis of our petrological and geochemical study of Sangilen mantle xenoliths, the following conclusions could be drawn: (i.) Sangilen xenoliths record a narrow range of equilibration temperature (*ca.* 1000–1100 °C) plotting along a relatively hot intracontinental geotherm at lithospheric depths from ~43 to 53 km (1.3 to 1.6 GPa); (ii.) Their variation of olivine Mg# (87.9–90.9) with spinel Cr# (9.5–45.7) indicates xenoliths are mostly residues of up to 10% melting of a depleted peridotite source; (iii.) The elevated Yb_N content of clinopyroxene (sample 5H-10) and the variable fractionation of LREE-MREE relative to HREE in clinopyroxene from other xenoliths indicate they underwent variable metasomatic processes. These processes probably consisted of episodes of percolation-reaction through peridotite of small-melt fractions of alkaline mafic melts precursor to Agardag alkaline lamprophyres; (iv.) The lack of correlation with depth of modal variations, textural types, and the inferred degrees of melting and trace element patterns of clinopyroxene, indicates the absence of a texturally or compositionally layering in the lithospheric mantle at the time of his sampling by Ordovician lamprophyres. As shown by numerical percolation-reaction

models, the observed compositionally variation of xenoliths is better accounted by depleted lithosphere variably metasomatized along a network of percolating alkaline mafic melts heterogeneously distributed throughout the Sangilen lithospheric mantle section.

8.2. SCLM in Supra-Subduction and Continental Delamination Settings

Plio-Pleistocene Alkali basalts—2-3 Ma—in the inner easternmost Betic Cordillera, have entrained numerous mantle xenoliths that provide a snapshot of the structure and composition of the lithospheric mantle beneath the NE termination of the Alboran arc system in the western Mediterranean. They also record the deformation of the lithospheric mantle and yield complementary information to seismological observations.

A synthesis of available *in situ* and whole-rock Os-isotope data on mantle-derived peridotites shows that maximum TRD ages of *ca.* 1.8 Ga is widespread in the subcontinental mantle of Europe and Africa outboard from the Betics-Maghrebides-Appennines front. In contrast, the mantle enclosed within the Alpine domain records TRD as old as 2.6 Ga in Tallante, revealing a previously unrecognized Archean domain or domains in the Central/Western Mediterranean. Our observations indicate that ancient fragments of subcontinental lithospheric mantle have played an important role in the development of the present architecture of the Mediterranean lithosphere. Re-depletion model ages of sulfides in peridotite xenoliths and U-Pb ages in lower crust xenoliths and anatectic melts in the Eastern Betics yield inherited Neoproterozoic ages similar to those reported in the Ronda orogenic peridotite and lower crust in the western Betics Alpujarrides. These ages indicate a non-Iberian provenance of the lower crust and subcrustal lithosphere in the eastern Betic. Despite their common Alboran provenance, eastern Betic mantle xenoliths sampled a more fertile mantle lithosphere recording a younger and distinct deformation regime than that preserved in the Ronda peridotite.

The detailed microstructural and crystal preferred orientation study of xenoliths provide important insights into the origin and deformation record of the mantle in the westernmost Mediterranean. CPOs of orthopyroxene in orthopyroxenite veins of composite xenoliths—formed at 2.2-4.4 Ma by silica-rich fluid/melt reaction with mantle peridotite—indicates that metasomatism was synkinematic with high-T ductile dislocation creep flow of mantle peridotite, demonstrating that ductile fabrics were developed sometime in the late Neogene. Peridotite xenoliths show a distinct olivine axial-[100] pattern that is characteristic of deformation under simple shear in a transtensional tectonic regime. Texture and composition of xenoliths record decompression from depths of at least 55-60 km up to

shallow subcrustal depths of 19-20 km. Synkinematic overprinting of mineral assemblages from the garnet-spinel to the plagioclase facies demonstrates that this 36-40 km uplift was continuously accommodated by ductile shear thinning of the lithospheric mantle. Lithospheric thinning had minimum stretching beta factors of *ca.* 1.5 and long-term high strain rates of *ca.* $9\cdot 7\cdot 10^{-13}$ s⁻¹, values that are characteristics of rapidly extending continental lithosphere with geothermal gradient in excess of 100 mW·m⁻².

As constrained by the calculate seismic properties of Eastern Betic mantle xenoliths, the N 69° strike of SKS and Pn seismic anisotropy in the eastern Betics can be explained by a shallow lithospheric mantle fabric with olivine [100]-axes subhorizontal and subparallel to the mantle flow direction. The current shallow mantle lithosphere thickness (40-80 km) and measured delays of SKS waves in the eastern Betics can only be accounted for by a steeply dipping mantle foliation and subhorizontal lineation; this geometry of the lithospheric mantle peridotite fabric implies active or frozen mantle flow with a dominantly strike-slip component subparallel to the paleo-Iberian margin. This configuration may reflect strike-slip deformation in the early Miocene during W-SW slab retreat of the Alboran lithosphere at the edge of the Iberian margin. Compositional profiles in xenoliths indicate that initiation of ductile thinning of the subcontinental mantle may have occurred sometime between 6.2 and 9.4 Ma. This time span broadly overlaps with deep processes events in the eastern Betics such as onset of lower crust anatexis (*ca.* 9 Ma) and the change from subduction-related to intraplate-type volcanism (6.3-4.8 Ma). These magmatic events are synchronous with uplift associated with the Messinian salinity crisis that some authors ascribe to asthenospheric upwelling and lithospheric edge delamination of the Iberian margin during westward rollback of subducted Tethys oceanic lithosphere. Edge delamination of the Iberian margin mantle thinning and decompression of hot extended lithospheric of Alboran provenance and its lateral westward inflow under the detached margins to fill the detached cold lithosphere following the inherited S-SW lithospheric anisotropy. This process would explain flat Moho, thin lithosphere, heating, crustal anatexis, shift of magmatism, and uplift in the late Miocene and Pliocene in the Eastern Betics. Detachment of the subducted lithospheric mantle and westward replacement by Alboran-type hot lower lithosphere would account for Alboran provenance of mantle and lower crustal in the Eastern Betics. This geological paroxysm was coeval to middle to late Miocene E-W opening and oceanic magmatic accretion of the Algero-Balearic basin. The existence of strike-slip inherited mantle fabrics may continue governing some deep processes in the Eastern Betics.

Detailed geochemical study of whole rock and mineral major- and trace elements, as well as Nd-Sr-Pb isotopic composition data on xenoliths provide key information on how these Alpine tectono-magmatic processes have affected the westernmost Mediterranean subcontinental mantle. The whole rock major element compositional variation, along with by their mineral chemistry, reflects increasing fertility from clinopyroxene-poor peridotites (Group I; Mg# up to 0.915), common lherzolites (Group II; Mg# up to 0.906) and fertile lherzolites (Group III; Mg# of 0.868-0.889) to wehrlites (Mg# of 0.867-0.874). The mineral major element chemistry records the geochemical imprint of maximum 10-12 % partial melting in the most depleted Group I peridotites. Trace element and isotopic data attest for various degrees of metasomatic enrichment that overprinted the previously depleted lithospheric mantle. Interaction with melts produced enrichment of LREE in Group II and Group III peridotites, as well as wehrlites. In contrast to major and trace elements, Nd-Sr-Pb radiogenic isotope systematic is unrelated to compositional groups and shows isotopic variations between DMM to EM2 end-member and contribution of an Atlantic sediment-like component. These geochemical evidences attest for the percolation of slab-derived, SiO₂-undersaturated melts (and hydrous fluids) with a sediment affinity in the supra-subduction continental lithospheric mantle beneath the Alboran Basin, possibly released from the subducted Tethys oceanic lithosphere.

Part IV

References

9. References

- Abramson, E.H., Brown, J.M., Slutsky, L.J., Zaug, J., 1997. The elastic constants of San Carlos olivine to 17 GPa. *Journal of Geophysical Research: Solid Earth* 102, 12253–12263.
- Acosta, J., Muñoz, A., Herranz, P., Palomo, C., Ballesteros, M., Vaquero, M., Uchupi, E., 2001. Geodynamics of the Emile Baudot Escarpment and the Balearic Promontory, western Mediterranean. *Marine and Petroleum Geology* 18, 349–369.
- Acosta-Vigil, A., Buick, I., Hermann, J., Cesare, B., Rubatto, D., London, D., Morgan, G.B., 2010. Mechanisms of Crustal Anatexis: a Geochemical Study of Partially Melted Metapelitic Enclaves and Host Dacite, SE Spain. *J. Petrology* 51, 785–821.
- Acosta-Vigil, A., Cesare, B., London, D., Morgan VI, G.B., 2007. Microstructures and composition of melt inclusions in a crustal anatectic environment, represented by metapelitic enclaves within El Hoyazo dacites, SE Spain. *Chemical Geology* 237, 450–465.
- Alard, O., Griffin, W.L., Pearson, N.J., Lorand, J.-P., O'Reilly, S.Y., 2002. New insights into the Re-Os systematics of sub-continental lithospheric mantle from in situ analysis of sulphides. *Earth and Planetary Science Letters* 203, 651–663.
- Alard, O., Luguët, A., Pearson, N.J., Griffin, W.L., Lorand, J.-P., Gannoun, A., Burton, K.W., O'Reilly, S.Y., 2005. In situ Os isotopes in abyssal peridotites bridge the isotopic gap between MORBs and their source mantle. *Nature* 436, 1005–1008.
- Allègre, C.J., Poirier, J.-P., Humler, E., Hofmann, A.W., 1995. The chemical composition of the Earth. *Earth and Planetary Science Letters* 134, 515–526.
- Álvarez, F., Aldaya, F., Navarro-Vilá, F., 1989. Miocene extensional deformations in the region of Aguilas-Mazarrón (Eastern Betic Cordilleras). *Estudios Geológicos* 45, 369–374.
- Álvarez-Valero, A.M., Kriegsman, L.M., 2007. Crustal thinning and mafic underplating beneath the Neogene Volcanic Province (Betic Cordillera, SE Spain): evidence from crustal xenoliths. *Terra Nova* 19, 266–271.
- Ancochea, E., 2004. La región volcánica del Campo de Calatrava, in: *Geología De España*. SGE-IGME, Madrid, pp. 676–677.
- Aoki, K.-I., 1971. Petrology of mafic inclusions from Itinome-gata, Japan. *Contr. Mineral. and Petrol.* 30, 314–331.
- Arai, S., 1994. Compositional variation of olivine-chromian spinel in Mg-rich magmas as a guide to their residual spinel peridotites. *Journal of Volcanology and Geothermal Research* 59, 279–293.
- Arai, S., Shimizu, Y., Gervilla, F., 2003. Quartz diorite veins in a peridotite xenolith from Tallante, Spain: implications for reaction and survival of slab-derived SiO₂-oversaturated melt in the upper mantle. *Proceedings of the Japan Academy, Series B* 79B, 145–150.
- Ashchepkov, I.V., André, L., Downes, H., Belyatsky, B.A., 2011. Pyroxenites and megacrysts from Vitim picrite-basalts (Russia): Polybaric fractionation of rising melts in the mantle? *Journal of Asian Earth Sciences* 42, 14–37.
- Ashchepkov, I.V., Pokhilenko, N.P., Vladykin, N.V., Logvinova, A.M., Afanasiev, V.P., Pokhilenko, L.N., Kuligin, S.S., Malygina, E.V., Alymova, N.A., Kostrovitsky, S.I., Rotman, A.Y., Mityukhin, S.I., Karpenko, M.A., Stegnitsky, Y.B., Khemelnikova, O.S., 2010. Structure and evolution of the lithospheric mantle beneath Siberian craton, thermobarometric study. *Tectonophysics* 485, 17–41.
- Azañón, J.-M., Crespo-Blanc, A., 2000. Exhumation during a continental collision inferred from the tectonometamorphic evolution of the Alpujarride Complex in the central Betics (Alboran Domain, SE Spain). *Tectonics* 19, 549–565.
- Azañón, J.M., Crespo-Blanc, A., García-Dueñas, V., 1997. Continental collision, crustal thinning and nappe forming during the pre-Miocene evolution of the Alpujarride Complex (Alboran Domain,

- Betics). *Journal of Structural Geology* 19, 1055-1071.
- Balanyá, J.C., García-Dueñas, V., Azañón, J.M., Sánchez-Gómez, M., 1997. Alternating contractional and extensional events in the Alpujarride nappes of the Alboran Domain (Betics, Gibraltar Arc). *Tectonics* 16, 226-238.
- Bali, E., Szabó, C., Vaselli, O., Török, K., 2002. Significance of silicate melt pockets in upper mantle xenoliths from the Bakony-Balaton Highland Volcanic Field, Western Hungary. *Lithos* 61, 79-102.
- Ballhaus, C., Berry, R.F., Green, D.H., 1991. High pressure experimental calibration of the olivine-orthopyroxene-spinel oxygen geobarometer: implications for the oxidation state of the upper mantle. *Contrib. Mineral. and Petrol.* 107, 27-40.
- Balogh, K., Ahijado, A., Casillas, R., Fernández, C., 1999. Contributions to the chronology of the Basal Complex of Fuerteventura, Canary Islands. *Journal of Volcanology and Geothermal Research* 90, 81-101.
- Banda, E., Ansorge, J., 1980. Crustal structure under the central and eastern part of the Betic Cordillera. *Geophys. J. Int.* 63, 515-532.
- Banda, E., Gallart, J., García-Dueñas, V., Dañobeitia, J.J., Makris, J., 1993. Lateral variation of the crust in the Iberian peninsula: New evidence from the Betic Cordillera. *Tectonophysics* 221, 53-66.
- Bandrés, A., Eguíluz, L., Pin, C., Paquette, J.L., Ordóñez, B., Fèvre, B.L., Ortega, L.A., Ibarguchi, J.I.G., 2004. The northern Ossa-Morena Cadomian batholith (Iberian Massif): magmatic arc origin and early evolution. *Int J Earth Sci (Geol Rundsch)* 93, 860-885.
- Baptiste, V., Tommasi, A., Demouchy, S., 2012. Deformation and hydration of the lithospheric mantle beneath the Kaapvaal craton, South Africa. *Lithos* 149, 31-50.
- Bartrina, M.T., Cabrera, L., Jurado, M.J., Guimerà, J., Roca, E., 1992. Evolution of the central Catalan margin of the Valencia trough (western Mediterranean). *Tectonophysics* 203, 219-247.
- Bascou, J., Tommasi, A., Mainprice, D., 2002. Plastic deformation and development of clinopyroxene lattice preferred orientations in eclogites. *Journal of Structural Geology* 24, 1357-1368.
- Beard, A.D., Downes, H., Mason, P.R.D., Vetrin, V.R., 2007. Depletion and enrichment processes in the lithospheric mantle beneath the Kola Peninsula (Russia): Evidence from spinel lherzolite and wehrlite xenoliths. *Lithos* 94, 1-24.
- Beccaluva, L., Azzouni-Sekkal, A., Benhallou, A., Bianchini, G., Ellam, R.M., Marzola, M., Siena, F., Stuart, F.M., 2007. Intracratonic asthenosphere upwelling and lithosphere rejuvenation beneath the Hoggar swell (Algeria): Evidence from HIMU metasomatised lherzolite mantle xenoliths. *Earth and Planetary Science Letters* 260, 482-494.
- Beccaluva, L., Bianchini, G., Bonadiman, C., Siena, F., Vaccaro, C., 2004. Coexisting anorogenic and subduction-related metasomatism in mantle xenoliths from the Betic Cordillera (southern Spain). *Lithos* 75, 67-87.
- Bedini, R., Bodinier, J.-L., 1999. Distribution of incompatible trace elements between the constituents of spinel peridotite xenoliths: ICP-MS data from the East African rift. *Geochimica et Cosmochimica Acta* 63, 3883-3900.
- Bedini, R.M., Bodinier, J.-L., Dautria, J.-M., Morten, L., 1997. Evolution of LILE-enriched small melt fractions in the lithospheric mantle: a case study from the East African Rift. *Earth and Planetary Science Letters* 153, 67-83.
- Behr, W.M., Platt, J.P., 2012. Kinematic and thermal evolution during two-stage exhumation of a Mediterranean subduction complex. *Tectonics* 31, n/a-n/a.
- Bell, D.R., Grégoire, M., Grove, T.L., Chatterjee, N., Carlson, R.W., Buseck, P.R., 2005. Silica and volatile-element metasomatism of Archean mantle: a xenolith-scale example from the Kaapvaal Craton. *Contrib Mineral Petrol* 150, 251-267.
- Bellon, H., Bordet, P., Montenat, C., 1983. Chronology of the Neogene Magmatism

- from Betic Ranges (southern Spain). *Bull. Soc. Geol. Fr.* 25, 205–217.
- Ben Ismail, W., Mainprice, D., 1998. An olivine fabric database: an overview of upper mantle fabrics and seismic anisotropy. *Tectonophysics* 296, 145–157.
- Ben Othman, D., White, W.M., Patchett, J., 1989. The geochemistry of marine sediments, island arc magma genesis, and crust-mantle recycling. *Earth and Planetary Science Letters* 94, 1–21.
- Benito, R., López-Ruiz, J., Cebriá, J.M., Hertogen, J., Doblas, M., Oyarzun, R., Demaiffe, D., 1999. Sr and O isotope constraints on source and crustal contamination in the high-K calc-alkaline and shoshonitic neogene volcanic rocks of SE Spain. *Lithos* 46, 773–802.
- Berzin, N.A., Coleman, R.G., Dobretsov, N.L., Zonenshain, L.P., Xiao, X., Chang, E., 1994. Geodynamic map of the western part of Paleasian ocean. *Russian Geology and Geophysics* 35, 5–52.
- Beyer, E.E., Griffin, W.L., O'reilly, S.Y., 2006. Transformation of Archaean Lithospheric Mantle by Refertilization: Evidence from Exposed Peridotites in the Western Gneiss Region, Norway. *J. Petrology* 47, 1611–1636.
- Bianchini, G., Beccaluva, L., Bonadiman, C., Nowell, G.M., Pearson, D.G., Siena, F., Wilson, M., 2010. Mantle metasomatism by melts of HIMU piclogite components: new insights from Fe-lherzolite xenoliths (Calatrava Volcanic District, Central Spain), in: Coltorti, M., Downes, H., Grégoire, M., O'Reilly, S.Y. (Eds.), *Petrological Evolution of the European Lithospheric Mantle*, Geological Society Special Publication. Geological Society, London, pp. 152–171.
- Bianchini, G., Beccaluva, L., Nowell, G.M., Pearson, D.G., Siena, F., 2011. Mantle xenoliths from Tallante (Betic Cordillera): Insights into the multi-stage evolution of the south Iberian lithosphere. *Lithos* 124, 308–318.
- Bina, C.R., 2003. 2.02 - Seismological Constraints upon Mantle Composition, in: Editors-in-Chief: Heinrich D. Holland, Karl K. Turekian (Eds.), *Treatise on Geochemistry*. Pergamon, Oxford, pp. 39–59.
- Blumenthal, M.M., 1929. Über das Alter der ersten postorogenetischen Sedimente in den westlichen betischen Kordilleren und die dadurch festgelegte Hauptphase der Gebirgsbildung. *Geol Rundsch* 20, 205–210.
- Bodinier, J.-L., Fabries, J., Lorand, J.P., Dostal, J., Dupuy, C., 1987. Geochemistry of amphibole pyroxenite veins from the Lherz and Freychinde ultramafic bodies (Ariège, French Pyrenées). *Bulletin de Minéralogie* 110, 345–358.
- Bodinier, J.-L., Garrido, C.J., Chanefo, I., Bruguier, O., Gervilla, F., 2008. Origin of Pyroxenite-Peridotite Veined Mantle by Refertilization Reactions: Evidence from the Ronda Peridotite (Southern Spain). *J. Petrology* 49, 999–1025.
- Bodinier, J.-L., Godard, M., 2003. 2.04 - Orogenic, Ophiolitic, and Abyssal Peridotites, in: Editors-in-Chief: Heinrich D. Holland, Karl K. Turekian (Eds.), *Treatise on Geochemistry*. Pergamon, Oxford, pp. 1–73.
- Bodinier, J.-L., Menzies, M.A., Shimizu, N., Frey, F.A., McPHERSON, E., 2004. Silicate, Hydrous and Carbonate Metasomatism at Lherz, France: Contemporaneous Derivatives of Silicate Melt-Harzburgite Reaction. *J. Petrology* 45, 299–320.
- Bodinier, J.L., Dupuy, C., Vernieres, J., 1988. Behaviour of trace elements during upper mantle metasomatism: Evidences from the Lherz massif. *Chemical Geology* 70, 152.
- Bodinier, J.L., Vasseur, G., Vernieres, J., Dupuy, C., Fabries, J., 1990. Mechanisms of Mantle Metasomatism: Geochemical Evidence from the Lherz Orogenic Peridotite. *J. Petrology* 31, 597–628.
- Boivin, P.A., 1982. Interaction entre magma basaltique et manteau supérieur. Exemple du Devés (Massif Central français) et du volcanisme quaternaire de la région de carthagène, Espagne. (Thèse Etat). University of Clermont-Ferrand, Clermont-Ferrand (France).
- Bokelmann, G., Maufray, E., Buontempo, L., Morales, J., Barruol, G., 2011. Testing oceanic subduction and convective removal models for the Gibraltar arc: Seismological constraints from dispersion and anisotropy. *Tectonophysics* 502, 28–37.

- Booth-Rea, G., Azañón, J.-M., Azor, A., García-Dueñas, V., 2004a. Influence of strike-slip fault segmentation on drainage evolution and topography. A case study: the Palomares Fault Zone (southeastern Betics, Spain). *Journal of Structural Geology* 26, 1615–1632.
- Booth-Rea, G., Azañón, J.M., García-Dueñas, V., 2004b. Extensional tectonics in the northeastern Betics (SE Spain): case study of extension in a multilayered upper crust with contrasting rheologies. *Journal of Structural Geology* 26, 2039–2058.
- Booth-Rea, G., Azañón, J.M., Martínez-Martínez, J.M., Vidal, O., García-Dueñas, V., 2005. Contrasting structural and P-T evolution of tectonic units in the southeastern Betics: Key for understanding the exhumation of the Alboran Domain HP/LT crustal rocks (western Mediterranean). *Tectonics* 24, n/a–n/a.
- Booth-Rea, G., Ranero, C.R., Martínez-Martínez, J.M., Grevemeyer, I., 2007. Crustal types and Tertiary tectonic evolution of the Alborán sea, western Mediterranean. *Geochem. Geophys. Geosyst.* 8, Q10005.
- Borghini, G., Fumagalli, P., Rampone, E., 2010. The Stability of Plagioclase in the Upper Mantle: Subsolvus Experiments on Fertile and Depleted Lherzolite. *J. Petrology* 51, 229–254.
- Borghini, G., Fumagalli, P., Rampone, E., 2011. The geobarometric significance of plagioclase in mantle peridotites: A link between nature and experiments. *Lithos* 126, 42–53.
- Boullier, A.M., Nicolas, A., 1975. Classification of textures and fabrics of peridotite xenoliths from South African kimberlites, in: Ahrens, L.H. (Ed.), *Classification of textures and fabrics of peridotite xenoliths from South African kimberlites*. Pergamon Press, Oxford; New York, pp. 97–105.
- Boyd, F., 1973. A pyroxene geotherm. *Geochimica et Cosmochimica Acta* 37, 2533–2546.
- Boyd, F.R., 1989. Compositional distinction between oceanic and cratonic lithosphere. *Earth and Planetary Science Letters* 96, 15–26.
- Boyd, F.R., Jones, R.A., Nixon, P.H., 1983. Mantle metasomatism: the Kimberley dunites. *Carnegie Institution of Washington Year Book* 82, 330–336.
- Boyd, F.R., Nixon, P.H., 1978. Ultramafic nodules from the Kimberley pipes, South Africa. *Geochimica et Cosmochimica Acta* 42, 1367–1382.
- Brandon, A.D., Becker, H., Carlson, R.W., Shirey, S.B., 1999. Isotopic constraints on time scales and mechanisms of slab material transport in the mantle wedge: evidence from the Simcoe mantle xenoliths, Washington, USA. *Chemical Geology* 160, 387–407.
- Brandon, A.D., Draper, D.S., 1996. Constraints on the origin of the oxidation state of mantle overlying subduction zones: An example from Simcoe, Washington, USA. *Geochimica et Cosmochimica Acta* 60, 1739–1749.
- Brey, G.P., Köhler, T., 1990. Geothermobarometry in Four-phase Lherzolites II. New Thermobarometers, and Practical Assessment of Existing Thermobarometers. *J. Petrology* 31, 1353–1378.
- Brey, G.P., Köhler, T., Nickel, K.G., 1990. Geothermobarometry in Four-phase Lherzolites I. Experimental Results from 10 to 60 kb. *J. Petrology* 31, 1313–1352.
- Bryndzia, L.T., Wood, B.J., 1990. Oxygen thermobarometry of abyssal spinel peridotites; the redox state and C-O-H volatile composition of the Earth's sub-oceanic upper mantle. *Am J Sci* 290, 1093–1116.
- Bucher, K., 1994. *Petrogenesis of metamorphic rocks*, 6th ed., complete revision of Winkler's textbook. ed. Springer-Verlag, Berlin; New York.
- Bufo, E., Bezzeghoud, M., Udías, A., Pro, C., 2004. Seismic Sources on the Iberia-African Plate Boundary and their Tectonic Implications. *Pure appl. geophys.* 161, 623–646.
- Buontempo, L., Bokelmann, G.H.R., Barruol, G., Morales, J., 2008. Seismic anisotropy beneath southern Iberia from SKS splitting.

- Earth and Planetary Science Letters 273, 237–250.
- Calvert, A., Sandvol, E., Seber, D., Barazangi, M., Roecker, S., Mourabit, T., Vidal, F., Alguacil, G., Jabour, N., 2000. Geodynamic evolution of the lithosphere and upper mantle beneath the Alboran region of the western Mediterranean: Constraints from travel time tomography. *J. Geophys. Res.* 105, 10871–10,898.
- Canil, D., 1999. Vanadium partitioning between orthopyroxene, spinel and silicate melt and the redox states of mantle source regions for primary magmas. *Geochimica et Cosmochimica Acta* 63, 557–572.
- Canil, D., 2002. Vanadium in peridotites, mantle redox and tectonic environments: Archean to present. *Earth and Planetary Science Letters* 195, 75–90.
- Canil, D., O'Neill, H.S.C., 1996. Distribution of Ferric Iron in some Upper-Mantle Assemblages. *J. Petrology* 37, 609–635.
- Canil, D., Virgo, D., Scarfe, C.M., 1990. Oxidation state of mantle xenoliths from British Columbia, Canada. *Contr. Mineral. and Petrol.* 104, 453–462.
- Capedri, S., Venturelli, G., Salviolimariani, E., Crawford, A., Barbieri, M., 1989. Upper-Mantle Xenoliths and Megacrysts in an Alkali Basalt from Tallante, Southeastern Spain. *Eur. J. Mineral.* 1, 685–699.
- Carlson, R.W., Pearson, D.G., James, D.E., 2005. Physical, chemical, and chronological characteristics of continental mantle. *Rev. Geophys.* 43, RG1001.
- Carminati, E., Lustrino, M., Doglioni, C., 2012. Geodynamic evolution of the central and western Mediterranean: Tectonics vs. igneous petrology constraints. *Tectonophysics* 579, 173–192.
- Carminati, E., Wortel, M.J., Spakman, W., Sabadini, R., 1998. The role of slab detachment processes in the opening of the western-central Mediterranean basins: some geological and geophysical evidence. *Earth and Planetary Science Letters* 160, 651–665.
- Cebriá, J.M., López-Ruiz, J., Carmona, J., Doblas, M., 2009. Quantitative petrogenetic constraints on the Pliocene alkali basaltic volcanism of the SE Spain Volcanic Province. *Journal of Volcanology and Geothermal Research* 185, 172–180.
- Cesare, B., Gómez-Pugnaire, M.T., 2001. Crustal melting in the alborán domain: constraints from xenoliths of the Neogene Volcanic Province. *Physics and Chemistry of the Earth, Part A: Solid Earth and Geodesy* 26, 255–260.
- Cesare, B., Gómez-Pugnaire, M.T., Rubatto, D., 2003. Residence time of S-type anatectic magmas beneath the Neogene Volcanic Province of SE Spain: a zircon and monazite SHRIMP study. *Contrib Mineral Petrol* 146, 28–43.
- Coe, R.S., Kirby, S.H., 1975. The orthoenstatite to clinoenstatite transformation by shearing and reversion by annealing: Mechanism and potential applications. *Contr. Mineral. and Petrol.* 52, 29–55.
- Coltorti, M., Bonadiman, C., Faccini, B., Ntaflos, T., Siena, F., 2007. Slab melt and intraplate metasomatism in Kapfenstein mantle xenoliths (Styrian Basin, Austria). *Lithos* 94, 66–89.
- Coltorti, M., Bonadiman, C., Hinton, R.W., Siena, F., Upton, B.G.J., 1999. Carbonatite Metasomatism of the Oceanic Upper Mantle: Evidence from Clinopyroxenes and Glasses in Ultramafic Xenoliths of Grande Comore, Indian Ocean. *J. Petrology* 40, 133–165.
- Comas, M.C., Platt, J.P., Soto, J.-I., Watts, A.B., 1999. The origin and tectonic history of the Alboran basin: insights from Leg 161 results, in: Zahn, R., Comas, M.C., Klaus, A. (Eds.), *Proceedings of the Ocean Drilling Program, 161 Scientific Results. Ocean Drilling Program*, pp. 1–27.
- Conticelli, S., Guarnieri, L., Farinelli, A., Mattei, M., Avanzinelli, R., Bianchini, G., Boari, E., Tommasini, S., Tiepolo, M., Prelević, D., Venturelli, G., 2009. Trace elements and Sr-Nd-Pb isotopes of K-rich, shoshonitic, and calc-alkaline magmatism of the Western Mediterranean Region: Genesis of ultrapotassic to calc-alkaline magmatic associations in a post-collisional geodynamic setting. *Lithos* 107, 68–92.

- Coulon, C., Megartsi, M., Fourcade, S., Maury, R.C., Bellon, H., Louni-Hacini, A., Cotten, J., Coutelle, A., Hermitte, D., 2002. Post-collisional transition from calc-alkaline to alkaline volcanism during the Neogene in Oranie (Algeria): magmatic expression of a slab breakoff. *Lithos* 62, 87–110.
- Dautria, J.M., Dupuy, C., Takherist, D., Dostal, J., 1992. Carbonate metasomatism in the lithospheric mantle: peridotitic xenoliths from a melilititic district of the Sahara basin. *Contrib Mineral Petrol* 111, 37–52.
- Dawson, J.B., Smith, J.V., 1977. The MARID (mica-amphibole-rutile-ilmenite-diopside) suite of xenoliths in kimberlite. *Geochimica et Cosmochimica Acta* 41, 309–323.
- De Larouzière, F.D., Bolze, J., Bordet, P., Hernandez, J., Montenat, C., Ott d'Estevou, P., 1988. The Betic segment of the lithospheric Trans-Alboran shear zone during the Late Miocene. *Tectonophysics* 152, 41–52.
- Dewey, J.F., Helman, M.L., Knott, S.D., Turco, E., Hutton, D.H.W., 1989. Kinematics of the western Mediterranean. *Geological Society, London, Special Publications* 45, 265–283.
- Dewey, J.F., Pitman, W.C., Ryan, W.B.F., Bonnin, J., 1973. Plate Tectonics and the Evolution of the Alpine System. *Geological Society of America Bulletin* 84, 3137–3180.
- Díaz de Federico, A., Torres-Roldán, R.L., Puga, E., 1990. The rock-series of the Betic substratum, in: Montenat, C. (Ed.), *Les Bassins Néogènes Du Domaine Betique Oriental (Espagne): Tectonique Et Sédimentation Dans Un Couloir De Décrochement*. Institut géologique Albert-de-Lapparent, Paris, pp. 19–29.
- Díaz, J., Gallart, J., Villaseñor, A., Mancilla, F., Pazos, A., Córdoba, D., Pulgar, J.A., Ibarra, P., Harnafi, M., 2010. Mantle dynamics beneath the Gibraltar Arc (western Mediterranean) from shear-wave splitting measurements on a dense seismic array. *Geophys. Res. Lett.* 37, L18304.
- Dickin, A.P., 2005. *Radiogenic isotope geology*. Cambridge University Press, Cambridge; New York.
- Doblas, M., López-Ruiz, J., Cebriá, J.-M., 2007. Cenozoic evolution of the Alboran Domain: A review of the tectonomagmatic models. *Geological Society of America Special Papers* 418, 303–320.
- Dobretsov, N.L., Buslov, M.M., 2007. Late Cambrian-Ordovician tectonics and geodynamics of Central Asia. *Russian Geology and Geophysics* 48, 71–82.
- Donnelly, K.E., Goldstein, S.L., Langmuir, C.H., Spiegelman, M., 2004. Origin of enriched ocean ridge basalts and implications for mantle dynamics. *Earth and Planetary Science Letters* 226, 347–366.
- Dornbush, H.J., Weber, K., Skrotzki, W., 1994. Development of microstructure and texture in high-temperature mylonites from the Ivrea Zone, in: Bunge, H.J., Siegesmund, D., Skrotzki, W., Weber, K. (Eds.), *Textures of geological materials*. DGM-Informationsgesellschaft-Verlag, Oberursel, pp. 187–201.
- Downes, H., 2001. Formation and Modification of the Shallow Sub-continental Lithospheric Mantle: a Review of Geochemical Evidence from Ultramafic Xenolith Suites and Tectonically Emplaced Ultramafic Massifs of Western and Central Europe. *J. Petrology* 42, 233–250.
- Downes, H., Dupuy, C., 1987. Textural, isotopic and REE variations in spinel peridotite xenoliths, Massif Central, France. *Earth and Planetary Science Letters* 82, 121–135.
- Downes, H., Embey-Isztin, A., Thirlwall, M.F., 1992. Petrology and geochemistry of spinel peridotite xenoliths from the western Pannonian Basin (Hungary): evidence for an association between enrichment and texture in the upper mantle. *Contr. Mineral. and Petrol.* 109, 340–354.
- Downes, H., Kempton, P.D., Briot, D., Harmon, R.S., Leyreloup, A.F., 1991. Pb and O isotope systematics in granulite facies xenoliths, French Massif Central: implications for crustal processes. *Earth and Planetary Science Letters* 102, 342–357.
- Duffy, T.S., Vaughan, M.T., 1988. Elasticity of enstatite and its relationship to crystal structure. *Journal of Geophysical Research: Solid Earth* 93, 383–391.

- Duggen, S., Hoernle, K., Bogaard, P.V.D., Garbe-Schönberg, D., 2005. Post-Collisional Transition from Subduction- to Intraplate-type Magmatism in the Westernmost Mediterranean: Evidence for Continental-Edge Delamination of Subcontinental Lithosphere. *J. Petrology* 46, 1155–1201.
- Duggen, S., Hoernle, K., Klügel, A., Geldmacher, J., Thirlwall, M., Hauff, F., Lowry, D., Oates, N., 2008. Geochemical zonation of the Miocene Alborán Basin volcanism (westernmost Mediterranean): geodynamic implications. *Contrib Mineral Petrol* 156, 577–593.
- Duggen, S., Hoernle, K., Van den Bogaard, P., Harris, C., 2004. Magmatic evolution of the Alboran region: The role of subduction in forming the western Mediterranean and causing the Messinian Salinity Crisis. *Earth and Planetary Science Letters* 218, 91–108.
- Duggen, S., Hoernle, K., Van den Bogaard, P., Rüpke, L., Morgan, J.P., 2003. Deep roots of the Messinian salinity crisis. *Nature* 422, 602–606.
- Dupuy, C., Dostal, J., Boivin, P., 1986. Geochemistry of Ultramafic Xenoliths and Their Host Alkali Basalts from Tallante, Southern Spain. *Mineral. Mag.* 50, 231–239.
- Egeler, C.G., 1964. On the tectonics of the eastern Betic Cordilleras (SE Spain). *Geol Rundsch* 53, 260–269.
- Egeler, C.G., Simon, O.J., 1969. Orogenic evolution of the Betic Zone (Betic Cordillera, Spain), with emphasis on the nappe structures. *Geologie en Mijnbouw* 48, 296–305.
- Egorova, V.V., Volkova, N.I., Shelepaev, R.A., Izokh, A.E., 2006. The lithosphere beneath the Sangilen Plateau, Siberia: evidence from peridotite, pyroxenite and gabbro xenoliths from alkaline basalts. *Mineralogy and Petrology* 88, 419–441.
- El Bakkali, S., Gourgaud, A., Bourdier, J.-L., Bellon, H., Gundogdu, N., 1998. Post-collision neogene volcanism of the Eastern Rif (Morocco): magmatic evolution through time. *Lithos* 45, 523–543.
- Embey-Isztin, A., 1976. Amphibolite/lherzolite composite xenolith from Szigliget, north of the lake Balaton, Hungary. *Earth and Planetary Science Letters* 31, 297–304.
- Embey-Isztin, A., Dobosi, G., Altherr, R., Meyer, H.-P., 2001. Thermal evolution of the lithosphere beneath the western Pannonian Basin: evidence from deep-seated xenoliths. *Tectonophysics* 331, 285–306.
- Esteban, J.J., Cuevas, J., Tubía, J.M., Sergeev, S., Larionov, A., 2011. A revised Aquitanian age for the emplacement of the Ronda peridotites (Betic Cordilleras, southern Spain). *Geological Magazine* 148, 183–187.
- Faccenna, C., Becker, T.W., 2010. Shaping mobile belts by small-scale convection. *Nature* 465, 602–605.
- Faccenna, C., Piromallo, C., Crespo-Blanc, A., Jolivet, L., Rossetti, F., 2004. Lateral slab deformation and the origin of the western Mediterranean arcs. *Tectonics* 23, n/a–n/a.
- Fernández-Soler, J.M., 1996. El volcanismo calco-alcalino del Parque Natural Cabo de Gata-Níjar (Almería): estudio volcanológico y petrológico. Monografías del Medio Natural de la Sociedad Española de Historia Natural, Junta de Andalucía, Spain.
- Fernández-Suárez, J., Dunning, G.R., Jenner, G.A., Gutiérrez-Alonso, G., 2000. Variscan collisional magmatism and deformation in NW Iberia: constraints from U–Pb geochronology of granitoids. *Journal of the Geological Society* 157, 565–576.
- Finnerty, A.A., Boyd, F.R., 1987. Thermobarometry for garnet peridotite xenoliths: basis for the determination of thermal and compositional structure of the upper mantle, in: Nixon, P.H. (Ed.), *Mantle Xenoliths*. John Wiley & Sons Ltd, Chichester, pp. 381–402.
- Fitton, G., 1997. X-Ray fluorescence spectrometry, in: Gill, R. (Ed.), *Modern analytical geochemistry: an introduction to quantitative chemical analysis techniques for earth, environmental and materials scientists*. Addison Wesley Longman, Harlow.
- Foley, S.F., 1984. Liquid immiscibility and melt segregation in alkaline lamprophyres from Labrador. *Lithos* 17, 127–137.

- Foley, S.F., 1990. A review and assessment of experiments on Kimberlites, Lamproites and Lamprophyres as a guide to their Origin. *Proc. Indian Acad. Sci. (Earth Planet Sci.)* 99, 57–80.
- Foley, S.F., Andronikov, A.V., Jacob, D.E., Melzer, S., 2006. Evidence from Antarctic mantle peridotite xenoliths for changes in mineralogy, geochemistry and geothermal gradients beneath a developing rift. *Geochimica et Cosmochimica Acta* 70, 3096–3120.
- Foley, S.F., Yaxley, G.M., Rosenthal, A., Buhre, S., Kiseeva, E.S., Rapp, R.P., Jacob, D.E., 2009. The composition of near-solidus melts of peridotite in the presence of CO₂ and H₂O between 40 and 60 kbar. *Lithos* 112, Supplement 1, 274–283.
- Fontbote, J.M., 1986. La cordillera Bética: Introducción, in: *Geología De España. Libro Jubilar J. M. Ríos*. Instituto Geológico y Minero de España, Madrid, pp. 205–218.
- Fouch, M.J., Rondenay, S., 2006. Seismic anisotropy beneath stable continental interiors. *Physics of the Earth and Planetary Interiors* 158, 292–320.
- Fourcade, S., Capdevila, R., Ouabadi, A., Martineau, F., 2001. The origin and geodynamic significance of the Alpine cordierite-bearing granitoids of northern Algeria. A combined petrological, mineralogical, geochemical and isotopic (O, H, Sr, Nd) study. *Lithos* 57, 187–216.
- Fraser, D.G., Lawless, P.J., 1978. Palaeogeotherms: implications of disequilibrium in garnet Iherzolite xenoliths (reply). *Nature* 276, 737–738.
- Frets, E., Tommasi, A., Garrido, C.J., Padrón-Navarta, J.A., Amri, I., Targuisti, K., 2012. Deformation processes and rheology of pyroxenites under lithospheric mantle conditions. *Journal of Structural Geology* 39, 138–157.
- Frey, F.A., Green, D.H., 1974. The mineralogy, geochemistry and origin of Iherzolite inclusions in Victorian basanites. *Geochimica et Cosmochimica Acta* 38, 1023–1059.
- Frey, F.A., John Suen, C., Stockman, H.W., 1985. The Ronda high temperature peridotite: Geochemistry and petrogenesis. *Geochimica et Cosmochimica Acta* 49, 2469–2491.
- Frost, D.J., McCammon, C.A., 2008. The Redox State of Earth's Mantle. *Annual Review of Earth and Planetary Sciences* 36, 389–420.
- Fullea, J., Fernández, M., Afonso, J.C., Vergés, J., Zeyen, H., 2010. The structure and evolution of the lithosphere–asthenosphere boundary beneath the Atlantic–Mediterranean Transition Region. *Lithos* 120, 74–95.
- Gaetani, G.A., Grove, T.L., 1998. The influence of water on melting of mantle peridotite. *Contrib Mineral Petrol* 131, 323–346.
- Galindo-Zaldívar, J., González Lodeiro, F., Jabaloy, A., 1989. Progressive extensional shear structures in a detachment contact in the western Sierra Nevada (Betic Cordilleras, Spain). *Geodinamica Acta* 3, 73–85.
- Garrido, C.J., Bodinier, J.-L., 1999. Diversity of Mafic Rocks in the Ronda Peridotite: Evidence for Pervasive Melt–Rock Reaction during Heating of Subcontinental Lithosphere by Upwelling Asthenosphere. *J. Petrology* 40, 729–754.
- Garrido, C.J., Bodinier, J.-L., Alard, O., 2000. Incompatible trace element partitioning and residence in anhydrous spinel peridotites and websterites from the Ronda orogenic peridotite. *Earth and Planetary Science Letters* 181, 341–358.
- Garrido, C.J., Gueydan, F., Booth-Rea, G., Precigout, J., Hidas, K., Padrón-Navarta, J.A., Marchesi, C., 2011. Garnet Iherzolite and garnet-spinel mylonite in the Ronda peridotite: Vestiges of Oligocene backarc mantle lithospheric extension in the western Mediterranean. *Geology* 39, 927–930.
- Giaconia, F., Booth-Rea, G., Martínez-Martínez, J.M., Azañón, J.M., Pérez-Romero, J., Villegas, I., 2013. Mountain front migration and drainage captures related to fault segment linkage and growth: The Polopos transpressive fault zone (southeastern Betics, SE Spain). *Journal of Structural Geology* 46, 76–91.

- Gibsher, A., Malkovets, V., Litasov, Y., Griffin, W., O'Reilly, S.Y., 2008. An evidence for the composition of the Ordovician upper mantle beneath West Sangilen (Southeast Tuva, Russia), in: Extended Abstract. Presented at the 9th International Kimberlite Conference, p. No. 9IKC-A-00153.
- Gibsher, A.A., Malkovets, V.G., Travin, A.V., Belousova, E.A., Sharygin, V.V., Konc, Z., 2012. The age of camptonite dikes of the Agardag alkali-basalt complex (western Sangilen): results of Ar/Ar and U/Pb dating. *Russian Geology and Geophysics* 53, 763–775.
- Gill, R.C.O., Aparicio, A., El Azzouzi, M., Hernandez, J., Thirlwall, M.F., Bourgois, J., Marriner, G.F., 2004. Depleted arc volcanism in the Alboran Sea and shoshonitic volcanism in Morocco: geochemical and isotopic constraints on Neogene tectonic processes. *Lithos* 78, 363–388.
- Godard, M., Bodinier, J.-L., Vasseur, G., 1995. Effects of mineralogical reactions on trace element redistributions in mantle rocks during percolation processes: A chromatographic approach. *Earth and Planetary Science Letters* 133, 449–461.
- Godard, M., Jousset, D., Bodinier, J.-L., 2000. Relationships between geochemistry and structure beneath a palaeo-spreading centre: a study of the mantle section in the Oman ophiolite. *Earth and Planetary Science Letters* 180, 133–148.
- Godey, S., Deschamps, F., Trampert, J., Snieder, R., 2004. Thermal and compositional anomalies beneath the North American continent. *J. Geophys. Res.* 109, B01308.
- Goes, S., Govers, R., Vacher, P., 2000. Shallow mantle temperatures under Europe from P and S wave tomography. *J. Geophys. Res.* 105, 11153–11169.
- Goetze, C., 1975. Sheared Iherzolites: From the point of view of rock mechanics. *Geology* 3, 172.
- Goffe, B., Michard, A., Garcia-Duenas, V., Gonzales-Lodeiro, F., Monie, P., Campos, J., Galindo-Zaldivar, J., Jabaloy, A., Martinez-Martinez, J.M., Simancas, J.F., 1989. First evidence of high-pressure, low-temperature metamorphism in the Alpujarride nappes, Betic Cordilleras (S. E. Spain). *European Journal of Mineralogy* 1, 139–142.
- Goldstein, J., 2003. Scanning electron microscopy and X-ray microanalysis. Springer, New York [etc.].
- Gomez, F., Beauchamp, W., Barazangi, M., 2000. Role of the Atlas Mountains (northwest Africa) within the African-Eurasian plate-boundary zone. *Geology* 28, 775–778.
- Gómez-Pugnaire, M.T., Chacón, J., Mitrofanov, F., Timofeev, V., 1982. First report on pre-Cambrian rocks in the graphite-bearing series of the Nevado-Filabride Complex (Betic Cordilleras, Spain). *Neues Jahrbuch für Geologie und Paläontologie* 3, 176–180.
- Gómez-Pugnaire, M.T., Rubatto, D., Fernández-Soler, J.M., Jabaloy, A., López-Sánchez-Vizcaíno, V., González-Lodeiro, F., Galindo-Zaldivar, J., Padrón-Navarta, J.A., 2012. Late Variscan magmatism in the Nevado-Filabride Complex: U-Pb geochronologic evidence for the pre-Mesozoic nature of the deepest Betic complex (SE Spain). *Lithos* 146–147, 93–111.
- González-Jiménez, J.M., Marchesi, C., Griffin, W.L., Gutiérrez-Narbona, R., Lorand, J.-P., O'Reilly, S.Y., Garrido, C.J., Gervilla, F., Pearson, N.J., Hidas, K., 2013a. Transfer of Os isotopic signatures from peridotite to chromitite in the subcontinental mantle: Insights from in situ analysis of platinum-group and base-metal minerals (Ojén peridotite massif, southern Spain). *Lithos*.
- González-Jiménez, J.M., Villaseca, C., Griffin, W.L., Belousova, E.A., Konc, Z., Ancochea, E., O'Reilly, S.Y., Pearson, N.J., Garrido, C.J., Gervilla, F., 2013b. The architecture of the European-Mediterranean Lithosphere: a synthesis of the Re-Os evidence. *Geology*.
- Govindaraju, K., 1994. Compilation of working values and sample description for 383 geostandards. *Geostandards Newsletter* 18, 1–158.
- Grégoire, M., Bell, D., Roex, A.L., 2002. Trace element geochemistry of phlogopite-rich mafic mantle xenoliths: their classification and their relationship to phlogopite-bearing

- peridotites and kimberlites revisited. *Contrib Mineral Petrol* 142, 603–625.
- Grégoire, M., Lorand, J.-P., Cottin, J.Y., Giret, A., Mattielli, N., Weis, D., 1997. Xenoliths evidence for a refractory oceanic mantle percolated by basaltic melts beneath the Kerguelen archipelago. *European Journal of Mineralogy* 9, 1085–1100.
- Grégoire, M., McInnes, B.I.A., O'Reilly, S.Y., 2001. Hydrous metasomatism of oceanic sub-arc mantle, Lihir, Papua New Guinea: Part 2. Trace element characteristics of slab-derived fluids. *Lithos* 59, 91–108.
- Grégoire, M., Moine, B.N., O'Reilly, S.Y., Cottin, J.Y., Giret, A., 2000. Trace Element Residence and Partitioning in Mantle Xenoliths Metasomatized by Highly Alkaline, Silicate- and Carbonate-rich Melts (Kerguelen Islands, Indian Ocean). *J. Petrology* 41, 477–509.
- Grégoire, M., Tinguely, C., Bell, D.R., Le Roex, A.P., 2005. Spinel Iherzolite xenoliths from the Premier kimberlite (Kaapvaal craton, South Africa): Nature and evolution of the shallow upper mantle beneath the Bushveld complex. *Lithos* 84, 185–205.
- Griffin, W., Graham, S., O'Reilly, S.Y., Pearson, N., 2004a. Lithosphere evolution beneath the Kaapvaal Craton: Re-Os systematics of sulfides in mantle-derived peridotites. *Chemical Geology* 208, 89–118.
- Griffin, W., Ryan, C., Kaminsky, F., O'Reilly, S.Y., Natapov, L., Win, T., Kinny, P., Ilupin, I., 1999a. The Siberian lithosphere traverse: mantle terranes and the assembly of the Siberian Craton. *Tectonophysics* 310, 1–35.
- Griffin, W.L., Doyle, B.J., Ryan, C.G., Pearson, N.J., Suzanne, Y.O., Davies, R., Kivi, K., Achterbergh, E.V., Natapov, L.M., 1999b. Layered Mantle Lithosphere in the Lac de Gras Area, Slave Craton: Composition, Structure and Origin. *J. Petrology* 40, 705–727.
- Griffin, W.L., O'Reilly, S.Y., Afonso, J.C., Begg, G.C., 2009. The Composition and Evolution of Lithospheric Mantle: a Re-evaluation and its Tectonic Implications. *J. Petrology* 50, 1185–1204.
- Griffin, W.L., O'Reilly, S.Y., Doyle, B.J., Pearson, N.J., Coopersmith, H., Kivi, K., Malkovets, V., Pokhilenko, N., 2004b. Lithosphere mapping beneath the North American plate. *Lithos* 77, 873–922.
- Griffin, W.L., O'Reilly, S.Y., Gaul, O., Ryan, C., 1999c. Secular evolution of subcontinental lithospheric mantle. *Ophiolite* 24, 101.
- Griffin, W.L., O'Reilly, S.Y., Natapov, L.M., Ryan, C.G., 2003. The evolution of lithospheric mantle beneath the Kalahari Craton and its margins. *Lithos* 71, 215–241.
- Gueguen, E., Doglioni, C., Fernandez, M., 1997. Lithospheric boudinage in the Western Mediterranean back-arc basin. *Terra Nova* 9, 184–187.
- Guerrera, F., Martín-Algarra, A., Martín-Martín, M., 2012. Tectono-sedimentary evolution of the “Numidian Formation” and Lateral Facies (southern branch of the western Tethys): constraints for central-western Mediterranean geodynamics. *Terra Nova* 24, 34–41.
- Günther, D., Hattendorf, B., 2005. Solid sample analysis using laser ablation inductively coupled plasma mass spectrometry. *TrAC Trends in Analytical Chemistry* 24, 255–265.
- Gurney, J.J., Harte, B., 1980. Chemical Variations in Upper Mantle Nodules from Southern African Kimberlites. *Phil. Trans. R. Soc. Lond. A* 297, 273–293.
- Gurría, E., Mezcuá, J., 2000. Seismic tomography of the crust and lithospheric mantle in the Betic Cordillera and Alboran Sea. *Tectonophysics* 329, 99–119.
- Gutscher, M.-A., Malod, J., Rehault, J.-P., Contrucci, I., Klingelhoefer, F., Mendes-Victor, L., Spakman, W., 2002. Evidence for active subduction beneath Gibraltar. *Geology* 30, 1071–1074.
- Halliday, A.N., Lee, D.-C., Christensen, J.N., Rehkämper, M., Yi, W., Luo, X., Hall, C.M., Ballentine, C.J., Pettke, T., Stirling, C., 1998. Applications of Multiple Collector-ICPMS to Cosmochemistry, Geochemistry, and Paleoclimatology. *Geochimica et Cosmochimica Acta* 62, 919–940.

- Hamelin, B., Allègre, C.J., 1988. Lead isotope study of orogenic lherzolite massifs. *Earth and Planetary Science Letters* 91, 117-131.
- Harley, S.L., 1984. An experimental study of the partitioning of Fe and Mg between garnet and orthopyroxene. *Contr. Mineral. and Petrol.* 86, 359-373.
- Hart, S.R., 1988. Heterogeneous mantle domains: signatures, genesis and mixing chronologies. *Earth and Planetary Science Letters* 90, 273-296.
- Hart, S.R., Zindler, A., 1986. In search of a bulk-Earth composition. *Chemical Geology* 57, 247-267.
- Harte, B., 1977. Rock Nomenclature with Particular Relation to Deformation and Recrystallisation Textures in Olivine-Bearing Xenoliths. *The Journal of Geology* 85, 279-288.
- Harte, B., Cox, K.G., Gurney, J.J., 1975. Petrography and geological history of upper mantle xenoliths from the matsoku kimberlite pipe. *Physics and Chemistry of the Earth* 9, 477-506.
- Harte, B., Hawkesworth, C.J., 1989. Mantle domains and mantle xenoliths, in: Ross, J. (Ed.), *Kimberlites and Related Rocks*, Geological Society of Australis Special Publication. Blackwell, Perth, pp. 649-686.
- Harte, B., Hunter, R.H., Kinny, P.D., 1993. Melt Geometry, Movement and Crystallization, in Relation to Mantle Dykes, Veins and Metasomatism. *Philosophical Transactions: Physical Sciences and Engineering* 342, 1-21.
- Hawkesworth, C.J., Rogers, N.W., Van Calsteren, P.W.C., Menzies, M.A., 1984. Mantle enrichment processes. *Nature* 311, 331-335.
- Hellebrand, E., Snow, J.E., Mühe, R., 2002. Mantle melting beneath Gakkel Ridge (Arctic Ocean): abyssal peridotite spinel compositions. *Chemical Geology* 182, 227-235.
- Hernandez, J., De Larouzière, F.D., Bolze, J., Bordet, P., 1987. Neogene magmatism in the western Mediterranean area (Southern Spain, North Africa)-Strike slip faulting and Calc-alkaline volcanism. *Bulletin De La Societe Geologique De France* 3, 257-267.
- Hidas, K., Booth-Rea, G., Garrido, C.J., Martínez-Martínez, J.M., Padrón-Navarta, J.A., Konc, Z., Giaconia, F., Frets, E., Marchesi, C., 2013. Backarc basin inversion and subcontinental mantle emplacement in the crust: kilometre-scale folding and shearing at the base of the proto-Alborán lithospheric mantle (Betic Cordillera, southern Spain). *Journal of the Geological Society* 170, 47-55.
- Hoernle, K., 1998. Geochemistry of Jurassic Oceanic Crust beneath Gran Canaria (Canary Islands): Implications for Crustal Recycling and Assimilation. *J. Petrology* 39, 859-880.
- Hoernle, K., Tilton, G., Bas, M.J.L., Duggen, S., Garbe-Schönberg, D., 2002. Geochemistry of oceanic carbonatites compared with continental carbonatites: mantle recycling of oceanic crustal carbonate. *Contrib Mineral Petrol* 142, 520-542.
- Hoernle, K., Van den Bogaard, P., Duggen, S., Mocek, B., Garbe-Schonberg, D., 1999. Evidence for Miocene subduction beneath the Alboran Sea: $^{40}\text{Ar}/^{39}\text{Ar}$ dating and geochemistry of volcanic rocks from Holes 977A and 978A. *Proceedings of the Ocean Drilling Program: Scientific Results* 161, 357-373.
- Hofmann, A.W., 1997. Mantle geochemistry: the message from oceanic volcanism. *Nature* 385, 219-229.
- Houseman, G., 1996. From mountains to basin. *Nature* 379, 771-772.
- Ilyin, A.V., 1990. Proterozoic supercontinent, its latest Precambrian rifting, breakup, dispersal into smaller continents, and subsidence of their margins: Evidence from Asia. *Geology* 18, 1231-1234.
- Ionov, D., 2002. Mantle structure and rifting processes in the Baikal-Mongolia region: geophysical data and evidence from xenoliths in volcanic rocks. *Tectonophysics* 351, 41-60.
- Ionov, D.A., Ashchepkov, I.V., Stosch, H.-G., Witt-Eickschen, G., Seck, H.A., 1993a. Garnet Peridotite Xenoliths from the Vitim Volcanic Field, Baikal Region: the Nature of

- the Garnet–Spinel Peridotite Transition Zone in the Continental Mantle. *J. Petrology* 34, 1141–1175.
- Ionov, D.A., Blichert-Toft, J., Weis, D., 2005. Hf isotope compositions and HREE variations in off-craton garnet and spinel peridotite xenoliths from central Asia. *Geochimica et Cosmochimica Acta* 69, 2399–2418.
- Ionov, D.A., Bodinier, J.-L., Mukasa, S.B., Zanetti, A., 2002a. Mechanisms and Sources of Mantle Metasomatism: Major and Trace Element Compositions of Peridotite Xenoliths from Spitsbergen in the Context of Numerical Modelling. *J. Petrology* 43, 2219–2259.
- Ionov, D.A., Dupuy, C., O'Reilly, S.Y., Kopylova, M.G., Genshaft, Y.S., 1993b. Carbonated peridotite xenoliths from Spitsbergen: implications for trace element signature of mantle carbonate metasomatism. *Earth and Planetary Science Letters* 119, 283–297.
- Ionov, D.A., Mukasa, S.B., Bodinier, J.-L., 2002b. Sr–Nd–Pb Isotopic Compositions of Peridotite Xenoliths from Spitsbergen: Numerical Modelling Indicates Sr–Nd Decoupling in the Mantle by Melt Percolation Metasomatism. *J. Petrology* 43, 2261–2278.
- Ionov, D.A., Wood, B.J., 1992. The oxidation state of subcontinental mantle: oxygen thermobarometry of mantle xenoliths from central Asia. *Contrib Mineral Petrol* 111, 179–193.
- Irving, A.J., Price, R.C., 1981. Geochemistry and evolution of Iherzolite-bearing phonolitic lavas from Nigeria, Australia, East Germany and New Zealand. *Geochimica et Cosmochimica Acta* 45, 1309–1320.
- Izokh, A.E., Polyakov, G.V., Mal'kovets, V.G., Shelepaev, R.A., Travin, A.V., Yu.D., L., Gibsher, A.A., 2001. The late Ordovician age of camptonites from the Agardag Complex of southeastern Tuva as an indicator of the plume-related magmatism during collision processes. *Doklady Earth Sciences* 379, 511–514.
- Jagoutz, E., Palme, H., Baddenhausen, H., Blum, K., Cendales, M., Dreibus, G., Spettel, B., Waenke, H., Lorenz, V., 1979. The abundances of major, minor and trace elements in the earth's mantle as derived from primitive ultramafic nodules. Presented at the Lunar and Planetary Science Conference Proceedings, pp. 2031–2050.
- James, D.E., Boyd, F.R., Schutt, D., Bell, D.R., Carlson, R.W., 2004. Xenolith constraints on seismic velocities in the upper mantle beneath southern Africa. *Geochem. Geophys. Geosyst.* 5, Q01002.
- Janssen, M.E., Torne, M., Cloetingh, S., Banda, E., 1993. Pliocene uplift of the eastern Iberian margin: Inferences from quantitative modelling of the Valencia Trough. *Earth and Planetary Science Letters* 119, 585–597.
- Jochum, K.P., Seufert, H.M., Thirlwall, M.F., 1990. High-sensitivity Nb analysis by spark-source mass spectrometry (SSMS) and calibration of XRF Nb and Zr. *Chemical Geology* 81, 1–16.
- Johnson, C., Harbury, N., Hurford, A.J., 1997. The role of extension in the Miocene denudation of the Nevado-Filábride Complex, Betic Cordillera (SE Spain). *Tectonics* 16, 189–204.
- Johnson, K.T.M., Dick, H.J.B., Shimizu, N., 1990. Melting in the oceanic upper mantle: An ion microprobe study of diopsides in abyssal peridotites. *J. Geophys. Res.* 95, 2661–2678.
- Jolivet, L., Faccenna, C., 2000. Mediterranean extension and the Africa-Eurasia collision. *Tectonics* 19, 1095–1106.
- Jolivet, L., Faccenna, C., Piromallo, C., 2009. From mantle to crust: Stretching the Mediterranean. *Earth and Planetary Science Letters* 285, 198–209.
- Jolly, W.T., Lidiak, E.G., Dickin, A.P., 2006. Cretaceous to Mid-Eocene pelagic sediment budget in Puerto Rico and the Virgin Islands (northeast Antilles Island arc). *Geologica Acta* 4, 35–62.
- Jordan, T.H., 1975. The continental tectosphere. *Reviews of Geophysics* 13, 1–12.
- Julià, J., Mancilla, F., Morales, J., 2005. Seismic signature of intracrustal magmatic intrusions in the Eastern Betics (Internal

- Zone), SE Iberia. *Geophys. Res. Lett.* 32, L16304.
- Jung, H., Karato, S., 2001. Water-induced fabric transitions in olivine. *Science* 293, 1460-1463.
- Jung, H., Park, M., Jung, S., Lee, J., 2010. Lattice preferred orientation, water content, and seismic anisotropy of orthopyroxene. *J. Earth Sci.* 21, 555-568.
- Karato, S., Jung, H., Katayama, I., Skemer, P., 2008. Geodynamic Significance of Seismic Anisotropy of the Upper Mantle: New Insights from Laboratory Studies. *Annual Review of Earth and Planetary Sciences* 36, 59-95.
- Kawamoto, T., Holloway, J.R., 1997. Melting Temperature and Partial Melt Chemistry of H₂O-Saturated Mantle Peridotite to 11 Gigapascals. *Science* 276, 240-243.
- Kelemen, P.B., Shimizu, N., Salters, V.J.M., 1995. Extraction of mid-ocean-ridge basalt from the upwelling mantle by focused flow of melt in dunite channels. *Nature* 375, 747-753.
- Khutorskoy, M.D., Yarmolyuk, V.V., 1989. Thermal and Magmatic Evolution of the Lithosphere of Mongolia. *International Geology Review* 31, 1084-1096.
- Kinzler, R.J., Grove, T.L., 1992. Primary magmas of mid-ocean ridge basalts 1. Experiments and methods. *J. Geophys. Res.* 97, 6885-6906.
- Kious, W.J., Tilling, R.I., 1994. This dynamic earth: the story of plate tectonics. U.S. Geological Survey: For sale by the U.S. G.P.O., Washington, D.C.
- Klemme, S., Van der Laan, S.R., Foley, S.F., Günther, D., 1995. Experimentally determined trace and minor element partitioning between clinopyroxene and carbonatite melt under upper mantle conditions. *Earth and Planetary Science Letters* 133, 439-448.
- Kogarko, L.N., Ryabchikov, I.D., Brey, G.P., Santin, S.F., Pacheco, H., 2001. Mantle rocks uplifted to crustal levels: Diffusion profiles in minerals of spinel-plagioclase lherzolites from Tallante, Spain. *Geochemistry International* 39, 355-371.
- Köhler, T., Brey, G., 1990. Calcium exchange between olivine and clinopyroxene calibrated as a geothermobarometer for natural peridotites from 2 to 60 kb with applications. *Geochimica et Cosmochimica Acta* 54, 2375-2388.
- Konc, Z., Garrido, C.J., Bosch, D., Marchesi, C., Hidas, K., Varas-Reus, M.I., Acosta-Vigil, A., submitted. Isotopic and geochemical composition of the subcontinental lithospheric mantle in the westernmost Mediterranean: Constrains from peridotite xenoliths in Plio-Pleistocene alkali basalts (eastern Betic Cordillera, SE Spain). *Chemical Geology*.
- Konc, Z., Garrido, C.J., Tommasi, A., Hidas, K., Vauchez, A., Padrón-Navarta, J.A., Acosta-Vigil, A., Szabó, Cs., Marhesi, C. submitted. Deformation record, seismic properties and flow of the shallow upper mantle in the westernmost Mediterranean: Insights from mantle xenoliths in Plio-Pleistocene alkali basalts from the eastern Betic Cordillera (SE Spain). *Geochemistry, Geophysics, Geosystems*
- Konc, Z., Marchesi, C., Garrido, C.J., González-Jiménez, J.M., Griffin, W.L., Alard, O., Hidas, K., O'Reilly, S.Y., Pearson, N., 2012. Provenance and evolution of the western Mediterranean lithospheric mantle beneath the eastern Betics (S. Spain): insights from in-situ analyses of Os isotopes and platinum-group elements in sulphides from the Tallante mantle xenoliths. Presented at the EGU General Assembly Conference Abstracts, p. 12929.
- Kovács, I., Falus, G., Stuart, G., Hidas, K., Szabó, C., Flower, M.F.J., Hegedüs, E., Posgay, K., Zilahi-Sebess, L., 2012. Seismic anisotropy and deformation patterns in upper mantle xenoliths from the central Carpathian-Pannonian region: Asthenospheric flow as a driving force for Cenozoic extension and extrusion? *Tectonophysics* 514-517, 168-179.
- Krogh, E.J., 1988. The garnet-clinopyroxene Fe-Mg geothermometer – a reinterpretation of existing experimental data. *Contr. Mineral. and Petrol.* 99, 44-48.
- Kumar, N., Reisberg, L., Zindler, A., 1996. A major and trace element and strontium, neodymium, and osmium isotopic study of

- a thick pyroxenite layer from the Beni Bousera Ultramafic Complex of northern Morocco. *Geochimica et Cosmochimica Acta* 60, 1429–1444.
- Kusznir, N.J., Park, R.G., 1987. The extensional strength of the continental lithosphere: its dependence on geothermal gradient, and crustal composition and thickness. Geological Society, London, Special Publications 28, 35–52.
- Lallemand, S., 1999. *La Subduction Océanique*. Gordon and Breach Science Publishers, [Amsterdam].
- Lazarov, M., Woodland, A.B., Brey, G.P., 2009. Thermal state and redox conditions of the Kaapvaal mantle: A study of xenoliths from the Finsch mine, South Africa. *Lithos* 112, Supplement 2, 913–923.
- Le Bas, M.J., Rex, D.C., Stillman, C.J., 2009. The early magmatic chronology of Fuerteventura, Canary Islands. *Geological Magazine* 123, 287.
- Le Bas, M.J., Streckeisen, A.L., 1991. The IUGS systematics of igneous rocks. *Journal of the Geological Society* 148, 825–833.
- Le Maitre, R.W., Streckeisen, A., Zanettin, B., Bas, M.J.L., Bonin, B., Bateman, P., 2002. *Igneous Rocks: A Classification and Glossary of Terms*, Second edition. ed. Cambridge University Press.
- Le Roux, V., Bodinier, J.-L., Tommasi, A., Alard, O., Dautria, J.-M., Vauchez, A., Riches, A.J.V., 2007. The Lherz spinel lherzolite: Refertilized rather than pristine mantle. *Earth and Planetary Science Letters* 259, 599–612.
- Lee, C.-T.A., 2003. Compositional variation of density and seismic velocities in natural peridotites at STP conditions: Implications for seismic imaging of compositional heterogeneities in the upper mantle. *J. Geophys. Res.* 108, 2441.
- Lee, C.-T.A., Brandon, A.D., Norman, M., 2003. Vanadium in peridotites as a proxy for paleo-fO₂ during partial melting: prospects, limitations, and implications. *Geochimica et Cosmochimica Acta* 67, 3045–3064.
- Lee, H.Y., Ganguly, J., 1988. Equilibrium Compositions of Coexisting Garnet and Orthopyroxene: Experimental Determinations in the System FeO-MgO-Al₂O₃-SiO₂, and Applications. *J. Petrology* 29, 93–113.
- Lenoir, X., Garrido, C.J., Bodinier, J.-L., Dautria, J.-M., 2000. Contrasting lithospheric mantle domains beneath the Massif Central (France) revealed by geochemistry of peridotite xenoliths. *Earth and Planetary Science Letters* 181, 359–375.
- Lenoir, X., Garrido, C.J., Bodinier, J.-L., Dautria, J.-M., Gervilla, F., 2001. The Recrystallization Front of the Ronda Peridotite: Evidence for Melting and Thermal Erosion of Subcontinental Lithospheric Mantle beneath the Alboran Basin. *J. Petrology* 42, 141–158.
- Lindsley, D.H., 1983. Pyroxene thermometry. *American Mineralogist* 68, 477–493.
- Lindstrom, D.J., 1976. Experimental study of the partitioning of the transition metals between clinopyroxene and coexisting silicate liquids (PhD thesis). University of Oregon, Eugene (USA).
- Litasov, K.D., Foley, S.F., Litasov, Y.D., 2000. Magmatic modification and metasomatism of the subcontinental mantle beneath the Vitim volcanic field (East Siberia): evidence from trace element data on pyroxenite and peridotite xenoliths from Miocene picrobasalt. *Lithos* 54, 83–114.
- Lonergan, L., 1993. Timing and kinematics of deformation in the Malaguide Complex, internal zone of the Betic Cordillera, southeast Spain. *Tectonics* 12, 460–476.
- Lonergan, L., Schreiber, B.C., 1993. Proximal deposits at a fault-controlled basin margin, Upper Miocene, SE Spain. *Journal of the Geological Society* 150, 719–727.
- Lonergan, L., White, N., 1997. Origin of the Betic-Rif mountain belt. *Tectonics* 16, 504–522.
- Long, M.D., Becker, T.W., 2010. Mantle dynamics and seismic anisotropy. *Earth and Planetary Science Letters* 297, 341–354.
- Long, M.D., Silver, P.G., 2009. Shear Wave Splitting and Mantle Anisotropy: Measurements, Interpretations, and New Directions. *Surv Geophys* 30, 407–461.

- López Sánchez-Vizcaíno, V., Rubatto, D., Gómez-Pugnaire, M.T., Trommsdorff, V., Müntener, O., 2001. Middle Miocene high-pressure metamorphism and fast exhumation of the Nevado-Filábride Complex, SE Spain. *Terra Nova* 13, 327-332.
- López-Ruiz, J., Cebriá, J.M., Doblas, M., 2002. Cenozoic volcanism I: The Iberian Peninsula, in: Gibbons, W. (Ed.), *The Geology of Spain*. Geological Society of London, London, pp. 417-438.
- López-Ruiz, J., Cebriá, J.M., Doblas, M., Benito, R., 2004. La región volcánica de Almería-Murcia, in: Vera, J.A. (Ed.), *Geología De España*. Instituto Geológico y Minero de España - Sociedad Geológica de España, Madrid, pp. 678-682.
- Luais, B., Telouk, P., Albaréde, F., 1997. Precise and accurate neodymium isotopic measurements by plasma-source mass spectrometry. *Geochimica et Cosmochimica Acta* 61, 4847-4854.
- Luján, M., Crespo-Blanc, A., Balanyá, J.C., 2006. The Flysch Trough thrust imbricate (Betic Cordillera): A key element of the Gibraltar Arc orogenic wedge. *Tectonics* 25, n/a-n/a.
- Lustrino, M., Duggen, S., Rosenberg, C.L., 2011. The Central-Western Mediterranean: Anomalous igneous activity in an anomalous collisional tectonic setting. *Earth-Science Reviews* 104, 1-40.
- Maaløe, S., Aoki, K., 1977. The major element composition of the upper mantle estimated from the composition of lherzolites. *Contrib. Mineral. and Petrol.* 63, 161-173.
- MacGregor, I.D., 1974. The system MgO-Al₂O₃-SiO₂: Solubility of Al₂O₃ in enstatite for spinel and garnet peridotite compositions. *American Mineralogist* 59, 110-119.
- Mainprice, D., Barruol, G., Ben Ismail, W., 2000. The anisotropy of the Earth's mantle: From single crystal to polycrystal, in: Karato, S.-I., Forte, A.M., Liebermann, R.C., Masters, G., Stixrude, L. (Eds.), *Mineral Physics and Seismic Tomography: From Atomic to Global*, AGU Geophysical Monograph. AGU, pp. 237-264.
- Mainprice, D., Humbert, M., 1994. Methods of calculating petrophysical properties from lattice preferred orientation data. *Surv Geophys* 15, 575-592.
- Mainprice, D., Silver, P.G., 1993. Interpretation of SKS-waves using samples from the subcontinental lithosphere. *Physics of the Earth and Planetary Interiors* 78, 257-280.
- Makar, A.B., McMartin, K.E., Palese, M., Tephly, T.R., 1975. Formate assay in body fluids: application in methanol poisoning. *Biochem Med* 13, 117-126.
- Marchesi, C., 2006. Petrogenesis of the ultramafic and mafic rocks from the Mayarí-Baracoa Ophiolitic Belt and the spatially-related volcanism (eastern Cuba) (PhD Thesis). Universidad de Granada. Departamento de Mineralogía y Petrología, Granada.
- Marchesi, C., Garrido, C.J., Bosch, D., Bodinier, J.-L., Hidas, K., Padrón-Navarta, Gervilla, F., 2012. A Late Oligocene Suprasubduction Setting in the Westernmost Mediterranean Revealed by Intrusive Pyroxenite Dikes in the Ronda Peridotite (Southern Spain). *The Journal of Geology* 120, 237-247.
- Marchesi, C., Griffin, W.L., Garrido, C.J., Bodinier, J.-L., O'Reilly, S.Y., Pearson, N.J., 2010. Persistence of mantle lithospheric Re-Os signature during asthenospherization of the subcontinental lithospheric mantle: insights from in situ isotopic analysis of sulfides from the Ronda peridotite (Southern Spain). *Contrib Mineral Petrol* 159, 315-330.
- Marchesi, C., Jolly, W.T., Lewis, J.F., Garrido, C.J., Proenza, J.A., Lidiak, E.G., 2011. Petrogenesis of fertile mantle peridotites from the Monte del Estado massif (Southwest Puerto Rico): a preserved section of Proto-Caribbean lithospheric mantle? *Geologica Acta* 9, 289-306.
- Martínez-Martínez, J.M., Booth-Rea, G., Azañón, J.M., Torcal, F., 2006. Active transfer fault zone linking a segmented extensional system (Betics, southern Spain): Insight into heterogeneous extension driven by edge delamination. *Tectonophysics* 422, 159-173.
- Martínez-Martínez, J.M., Soto, J.I., Balanyá, J.C., 2002. Orthogonal folding of

- extensional detachments: Structure and origin of the Sierra Nevada elongated dome (Betics, SE Spain). *Tectonics* 21, 3-1-3-20.
- Mauffret, A., Frizon de Lamotte, D., Lallemand, S., Gorini, C., Maillard, A., 2004. E-W opening of the Algerian Basin (Western Mediterranean). *Terra Nova* 16, 257-264.
- Maury, R.C., Fourcade, S., Coulon, C., El Azzouzi, M., Bellon, H., Coutelle, A., Ouabadi, A., Semroud, B., Megartsi, M., Cotten, J., Belanteur, O., Louni-Hacini, A., Piqué, A., Capdevila, R., Hernandez, J., Réhault, J.-P., 2000. Post-collisional Neogene magmatism of the Mediterranean Maghreb margin: a consequence of slab breakoff. *Comptes Rendus de l'Académie des Sciences - Series IIA - Earth and Planetary Science* 331, 159-173.
- McDonough, W.F., Frey, F.A., 1989. Rare earth elements in upper mantle rocks. *Reviews in Mineralogy and Geochemistry* 21, 100-145.
- McDonough, W.F., Sun, S. -s., 1995. The composition of the Earth. *Chemical Geology* 120, 223-253.
- McInnes, B.I., Gregoire, M., Binns, R.A., Herzig, P.M., Hannington, M.D., 2001. Hydrous metasomatism of oceanic sub-arc mantle, Lihir, Papua New Guinea: petrology and geochemistry of fluid-metasomatised mantle wedge xenoliths. *Earth and Planetary Science Letters* 188, 169-183.
- McKenzie, D., 1989. Some remarks on the movement of small melt fractions in the mantle. *Earth and Planetary Science Letters* 95, 53-72.
- McKenzie, D., O'nions, R.K., 1991. Partial Melt Distributions from Inversion of Rare Earth Element Concentrations. *J. Petrology* 32, 1021-1091.
- McLaren, A.C., Etheridge, M.A., 1976. A transmission electron microscope study of naturally deformed orthopyroxene. *Contr. Mineral. and Petrol.* 57, 163-177.
- Meijninger, B.M.L., Vissers, R.L.M., 2006. Miocene extensional basin development in the Betic Cordillera, SE Spain revealed through analysis of the Alhama de Murcia and Crevillente Faults. *Basin Research* 18, 547-571.
- Menzies, M., Dupuy, C., Nicolas, A., 1991. Orogenic Lherzolites and Mantle Processes. *Terra Nova* 3, 6-8.
- Menzies, M., Hawkesworth, C.J., 1987a. Upper mantle processes and composition, in: Nixon, P.H. (Ed.), *Mantle Xenoliths*. John Wiley & Sons Ltd, Chichester, United Kingdom, pp. 725-738.
- Menzies, M.A., 1990. *Continental mantle*. Clarendon Press; Oxford University Press, Oxford [England]; New York.
- Menzies, M.A., Hawkesworth, C.J., 1987b. *Mantle metasomatism*. Academic Press, London; Orlando.
- Mercier, J.-C.C., 1985. Olivine and pyroxene, in: Wenk, H.R. (Ed.), *Preferred Orientation in Deformed Metal and Rocks: An Introduction to Modern Texture Analysis*. Academic Press, pp. 407-430.
- Mercier, J.-C.C., Nicolas, A., 1975. Textures and Fabrics of Upper-Mantle Peridotites as Illustrated by Xenoliths from Basalts. *J. Petrology* 16, 454-487.
- Michard, A., Chalouan, A., Feinberg, H., Goffé, B., Montigny, R., 2002. How does the Alpine belt end between Spain and Morocco? *Bulletin de la Societe Geologique de France* 173, 3-15.
- Mitchell, R.H., 1995. *Kimberlites, orangeites, and related rocks*. Plenum Press.
- Montenat, C., Ott d'Estevou, P., 1990. Eastern betic Neogene basins, in: Montenat, C. (Ed.), *Les bassins néogènes du domaine bétique oriental (Espagne): tectonique et sédimentation dans un couloir de décrochement*. IGAL, Paris, pp. 9-15.
- Morales, J., Serrano, I., Jabaloy, A., Galindo-Zaldívar, J., Zhao, D., Torcal, F., Vidal, F., Lodeiro, F.G., 1999. Active continental subduction beneath the Betic Cordillera and the Alborán Sea. *Geology* 27, 735-738.
- Mossakovskii, A.A., Ruzhentsev, S.V., Samygin, S.G., Kheraskova, T.N., 1993. The Central Asian Fold Belt: Geodynamic Evolution and History of Formation. *Geotectonics* 6, 3-33.
- Navon, O., Stolper, E., 1987. Geochemical Consequences of Melt Percolation: The

- Upper Mantle as a Chromatographic Column. *The Journal of Geology* 95, 285-307.
- Naze, L., Doukhan, N., Doukhan, J.-C., Latrous, K., 1987. A TEM study of lattice defects in naturally and experimentally deformed orthopyroxenes. *Bulletin de Minéralogie* 110, 497-512.
- Negredo, A.M., Bird, P., Galdeano, C.S. de, Buforn, E., 2002. Neotectonic modeling of the Ibero-Maghrebian region. *J. Geophys. Res.* 107, 2292.
- Nelson, D.R., McCulloch, M.T., Sun, S.-S., 1986. The origins of ultrapotassic rocks as inferred from Sr, Nd and Pb isotopes. *Geochimica et Cosmochimica Acta* 50, 231-245.
- Nickel, K.G., Brey, G., 1984. Subsolidus orthopyroxene-clinopyroxene systematics in the system CaO-MgO-SiO₂ to 60 kb: a re-evaluation of the regular solution model. *Contr. Mineral. and Petrol.* 87, 35-42.
- Nickel, K.G., Brey, G.P., Kogarko, L., 1985. Orthopyroxene-clinopyroxene equilibria in the system CaO-MgO-Al₂O₃-SiO₂ (CMAS): new experimental results and implications for two-pyroxene thermometry. *Contrib Mineral Petrol* 91, 44-53.
- Nickel, K.G., Green, D.H., 1985. Empirical geothermobarometry for garnet peridotites and implications for the nature of the lithosphere, kimberlites and diamonds. *Earth and Planetary Science Letters* 73, 158-170.
- Nicolas, A., Christensen, N.I., 1987. Formation of anisotropy in upper mantle peridotites: A review, in: Fuchs, K., Froidevaux, C. (Eds.), *Geodynamics Series*. American Geophysical Union, Washington, D. C., pp. 111-123.
- Nicolas, A., Dupuy, C., 1984. Origin of ophiolitic and oceanic lherzolites. *Tectonophysics* 110, 177-187.
- Nimis, P., Grütter, H., 2010. Internally consistent geothermometers for garnet peridotites and pyroxenites. *Contrib Mineral Petrol* 159, 411-427.
- Nimis, P., Taylor, W.R., 2000. Single clinopyroxene thermobarometry for garnet peridotites. Part I. Calibration and testing of a Cr-in-Cpx barometer and an enstatite-in-Cpx thermometer. *Contrib Mineral Petrol* 139, 541-554.
- Niu, Y., 1997. Mantle Melting and Melt Extraction Processes beneath Ocean Ridges: Evidence from Abyssal Peridotites. *J. Petrology* 38, 1047-1074.
- Nixon, P.H., 1987. *Mantle Xenoliths*. John Wiley & Sons Ltd.
- Nixon, P.H., Boyd, F.R., 1973. Petrogenesis of the granular and sheared ultrabasic nodule suite in kimberlite, in: Nixon, P.H. (Ed.), *Lesotho Kimberlites*. Lesotho National Development Corporation, Maseru, Lesotho, pp. 48-56.
- O'Neill, H.S.C., 1981. The transition between spinel lherzolite and garnet lherzolite, and its use as a Geobarometer. *Contr. Mineral. and Petrol.* 77, 185-194.
- O'Neill, H.S.C., Wood, B.J., 1979. An experimental study of Fe-Mg partitioning between garnet and olivine and its calibration as a geothermometer. *Contr. Mineral. and Petrol.* 70, 59-70.
- O'Reilly, S.Y., Griffin, W.L., 1985. A xenolith-derived geotherm for southeastern Australia and its geophysical implications. *Tectonophysics* 111, 41-63.
- O'Reilly, S.Y., Griffin, W.L., 1988. Mantle metasomatism beneath western Victoria, Australia: I. Metasomatic processes in Cr-diopside lherzolites. *Geochimica et Cosmochimica Acta* 52, 433-447.
- O'Reilly, S.Y., Griffin, W.L., 1996. 4-D Lithosphere Mapping: methodology and examples. *Tectonophysics* 262, 3-18.
- O'Reilly, S.Y., Griffin, W.L., 2013. Mantle Metasomatism, in: *Metasomatism and the Chemical Transformation of Rock*, Lecture Notes in Earth System Sciences. Springer Berlin Heidelberg, Berlin, Heidelberg, pp. 471-533.
- O'Reilly, S.Y., Zhang, M., Griffin, W.L., Begg, G., Hronsky, J., 2009. Ultradeep continental roots and their oceanic remnants: A solution to the geochemical "mantle reservoir" problem? *Lithos* 112, Supplement 2, 1043-1054.

- Obata, M., 1980. The Ronda Peridotite: Garnet-, Spinel-, and Plagioclase-Lherzolite Facies and the P-T Trajectories of a High-Temperature Mantle Intrusion. *J. Petrology* 21, 533-572.
- Orejana, D., Villaseca, C., Billström, K., Paterson, B.A., 2008. Petrogenesis of Permian alkaline lamprophyres and diabases from the Spanish Central System and their geodynamic context within western Europe. *Contr. Mineral. and Petrol.* 156, 477-500.
- Orejana, D., Villaseca, C., Pérez-Soba, C., López-García, J.A., Billström, K., 2009. The Variscan gabbros from the Spanish Central System: A case for crustal recycling in the sub-continental lithospheric mantle? *Lithos* 110, 262-276.
- Ozawa, K., 2004. Thermal History of the Horoman Peridotite Complex: A Record of Thermal Perturbation in the Lithospheric Mantle. *J. Petrology* 45, 253-273.
- Ozawa, K., Shimizu, N., 1995. Open-system melting in the upper mantle: Constraints from the Hayachine-Miyamori ophiolite, northeastern Japan. *Journal of Geophysical Research: Solid Earth* 100, 22315-22335.
- Padrón-Navarta, J.A., Garrido, C.J., Sánchez-Navas, A., Tommasi, A., Sánchez-Vizcaíno, V.L., Gómez-Pugnaire, M.T., Hussain, S.S., 2008. Oriented growth of garnet by topotactic reactions and epitaxy in high-pressure, mafic garnet granulite formed by dehydration melting of metastable hornblende-gabbroicite (Jijal Complex, Kohistan Complex, north Pakistan). *Journal of Metamorphic Geology* 26, 855-870.
- Palme, H., O'Neill, H.S.C., 2003. 2.01 - Cosmochemical Estimates of Mantle Composition, in: Editors-in-Chief: Heinrich D. Holland, Karl K. Turekian (Eds.), *Treatise on Geochemistry*. Pergamon, Oxford, pp. 1-38.
- Parkinson, I.J., Arculus, R.J., Eggins, S.M., 2003. Peridotite xenoliths from Grenada, Lesser Antilles Island Arc. *Contrib Mineral Petrol* 146, 241-262.
- Pasquale, V., Verdoya, M., Chiozzi, P., 1996. Some geophysical constraints to dynamic processes in the Southwestern Mediterranean. *Annals of Geophysics* 39.
- Pearce, J.A., Barker, P.F., Edwards, S.J., Parkinson, I.J., Leat, P.T., 2000. Geochemistry and tectonic significance of peridotites from the South Sandwich arc-basin system, South Atlantic. *Contrib Mineral Petrol* 139, 36-53.
- Pearce, N.J.G., Perkins, W.T., Westgate, J.A., Gorton, M.P., Jackson, S.E., Neal, C.R., Chenery, S.P., 1997. A Compilation of New and Published Major and Trace Element Data for NIST SRM 610 and NIST SRM 612 Glass Reference Materials. *Geostandards Newsletter* 21, 115-144.
- Pearson, D.G., 1999. Evolution of cratonic lithospheric mantle: an isotopic perspective, in: Boyd, F.R., Fei, Y., Bertka, C.M., Mysen, B.O. (Eds.), *Mantle Petrology Field Observations and High Pressure Experimentation*, Special Publication Number. Geochemical Society.
- Pearson, D.G., Canil, D., Shirey, S.B., 2003. 2.05 - Mantle Samples Included in Volcanic Rocks: Xenoliths and Diamonds, in: Editors-in-Chief: Heinrich D. Holland, Karl K. Turekian (Eds.), *Treatise on Geochemistry*. Pergamon, Oxford, pp. 171-275.
- Pearson, D.G., Nowell, G.M., 2002. The continental lithospheric mantle: characteristics and significance as a mantle reservoir. *Phil. Trans. R. Soc. Lond. A* 360, 2383-2410.
- Pearson, D.G., Nowell, G.M., 2004. Re-Os and Lu-Hf Isotope Constraints on the Origin and Age of Pyroxenites from the Beni Bousera Peridotite Massif: Implications for Mixed Peridotite-Pyroxenite Mantle Sources. *J. Petrology* 45, 439-455.
- Pearson, D.G., Parman, S.W., Nowell, G.M., 2007. A link between large mantle melting events and continent growth seen in osmium isotopes. *Nature* 449, 202-205.
- Pearson, N.J., Alard, O., Griffin, W.L., Jackson, S.E., O'Reilly, S.Y., 2002. In situ measurement of Re-Os isotopes in mantle sulfides by laser ablation multicollector-inductively coupled plasma mass spectrometry: analytical methods and preliminary results. *Geochimica et Cosmochimica Acta* 66, 1037-1050.

- Pedreira, A., De Lis Mancilla, F., Ruiz-Constán, A., Galindo-Zaldívar, J., Morales, J., Arzate, J., Marín-Lechado, C., Ruano, P., Buontempo, L., Anahnah, F., Stich, D., 2010. Crustal-scale transcurrent fault development in a weak-layered crust from an integrated geophysical research: Carboneras Fault Zone, eastern Betic Cordillera, Spain. *Geochemistry, Geophysics, Geosystems* 11, n/a-n/a.
- Pereira, M.F., Apraiz, A., Chichorro, M., Silva, J.B., Armstrong, R.A., 2010. Exhumation of high-pressure rocks in northern Gondwana during the Early Carboniferous (Coimbra-Cordoba shear zone, SW Iberian Massif): Tectonothermal analysis and U-Th-Pb SHRIMP in-situ zircon geochronology. *Gondwana Research* 17, 440-460.
- Perkins, D., Newton, R.C., 1981. The compositions of coexisting pyroxenes and garnet in the system CaO-MgO-Al₂O₃-SiO₂ at 900°-1,100°C and high pressures. *Contrib. Mineral. and Petrol.* 75, 291-300.
- Pin, C., Briot, D., Bassin, C., Poitrasson, F., 1994. Concomitant separation of strontium and samarium-neodymium for isotopic analysis in silicate samples, based on specific extraction chromatography. *Analytica Chimica Acta* 298, 209-217.
- Piqué, A., Aït Brahim, L., Azzouzi, M.E., Maury, R.C., Bellon, H., Semroud, B., Laville, E., 1998. Le poinçon maghrébin: contraintes structurales et géochimiques. *Comptes Rendus de l'Académie des Sciences - Series IIA - Earth and Planetary Science* 326, 575-581.
- Platt, J.P., Anczkiewicz, R., Soto, J.-I., Kelley, S.P., Thirlwall, M., 2006. Early Miocene continental subduction and rapid exhumation in the western Mediterranean. *Geology* 34, 981-984.
- Platt, J.P., Kelley, S.P., Carter, A., Orozco, M., 2005. Timing of tectonic events in the Alpujarride Complex, Betic Cordillera, southern Spain. *Journal of the Geological Society* 162, 451-462.
- Platt, J.P., Soto, J.-I., Whitehouse, M.J., Hurford, A.J., Kelley, S.P., 1998. Thermal evolution, rate of exhumation, and tectonic significance of metamorphic rocks from the floor of the Alboran extensional basin, western Mediterranean. *Tectonics* 17, 671-689.
- Platt, J.P., Vissers, R.L.M., 1989. Extensional collapse of thickened continental lithosphere: A working hypothesis for the Alboran Sea and Gibraltar arc. *Geology* 17, 540-543.
- Plomerová, J., Payo, G., Babuška, V., 1993. Teleseismic P-residual study in the Iberian Peninsula. *Tectonophysics* 221, 1-12.
- Pokhilenko, N.P., Sobolev, N.V., Boyd, F.R., Pearson, D.G., Shimizu, N., 1993. Megacrystalline pyrope peridotites in the lithosphere of the Siberian platform: mineralogy, geochemical peculiarities and the problem of their origin. *Russian Geology and Geophysics* 34, 56-67.
- Poli, S., Schmidt, M.W., 2002. Petrology of Subducted Slabs. *Annual Review of Earth and Planetary Sciences* 30, 207-235.
- Poudjom Djomani, Y.H., O'Reilly, S.Y., Griffin, W.L., Natapov, L.M., Erinchek, Y., Hronsky, J., 2003. Upper mantle structure beneath eastern Siberia: Evidence from gravity modeling and mantle petrology. *Geochemistry, Geophysics, Geosystems* 4, n/a-n/a.
- Powell, W., Zhang, M., O'Reilly, S.Y., Tiepolo, M., 2004. Mantle amphibole trace-element and isotopic signatures trace multiple metasomatic episodes in lithospheric mantle, western Victoria, Australia. *Lithos* 75, 141-171.
- Precigout, J., Gueydan, F., Gapais, D., Garrido, C.J., Essaifi, A., 2007. Strain localisation in the subcontinental mantle – a ductile alternative to the brittle mantle. *Tectonophysics* 445, 318-336.
- Prelević, D., Akal, C., Romer, R.L., Foley, S.F., 2010. Lamproites as indicators of accretion and/or shallow subduction in the assembly of south-western Anatolia, Turkey. *Terra Nova* 22, 443-452.
- Prelević, D., Foley, S.F., Romer, R., Conticelli, S., 2008. Mediterranean Tertiary lamproites derived from multiple source components in postcollisional geodynamics. *Geochimica et Cosmochimica Acta* 72, 2125-2156.

- Prior, D.J., Boyle, A.P., Brenker, F., Cheadle, M.C., Austin, D., Lopez, G., Peruzzo, L., Potts, G.J., Reddy, S., Spiess, R., Timms, N.E., Trimby, P., Wheeler, J., Zetterström, L., 1999. The application of electron backscatter diffraction and orientation contrast imaging in the SEM to textural problems in rocks. *American Mineralogist* 84, 1741–1759.
- Puga, E., De Federico, A.D., Nieto, J.M., 2002. Tectonostratigraphic subdivision and petrological characterisation of the deepest complexes of the Betic zone: a review. *Geodinamica Acta* 15, 23–43.
- Raffone, N., Chazot, G., Pin, C., Vannucci, R., Zanetti, A., 2009. Metasomatism in the Lithospheric Mantle beneath Middle Atlas (Morocco) and the Origin of Fe- and Mg-rich Wehrlites. *J. Petrology* 50, 197–249.
- Rampone, E., Bottazzi, P., Ottolini, L., 1991. Complementary Ti and Zr anomalies in orthopyroxene and clinopyroxene from mantle peridotites. *Nature* 354, 518–520.
- Rampone, E., Piccardo, G.B., Vannucci, R., Bottazzi, P., 1997. Chemistry and origin of trapped melts in ophiolitic peridotites. *Geochimica et Cosmochimica Acta* 61, 4557–4569.
- Rampone, E., Piccardo, G.B., Vannucci, R., Bottazzi, P., Zanetti, A., 1994. Melt impregnation in ophiolitic peridotite: an ion microprobe study of clinopyroxene and plagioclase. *Mineralogical Magazine* 58, 756–757.
- Rampone, E., Romairone, A., Abouchami, W., Piccardo, G.B., Hofmann, A.W., 2005. Chronology, Petrology and Isotope Geochemistry of the Erro-Tobbio Peridotites (Ligurian Alps, Italy): Records of Late Palaeozoic Lithospheric Extension. *J. Petrology* 46, 799–827.
- Rampone, E., Vissers, R.L.M., Poggio, M., Scambelluri, M., Zanetti, A., 2010. Melt Migration and Intrusion during Exhumation of the Alboran Lithosphere: the Tallante Mantle Xenolith Record (Betic Cordillera, SE Spain). *J. Petrology* 51, 295–325.
- Reed, S.J.B., 1995. Electron Microprobe Microanalysis, in: Potts, P.J., Bowles, J.F., Reed, S.J.B. (Eds.), *Microprobe Techniques in the Earth Sciences*, The Mineralogical Society Series. pp. 49–90.
- Reed, S.J.B., 2005. *Electron microprobe analysis and scanning electron microscopy in geology*. Cambridge University Press, Cambridge.
- Reiners, P.W., 1998. Reactive Melt Transport in the Mantle and Geochemical Signatures of Mantle-derived Magmas. *J. Petrology* 39, 1039–1061.
- Reisberg, L., Zindler, A., 1986. Extreme isotopic variations in the upper mantle: evidence from Ronda. *Earth and Planetary Science Letters* 81, 29–45.
- Reisberg, L., Zindler, A., Jagoutz, E., 1989. Further Sr and Nd isotopic results from peridotites of the Ronda Ultramafic Complex. *Earth and Planetary Science Letters* 96, 161–180.
- Revel, M., Cremer, M., Grousset, F.E., Labeyrie, L., 1996. Grain-size and Sr-Nd isotopes as tracer of paleo-bottom current strength, Northeast Atlantic Ocean. *Marine Geology* 131, 233–249.
- Richard, P., Shimizu, N., Allègre, C.J., 1976. $^{143}\text{Nd}/^{146}\text{Nd}$, a natural tracer: an application to oceanic basalts. *Earth and Planetary Science Letters* 31, 269–278.
- Ringwood, A.E., 1969. Composition and evolution of the upper mantle. *Geophys. Monogr. Ser.* 13, 1–17.
- Ringwood, A.E., 1991. Phase transformations and their bearing on the constitution and dynamics of the mantle. *Geochimica et Cosmochimica Acta* 55, 2083–2110.
- Ritsema, J., Heijst, H.J. van, Woodhouse, J.H., 2004. Global transition zone tomography. *J. Geophys. Res.* 109, B02302.
- Rivalenti, G., Vannucci, R., Rampone, E., Mazzucchelli, M., Piccardo, G.B., Piccirillo, E.M., Bottazzi, P., Ottolini, L., 1996. Peridotite clinopyroxene chemistry reflects mantle processes rather than continental versus oceanic settings. *Earth and Planetary Science Letters* 139, 423–437.
- Rock, N.M.S., 1991. *Lamprophyres*. Blackie.

- Rosenbaum, J.M., Wilson, M., Downes, H., 1997. Multiple enrichment of the Carpathian-Pannonian mantle: Pb-Sr-Nd isotope and trace element constraints. *J. Geophys. Res.* 102, 14947-14,961.
- Royer, J.-Y., Gordon, R.G., 1997. The Motion and Boundary Between the Capricorn and Australian Plates. *Science* 277, 1268-1274.
- Rudnick, R.L., Gao, S., 2003. 3.01 - Composition of the Continental Crust, in: Editors-in-Chief: Heinrich D. Holland, Karl K. Turekian (Eds.), *Treatise on Geochemistry*. Pergamon, Oxford, pp. 1-64.
- Rudnick, R.L., McDonough, W.F., Chappell, B.W., 1993. Carbonatite metasomatism in the northern Tanzanian mantle: Petrographic and geochemical characteristics. *Earth and Planetary Science Letters* 114, 463-475.
- Rudnick, R.L., McDonough, W.F., O'Connell, R.J., 1998. Thermal structure, thickness and composition of continental lithosphere. *Chemical Geology* 145, 395-411.
- Rudnick, R.L., Walker, R.J., 2009. Interpreting ages from Re-Os isotopes in peridotites. *Lithos* 112, Supplement 2, 1083-1095.
- Sack, R.O., Ghiorso, M.S., 1994. Thermodynamics of multicomponent pyroxenes: II. Phase relations in the quadrilateral. *Contr. Mineral. and Petrol.* 116, 287-300.
- Salters, V.J.M., Stracke, A., 2004. Composition of the depleted mantle. *Geochem. Geophys. Geosyst.* 5, Q05B07.
- Sapienza, G.T., Griffin, W.L., O'Reilly, S.Y., Morten, L., 2007. Crustal zircons and mantle sulfides: Archean to Triassic events in the lithosphere beneath south-eastern Sicily. *Lithos* 96, 503-523.
- Schaefer, B.F., Parkinson, I.J., Hawkesworth, C.J., 2000. Deep mantle plume osmium isotope signature from West Greenland Tertiary picrites. *Earth and Planetary Science Letters* 175, 105-118.
- Schutt, D.L., Leshner, C.E., 2006. Effects of melt depletion on the density and seismic velocity of garnet and spinel lherzolite. *J. Geophys. Res.* 111, B05401.
- Seghedi, I., Brandle, J.L., Szakács, A., Ancochea, E., Vaselli, O., 2002. El manto litosférico en el sureste de España: Aportaciones de los cenolitos englobados en rocas alcalinas del mioceno-plioceno. *Geogaceta* 32, 27-30.
- Serrano, I., Hearn, T.M., Morales, J., Torcal, F., 2005. Seismic anisotropy and velocity structure beneath the southern half of the Iberian Peninsula. *Physics of the Earth and Planetary Interiors* 150, 317-330.
- Shaw, D.M., 1970. Trace element fractionation during anatexis. *Geochimica et Cosmochimica Acta* 34, 237-243.
- Shimizu, Y., Arai, S., Morishita, T., Ishida, Y., 2008. Origin and significance of spinel-pyroxene symplectite in lherzolite xenoliths from Tallante, SE Spain. *Miner Petrol* 94, 27-43.
- Shimizu, Y., Arai, S., Morishita, T., Yurimoto, H., Gervilla, F., 2004. Petrochemical characteristics of felsic veins in mantle xenoliths from Tallante (SE Spain): an insight into activity of silicic melt within the mantle wedge. *Earth and Environmental Science Transactions of the Royal Society of Edinburgh* 95, 265-276.
- Silver, P.G., 1996. SEISMIC ANISOTROPY BENEATH THE CONTINENTS: Probing the Depths of Geology. *Annual Review of Earth and Planetary Sciences* 24, 385-432.
- Simon, N.S.C., Carlson, R.W., Pearson, D.G., Davies, G.R., 2007. The Origin and Evolution of the Kaapvaal Cratonic Lithospheric Mantle. *J. Petrology* 48, 589-625.
- Smith, D., Boyd, F.R., 1992. Compositional zonation in garnets in peridotite xenoliths. *Contrib Mineral Petrol* 112, 134-147.
- Sobolev, N.V., Lavrent'ev, Y.G., Pokhilenko, N.P., Usova, L.V., 1973. Chrome-rich garnets from the kimberlites of Yakutia and their parageneses. *Contr. Mineral. and Petrol.* 40, 39-52.
- Soto, J.I., Fernández-Ibáñez, F., Fernández, M., García-Casco, A., 2008. Thermal structure of the crust in the Gibraltar Arc: Influence on active tectonics in the western Mediterranean. *Geochemistry, Geophysics, Geosystems* 9, n/a-n/a.

- Soustelle, V., Tommasi, A., Bodinier, J.L., Garrido, C.J., Vauchez, A., 2009. Deformation and Reactive Melt Transport in the Mantle Lithosphere above a Large-scale Partial Melting Domain: the Ronda Peridotite Massif, Southern Spain. *J. Petrology* 50, 1235–1266.
- Soustelle, V., Tommasi, A., Demouchy, S., Ionov, D.A., 2010. Deformation and Fluid-Rock Interaction in the Supra-subduction Mantle: Microstructures and Water Contents in Peridotite Xenoliths from the Avacha Volcano, Kamchatka. *J. Petrology* 51, 363–394.
- Spakman, W., Wortel, R., 2004. A Tomographic View on Western Mediterranean Geodynamics, in: Cavazza, P.D.W., Roure, D.F., Spakman, P.W., Stampfli, P.G.M., Ziegler, P.P.A. (Eds.), *The TRANSMED Atlas. The Mediterranean Region from Crust to Mantle*. Springer Berlin Heidelberg, pp. 31–52.
- Stern, R.J., 2002. Subduction zones. *Rev. Geophys.* 40, 1012.
- Stern, R.J., 2004. Subduction initiation: spontaneous and induced. *Earth and Planetary Science Letters* 226, 275–292.
- Stich, D., Serpelloni, E., De Lis Mancilla, F., Morales, J., 2006. Kinematics of the Iberia-Maghreb plate contact from seismic moment tensors and GPS observations. *Tectonophysics* 426, 295–317.
- Stosch, H.-G., 1982. Rare earth element partitioning between minerals from anhydrous spinel peridotite xenoliths. *Geochimica et Cosmochimica Acta* 46, 793–811.
- Streckeisen, A., 1976. To each plutonic rock its proper name. *Earth-Science Reviews* 12, 1–33.
- Streckeisen, P.D.A., 1974. Classification and nomenclature of plutonic rocks recommendations of the IUGS subcommission on the systematics of Igneous Rocks. *Geol Rundsch* 63, 773–786.
- Su, Y., Langmuir, C.H., 2003. Global MORB chemistry compilation at the segment scale (PhD Thesis). Columbia University, New York.
- Suhr, G., 1999. Melt Migration under Oceanic Ridges: Inferences from Reactive Transport Modelling of Upper Mantle Hosted Dunites. *J. Petrology* 40, 575–599.
- Sun, S.-., McDonough, W.F., 1989. Chemical and isotopic systematics of oceanic basalts: implications for mantle composition and processes. *Geological Society, London, Special Publications* 42, 313–345.
- Szabó, C., Falus, G., Zajacz, Z., Kovács, I., Bali, E., 2004. Composition and evolution of lithosphere beneath the Carpathian-Pannonian Region: a review. *Tectonophysics* 393, 119–137.
- Takazawa, E., Frey, F.A., Shimizu, N., Obata, M., Bodinier, J.L., 1992. Geochemical evidence for melt migration and reaction in the upper mantle. *Nature* 359, 55–58.
- Tarantola, A., Valette, B., 1982. Generalized nonlinear inverse problems solved using the least squares criterion. *Reviews of Geophysics* 20, 219–232.
- Taylor, W.R., 1998. An experimental test of some geothermometer and geobarometer formulations for upper mantle peridotites with application to the thermobarometry of fertile lherzolite and garnet websterite. *Neues Jahrbuch für Mineralogie* 172, 381–408.
- Todt, W., Cliff, R., Hanser, A., Hofmann, A., 1996. Evaluation of a ^{202}Pb - ^{205}Pb double spike for high - precision lead isotope analysis. *Geophys. Monogr. Ser.* 95, 429–437.
- Tommasi, A., Mainprice, D., Canova, G., Chastel, Y., 2000. Viscoplastic self-consistent and equilibrium-based modeling of olivine lattice preferred orientations: Implications for the upper mantle seismic anisotropy. *J. Geophys. Res.* 105, 7893–7908.
- Tommasi, A., Mainprice, D., Cordier, P., Thoraval, C., Couvy, H., 2004. Strain-induced seismic anisotropy of wadsleyite polycrystals and flow patterns in the mantle transition zone. *Journal of Geophysical Research: Solid Earth* 109, n/a-n/a.
- Tommasi, A., Tikoff, B., Vauchez, A., 1999. Upper mantle tectonics: three-dimensional deformation, olivine crystallographic

- fabrics and seismic properties. *Earth and Planetary Science Letters* 168, 173–186.
- Tommasi, A., Vauchez, A., Ionov, D.A., 2008. Deformation, static recrystallization, and reactive melt transport in shallow subcontinental mantle xenoliths (Tok Cenozoic volcanic field, SE Siberia). *Earth and Planetary Science Letters* 272, 65–77.
- Torne, M., Fernández, M., Comas, M.C., Soto, J.I., 2000. Lithospheric Structure Beneath the Alboran Basin: Results from 3D Gravity Modeling and Tectonic Relevance. *J. Geophys. Res.* 105, 3209–3228.
- Torres-Roldán, R.L., Poli, G., Peccerillo, A., 1986. An early Miocene arc-tholeiitic magmatic dike event from the Alboran Sea – Evidence for precollisional subduction and back-arc crustal extension in the westernmost Mediterranean. *Geol Rundsch* 75, 219–234.
- Toscani, L., Venturelli, G., Barbieri, M., Capedri, S., Soler, J.M.F., Oddone, M., 1990. Geochemistry and petrogenesis of two-Pyroxene andesites from Sierra de Gata (SE Spain). *Mineralogy and Petrology* 41, 199–213.
- Tubía, J.M., 1988. Estructura de los Alpujarrides occidentales: cinemática y condiciones de emplazamiento de las peridotitas de Ronda. Parte III, tectónica de la aureola dinamo-térmica del manto de Ojén. *Boletín geológico y minero* 99, 20–45.
- Turner, S.P., Platt, J.P., George, R.M.M., Kelley, S.P., Pearson, D.G., Nowell, G.M., 1999. Magmatism Associated with Orogenic Collapse of the Betic-Alboran Domain, SE Spain. *J. Petrology* 40, 1011–1036.
- Van Achtebergh, E., Ryan, C.G., Jackson, S.E., Griffin, W.L., 2001. Data reduction software for LA-ICP-MS, in: Sylvester, P.J. (Ed.), *Laser-ablation-ICPMS in the Earth Sciences: Principles and Applications*. Mineralogical Association of Canada, pp. 239–243.
- Van Bemmelen, R.W., 1927. *Bijdrage tot de geologie der Betisch Ketens in de provincie Granada* (PhD Thesis). University of Delft, Netherlands.
- Van der Wal, D., Bodinier, J.-L., 1996. Origin of the recrystallisation front in the Ronda peridotite by km-scale pervasive porous melt flow. *Contrib Mineral Petrol* 122, 387–405.
- Van der Wal, D., Vissers, R.L.M., 1993. Uplift and emplacement of upper mantle rocks in the western Mediterranean. *Geology* 21, 1119–1122.
- Van der Wal, D., Vissers, R.L.M., 1996. Structural Petrology of the Ronda Peridotite, SW Spain: Deformation History. *J. Petrology* 37, 23–43.
- Van der Wal, D., Vissers, R.L.M., Drury, M.R., Hoogerduijn Strating, E.H., 1992. Oblique fabrics in porphyroclastic Alpine-type peridotites: a shear-sense indicator for upper mantle flow. *Journal of Structural Geology* 14, 839–846.
- Vasseur, G., Vernières, J., Bodinier, J.-L., 1991. Modelling of Trace Element Transfer between Mantle Melt and Heterogeneous Peridotite Matrix. *Journal of Petrology Special Volume*, 41–54.
- Vauchez, A., Dineur, F., Rudnick, R., 2005. Microstructure, texture and seismic anisotropy of the lithospheric mantle above a mantle plume: Insights from the Labait volcano xenoliths (Tanzania). *Earth and Planetary Science Letters* 232, 295–314.
- Vauchez, A., Garrido, C.J., 2001. Seismic properties of an asthenospherized lithospheric mantle: constraints from lattice preferred orientations in peridotite from the Ronda massif. *Earth and Planetary Science Letters* 192, 235–249.
- Vauchez, A., Nicolas, A., 1991. Mountain building: strike-parallel motion and mantle anisotropy. *Tectonophysics* 185, 183–201.
- Vauchez, A., Tommasi, A., Mainprice, D., 2012. Faults (shear zones) in the Earth's mantle. *Tectonophysics* 558–559, 1–27.
- Venturelli, G., Capedri, S., Di Battistini, G., Crawford, A., Kogarko, L.N., Celestini, S., 1984. The ultrapotassic rocks from southeastern Spain. *Lithos* 17, 37–54.
- Vernières, J., Godard, M., Bodinier, J.-L., 1997. A plate model for the simulation of trace element fractionation during partial melting and magma transport in the Earth's upper mantle. *Journal of Geophysical Research: Solid Earth* 102, 24771–24784.

- Vielzeuf, D., 1983. The spinel and quartz associations in high grade xenoliths from Tallante (S.E. Spain) and their potential use in geothermometry and barometry. *Contrib Mineral Petrol* 82, 301-311.
- Villaseca, C., Ancochea, E., Orejana, D., Jeffries, T.E., 2010. Composition and evolution of the lithospheric mantle in central Spain: inferences from peridotite xenoliths from the Cenozoic Calatrava volcanic field. Geological Society, London, Special Publications 337, 125-151.
- Villaseca, C., Barbero, L., Rogers, G., 1998. Crustal origin of Hercynian peraluminous granitic batholiths of Central Spain: petrological, geochemical and isotopic (Sr, Nd) constraints. *Lithos* 43, 55-79.
- Villaseca, C., Belousova, E., Orejana, D., Castiñeiras, P., Pérez-Soba, C., 2011a. Presence of Palaeoproterozoic and Archean components in the granulite-facies rocks of central Iberia: The Hf isotopic evidence. *Precambrian Research* 187, 143-154.
- Villaseca, C., Orejana, D., Belousova, E., Armstrong, R.A., Pérez-Soba, C., Jeffries, T.E., 2011b. U-Pb isotopic ages and Hf isotope composition of zircons in Variscan gabbros from central Spain: evidence of variable crustal contamination. *Miner Petrol* 101, 151-167.
- Vladimirov, V.G., Vladimirov, A.G., Gibsher, A.S., Travin, A.V., Rudnev, S.N., Shemelina, I.V., Barabash, N.V., Savinykh, Y.V., 2005. Model of the tectonometamorphic evolution for the Sangilen Block (southeastern Tuva, Central Asia) as a reflection of the early Caledonian accretion-collision tectogenesis. *Doklady Earth Sciences* 405, 1159-1165.
- Vollmer, F.W., 1990. An application of eigenvalue methods to structural domain analysis. *Geological Society of America Bulletin* 102, 786-791.
- Vonlanthen, P., Kunze, K., Burlini, L., Grobety, B., 2006. Seismic properties of the upper mantle beneath Lanzarote (Canary Islands): Model predictions based on texture measurements by EBSD. *Tectonophysics* 428, 65-85.
- Walker, R., Horan, M., Morgan, J., Becker, H., Grossman, J., Rubin, A., 2002. Comparative 187Re-187Os systematics of chondrites: Implications regarding early solar system processes. *Geochimica et Cosmochimica Acta* 66, 4187-4201.
- Walter, M.J., 1998. Melting of Garnet Peridotite and the Origin of Komatiite and Depleted Lithosphere. *J. Petrology* 39, 29-60.
- Watson, E.B., Brenan, J.M., 1987. Fluids in the lithosphere, 1. Experimentally-determined wetting characteristics of CO₂H₂O fluids and their implications for fluid transport, host-rock physical properties, and fluid inclusion formation. *Earth and Planetary Science Letters* 85, 497-515.
- Webb, S.A.C., Wood, B.J., 1986. Spinel-pyroxene-garnet relationships and their dependence on Cr/Al ratio. *Contrib Mineral and Petrol* 92, 471-480.
- Weijermars, R., 1991. Geology and tectonics of the Betic Zone, SE Spain. *Earth-Science Reviews* 31, 153-236.
- White, W.M., 2005. *Geochemistry*. John-Hopkins University Press, Baltimore, Maryland.
- White, W.M., Albarède, F., Télouk, P., 2000. High-precision analysis of Pb isotope ratios by multi-collector ICP-MS. *Chemical Geology* 167, 257-270.
- Wiechert, U., Ionov, D.A., Wedepohl, K.H., 1997. Spinel peridotite xenoliths from the Atsagin-Dush volcano, Dariganga lava plateau, Mongolia: a record of partial melting and cryptic metasomatism in the upper mantle. *Contrib Mineral Petrol* 126, 345-364.
- Wilshire, H.G., 1987. A model of mantle metasomatism, in: Mullen, E.D., Pasteris, J.D. (Eds.), *Mantle Metasomatism and Alkaline Magmatism*, Geological Society of America Special Paper. GSA, Boulder, Colorado, pp. 47-60.
- Wilshire, H.G., Shervais, J.W., 1975. Al-augite and Cr-diopside ultramafic xenoliths in basaltic rocks from western United States. *Physics and Chemistry of the Earth* 9, 257-272.
- Witt-Eickschen, G., Seck, H.A., 1991. Solubility of Ca and Al in orthopyroxene from spinel peridotite: an improved version of an

- empirical geothermometer. *Contr. Mineral. and Petrol.* 106, 431–439.
- Wood, B.J., Virgo, D., 1989. Upper mantle oxidation state: Ferric iron contents of Iherzolite spinels by ^{57}Fe Mössbauer spectroscopy and resultant oxygen fugacities. *Geochimica et Cosmochimica Acta* 53, 1277–1291.
- Woodland, A.B., Kornprobst, J., McPherson, E., Bodinier, J.-L., Menzies, M.A., 1996. Metasomatic interactions in the lithospheric mantle: petrologic evidence from the Lherz massif, French Pyrenees. *Chemical Geology* 134, 83–112.
- Woodland, A.B., Kornprobst, J., Tabit, A., 2006. Ferric iron in orogenic Iherzolite massifs and controls of oxygen fugacity in the upper mantle. *Lithos* 89, 222–241.
- Woodland, A.B., Kornprobst, J., Wood, B.J., 1992. Oxygen Thermobarometry of Orogenic Iherzolite Massifs. *J. Petrology* 33, 203–230.
- Xu, Y.-G., Menzies, M.A., Bodinier, J.-L., Bedini, R.M., Vroon, P., Mercier, J.-C.C., 1998. Melt percolation and reaction atop a plume: evidence from the poikiloblastic peridotite xenoliths from Borée (Massif Central, France). *Contrib Mineral Petrol* 132, 65–84.
- Xu, Y.-G., Menzies, M.A., Thirlwall, M.F., Huang, X.-L., Liu, Y., Chen, X.-M., 2003. “Reactive” harzburgites from Huinan, NE China: products of the lithosphere-asthenosphere interaction during lithospheric thinning? *Geochimica et Cosmochimica Acta* 67, 487–505.
- Yaxley, G.M., Crawford, A.J., Green, D.H., 1991. Evidence for carbonatite metasomatism in spinel peridotite xenoliths from western Victoria, Australia. *Earth and Planetary Science Letters* 107, 305–317.
- Zangana, N.A., Downes, H., Thirlwall, M.F., Hegner, E., 1997. Relationship between deformation, equilibration temperatures, REE and radiogenic isotopes in mantle xenoliths (Ray Pic, Massif Central, France): an example of plume-lithosphere interaction? *Contrib Mineral Petrol* 127, 187–203.
- Zeck, H., Albat, F., Hansen, B., Torres-Roldán, R., Garcá-Casco, A., Martín-Algarra, A., 1989. A 21 ± 2 Ma age for the termination of the ductile alpine deformation in the internal zone of the betic cordilleras, South Spain. *Tectonophysics* 169, 215–220.
- Zeck, H.P., Kristensen, A.B., Nakamura, E., 1999. Inherited Palaeozoic and Mesozoic Rb–Sr Isotopic Signatures in Neogene Calc-alkaline Volcanics, Alborán Volcanic Province, SE Spain. *J. Petrology* 40, 511–524.
- Zeck, H.P., Maluski, H., Kristensen, A.B., 2000. Revised geochronology of the Neogene calc-alkaline volcanic suite in Sierra de Gata, Alborán volcanic province, SE Spain. *Journal of the Geological Society* 157, 75–81.
- Zeck, H.P., Whitehouse, M.J., 1999. Hercynian, Pan-African, Proterozoic and Archean ion-microprobe zircon ages for a Betic-Rif core complex, Alpine belt, W Mediterranean – consequences for its P-T-t path. *Contrib Mineral Petrol* 134, 134–149.
- Zeck, H.P., Williams, I.S., 2001. Hercynian Metamorphism in Nappe Core Complexes of the Alpine Betic-Rif Belt, Western Mediterranean – a SHRIMP Zircon Study. *J. Petrology* 42, 1373–1385.
- Zindler, A., Hart, S., 1986. Chemical Geodynamics. *Annual Review of Earth and Planetary Sciences* 14, 493–571.
- Zinngrebe, E., Foley, S.F., 1995. Metasomatism in mantle xenoliths from Gees, West Eifel, Germany: evidence for the genesis of calc-alkaline glasses and metasomatic Ca-enrichment. *Contrib Mineral Petrol* 122, 79–96.
- Zonenshain, L.P., Kuzmin, M.I., Natapov, L.M., Page, B.M., 1990. Geology of the USSR: a plate-tectonic synthesis, Geodynamics series. American Geophysical Union, Washington, D.C.
- Zonenshain, L.P., Kuzmin, M.I., Natapov, L.M., Page, B.M., 1990. Geology of the USSR: A Plate-Tectonic Synthesis. *Geodyn. Ser.* 21, 1–242.
- Zorin, Y.A., Novoselova, M.R., Turutanov, E.K., Kozhevnikov, V.M., 1990. Structure of the lithosphere of the Mongolian-Siberian mountainous province. *Journal of Geodynamics* 11, 327–342.

Part V

Appendix

Sample List

| Sample code | Location | TS | EBSD | XRF | ICP-MS | EPMA | LA-ICP-MS | MC-ICP-MS & TIMS | Rock type |
|-------------|---------------------------|-------------------------------------|-------------------------------------|-------------------------------------|-------------------------------------|-------------------------------------|-------------------------------------|-------------------------------------|------------|
| LP08-01 | Los Perez (Murcia, Spain) | <input checked="" type="checkbox"/> | <input type="checkbox"/> | <input type="checkbox"/> | <input type="checkbox"/> | <input checked="" type="checkbox"/> | <input checked="" type="checkbox"/> | <input type="checkbox"/> | Peridotite |
| LP08-02 | Los Perez (Murcia, Spain) | <input checked="" type="checkbox"/> | <input checked="" type="checkbox"/> | <input checked="" type="checkbox"/> | <input type="checkbox"/> | <input checked="" type="checkbox"/> | <input checked="" type="checkbox"/> | <input checked="" type="checkbox"/> | Lherzolite |
| LP08-03 | Los Perez (Murcia, Spain) | <input checked="" type="checkbox"/> | <input type="checkbox"/> | <input checked="" type="checkbox"/> | <input checked="" type="checkbox"/> | <input checked="" type="checkbox"/> | <input type="checkbox"/> | <input checked="" type="checkbox"/> | Lherzolite |
| LP08-04 | Los Perez (Murcia, Spain) | <input checked="" type="checkbox"/> | <input type="checkbox"/> | <input type="checkbox"/> | <input type="checkbox"/> | <input checked="" type="checkbox"/> | <input checked="" type="checkbox"/> | <input type="checkbox"/> | Peridotite |
| LP08-05 | Los Perez (Murcia, Spain) | <input checked="" type="checkbox"/> | <input type="checkbox"/> | <input type="checkbox"/> | <input type="checkbox"/> | <input checked="" type="checkbox"/> | <input checked="" type="checkbox"/> | <input type="checkbox"/> | Peridotite |
| LP08-06 | Los Perez (Murcia, Spain) | <input checked="" type="checkbox"/> | <input type="checkbox"/> | <input type="checkbox"/> | <input type="checkbox"/> | <input checked="" type="checkbox"/> | <input type="checkbox"/> | <input type="checkbox"/> | Peridotite |
| LP08-07 | Los Perez (Murcia, Spain) | <input checked="" type="checkbox"/> | <input type="checkbox"/> | <input type="checkbox"/> | <input type="checkbox"/> | <input checked="" type="checkbox"/> | <input checked="" type="checkbox"/> | <input type="checkbox"/> | Peridotite |
| LP08-08 | Los Perez (Murcia, Spain) | <input checked="" type="checkbox"/> | <input type="checkbox"/> | <input type="checkbox"/> | <input type="checkbox"/> | <input checked="" type="checkbox"/> | <input checked="" type="checkbox"/> | <input type="checkbox"/> | Peridotite |
| LP08-09 | Los Perez (Murcia, Spain) | <input checked="" type="checkbox"/> | <input type="checkbox"/> | <input type="checkbox"/> | <input type="checkbox"/> | <input checked="" type="checkbox"/> | <input checked="" type="checkbox"/> | <input type="checkbox"/> | Peridotite |
| LP08-10 | Los Perez (Murcia, Spain) | <input checked="" type="checkbox"/> | <input type="checkbox"/> | <input type="checkbox"/> | <input type="checkbox"/> | <input checked="" type="checkbox"/> | <input checked="" type="checkbox"/> | <input type="checkbox"/> | Peridotite |
| LP08-11 | Los Perez (Murcia, Spain) | <input checked="" type="checkbox"/> | <input type="checkbox"/> | <input type="checkbox"/> | <input type="checkbox"/> | <input checked="" type="checkbox"/> | <input type="checkbox"/> | <input type="checkbox"/> | Peridotite |
| LP08-12 | Los Perez (Murcia, Spain) | <input checked="" type="checkbox"/> | <input checked="" type="checkbox"/> | <input type="checkbox"/> | <input type="checkbox"/> | <input checked="" type="checkbox"/> | <input checked="" type="checkbox"/> | <input type="checkbox"/> | Wehrlite |
| LP08-13 | Los Perez (Murcia, Spain) | <input checked="" type="checkbox"/> | <input type="checkbox"/> | <input type="checkbox"/> | <input type="checkbox"/> | <input checked="" type="checkbox"/> | <input checked="" type="checkbox"/> | <input type="checkbox"/> | Peridotite |
| LP08-14 | Los Perez (Murcia, Spain) | <input checked="" type="checkbox"/> | <input type="checkbox"/> | <input checked="" type="checkbox"/> | <input checked="" type="checkbox"/> | <input type="checkbox"/> | <input checked="" type="checkbox"/> | <input checked="" type="checkbox"/> | Lherzolite |
| LP08-15 | Los Perez (Murcia, Spain) | <input checked="" type="checkbox"/> | <input type="checkbox"/> | <input type="checkbox"/> | <input type="checkbox"/> | <input checked="" type="checkbox"/> | <input type="checkbox"/> | <input type="checkbox"/> | Peridotite |
| LP08-16 | Los Perez (Murcia, Spain) | <input checked="" type="checkbox"/> | <input type="checkbox"/> | <input type="checkbox"/> | <input type="checkbox"/> | <input checked="" type="checkbox"/> | <input checked="" type="checkbox"/> | <input type="checkbox"/> | Peridotite |
| LPE-001 | Los Perez (Murcia, Spain) | <input type="checkbox"/> | <input type="checkbox"/> | <input type="checkbox"/> | <input type="checkbox"/> | <input type="checkbox"/> | <input type="checkbox"/> | <input type="checkbox"/> | |
| LPE-002 | Los Perez (Murcia, Spain) | <input checked="" type="checkbox"/> | <input checked="" type="checkbox"/> | <input type="checkbox"/> | <input type="checkbox"/> | <input checked="" type="checkbox"/> | <input type="checkbox"/> | <input type="checkbox"/> | Lherzolite |
| LPE-003 | Los Perez (Murcia, Spain) | <input type="checkbox"/> | <input type="checkbox"/> | <input type="checkbox"/> | <input type="checkbox"/> | <input type="checkbox"/> | <input type="checkbox"/> | <input type="checkbox"/> | |
| LPE-004 | Los Perez (Murcia, Spain) | <input checked="" type="checkbox"/> | <input type="checkbox"/> | <input type="checkbox"/> | <input type="checkbox"/> | <input type="checkbox"/> | <input type="checkbox"/> | <input type="checkbox"/> | Peridotite |
| LPE-005 | Los Perez (Murcia, Spain) | <input type="checkbox"/> | <input type="checkbox"/> | <input type="checkbox"/> | <input type="checkbox"/> | <input type="checkbox"/> | <input type="checkbox"/> | <input type="checkbox"/> | |
| LPE-006 | Los Perez (Murcia, Spain) | <input type="checkbox"/> | <input type="checkbox"/> | <input type="checkbox"/> | <input type="checkbox"/> | <input type="checkbox"/> | <input type="checkbox"/> | <input type="checkbox"/> | |
| LPE-007 | Los Perez (Murcia, Spain) | <input type="checkbox"/> | <input type="checkbox"/> | <input type="checkbox"/> | <input type="checkbox"/> | <input type="checkbox"/> | <input type="checkbox"/> | <input type="checkbox"/> | |
| LPE-008 | Los Perez (Murcia, Spain) | <input checked="" type="checkbox"/> | <input checked="" type="checkbox"/> | <input type="checkbox"/> | <input type="checkbox"/> | <input type="checkbox"/> | <input type="checkbox"/> | <input type="checkbox"/> | Composite |
| LPE-009 | Los Perez (Murcia, Spain) | <input checked="" type="checkbox"/> | <input type="checkbox"/> | <input type="checkbox"/> | <input type="checkbox"/> | <input type="checkbox"/> | <input type="checkbox"/> | <input type="checkbox"/> | Peridotite |
| LPE-010 | Los Perez (Murcia, Spain) | <input type="checkbox"/> | <input type="checkbox"/> | <input type="checkbox"/> | <input type="checkbox"/> | <input type="checkbox"/> | <input type="checkbox"/> | <input type="checkbox"/> | |
| LPE-011 | Los Perez (Murcia, Spain) | <input type="checkbox"/> | <input type="checkbox"/> | <input type="checkbox"/> | <input type="checkbox"/> | <input type="checkbox"/> | <input type="checkbox"/> | <input type="checkbox"/> | |
| LPE-012 | Los Perez (Murcia, Spain) | <input type="checkbox"/> | <input type="checkbox"/> | <input type="checkbox"/> | <input type="checkbox"/> | <input type="checkbox"/> | <input type="checkbox"/> | <input type="checkbox"/> | |
| LPE-013 | Los Perez (Murcia, Spain) | <input type="checkbox"/> | <input type="checkbox"/> | <input type="checkbox"/> | <input type="checkbox"/> | <input type="checkbox"/> | <input type="checkbox"/> | <input type="checkbox"/> | |
| LPE-014 | Los Perez (Murcia, Spain) | <input type="checkbox"/> | <input type="checkbox"/> | <input type="checkbox"/> | <input type="checkbox"/> | <input type="checkbox"/> | <input type="checkbox"/> | <input type="checkbox"/> | |
| LPE-015 | Los Perez (Murcia, Spain) | <input type="checkbox"/> | <input type="checkbox"/> | <input type="checkbox"/> | <input type="checkbox"/> | <input type="checkbox"/> | <input type="checkbox"/> | <input type="checkbox"/> | |
| LPE-016 | Los Perez (Murcia, Spain) | <input checked="" type="checkbox"/> | <input checked="" type="checkbox"/> | <input type="checkbox"/> | <input type="checkbox"/> | <input type="checkbox"/> | <input type="checkbox"/> | <input type="checkbox"/> | Lherzolite |
| LPE-017 | Los Perez (Murcia, Spain) | <input checked="" type="checkbox"/> | <input type="checkbox"/> | <input type="checkbox"/> | <input type="checkbox"/> | <input type="checkbox"/> | <input type="checkbox"/> | <input type="checkbox"/> | Peridotite |
| LPE-018 | Los Perez (Murcia, Spain) | <input type="checkbox"/> | <input type="checkbox"/> | <input type="checkbox"/> | <input type="checkbox"/> | <input type="checkbox"/> | <input type="checkbox"/> | <input type="checkbox"/> | |
| LPE-019 | Los Perez (Murcia, Spain) | <input type="checkbox"/> | <input type="checkbox"/> | <input type="checkbox"/> | <input type="checkbox"/> | <input type="checkbox"/> | <input type="checkbox"/> | <input type="checkbox"/> | |
| LPE-020 | Los Perez (Murcia, Spain) | <input type="checkbox"/> | <input type="checkbox"/> | <input type="checkbox"/> | <input type="checkbox"/> | <input type="checkbox"/> | <input type="checkbox"/> | <input type="checkbox"/> | |
| LPE-021 | Los Perez (Murcia, Spain) | <input checked="" type="checkbox"/> | <input type="checkbox"/> | <input type="checkbox"/> | <input type="checkbox"/> | <input type="checkbox"/> | <input type="checkbox"/> | <input type="checkbox"/> | Peridotite |
| LPE-022 | Los Perez (Murcia, Spain) | <input type="checkbox"/> | <input type="checkbox"/> | <input type="checkbox"/> | <input type="checkbox"/> | <input type="checkbox"/> | <input type="checkbox"/> | <input type="checkbox"/> | |
| LPE-023 | Los Perez (Murcia, Spain) | <input checked="" type="checkbox"/> | <input type="checkbox"/> | <input type="checkbox"/> | <input type="checkbox"/> | <input type="checkbox"/> | <input type="checkbox"/> | <input type="checkbox"/> | Peridotite |
| LPE-024 | Los Perez (Murcia, Spain) | <input type="checkbox"/> | <input type="checkbox"/> | <input type="checkbox"/> | <input type="checkbox"/> | <input type="checkbox"/> | <input type="checkbox"/> | <input type="checkbox"/> | |
| LPE-025 | Los Perez (Murcia, Spain) | <input checked="" type="checkbox"/> | <input checked="" type="checkbox"/> | <input type="checkbox"/> | <input type="checkbox"/> | <input type="checkbox"/> | <input type="checkbox"/> | <input type="checkbox"/> | Lherzolite |
| LPE-026 | Los Perez (Murcia, Spain) | <input type="checkbox"/> | <input type="checkbox"/> | <input type="checkbox"/> | <input type="checkbox"/> | <input type="checkbox"/> | <input type="checkbox"/> | <input type="checkbox"/> | |
| LPE-027 | Los Perez (Murcia, Spain) | <input type="checkbox"/> | <input type="checkbox"/> | <input type="checkbox"/> | <input type="checkbox"/> | <input type="checkbox"/> | <input type="checkbox"/> | <input type="checkbox"/> | |
| LPE-028 | Los Perez (Murcia, Spain) | <input checked="" type="checkbox"/> | <input checked="" type="checkbox"/> | <input checked="" type="checkbox"/> | <input checked="" type="checkbox"/> | <input checked="" type="checkbox"/> | <input checked="" type="checkbox"/> | <input checked="" type="checkbox"/> | Wehrlite |
| LPE-029 | Los Perez (Murcia, Spain) | <input checked="" type="checkbox"/> | <input checked="" type="checkbox"/> | <input checked="" type="checkbox"/> | <input checked="" type="checkbox"/> | <input checked="" type="checkbox"/> | <input checked="" type="checkbox"/> | <input checked="" type="checkbox"/> | Lherzolite |
| LPE-030 | Los Perez (Murcia, Spain) | <input type="checkbox"/> | <input type="checkbox"/> | <input type="checkbox"/> | <input type="checkbox"/> | <input type="checkbox"/> | <input type="checkbox"/> | <input type="checkbox"/> | |
| LPE-031 | Los Perez (Murcia, Spain) | <input type="checkbox"/> | <input type="checkbox"/> | <input type="checkbox"/> | <input type="checkbox"/> | <input type="checkbox"/> | <input type="checkbox"/> | <input type="checkbox"/> | |
| LPE-032 | Los Perez (Murcia, Spain) | <input type="checkbox"/> | <input type="checkbox"/> | <input type="checkbox"/> | <input type="checkbox"/> | <input type="checkbox"/> | <input type="checkbox"/> | <input type="checkbox"/> | |
| LPE-033 | Los Perez (Murcia, Spain) | <input type="checkbox"/> | <input type="checkbox"/> | <input type="checkbox"/> | <input type="checkbox"/> | <input type="checkbox"/> | <input type="checkbox"/> | <input type="checkbox"/> | |
| LPE-034 | Los Perez (Murcia, Spain) | <input type="checkbox"/> | <input type="checkbox"/> | <input type="checkbox"/> | <input type="checkbox"/> | <input type="checkbox"/> | <input type="checkbox"/> | <input type="checkbox"/> | |

| Sample code | Location | TS | EBSD | XRF | ICP-MS | EPMA | LA-ICP-MS | MC-ICP-MS & TIMS | Rock type |
|-------------|---------------------------|-------------------------------------|-------------------------------------|-------------------------------------|-------------------------------------|-------------------------------------|-------------------------------------|-------------------------------------|------------|
| LPE-035 | Los Perez (Murcia, Spain) | <input type="checkbox"/> | <input type="checkbox"/> | <input type="checkbox"/> | <input type="checkbox"/> | <input type="checkbox"/> | <input type="checkbox"/> | <input type="checkbox"/> | |
| LPE-036 | Los Perez (Murcia, Spain) | <input type="checkbox"/> | <input type="checkbox"/> | <input type="checkbox"/> | <input type="checkbox"/> | <input type="checkbox"/> | <input type="checkbox"/> | <input type="checkbox"/> | |
| LPE-037 | Los Perez (Murcia, Spain) | <input type="checkbox"/> | <input type="checkbox"/> | <input type="checkbox"/> | <input type="checkbox"/> | <input type="checkbox"/> | <input type="checkbox"/> | <input type="checkbox"/> | |
| LPE-038 | Los Perez (Murcia, Spain) | <input type="checkbox"/> | <input type="checkbox"/> | <input type="checkbox"/> | <input type="checkbox"/> | <input type="checkbox"/> | <input type="checkbox"/> | <input type="checkbox"/> | |
| LPE-039 | Los Perez (Murcia, Spain) | <input checked="" type="checkbox"/> | <input type="checkbox"/> | <input type="checkbox"/> | <input type="checkbox"/> | <input type="checkbox"/> | <input type="checkbox"/> | <input type="checkbox"/> | Peridotite |
| LPE-040 | Los Perez (Murcia, Spain) | <input type="checkbox"/> | <input type="checkbox"/> | <input type="checkbox"/> | <input type="checkbox"/> | <input type="checkbox"/> | <input type="checkbox"/> | <input type="checkbox"/> | |
| LPE-041 | Los Perez (Murcia, Spain) | <input type="checkbox"/> | <input type="checkbox"/> | <input type="checkbox"/> | <input type="checkbox"/> | <input type="checkbox"/> | <input type="checkbox"/> | <input type="checkbox"/> | |
| LPE-042 | Los Perez (Murcia, Spain) | <input checked="" type="checkbox"/> | <input checked="" type="checkbox"/> | <input checked="" type="checkbox"/> | <input checked="" type="checkbox"/> | <input type="checkbox"/> | <input checked="" type="checkbox"/> | <input checked="" type="checkbox"/> | Lherzolite |
| LPE-043 | Los Perez (Murcia, Spain) | <input type="checkbox"/> | <input type="checkbox"/> | <input type="checkbox"/> | <input type="checkbox"/> | <input type="checkbox"/> | <input type="checkbox"/> | <input type="checkbox"/> | |
| LPE-044 | Los Perez (Murcia, Spain) | <input type="checkbox"/> | <input type="checkbox"/> | <input type="checkbox"/> | <input type="checkbox"/> | <input type="checkbox"/> | <input type="checkbox"/> | <input type="checkbox"/> | |
| LPE-045 | Los Perez (Murcia, Spain) | <input type="checkbox"/> | <input type="checkbox"/> | <input type="checkbox"/> | <input type="checkbox"/> | <input type="checkbox"/> | <input type="checkbox"/> | <input type="checkbox"/> | |
| LPE-046 | Los Perez (Murcia, Spain) | <input checked="" type="checkbox"/> | <input type="checkbox"/> | <input checked="" type="checkbox"/> | <input checked="" type="checkbox"/> | <input type="checkbox"/> | <input type="checkbox"/> | <input checked="" type="checkbox"/> | Lherzolite |
| LPE-047 | Los Perez (Murcia, Spain) | <input checked="" type="checkbox"/> | <input type="checkbox"/> | <input type="checkbox"/> | <input type="checkbox"/> | <input type="checkbox"/> | <input type="checkbox"/> | <input checked="" type="checkbox"/> | Peridotite |
| LPE-048 | Los Perez (Murcia, Spain) | <input checked="" type="checkbox"/> | <input checked="" type="checkbox"/> | <input checked="" type="checkbox"/> | <input checked="" type="checkbox"/> | <input checked="" type="checkbox"/> | <input checked="" type="checkbox"/> | <input checked="" type="checkbox"/> | Lherzolite |
| LPE-049 | Los Perez (Murcia, Spain) | <input type="checkbox"/> | <input type="checkbox"/> | <input type="checkbox"/> | <input type="checkbox"/> | <input type="checkbox"/> | <input type="checkbox"/> | <input type="checkbox"/> | |
| LPE-050 | Los Perez (Murcia, Spain) | <input type="checkbox"/> | <input type="checkbox"/> | <input type="checkbox"/> | <input type="checkbox"/> | <input type="checkbox"/> | <input type="checkbox"/> | <input type="checkbox"/> | |
| LPE-051 | Los Perez (Murcia, Spain) | <input type="checkbox"/> | <input type="checkbox"/> | <input type="checkbox"/> | <input type="checkbox"/> | <input type="checkbox"/> | <input type="checkbox"/> | <input type="checkbox"/> | |
| LPE-052 | Los Perez (Murcia, Spain) | <input type="checkbox"/> | <input type="checkbox"/> | <input type="checkbox"/> | <input type="checkbox"/> | <input type="checkbox"/> | <input type="checkbox"/> | <input type="checkbox"/> | |
| LPE-053 | Los Perez (Murcia, Spain) | <input type="checkbox"/> | <input type="checkbox"/> | <input type="checkbox"/> | <input type="checkbox"/> | <input type="checkbox"/> | <input type="checkbox"/> | <input type="checkbox"/> | |
| LPE-054 | Los Perez (Murcia, Spain) | <input type="checkbox"/> | <input type="checkbox"/> | <input type="checkbox"/> | <input type="checkbox"/> | <input type="checkbox"/> | <input type="checkbox"/> | <input type="checkbox"/> | |
| LPE-055 | Los Perez (Murcia, Spain) | <input type="checkbox"/> | <input type="checkbox"/> | <input type="checkbox"/> | <input type="checkbox"/> | <input type="checkbox"/> | <input type="checkbox"/> | <input type="checkbox"/> | |
| LPE-056 | Los Perez (Murcia, Spain) | <input type="checkbox"/> | <input type="checkbox"/> | <input type="checkbox"/> | <input type="checkbox"/> | <input type="checkbox"/> | <input type="checkbox"/> | <input type="checkbox"/> | |
| LPE-057 | Los Perez (Murcia, Spain) | <input type="checkbox"/> | <input type="checkbox"/> | <input type="checkbox"/> | <input type="checkbox"/> | <input type="checkbox"/> | <input type="checkbox"/> | <input type="checkbox"/> | |
| LPE-058 | Los Perez (Murcia, Spain) | <input checked="" type="checkbox"/> | <input checked="" type="checkbox"/> | <input type="checkbox"/> | <input type="checkbox"/> | <input type="checkbox"/> | <input type="checkbox"/> | <input type="checkbox"/> | Lherzolite |
| LPE-059 | Los Perez (Murcia, Spain) | <input type="checkbox"/> | <input type="checkbox"/> | <input type="checkbox"/> | <input type="checkbox"/> | <input type="checkbox"/> | <input type="checkbox"/> | <input type="checkbox"/> | |
| LPE-060 | Los Perez (Murcia, Spain) | <input type="checkbox"/> | <input type="checkbox"/> | <input type="checkbox"/> | <input type="checkbox"/> | <input type="checkbox"/> | <input type="checkbox"/> | <input type="checkbox"/> | |
| LPE-061 | Los Perez (Murcia, Spain) | <input checked="" type="checkbox"/> | <input checked="" type="checkbox"/> | <input checked="" type="checkbox"/> | <input checked="" type="checkbox"/> | <input checked="" type="checkbox"/> | <input checked="" type="checkbox"/> | <input checked="" type="checkbox"/> | Lherzolite |
| LPE-062 | Los Perez (Murcia, Spain) | <input checked="" type="checkbox"/> | <input checked="" type="checkbox"/> | <input checked="" type="checkbox"/> | <input checked="" type="checkbox"/> | <input type="checkbox"/> | <input checked="" type="checkbox"/> | <input checked="" type="checkbox"/> | Lherzolite |
| LPE-063 | Los Perez (Murcia, Spain) | <input type="checkbox"/> | <input type="checkbox"/> | <input type="checkbox"/> | <input type="checkbox"/> | <input type="checkbox"/> | <input type="checkbox"/> | <input type="checkbox"/> | |
| LPE-064 | Los Perez (Murcia, Spain) | <input type="checkbox"/> | <input type="checkbox"/> | <input type="checkbox"/> | <input type="checkbox"/> | <input type="checkbox"/> | <input type="checkbox"/> | <input type="checkbox"/> | |
| LPE-065 | Los Perez (Murcia, Spain) | <input type="checkbox"/> | <input type="checkbox"/> | <input type="checkbox"/> | <input type="checkbox"/> | <input type="checkbox"/> | <input type="checkbox"/> | <input type="checkbox"/> | |
| LPE-066 | Los Perez (Murcia, Spain) | <input type="checkbox"/> | <input type="checkbox"/> | <input type="checkbox"/> | <input type="checkbox"/> | <input type="checkbox"/> | <input type="checkbox"/> | <input type="checkbox"/> | |
| LPE-067 | Los Perez (Murcia, Spain) | <input type="checkbox"/> | <input type="checkbox"/> | <input type="checkbox"/> | <input type="checkbox"/> | <input type="checkbox"/> | <input type="checkbox"/> | <input type="checkbox"/> | |
| LPE-068 | Los Perez (Murcia, Spain) | <input type="checkbox"/> | <input type="checkbox"/> | <input type="checkbox"/> | <input type="checkbox"/> | <input type="checkbox"/> | <input type="checkbox"/> | <input type="checkbox"/> | |
| LPE-069 | Los Perez (Murcia, Spain) | <input type="checkbox"/> | <input type="checkbox"/> | <input type="checkbox"/> | <input type="checkbox"/> | <input type="checkbox"/> | <input type="checkbox"/> | <input type="checkbox"/> | |
| LPE-070 | Los Perez (Murcia, Spain) | <input type="checkbox"/> | <input type="checkbox"/> | <input type="checkbox"/> | <input type="checkbox"/> | <input type="checkbox"/> | <input type="checkbox"/> | <input type="checkbox"/> | |
| TAL-001 | Tallante (Murcia, Spain) | <input checked="" type="checkbox"/> | <input checked="" type="checkbox"/> | <input checked="" type="checkbox"/> | <input checked="" type="checkbox"/> | <input checked="" type="checkbox"/> | <input checked="" type="checkbox"/> | <input checked="" type="checkbox"/> | Lherzolite |
| TAL-002 | Tallante (Murcia, Spain) | <input type="checkbox"/> | <input type="checkbox"/> | <input type="checkbox"/> | <input type="checkbox"/> | <input type="checkbox"/> | <input type="checkbox"/> | <input type="checkbox"/> | |
| TAL-003 | Tallante (Murcia, Spain) | <input type="checkbox"/> | <input type="checkbox"/> | <input type="checkbox"/> | <input type="checkbox"/> | <input type="checkbox"/> | <input type="checkbox"/> | <input type="checkbox"/> | |
| TAL-004 | Tallante (Murcia, Spain) | <input type="checkbox"/> | <input type="checkbox"/> | <input type="checkbox"/> | <input type="checkbox"/> | <input type="checkbox"/> | <input type="checkbox"/> | <input type="checkbox"/> | |
| TAL-005 | Tallante (Murcia, Spain) | <input type="checkbox"/> | <input type="checkbox"/> | <input type="checkbox"/> | <input type="checkbox"/> | <input type="checkbox"/> | <input type="checkbox"/> | <input type="checkbox"/> | |
| TAL-006 | Tallante (Murcia, Spain) | <input type="checkbox"/> | <input type="checkbox"/> | <input type="checkbox"/> | <input type="checkbox"/> | <input type="checkbox"/> | <input type="checkbox"/> | <input type="checkbox"/> | |
| TAL-007 | Tallante (Murcia, Spain) | <input type="checkbox"/> | <input type="checkbox"/> | <input type="checkbox"/> | <input type="checkbox"/> | <input type="checkbox"/> | <input type="checkbox"/> | <input type="checkbox"/> | |
| TAL-008 | Tallante (Murcia, Spain) | <input type="checkbox"/> | <input type="checkbox"/> | <input type="checkbox"/> | <input type="checkbox"/> | <input type="checkbox"/> | <input type="checkbox"/> | <input type="checkbox"/> | |
| TAL-009 | Tallante (Murcia, Spain) | <input type="checkbox"/> | <input type="checkbox"/> | <input type="checkbox"/> | <input type="checkbox"/> | <input type="checkbox"/> | <input type="checkbox"/> | <input type="checkbox"/> | |
| TAL-010 | Tallante (Murcia, Spain) | <input type="checkbox"/> | <input type="checkbox"/> | <input type="checkbox"/> | <input type="checkbox"/> | <input type="checkbox"/> | <input type="checkbox"/> | <input type="checkbox"/> | |
| TAL-011 | Tallante (Murcia, Spain) | <input type="checkbox"/> | <input type="checkbox"/> | <input type="checkbox"/> | <input type="checkbox"/> | <input type="checkbox"/> | <input type="checkbox"/> | <input type="checkbox"/> | |
| TAL-012 | Tallante (Murcia, Spain) | <input type="checkbox"/> | <input type="checkbox"/> | <input type="checkbox"/> | <input type="checkbox"/> | <input type="checkbox"/> | <input type="checkbox"/> | <input type="checkbox"/> | |
| TAL-013 | Tallante (Murcia, Spain) | <input type="checkbox"/> | <input type="checkbox"/> | <input type="checkbox"/> | <input type="checkbox"/> | <input type="checkbox"/> | <input type="checkbox"/> | <input type="checkbox"/> | |
| TAL-014 | Tallante (Murcia, Spain) | <input checked="" type="checkbox"/> | <input checked="" type="checkbox"/> | <input checked="" type="checkbox"/> | <input checked="" type="checkbox"/> | <input checked="" type="checkbox"/> | <input checked="" type="checkbox"/> | <input checked="" type="checkbox"/> | Lherzolite |
| TAL-015 | Tallante (Murcia, Spain) | <input type="checkbox"/> | <input type="checkbox"/> | <input type="checkbox"/> | <input type="checkbox"/> | <input type="checkbox"/> | <input type="checkbox"/> | <input type="checkbox"/> | |

| Sample code | Location | TS | EBSD | XRF | ICP-MS | EPMA | LA-ICP-MS | MC-ICP-MS & TIMS | Rock type |
|-------------|--------------------------|-------------------------------------|-------------------------------------|-------------------------------------|-------------------------------------|--------------------------|-------------------------------------|-------------------------------------|------------|
| TAL-016 | Tallante (Murcia, Spain) | <input type="checkbox"/> | <input type="checkbox"/> | <input type="checkbox"/> | <input type="checkbox"/> | <input type="checkbox"/> | <input type="checkbox"/> | <input type="checkbox"/> | |
| TAL-017 | Tallante (Murcia, Spain) | <input type="checkbox"/> | <input type="checkbox"/> | <input type="checkbox"/> | <input type="checkbox"/> | <input type="checkbox"/> | <input type="checkbox"/> | <input type="checkbox"/> | |
| TAL-018 | Tallante (Murcia, Spain) | <input type="checkbox"/> | <input type="checkbox"/> | <input type="checkbox"/> | <input type="checkbox"/> | <input type="checkbox"/> | <input type="checkbox"/> | <input type="checkbox"/> | |
| TAL-019 | Tallante (Murcia, Spain) | <input type="checkbox"/> | <input type="checkbox"/> | <input type="checkbox"/> | <input type="checkbox"/> | <input type="checkbox"/> | <input type="checkbox"/> | <input type="checkbox"/> | |
| TAL-020 | Tallante (Murcia, Spain) | <input type="checkbox"/> | <input type="checkbox"/> | <input type="checkbox"/> | <input type="checkbox"/> | <input type="checkbox"/> | <input type="checkbox"/> | <input type="checkbox"/> | |
| TAL-021 | Tallante (Murcia, Spain) | <input type="checkbox"/> | <input type="checkbox"/> | <input type="checkbox"/> | <input type="checkbox"/> | <input type="checkbox"/> | <input type="checkbox"/> | <input type="checkbox"/> | |
| TAL-022 | Tallante (Murcia, Spain) | <input type="checkbox"/> | <input type="checkbox"/> | <input type="checkbox"/> | <input type="checkbox"/> | <input type="checkbox"/> | <input type="checkbox"/> | <input type="checkbox"/> | |
| TAL-023 | Tallante (Murcia, Spain) | <input type="checkbox"/> | <input type="checkbox"/> | <input type="checkbox"/> | <input type="checkbox"/> | <input type="checkbox"/> | <input type="checkbox"/> | <input type="checkbox"/> | |
| TAL-024 | Tallante (Murcia, Spain) | <input type="checkbox"/> | <input type="checkbox"/> | <input type="checkbox"/> | <input type="checkbox"/> | <input type="checkbox"/> | <input type="checkbox"/> | <input type="checkbox"/> | |
| TAL-025 | Tallante (Murcia, Spain) | <input type="checkbox"/> | <input type="checkbox"/> | <input type="checkbox"/> | <input type="checkbox"/> | <input type="checkbox"/> | <input type="checkbox"/> | <input type="checkbox"/> | |
| TAL-026 | Tallante (Murcia, Spain) | <input type="checkbox"/> | <input type="checkbox"/> | <input type="checkbox"/> | <input type="checkbox"/> | <input type="checkbox"/> | <input type="checkbox"/> | <input type="checkbox"/> | |
| TAL-027 | Tallante (Murcia, Spain) | <input type="checkbox"/> | <input type="checkbox"/> | <input type="checkbox"/> | <input type="checkbox"/> | <input type="checkbox"/> | <input type="checkbox"/> | <input type="checkbox"/> | |
| TAL-028 | Tallante (Murcia, Spain) | <input type="checkbox"/> | <input type="checkbox"/> | <input type="checkbox"/> | <input type="checkbox"/> | <input type="checkbox"/> | <input type="checkbox"/> | <input type="checkbox"/> | |
| TAL-029 | Tallante (Murcia, Spain) | <input type="checkbox"/> | <input type="checkbox"/> | <input type="checkbox"/> | <input type="checkbox"/> | <input type="checkbox"/> | <input type="checkbox"/> | <input type="checkbox"/> | |
| TAL-030 | Tallante (Murcia, Spain) | <input type="checkbox"/> | <input type="checkbox"/> | <input type="checkbox"/> | <input type="checkbox"/> | <input type="checkbox"/> | <input type="checkbox"/> | <input type="checkbox"/> | |
| TAL-031 | Tallante (Murcia, Spain) | <input type="checkbox"/> | <input type="checkbox"/> | <input type="checkbox"/> | <input type="checkbox"/> | <input type="checkbox"/> | <input type="checkbox"/> | <input type="checkbox"/> | |
| TAL-032 | Tallante (Murcia, Spain) | <input type="checkbox"/> | <input type="checkbox"/> | <input type="checkbox"/> | <input type="checkbox"/> | <input type="checkbox"/> | <input type="checkbox"/> | <input type="checkbox"/> | |
| TAL-033 | Tallante (Murcia, Spain) | <input type="checkbox"/> | <input type="checkbox"/> | <input type="checkbox"/> | <input type="checkbox"/> | <input type="checkbox"/> | <input type="checkbox"/> | <input type="checkbox"/> | |
| TAL-034 | Tallante (Murcia, Spain) | <input type="checkbox"/> | <input type="checkbox"/> | <input type="checkbox"/> | <input type="checkbox"/> | <input type="checkbox"/> | <input type="checkbox"/> | <input type="checkbox"/> | |
| TAL-035 | Tallante (Murcia, Spain) | <input type="checkbox"/> | <input type="checkbox"/> | <input type="checkbox"/> | <input type="checkbox"/> | <input type="checkbox"/> | <input type="checkbox"/> | <input type="checkbox"/> | |
| TAL-036 | Tallante (Murcia, Spain) | <input checked="" type="checkbox"/> | <input type="checkbox"/> | <input type="checkbox"/> | <input type="checkbox"/> | <input type="checkbox"/> | <input type="checkbox"/> | <input type="checkbox"/> | Peridotite |
| TAL-037 | Tallante (Murcia, Spain) | <input type="checkbox"/> | <input type="checkbox"/> | <input type="checkbox"/> | <input type="checkbox"/> | <input type="checkbox"/> | <input type="checkbox"/> | <input type="checkbox"/> | |
| TAL-038 | Tallante (Murcia, Spain) | <input type="checkbox"/> | <input type="checkbox"/> | <input type="checkbox"/> | <input type="checkbox"/> | <input type="checkbox"/> | <input type="checkbox"/> | <input type="checkbox"/> | |
| TAL-039 | Tallante (Murcia, Spain) | <input type="checkbox"/> | <input type="checkbox"/> | <input type="checkbox"/> | <input type="checkbox"/> | <input type="checkbox"/> | <input type="checkbox"/> | <input type="checkbox"/> | |
| TAL-040 | Tallante (Murcia, Spain) | <input type="checkbox"/> | <input type="checkbox"/> | <input type="checkbox"/> | <input type="checkbox"/> | <input type="checkbox"/> | <input type="checkbox"/> | <input type="checkbox"/> | |
| TAL-041 | Tallante (Murcia, Spain) | <input type="checkbox"/> | <input type="checkbox"/> | <input type="checkbox"/> | <input type="checkbox"/> | <input type="checkbox"/> | <input type="checkbox"/> | <input type="checkbox"/> | |
| TAL-042 | Tallante (Murcia, Spain) | <input type="checkbox"/> | <input type="checkbox"/> | <input type="checkbox"/> | <input type="checkbox"/> | <input type="checkbox"/> | <input type="checkbox"/> | <input type="checkbox"/> | |
| TAL-043 | Tallante (Murcia, Spain) | <input type="checkbox"/> | <input type="checkbox"/> | <input type="checkbox"/> | <input type="checkbox"/> | <input type="checkbox"/> | <input type="checkbox"/> | <input type="checkbox"/> | |
| TAL-044 | Tallante (Murcia, Spain) | <input type="checkbox"/> | <input type="checkbox"/> | <input type="checkbox"/> | <input type="checkbox"/> | <input type="checkbox"/> | <input type="checkbox"/> | <input type="checkbox"/> | |
| TAL-045 | Tallante (Murcia, Spain) | <input checked="" type="checkbox"/> | <input type="checkbox"/> | <input type="checkbox"/> | <input type="checkbox"/> | <input type="checkbox"/> | <input type="checkbox"/> | <input type="checkbox"/> | Peridotite |
| TAL-046 | Tallante (Murcia, Spain) | <input checked="" type="checkbox"/> | <input type="checkbox"/> | <input type="checkbox"/> | <input type="checkbox"/> | <input type="checkbox"/> | <input type="checkbox"/> | <input type="checkbox"/> | Peridotite |
| TAL-047 | Tallante (Murcia, Spain) | <input checked="" type="checkbox"/> | <input checked="" type="checkbox"/> | <input checked="" type="checkbox"/> | <input checked="" type="checkbox"/> | <input type="checkbox"/> | <input checked="" type="checkbox"/> | <input type="checkbox"/> | Lherzolite |
| TAL-048 | Tallante (Murcia, Spain) | <input type="checkbox"/> | <input type="checkbox"/> | <input type="checkbox"/> | <input type="checkbox"/> | <input type="checkbox"/> | <input type="checkbox"/> | <input type="checkbox"/> | |
| TAL-049 | Tallante (Murcia, Spain) | <input type="checkbox"/> | <input type="checkbox"/> | <input type="checkbox"/> | <input type="checkbox"/> | <input type="checkbox"/> | <input type="checkbox"/> | <input type="checkbox"/> | |
| TAL-050 | Tallante (Murcia, Spain) | <input type="checkbox"/> | <input type="checkbox"/> | <input type="checkbox"/> | <input type="checkbox"/> | <input type="checkbox"/> | <input type="checkbox"/> | <input type="checkbox"/> | |
| TAL-051 | Tallante (Murcia, Spain) | <input type="checkbox"/> | <input type="checkbox"/> | <input type="checkbox"/> | <input type="checkbox"/> | <input type="checkbox"/> | <input type="checkbox"/> | <input type="checkbox"/> | |
| TAL-052 | Tallante (Murcia, Spain) | <input checked="" type="checkbox"/> | <input type="checkbox"/> | <input checked="" type="checkbox"/> | <input checked="" type="checkbox"/> | <input type="checkbox"/> | <input type="checkbox"/> | <input checked="" type="checkbox"/> | Lherzolite |
| TAL-053 | Tallante (Murcia, Spain) | <input type="checkbox"/> | <input type="checkbox"/> | <input type="checkbox"/> | <input type="checkbox"/> | <input type="checkbox"/> | <input type="checkbox"/> | <input type="checkbox"/> | |
| TAL-054 | Tallante (Murcia, Spain) | <input type="checkbox"/> | <input type="checkbox"/> | <input type="checkbox"/> | <input type="checkbox"/> | <input type="checkbox"/> | <input type="checkbox"/> | <input type="checkbox"/> | |
| TAL-055 | Tallante (Murcia, Spain) | <input type="checkbox"/> | <input type="checkbox"/> | <input type="checkbox"/> | <input type="checkbox"/> | <input type="checkbox"/> | <input type="checkbox"/> | <input type="checkbox"/> | |
| TAL-056 | Tallante (Murcia, Spain) | <input checked="" type="checkbox"/> | <input checked="" type="checkbox"/> | <input checked="" type="checkbox"/> | <input checked="" type="checkbox"/> | <input type="checkbox"/> | <input checked="" type="checkbox"/> | <input checked="" type="checkbox"/> | Lherzolite |
| TAL-057 | Tallante (Murcia, Spain) | <input type="checkbox"/> | <input type="checkbox"/> | <input type="checkbox"/> | <input type="checkbox"/> | <input type="checkbox"/> | <input type="checkbox"/> | <input type="checkbox"/> | |
| TAL-058 | Tallante (Murcia, Spain) | <input type="checkbox"/> | <input type="checkbox"/> | <input type="checkbox"/> | <input type="checkbox"/> | <input type="checkbox"/> | <input type="checkbox"/> | <input type="checkbox"/> | |
| TAL-059 | Tallante (Murcia, Spain) | <input type="checkbox"/> | <input type="checkbox"/> | <input type="checkbox"/> | <input type="checkbox"/> | <input type="checkbox"/> | <input type="checkbox"/> | <input type="checkbox"/> | |
| TAL-060 | Tallante (Murcia, Spain) | <input type="checkbox"/> | <input type="checkbox"/> | <input type="checkbox"/> | <input type="checkbox"/> | <input type="checkbox"/> | <input type="checkbox"/> | <input type="checkbox"/> | |
| TAL-061 | Tallante (Murcia, Spain) | <input type="checkbox"/> | <input type="checkbox"/> | <input type="checkbox"/> | <input type="checkbox"/> | <input type="checkbox"/> | <input type="checkbox"/> | <input type="checkbox"/> | |
| TAL-062 | Tallante (Murcia, Spain) | <input checked="" type="checkbox"/> | <input type="checkbox"/> | <input type="checkbox"/> | <input type="checkbox"/> | <input type="checkbox"/> | <input type="checkbox"/> | <input type="checkbox"/> | Peridotite |
| TAL-063 | Tallante (Murcia, Spain) | <input type="checkbox"/> | <input type="checkbox"/> | <input type="checkbox"/> | <input type="checkbox"/> | <input type="checkbox"/> | <input type="checkbox"/> | <input type="checkbox"/> | |
| TAL-064 | Tallante (Murcia, Spain) | <input type="checkbox"/> | <input type="checkbox"/> | <input type="checkbox"/> | <input type="checkbox"/> | <input type="checkbox"/> | <input type="checkbox"/> | <input type="checkbox"/> | |
| TAL-065 | Tallante (Murcia, Spain) | <input type="checkbox"/> | <input type="checkbox"/> | <input type="checkbox"/> | <input type="checkbox"/> | <input type="checkbox"/> | <input type="checkbox"/> | <input type="checkbox"/> | |
| TAL-066 | Tallante (Murcia, Spain) | <input type="checkbox"/> | <input type="checkbox"/> | <input type="checkbox"/> | <input type="checkbox"/> | <input type="checkbox"/> | <input type="checkbox"/> | <input type="checkbox"/> | |

| Sample code | Location | TS | EBSD | XRF | ICP-MS | EPMA | LA-ICP-MS | MC-ICP-MS & TIMS | Rock type |
|-------------|--------------------------|-------------------------------------|-------------------------------------|-------------------------------------|-------------------------------------|-------------------------------------|-------------------------------------|-------------------------------------|------------------------|
| TAL-067 | Tallante (Murcia, Spain) | <input type="checkbox"/> | <input type="checkbox"/> | <input type="checkbox"/> | <input type="checkbox"/> | <input type="checkbox"/> | <input type="checkbox"/> | <input type="checkbox"/> | |
| TAL-068 | Tallante (Murcia, Spain) | <input type="checkbox"/> | <input type="checkbox"/> | <input type="checkbox"/> | <input type="checkbox"/> | <input type="checkbox"/> | <input type="checkbox"/> | <input type="checkbox"/> | |
| TAL-069 | Tallante (Murcia, Spain) | <input type="checkbox"/> | <input type="checkbox"/> | <input type="checkbox"/> | <input type="checkbox"/> | <input type="checkbox"/> | <input type="checkbox"/> | <input type="checkbox"/> | |
| TAL-070 | Tallante (Murcia, Spain) | <input type="checkbox"/> | <input type="checkbox"/> | <input type="checkbox"/> | <input type="checkbox"/> | <input type="checkbox"/> | <input type="checkbox"/> | <input type="checkbox"/> | |
| TAL-071 | Tallante (Murcia, Spain) | <input type="checkbox"/> | <input type="checkbox"/> | <input type="checkbox"/> | <input type="checkbox"/> | <input type="checkbox"/> | <input type="checkbox"/> | <input type="checkbox"/> | |
| TAL-072 | Tallante (Murcia, Spain) | <input type="checkbox"/> | <input type="checkbox"/> | <input type="checkbox"/> | <input type="checkbox"/> | <input type="checkbox"/> | <input type="checkbox"/> | <input type="checkbox"/> | |
| TAL-073 | Tallante (Murcia, Spain) | <input type="checkbox"/> | <input type="checkbox"/> | <input type="checkbox"/> | <input type="checkbox"/> | <input type="checkbox"/> | <input type="checkbox"/> | <input type="checkbox"/> | |
| TAL-074 | Tallante (Murcia, Spain) | <input type="checkbox"/> | <input type="checkbox"/> | <input type="checkbox"/> | <input type="checkbox"/> | <input type="checkbox"/> | <input type="checkbox"/> | <input type="checkbox"/> | |
| TAL-075 | Tallante (Murcia, Spain) | <input type="checkbox"/> | <input type="checkbox"/> | <input type="checkbox"/> | <input type="checkbox"/> | <input type="checkbox"/> | <input type="checkbox"/> | <input type="checkbox"/> | |
| TAL-076 | Tallante (Murcia, Spain) | <input type="checkbox"/> | <input type="checkbox"/> | <input type="checkbox"/> | <input type="checkbox"/> | <input type="checkbox"/> | <input type="checkbox"/> | <input type="checkbox"/> | |
| TAL-077 | Tallante (Murcia, Spain) | <input checked="" type="checkbox"/> | <input type="checkbox"/> | <input checked="" type="checkbox"/> | <input checked="" type="checkbox"/> | <input type="checkbox"/> | <input type="checkbox"/> | <input type="checkbox"/> | Harzburgite |
| TAL-078 | Tallante (Murcia, Spain) | <input type="checkbox"/> | <input type="checkbox"/> | <input type="checkbox"/> | <input type="checkbox"/> | <input type="checkbox"/> | <input type="checkbox"/> | <input type="checkbox"/> | |
| TAL-079 | Tallante (Murcia, Spain) | <input type="checkbox"/> | <input type="checkbox"/> | <input type="checkbox"/> | <input type="checkbox"/> | <input type="checkbox"/> | <input type="checkbox"/> | <input type="checkbox"/> | |
| TAL-080 | Tallante (Murcia, Spain) | <input type="checkbox"/> | <input type="checkbox"/> | <input type="checkbox"/> | <input type="checkbox"/> | <input type="checkbox"/> | <input type="checkbox"/> | <input type="checkbox"/> | |
| TAL-081 | Tallante (Murcia, Spain) | <input type="checkbox"/> | <input type="checkbox"/> | <input type="checkbox"/> | <input type="checkbox"/> | <input type="checkbox"/> | <input type="checkbox"/> | <input type="checkbox"/> | |
| TAL-082 | Tallante (Murcia, Spain) | <input checked="" type="checkbox"/> | <input type="checkbox"/> | <input type="checkbox"/> | <input type="checkbox"/> | <input type="checkbox"/> | <input type="checkbox"/> | <input type="checkbox"/> | Peridotite |
| TAL-083 | Tallante (Murcia, Spain) | <input type="checkbox"/> | <input type="checkbox"/> | <input type="checkbox"/> | <input type="checkbox"/> | <input type="checkbox"/> | <input type="checkbox"/> | <input type="checkbox"/> | |
| TAL-084 | Tallante (Murcia, Spain) | <input checked="" type="checkbox"/> | <input checked="" type="checkbox"/> | <input checked="" type="checkbox"/> | <input checked="" type="checkbox"/> | <input checked="" type="checkbox"/> | <input checked="" type="checkbox"/> | <input checked="" type="checkbox"/> | Lherzolite-Harzburgite |
| TAL-085 | Tallante (Murcia, Spain) | <input type="checkbox"/> | <input type="checkbox"/> | <input type="checkbox"/> | <input type="checkbox"/> | <input type="checkbox"/> | <input type="checkbox"/> | <input type="checkbox"/> | |
| TAL-086 | Tallante (Murcia, Spain) | <input checked="" type="checkbox"/> | <input type="checkbox"/> | <input type="checkbox"/> | <input type="checkbox"/> | <input type="checkbox"/> | <input type="checkbox"/> | <input type="checkbox"/> | Peridotite |
| TAL-087 | Tallante (Murcia, Spain) | <input type="checkbox"/> | <input type="checkbox"/> | <input type="checkbox"/> | <input type="checkbox"/> | <input type="checkbox"/> | <input type="checkbox"/> | <input type="checkbox"/> | |
| TAL-088 | Tallante (Murcia, Spain) | <input type="checkbox"/> | <input type="checkbox"/> | <input type="checkbox"/> | <input type="checkbox"/> | <input type="checkbox"/> | <input type="checkbox"/> | <input type="checkbox"/> | |
| TAL-089 | Tallante (Murcia, Spain) | <input type="checkbox"/> | <input type="checkbox"/> | <input type="checkbox"/> | <input type="checkbox"/> | <input type="checkbox"/> | <input type="checkbox"/> | <input type="checkbox"/> | |
| TAL-090 | Tallante (Murcia, Spain) | <input checked="" type="checkbox"/> | <input type="checkbox"/> | <input type="checkbox"/> | <input type="checkbox"/> | <input type="checkbox"/> | <input type="checkbox"/> | <input type="checkbox"/> | Peridotite |
| TAL-091 | Tallante (Murcia, Spain) | <input type="checkbox"/> | <input type="checkbox"/> | <input type="checkbox"/> | <input type="checkbox"/> | <input type="checkbox"/> | <input type="checkbox"/> | <input type="checkbox"/> | |
| TAL-092 | Tallante (Murcia, Spain) | <input checked="" type="checkbox"/> | <input type="checkbox"/> | <input type="checkbox"/> | <input type="checkbox"/> | <input type="checkbox"/> | <input type="checkbox"/> | <input type="checkbox"/> | Peridotite |
| TAL-093 | Tallante (Murcia, Spain) | <input type="checkbox"/> | <input type="checkbox"/> | <input type="checkbox"/> | <input type="checkbox"/> | <input type="checkbox"/> | <input type="checkbox"/> | <input type="checkbox"/> | |
| TAL-094 | Tallante (Murcia, Spain) | <input checked="" type="checkbox"/> | <input checked="" type="checkbox"/> | <input checked="" type="checkbox"/> | <input checked="" type="checkbox"/> | <input checked="" type="checkbox"/> | <input type="checkbox"/> | <input checked="" type="checkbox"/> | Lherzolite-Harzburgite |
| TAL-095 | Tallante (Murcia, Spain) | <input type="checkbox"/> | <input type="checkbox"/> | <input type="checkbox"/> | <input type="checkbox"/> | <input type="checkbox"/> | <input type="checkbox"/> | <input type="checkbox"/> | |
| TAL-096 | Tallante (Murcia, Spain) | <input checked="" type="checkbox"/> | <input type="checkbox"/> | <input type="checkbox"/> | <input type="checkbox"/> | <input type="checkbox"/> | <input type="checkbox"/> | <input type="checkbox"/> | Peridotite |
| TAL-097 | Tallante (Murcia, Spain) | <input type="checkbox"/> | <input type="checkbox"/> | <input type="checkbox"/> | <input type="checkbox"/> | <input type="checkbox"/> | <input type="checkbox"/> | <input type="checkbox"/> | |
| TAL-098 | Tallante (Murcia, Spain) | <input type="checkbox"/> | <input type="checkbox"/> | <input type="checkbox"/> | <input type="checkbox"/> | <input type="checkbox"/> | <input type="checkbox"/> | <input type="checkbox"/> | |
| TAL-099 | Tallante (Murcia, Spain) | <input checked="" type="checkbox"/> | <input type="checkbox"/> | <input checked="" type="checkbox"/> | <input checked="" type="checkbox"/> | <input type="checkbox"/> | <input type="checkbox"/> | <input type="checkbox"/> | Lherzolite |
| TAL-100 | Tallante (Murcia, Spain) | <input checked="" type="checkbox"/> | <input type="checkbox"/> | <input type="checkbox"/> | <input type="checkbox"/> | <input type="checkbox"/> | <input type="checkbox"/> | <input type="checkbox"/> | Peridotite |
| TAL-101 | Tallante (Murcia, Spain) | <input checked="" type="checkbox"/> | <input type="checkbox"/> | <input type="checkbox"/> | <input type="checkbox"/> | <input type="checkbox"/> | <input type="checkbox"/> | <input type="checkbox"/> | Peridotite |
| TAL-102 | Tallante (Murcia, Spain) | <input checked="" type="checkbox"/> | <input type="checkbox"/> | <input checked="" type="checkbox"/> | <input checked="" type="checkbox"/> | <input type="checkbox"/> | <input checked="" type="checkbox"/> | <input type="checkbox"/> | Harzburgite |
| TAL-103 | Tallante (Murcia, Spain) | <input checked="" type="checkbox"/> | <input type="checkbox"/> | <input type="checkbox"/> | <input type="checkbox"/> | <input type="checkbox"/> | <input type="checkbox"/> | <input type="checkbox"/> | Peridotite |
| TAL-104 | Tallante (Murcia, Spain) | <input checked="" type="checkbox"/> | <input type="checkbox"/> | <input type="checkbox"/> | <input type="checkbox"/> | <input type="checkbox"/> | <input type="checkbox"/> | <input type="checkbox"/> | Peridotite |
| TAL-105 | Tallante (Murcia, Spain) | <input type="checkbox"/> | <input type="checkbox"/> | <input type="checkbox"/> | <input type="checkbox"/> | <input type="checkbox"/> | <input type="checkbox"/> | <input type="checkbox"/> | |
| TAL-106 | Tallante (Murcia, Spain) | <input checked="" type="checkbox"/> | <input checked="" type="checkbox"/> | <input checked="" type="checkbox"/> | <input checked="" type="checkbox"/> | <input type="checkbox"/> | <input type="checkbox"/> | <input checked="" type="checkbox"/> | Lherzolite |
| TAL-107 | Tallante (Murcia, Spain) | <input type="checkbox"/> | <input type="checkbox"/> | <input type="checkbox"/> | <input type="checkbox"/> | <input type="checkbox"/> | <input type="checkbox"/> | <input type="checkbox"/> | |
| TAL-108 | Tallante (Murcia, Spain) | <input checked="" type="checkbox"/> | <input type="checkbox"/> | <input type="checkbox"/> | <input type="checkbox"/> | <input type="checkbox"/> | <input type="checkbox"/> | <input type="checkbox"/> | Peridotite |
| TAL-109 | Tallante (Murcia, Spain) | <input type="checkbox"/> | <input type="checkbox"/> | <input type="checkbox"/> | <input type="checkbox"/> | <input type="checkbox"/> | <input type="checkbox"/> | <input type="checkbox"/> | |
| TAL-110 | Tallante (Murcia, Spain) | <input checked="" type="checkbox"/> | <input type="checkbox"/> | <input checked="" type="checkbox"/> | <input checked="" type="checkbox"/> | <input type="checkbox"/> | <input type="checkbox"/> | <input type="checkbox"/> | Lherzolite |
| TAL-111 | Tallante (Murcia, Spain) | <input type="checkbox"/> | <input type="checkbox"/> | <input type="checkbox"/> | <input type="checkbox"/> | <input type="checkbox"/> | <input type="checkbox"/> | <input type="checkbox"/> | |
| TAL-112 | Tallante (Murcia, Spain) | <input checked="" type="checkbox"/> | <input checked="" type="checkbox"/> | <input checked="" type="checkbox"/> | <input checked="" type="checkbox"/> | <input checked="" type="checkbox"/> | <input type="checkbox"/> | <input checked="" type="checkbox"/> | Lherzolite |
| TAL-113 | Tallante (Murcia, Spain) | <input type="checkbox"/> | <input type="checkbox"/> | <input type="checkbox"/> | <input type="checkbox"/> | <input type="checkbox"/> | <input type="checkbox"/> | <input type="checkbox"/> | |
| TAL-114 | Tallante (Murcia, Spain) | <input type="checkbox"/> | <input type="checkbox"/> | <input type="checkbox"/> | <input type="checkbox"/> | <input type="checkbox"/> | <input type="checkbox"/> | <input type="checkbox"/> | |
| TAL-115 | Tallante (Murcia, Spain) | <input checked="" type="checkbox"/> | <input type="checkbox"/> | <input type="checkbox"/> | <input type="checkbox"/> | <input type="checkbox"/> | <input type="checkbox"/> | <input type="checkbox"/> | Peridotite |
| TAL-116 | Tallante (Murcia, Spain) | <input type="checkbox"/> | <input type="checkbox"/> | <input type="checkbox"/> | <input type="checkbox"/> | <input type="checkbox"/> | <input type="checkbox"/> | <input type="checkbox"/> | |
| TAL-117 | Tallante (Murcia, Spain) | <input checked="" type="checkbox"/> | <input type="checkbox"/> | <input type="checkbox"/> | <input type="checkbox"/> | <input type="checkbox"/> | <input type="checkbox"/> | <input type="checkbox"/> | Peridotite |

| Sample code | Location | TS | EBSD | XRF | ICP-MS | EPMA | LA-ICP-MS | MC-ICP-MS & TIMS | Rock type |
|-------------|--------------------------|-------------------------------------|-------------------------------------|-------------------------------------|-------------------------------------|-------------------------------------|-------------------------------------|-------------------------------------|-------------|
| TAL-118 | Tallante (Murcia, Spain) | <input type="checkbox"/> | <input type="checkbox"/> | <input type="checkbox"/> | <input type="checkbox"/> | <input type="checkbox"/> | <input type="checkbox"/> | <input type="checkbox"/> | |
| TAL-119 | Tallante (Murcia, Spain) | <input type="checkbox"/> | <input type="checkbox"/> | <input type="checkbox"/> | <input type="checkbox"/> | <input type="checkbox"/> | <input type="checkbox"/> | <input type="checkbox"/> | |
| TAL-120 | Tallante (Murcia, Spain) | <input type="checkbox"/> | <input type="checkbox"/> | <input type="checkbox"/> | <input type="checkbox"/> | <input type="checkbox"/> | <input type="checkbox"/> | <input type="checkbox"/> | |
| TAL-121 | Tallante (Murcia, Spain) | <input type="checkbox"/> | <input type="checkbox"/> | <input type="checkbox"/> | <input type="checkbox"/> | <input type="checkbox"/> | <input type="checkbox"/> | <input type="checkbox"/> | |
| TAL-122 | Tallante (Murcia, Spain) | <input checked="" type="checkbox"/> | <input type="checkbox"/> | <input type="checkbox"/> | <input type="checkbox"/> | <input type="checkbox"/> | <input type="checkbox"/> | <input type="checkbox"/> | Peridotite |
| TAL-123 | Tallante (Murcia, Spain) | <input type="checkbox"/> | <input type="checkbox"/> | <input type="checkbox"/> | <input type="checkbox"/> | <input type="checkbox"/> | <input type="checkbox"/> | <input type="checkbox"/> | |
| TAL-124 | Tallante (Murcia, Spain) | <input checked="" type="checkbox"/> | <input checked="" type="checkbox"/> | <input type="checkbox"/> | <input type="checkbox"/> | <input type="checkbox"/> | <input type="checkbox"/> | <input type="checkbox"/> | Harzburgite |
| TAL-125 | Tallante (Murcia, Spain) | <input checked="" type="checkbox"/> | <input type="checkbox"/> | <input checked="" type="checkbox"/> | <input checked="" type="checkbox"/> | <input type="checkbox"/> | <input type="checkbox"/> | <input type="checkbox"/> | Lherzolite |
| TAL-126 | Tallante (Murcia, Spain) | <input checked="" type="checkbox"/> | <input type="checkbox"/> | <input type="checkbox"/> | <input type="checkbox"/> | <input type="checkbox"/> | <input type="checkbox"/> | <input type="checkbox"/> | Peridotite |
| TAL-127 | Tallante (Murcia, Spain) | <input checked="" type="checkbox"/> | <input checked="" type="checkbox"/> | <input checked="" type="checkbox"/> | <input checked="" type="checkbox"/> | <input checked="" type="checkbox"/> | <input checked="" type="checkbox"/> | <input checked="" type="checkbox"/> | Lherzolite |
| TAL-128 | Tallante (Murcia, Spain) | <input checked="" type="checkbox"/> | <input type="checkbox"/> | <input type="checkbox"/> | <input type="checkbox"/> | <input type="checkbox"/> | <input type="checkbox"/> | <input type="checkbox"/> | Peridotite |
| TAL-129 | Tallante (Murcia, Spain) | <input checked="" type="checkbox"/> | <input type="checkbox"/> | <input type="checkbox"/> | <input type="checkbox"/> | <input type="checkbox"/> | <input type="checkbox"/> | <input type="checkbox"/> | Peridotite |
| TAL-130 | Tallante (Murcia, Spain) | <input checked="" type="checkbox"/> | <input type="checkbox"/> | <input type="checkbox"/> | <input type="checkbox"/> | <input type="checkbox"/> | <input type="checkbox"/> | <input type="checkbox"/> | Peridotite |
| TAL-131 | Tallante (Murcia, Spain) | <input checked="" type="checkbox"/> | <input type="checkbox"/> | <input checked="" type="checkbox"/> | <input checked="" type="checkbox"/> | <input type="checkbox"/> | <input type="checkbox"/> | <input type="checkbox"/> | Lherzolite |
| TAL-132 | Tallante (Murcia, Spain) | <input checked="" type="checkbox"/> | <input type="checkbox"/> | <input type="checkbox"/> | <input type="checkbox"/> | <input type="checkbox"/> | <input type="checkbox"/> | <input type="checkbox"/> | Peridotite |
| TAL-133 | Tallante (Murcia, Spain) | <input type="checkbox"/> | <input type="checkbox"/> | <input type="checkbox"/> | <input type="checkbox"/> | <input type="checkbox"/> | <input type="checkbox"/> | <input type="checkbox"/> | |
| TAL-134 | Tallante (Murcia, Spain) | <input checked="" type="checkbox"/> | <input checked="" type="checkbox"/> | <input checked="" type="checkbox"/> | <input checked="" type="checkbox"/> | <input checked="" type="checkbox"/> | <input checked="" type="checkbox"/> | <input checked="" type="checkbox"/> | Lherzolite |
| TAL-135 | Tallante (Murcia, Spain) | <input type="checkbox"/> | <input type="checkbox"/> | <input type="checkbox"/> | <input type="checkbox"/> | <input type="checkbox"/> | <input type="checkbox"/> | <input type="checkbox"/> | |
| TAL-136 | Tallante (Murcia, Spain) | <input type="checkbox"/> | <input type="checkbox"/> | <input type="checkbox"/> | <input type="checkbox"/> | <input type="checkbox"/> | <input type="checkbox"/> | <input type="checkbox"/> | |
| TAL-137 | Tallante (Murcia, Spain) | <input type="checkbox"/> | <input type="checkbox"/> | <input type="checkbox"/> | <input type="checkbox"/> | <input type="checkbox"/> | <input type="checkbox"/> | <input type="checkbox"/> | |
| TAL-138 | Tallante (Murcia, Spain) | <input type="checkbox"/> | <input type="checkbox"/> | <input type="checkbox"/> | <input type="checkbox"/> | <input type="checkbox"/> | <input type="checkbox"/> | <input type="checkbox"/> | |
| TAL-139 | Tallante (Murcia, Spain) | <input type="checkbox"/> | <input type="checkbox"/> | <input type="checkbox"/> | <input type="checkbox"/> | <input type="checkbox"/> | <input type="checkbox"/> | <input type="checkbox"/> | |
| TAL-140 | Tallante (Murcia, Spain) | <input type="checkbox"/> | <input type="checkbox"/> | <input type="checkbox"/> | <input type="checkbox"/> | <input type="checkbox"/> | <input type="checkbox"/> | <input type="checkbox"/> | |
| TAL-141 | Tallante (Murcia, Spain) | <input type="checkbox"/> | <input type="checkbox"/> | <input type="checkbox"/> | <input type="checkbox"/> | <input type="checkbox"/> | <input type="checkbox"/> | <input type="checkbox"/> | |
| TAL-142 | Tallante (Murcia, Spain) | <input type="checkbox"/> | <input type="checkbox"/> | <input type="checkbox"/> | <input type="checkbox"/> | <input type="checkbox"/> | <input type="checkbox"/> | <input type="checkbox"/> | |
| TAL-143 | Tallante (Murcia, Spain) | <input checked="" type="checkbox"/> | <input type="checkbox"/> | <input checked="" type="checkbox"/> | <input checked="" type="checkbox"/> | <input type="checkbox"/> | <input type="checkbox"/> | <input checked="" type="checkbox"/> | Lherzolite |
| TAL-144 | Tallante (Murcia, Spain) | <input checked="" type="checkbox"/> | <input type="checkbox"/> | <input type="checkbox"/> | <input type="checkbox"/> | <input type="checkbox"/> | <input type="checkbox"/> | <input type="checkbox"/> | Peridotite |
| TAL-145 | Tallante (Murcia, Spain) | <input type="checkbox"/> | <input type="checkbox"/> | <input type="checkbox"/> | <input type="checkbox"/> | <input type="checkbox"/> | <input type="checkbox"/> | <input type="checkbox"/> | |
| TAL-146 | Tallante (Murcia, Spain) | <input checked="" type="checkbox"/> | <input type="checkbox"/> | <input type="checkbox"/> | <input type="checkbox"/> | <input type="checkbox"/> | <input type="checkbox"/> | <input type="checkbox"/> | Peridotite |
| TAL-147 | Tallante (Murcia, Spain) | <input type="checkbox"/> | <input type="checkbox"/> | <input type="checkbox"/> | <input type="checkbox"/> | <input type="checkbox"/> | <input type="checkbox"/> | <input type="checkbox"/> | |
| TAL-148 | Tallante (Murcia, Spain) | <input checked="" type="checkbox"/> | <input checked="" type="checkbox"/> | <input type="checkbox"/> | <input type="checkbox"/> | <input type="checkbox"/> | <input type="checkbox"/> | <input type="checkbox"/> | Lherzolite |
| TAL-149 | Tallante (Murcia, Spain) | <input checked="" type="checkbox"/> | <input type="checkbox"/> | <input checked="" type="checkbox"/> | <input checked="" type="checkbox"/> | <input type="checkbox"/> | <input type="checkbox"/> | <input type="checkbox"/> | Lherzolite |
| 3H-2 | Sangilen (Tuva, Russia) | <input checked="" type="checkbox"/> | <input type="checkbox"/> | <input type="checkbox"/> | <input type="checkbox"/> | <input checked="" type="checkbox"/> | <input checked="" type="checkbox"/> | <input type="checkbox"/> | Lherzolite |
| 3H-4 | Sangilen (Tuva, Russia) | <input checked="" type="checkbox"/> | <input type="checkbox"/> | <input type="checkbox"/> | <input type="checkbox"/> | <input checked="" type="checkbox"/> | <input checked="" type="checkbox"/> | <input type="checkbox"/> | Lherzolite |
| 3H-8 | Sangilen (Tuva, Russia) | <input checked="" type="checkbox"/> | <input type="checkbox"/> | <input type="checkbox"/> | <input type="checkbox"/> | <input checked="" type="checkbox"/> | <input checked="" type="checkbox"/> | <input type="checkbox"/> | Lherzolite |
| 5H-2 | Sangilen (Tuva, Russia) | <input checked="" type="checkbox"/> | <input type="checkbox"/> | <input type="checkbox"/> | <input type="checkbox"/> | <input checked="" type="checkbox"/> | <input checked="" type="checkbox"/> | <input type="checkbox"/> | Lherzolite |
| 5H-3 | Sangilen (Tuva, Russia) | <input checked="" type="checkbox"/> | <input type="checkbox"/> | <input type="checkbox"/> | <input type="checkbox"/> | <input checked="" type="checkbox"/> | <input checked="" type="checkbox"/> | <input type="checkbox"/> | Lherzolite |
| 5H-7 | Sangilen (Tuva, Russia) | <input checked="" type="checkbox"/> | <input type="checkbox"/> | <input type="checkbox"/> | <input type="checkbox"/> | <input checked="" type="checkbox"/> | <input checked="" type="checkbox"/> | <input type="checkbox"/> | Lherzolite |
| 5H-9 | Sangilen (Tuva, Russia) | <input checked="" type="checkbox"/> | <input type="checkbox"/> | <input type="checkbox"/> | <input type="checkbox"/> | <input checked="" type="checkbox"/> | <input checked="" type="checkbox"/> | <input type="checkbox"/> | Lherzolite |
| 5H-10 | Sangilen (Tuva, Russia) | <input checked="" type="checkbox"/> | <input type="checkbox"/> | <input type="checkbox"/> | <input type="checkbox"/> | <input checked="" type="checkbox"/> | <input checked="" type="checkbox"/> | <input type="checkbox"/> | Lherzolite |
| 5H-13 | Sangilen (Tuva, Russia) | <input checked="" type="checkbox"/> | <input type="checkbox"/> | <input type="checkbox"/> | <input type="checkbox"/> | <input checked="" type="checkbox"/> | <input checked="" type="checkbox"/> | <input type="checkbox"/> | Lherzolite |

Whole Rock Major Elements

| Sample | SiO ₂ | Al ₂ O ₃ | FeO ^t | MnO | MgO | CaO | TiO ₂ | P ₂ O ₅ | Mg# | V (ppm) | Cr (ppm) | Co (ppm) | Ni (ppm) | Zn (ppm) |
|----------|------------------|--------------------------------|------------------|------|------|------|------------------|-------------------------------|------|---------|----------|----------|----------|----------|
| LP08-02 | 46.3 | 4.60 | 8.08 | 0.14 | 36.4 | 3.41 | 0.51 | 0.10 | 0.89 | 97.5 | 2013.8 | 122.5 | 1729.5 | 54.0 |
| LP08-03 | 45.3 | 2.53 | 8.07 | 0.14 | 41.3 | 2.49 | 0.20 | 0.01 | 0.90 | 64.7 | 2399.1 | 134.8 | 2030.5 | 49.9 |
| LP08-12* | 41.9 | 0.98 | 11.0 | 0.19 | 40.4 | 3.87 | 0.13 | - | 0.87 | - | - | - | - | - |
| LP08-14 | 45.8 | 3.14 | 8.22 | 0.15 | 39.8 | 2.56 | 0.19 | 0.04 | 0.90 | 79.3 | 2161.1 | 135.2 | 1909.2 | 50.1 |
| LPE-028 | 42.6 | 1.15 | 10.7 | 0.20 | 41.6 | 3.46 | 0.19 | 0.02 | 0.87 | 58.0 | 2488.3 | 113.7 | 2084.8 | 81.1 |
| LPE-029 | 45.0 | 2.74 | 8.80 | 0.14 | 40.9 | 2.27 | 0.18 | 0.02 | 0.89 | 54.7 | 2383.1 | 131.9 | 2005.1 | 58.4 |
| LPE-042 | 45.4 | 3.09 | 8.04 | 0.14 | 40.4 | 2.72 | 0.22 | 0.01 | 0.90 | 71.7 | 2462.4 | 143.4 | 2023.3 | 53.6 |
| LPE-046 | 45.3 | 2.79 | 8.17 | 0.15 | 40.8 | 2.54 | 0.19 | 0.02 | 0.90 | 64.4 | 2261.6 | 142.8 | 2007.8 | 51.6 |
| LPE-048 | 44.6 | 2.53 | 8.46 | 0.14 | 41.6 | 2.55 | 0.13 | 0.02 | 0.90 | 62.1 | 2506.1 | 133.5 | 2084.1 | 57.0 |
| LPE-061 | 45.0 | 3.20 | 8.52 | 0.14 | 40.3 | 2.60 | 0.19 | 0.02 | 0.89 | 67.4 | 2436.6 | 124.8 | 1993.5 | 55.1 |
| LPE-062 | 45.4 | 3.66 | 10.0 | 0.18 | 37.1 | 3.30 | 0.28 | 0.02 | 0.87 | 84.1 | 2273.6 | 119.6 | 1826.7 | 71.1 |
| TAL-001 | 45.0 | 2.82 | 8.00 | 0.15 | 41.5 | 2.40 | 0.09 | 0.02 | 0.90 | 67.4 | 2519.9 | 131.8 | 2045.0 | 52.8 |
| TAL-014 | 46.6 | 2.75 | 7.56 | 0.13 | 40.8 | 1.92 | 0.21 | 0.02 | 0.91 | 61.6 | 2326.2 | 132.1 | 1971.1 | 49.1 |
| TAL-047 | 44.8 | 1.67 | 7.66 | 0.13 | 44.1 | 1.39 | 0.16 | 0.01 | 0.91 | 46.9 | 3093.0 | 134.6 | 2235.9 | 53.0 |
| TAL-052 | 44.9 | 2.02 | 8.08 | 0.14 | 43.2 | 1.56 | 0.11 | 0.02 | 0.90 | 52.1 | 2512.5 | 133.4 | 2098.1 | 50.1 |
| TAL-056 | 44.3 | 2.29 | 8.01 | 0.14 | 43.3 | 1.76 | 0.11 | 0.01 | 0.91 | 46.9 | 2668.2 | 136.7 | 2202.5 | 53.6 |
| TAL-077 | 44.8 | 1.35 | 7.49 | 0.13 | 45.0 | 1.02 | 0.18 | 0.01 | 0.91 | 28.6 | 2668.0 | 143.0 | 2224.2 | 47.5 |
| TAL-084 | 44.4 | 1.83 | 7.72 | 0.13 | 44.5 | 1.34 | 0.10 | 0.01 | 0.91 | 37.9 | 2587.1 | 142.9 | 2232.8 | 49.1 |
| TAL-094 | 44.3 | 1.72 | 7.87 | 0.13 | 44.5 | 1.32 | 0.16 | 0.01 | 0.91 | 38.3 | 2299.1 | 137.9 | 2251.4 | 51.9 |
| TAL-099 | 44.6 | 2.09 | 7.76 | 0.14 | 43.4 | 1.85 | 0.13 | 0.02 | 0.91 | 53.5 | 2751.8 | 134.8 | 2179.3 | 50.5 |
| TAL-102 | 45.6 | 1.37 | 7.45 | 0.13 | 44.3 | 0.99 | 0.16 | 0.01 | 0.91 | 36.1 | 2554.7 | 136.8 | 2194.3 | 49.5 |
| TAL-106 | 44.8 | 2.23 | 7.85 | 0.14 | 42.6 | 2.21 | 0.14 | 0.01 | 0.91 | 57.9 | 2595.1 | 142.0 | 2155.7 | 51.1 |
| TAL-110 | 44.5 | 1.53 | 7.58 | 0.13 | 44.6 | 1.51 | 0.11 | 0.01 | 0.91 | 38.2 | 2548.0 | 151.4 | 2245.2 | 47.3 |
| TAL-112 | 45.0 | 2.85 | 8.06 | 0.14 | 41.4 | 2.44 | 0.16 | 0.01 | 0.90 | 61.6 | 2385.6 | 136.5 | 2025.6 | 53.4 |
| TAL-125 | 44.2 | 2.19 | 8.18 | 0.14 | 43.5 | 1.60 | 0.17 | 0.02 | 0.90 | 53.5 | 2330.3 | 140.3 | 2149.4 | 50.9 |
| TAL-127 | 44.7 | 2.45 | 7.81 | 0.14 | 42.2 | 2.46 | 0.19 | 0.01 | 0.91 | 61.4 | 2644.4 | 130.6 | 2164.9 | 51.8 |
| TAL-131 | 44.3 | 2.29 | 8.35 | 0.14 | 43.0 | 1.76 | 0.07 | 0.01 | 0.90 | 46.4 | 2548.4 | 138.4 | 2177.5 | 55.8 |
| TAL-134 | 45.1 | 2.42 | 8.22 | 0.14 | 41.7 | 2.28 | 0.09 | 0.01 | 0.90 | 56.9 | 2029.3 | 131.7 | 2046.1 | 48.0 |
| TAL-143 | 44.1 | 1.43 | 7.63 | 0.13 | 45.3 | 1.39 | 0.06 | 0.01 | 0.91 | 35.5 | 3059.1 | 150.3 | 2267.5 | 48.8 |
| TAL-149 | 44.9 | 1.70 | 7.33 | 0.13 | 44.2 | 1.55 | 0.20 | 0.02 | 0.91 | 43.0 | 2647.2 | 143.9 | 2238.8 | 48.6 |

* Whole rock composition by mass balance compilation

Mineral Major Elements

| Sample code | LP08-02 | | | | LPE-029 | | | | LPE-048 | | | | LPE-061 | | | |
|--------------------------------|---------|-------|-------|-------|---------|-------|-------|-------|---------|-------|-------|-------|---------|-------|-------|-------|
| | OI | Opx | Cpx | Spl | OI | Opx | Cpx | Spl | OI | Opx | Cpx | Spl | OI | Opx | Cpx | Spl |
| SiO ₂ | 41.1 | 55.8 | 51.3 | 0.01 | 41.1 | 56.1 | 52.0 | 0.01 | 40.8 | 55.3 | 51.3 | 0.08 | 41.0 | 55.4 | 51.8 | 0.08 |
| Al ₂ O ₃ | 0.01 | 3.76 | 5.98 | 51.2 | - | 3.64 | 5.49 | 56.3 | - | 3.70 | 5.06 | 48.7 | - | 4.53 | 4.81 | 47.7 |
| Cr ₂ O ₃ | - | 0.53 | 1.00 | 17.5 | - | 0.34 | 0.79 | 12.1 | - | 0.48 | 0.96 | 17.8 | - | 0.70 | 1.02 | 22.18 |
| TiO ₂ | - | 0.15 | 0.71 | 0.08 | - | 0.12 | 0.52 | 0.08 | - | 0.16 | 0.63 | 0.14 | - | - | 0.80 | 0.06 |
| Na ₂ O | - | - | 0.73 | - | - | - | 0.53 | - | - | 0.06 | 0.74 | - | - | - | 0.61 | - |
| MgO | 49.0 | 33.1 | 15.4 | 19.1 | 48.1 | 32.8 | 16.2 | 19.8 | 48.0 | 32.1 | 16.0 | 18.9 | 47.6 | 32.26 | 15.7 | 17.5 |
| MnO | 0.16 | 0.15 | 0.09 | 0.17 | 0.14 | 0.15 | 0.08 | 0.12 | 0.13 | 0.14 | 0.09 | 0.17 | 0.15 | 0.14 | 0.09 | 0.16 |
| FeO ^t | 10.0 | 6.44 | 2.26 | 11.0 | 11.0 | 6.95 | 2.63 | 10.7 | 9.54 | 6.09 | 2.71 | 12.2 | 10.4 | 6.29 | 2.34 | 12.0 |
| K ₂ O | - | - | - | - | - | - | - | - | - | - | - | - | - | - | - | - |
| CaO | 0.05 | 0.60 | 22.45 | - | - | 0.60 | 21.8 | - | 0.06 | 0.96 | 21.1 | - | - | 1.30 | 22.7 | - |
| NiO | 0.38 | 0.09 | - | 0.29 | 0.38 | 0.09 | 0.06 | 0.36 | 0.38 | 0.10 | 0.07 | 0.32 | 0.36 | 0.07 | 0.05 | 0.25 |
| Σ | 100.8 | 100.6 | 100.0 | 99.4 | 100.7 | 100.8 | 100.1 | 99.4 | 99.0 | 99.1 | 98.6 | 98.2 | 99.6 | 100.7 | 99.9 | 99.9 |
| mg# | 0.897 | 0.902 | 0.924 | 0.756 | 0.886 | 0.894 | 0.917 | 0.768 | 0.900 | 0.904 | 0.913 | 0.735 | 0.891 | 0.901 | 0.923 | 0.723 |
| cr# | 0.186 | 0.186 | 0.186 | 0.126 | 0.126 | 0.126 | 0.126 | 0.126 | 0.197 | 0.197 | 0.197 | 0.197 | 0.238 | 0.238 | 0.238 | 0.238 |

| Sample code | TAL-001 | | | | TAL-014 | | | | TAL-084 | | | | TAL-094 | | | |
|--------------------------------|---------|-------|-------|-------|---------|-------|-------|-------|---------|-------|-------|-------|---------|-------|-------|-------|
| | OI | Opx | Cpx | Spl | OI | Opx | Cpx | Spl | OI | Opx | Cpx | Spl | OI | Opx | Cpx | Spl |
| SiO ₂ | 40.8 | 55.4 | 51.2 | 0.10 | 41.3 | 55.4 | 51.8 | 0.01 | 41.1 | 55.8 | 52.4 | 0.09 | 41.2 | 55.4 | 51.8 | 0.01 |
| Al ₂ O ₃ | - | 3.36 | 5.14 | 51.0 | - | 4.35 | 5.22 | 49.3 | - | 3.70 | 4.81 | 48.8 | - | 4.34 | 5.70 | 50.1 |
| Cr ₂ O ₃ | - | 0.43 | 1.04 | 17.2 | - | 0.70 | 1.20 | 19.2 | - | 0.59 | 1.17 | 21.7 | - | 0.67 | 1.20 | 18.1 |
| TiO ₂ | - | 0.14 | 0.65 | 0.05 | - | 0.21 | 0.81 | 0.11 | - | 0.07 | 0.26 | 0.07 | - | 0.09 | 0.39 | - |
| Na ₂ O | - | - | 0.74 | - | - | 0.08 | 0.83 | - | - | - | 0.82 | - | - | - | 0.93 | - |
| MgO | 48.0 | 32.6 | 15.5 | 18.9 | 49.1 | 32.3 | 15.7 | 19.2 | 48.4 | 32.7 | 15.7 | 19.7 | 49.4 | 33.1 | 15.7 | 19.5 |
| MnO | 0.13 | 0.15 | 0.09 | 0.16 | 0.14 | 0.15 | 0.07 | 0.17 | 0.13 | 0.13 | 0.09 | 0.15 | 0.14 | 0.14 | 0.09 | 0.16 |
| FeO ^t | 9.92 | 6.22 | 2.39 | 10.0 | 9.95 | 6.30 | 2.36 | 11.3 | 9.07 | 5.77 | 2.19 | 8.32 | 9.46 | 6.14 | 2.44 | 11.5 |
| K ₂ O | - | - | - | - | - | - | - | - | - | - | - | - | - | - | - | - |
| CaO | 0.05 | 0.73 | 21.95 | - | 0.05 | 1.55 | 22.11 | - | 0.05 | 0.66 | 22.1 | - | 0.05 | 0.71 | 21.9 | - |
| NiO | 0.37 | 0.08 | - | 0.34 | 0.41 | 0.08 | - | 0.33 | 0.38 | 0.07 | 0.05 | 0.26 | 0.40 | 0.07 | - | 0.33 |
| Σ | 99.3 | 99.1 | 98.8 | 97.7 | 100.9 | 101.1 | 100.1 | 99.7 | 99.2 | 99.5 | 99.5 | 99.2 | 100.7 | 100.7 | 100.2 | 99.7 |
| mg# | 0.896 | 0.903 | 0.920 | 0.771 | 0.898 | 0.901 | 0.922 | 0.753 | 0.905 | 0.910 | 0.927 | 0.809 | 0.903 | 0.906 | 0.920 | 0.752 |
| cr# | 0.184 | 0.184 | 0.184 | 0.184 | 0.207 | 0.207 | 0.207 | 0.207 | 0.230 | 0.230 | 0.230 | 0.230 | 0.195 | 0.195 | 0.195 | 0.195 |

| Sample code | TAL-112 | | | | TAL-127 | | | | TAL-134 | | | | 3H-2 | | | |
|--------------------------------|---------|-------|-------|-------|---------|-------|-------|-------|---------|-------|-------|-------|-------|------|------|------|
| | OI | Opx | Cpx | Spl | OI | Opx | Cpx | Spl | OI | Opx | Cpx | Spl | OI | Opx | Cpx | Spl |
| SiO ₂ | 41.3 | 55.9 | 52.1 | 0.02 | 41.2 | 55.4 | 51.77 | 0.09 | 40.7 | 55.9 | 51.2 | 0.08 | 40.9 | 55.8 | 53.1 | 0.07 |
| Al ₂ O ₃ | - | 4.01 | 5.72 | 57.3 | - | 4.21 | 5.22 | 55.4 | - | 4.03 | 5.89 | 56.0 | - | 2.79 | 3.49 | 29.4 |
| Cr ₂ O ₃ | - | 0.39 | 0.78 | 11.6 | - | 0.49 | 1.20 | 14.4 | - | 0.38 | 0.81 | 11.7 | - | 0.70 | 1.27 | 36.8 |
| TiO ₂ | - | 0.11 | 0.57 | 0.06 | - | 0.11 | 0.80 | - | - | 0.12 | 0.54 | 0.06 | - | 0.05 | 0.13 | 0.22 |
| Na ₂ O | - | - | 0.78 | - | - | - | 0.53 | - | - | - | 0.82 | - | - | 0.08 | 0.87 | - |
| MgO | 48.8 | 32.9 | 15.7 | 20.4 | 48.0 | 32.3 | 15.68 | 19.6 | 48.3 | 32.9 | 15.4 | 20.2 | 48.8 | 32.5 | 16.9 | 16.0 |
| MnO | 0.13 | 0.14 | 0.08 | 0.13 | 0.15 | 0.14 | 0.07 | 0.13 | 0.14 | 0.15 | 0.08 | 0.14 | 0.13 | 0.12 | 0.09 | 0.12 |
| FeO ^t | 10.1 | 6.43 | 2.37 | 9.80 | 9.81 | 6.24 | 2.355 | 10.2 | 9.98 | 6.43 | 2.38 | 9.55 | 9.86 | 6.21 | 3.06 | 16.1 |
| K ₂ O | - | - | - | - | - | - | - | - | - | - | - | - | - | - | - | - |
| CaO | 0.05 | 0.67 | 22.27 | - | 0.05 | 0.65 | 22.11 | - | 0.05 | 0.67 | 21.81 | - | 0.09 | 1.08 | 19.6 | - |
| NiO | 0.38 | 0.10 | 0.05 | 0.34 | 0.38 | 0.09 | - | 0.31 | 0.36 | 0.09 | 0.08 | 0.33 | 0.32 | 0.09 | - | 0.19 |
| Σ | 100.7 | 100.8 | 100.4 | 99.6 | 99.7 | 99.7 | 99.7 | 100.3 | 99.5 | 100.8 | 99.1 | 98.0 | 100.2 | 99.4 | 98.5 | 99.0 |
| mg# | 0.895 | 0.901 | 0.922 | 0.788 | 0.897 | 0.902 | 0.922 | 0.775 | 0.896 | 0.901 | 0.920 | 0.790 | 89.8 | 90.3 | 90.7 | 63.9 |
| cr# | 0.120 | 0.120 | 0.120 | 0.149 | 0.149 | 0.149 | 0.149 | 0.149 | 0.123 | 0.123 | 0.123 | 0.123 | 45.7 | 45.7 | 45.7 | 45.7 |

| Sample code | 3H-4 | | | | 5H-2 | | | | 5H-3 | | | | | | | |
|--------------------------------|------|------|------|------|-------|-------|------|------|-------|-------|------|-------|------|------|------|-------|
| | OI | Opx | Cpx | Spl | OI | Opx | Cpx | Spl | OI | Opx | Cpx | Spl | | | | |
| SiO ₂ | 40.7 | 54.2 | 51.5 | 0.15 | 40.5 | 53.7 | 51.0 | 0.06 | 40.0 | 54.1 | 51.3 | 0.06 | 40.5 | 53.8 | 51.8 | 0.06 |
| Al ₂ O ₃ | - | 5.70 | 7.64 | 57.8 | - | 5.20 | 7.03 | 55.6 | - | 5.04 | 7.20 | 57.2 | - | 4.64 | 5.52 | 50.2 |
| Cr ₂ O ₃ | - | 0.42 | 0.73 | 9.07 | - | 0.40 | 0.78 | 9.99 | - | 0.39 | 0.84 | 10.3 | - | 0.55 | 0.92 | 16.17 |
| TiO ₂ | - | 0.14 | 0.55 | 0.18 | - | 0.18 | 0.59 | 0.19 | - | 0.14 | 0.53 | 0.14 | - | 0.04 | 0.11 | 0.06 |
| Na ₂ O | - | 0.15 | 1.67 | - | - | 0.15 | 1.69 | - | - | 0.14 | 1.75 | - | - | 0.10 | 0.92 | - |
| MgO | 47.2 | 31.1 | 15.0 | 20.2 | 48.2 | 31.4 | 15.0 | 20.2 | 48.8 | 32.6 | 15.8 | 20.7 | 48.8 | 31.5 | 16.4 | 19.5 |
| MnO | 0.15 | 0.13 | 0.10 | 0.11 | 0.13 | 0.15 | 0.09 | 0.10 | 0.18 | 0.18 | 0.13 | 0.22 | 0.13 | 0.14 | 0.09 | 0.08 |
| FeO ^t | 10.2 | 6.48 | 3.43 | 10.9 | 10.8 | 6.92 | 3.57 | 11.9 | 10.27 | 6.58 | 3.33 | 11.1 | 9.9 | 6.17 | 3.15 | 11.7 |
| K ₂ O | - | - | - | - | - | - | - | - | - | - | - | - | - | - | - | - |
| CaO | 0.11 | 1.01 | 19.2 | - | 0.09 | 0.962 | 18.9 | - | 0.08 | 0.85 | 18.6 | - | 0.10 | 1.09 | 20.0 | - |
| NiO | 0.34 | 0.11 | - | 0.36 | 0.33 | 0.12 | - | 0.33 | 0.39 | 0.11 | - | 0.39 | 0.32 | 0.09 | - | 0.28 |
| Σ | 98.8 | 99.4 | 99.9 | 98.7 | 100.1 | 99.2 | 98.7 | 98.3 | 99.8 | 100.1 | 99.6 | 100.1 | 99.7 | 98.1 | 98.9 | 98.1 |
| mg# | 89.2 | 89.5 | 89.9 | 78.2 | 88.9 | 89.0 | 88.3 | 74.6 | 89.4 | 89.9 | 89.5 | 77.0 | 89.8 | 90.1 | 90.3 | 74.9 |
| cr# | 9.52 | 9.52 | 9.52 | 10.7 | 10.7 | 10.7 | 10.7 | 10.7 | 10.8 | 10.8 | 10.8 | 10.8 | 17.8 | 17.8 | 17.8 | 17.8 |

| Sample code | 5H-7 | | | | 5H-9 | | | | 5H-10 | | | | 5H-13 | | | |
|--------------------------------|-------|-------|-------|-------|-------|-------|------|------|-------|------|------|-------|-------|-------|-------|-------|
| | OI | Opx | Cpx | Spl | OI | Opx | Cpx | Spl | OI | Opx | Cpx | Spl | OI | Opx | Cpx | Spl |
| SiO ₂ | 40.7 | 55.0 | 52.7 | 0.05 | 40.3 | 54.6 | 51.7 | 0.05 | 41.1 | 54.9 | 52.0 | 0.12 | 40.9 | 56.2 | 53.2 | 0.06 |
| Al ₂ O ₃ | - | 4.80 | 6.53 | 54.0 | - | 4.68 | 6.03 | 48.7 | - | 4.18 | 5.95 | 44.7 | - | 2.88 | 3.95 | 31.1 |
| Cr ₂ O ₃ | - | 0.53 | 1.03 | 14.43 | - | 0.61 | 1.06 | 17.4 | - | 0.63 | 1.38 | 22.82 | - | 0.77 | 1.64 | 37.02 |
| TiO ₂ | - | 0.07 | 0.23 | 0.08 | - | 0.16 | 0.48 | 0.28 | - | 0.11 | 0.31 | 0.21 | - | 0.08 | 0.19 | 0.24 |
| Na ₂ O | - | 0.13 | 1.59 | - | - | 0.09 | 1.19 | - | - | 0.15 | 1.61 | - | - | 0.08 | 1.14 | - |
| MgO | 48.9 | 32.8 | 16.0 | 20.1 | 47.6 | 31.9 | 16.4 | 18.5 | 48.2 | 32.0 | 15.4 | 18.2 | 49.6 | 33.7 | 17.2 | 16.5 |
| MnO | 0.16 | 0.17 | 0.13 | 0.27 | 0.18 | 0.18 | 0.13 | 0.33 | 0.14 | 0.15 | 0.09 | 0.15 | 0.15 | 0.16 | 0.12 | 0.54 |
| FeO ^t | 10.1 | 6.37 | 3.10 | 11.1 | 11.73 | 7.45 | 3.90 | 14.2 | 9.9 | 6.27 | 3.12 | 13.4 | 8.81 | 5.57 | 2.75 | 14.0 |
| K ₂ O | 0.07 | 0.88 | 19.1 | - | 0.09 | 1.03 | 19.0 | - | 0.08 | 0.96 | 19.3 | - | 0.08 | 0.96 | 19.8 | - |
| CaO | 0.39 | 0.10 | - | 0.36 | 0.37 | 0.10 | - | 0.31 | 0.36 | 0.10 | - | 0.27 | 0.38 | 0.11 | - | 0.20 |
| NiO | 100.4 | 100.8 | 100.5 | 100.3 | 100.4 | 100.8 | 99.9 | 99.9 | 99.8 | 99.4 | 99.3 | 99.8 | 99.9 | 100.5 | 100.1 | 99.7 |
| Σ | 89.6 | 90.2 | 90.2 | 76.4 | 87.9 | 88.4 | 88.2 | 70.0 | 89.7 | 90.1 | 91.0 | 74.0 | 90.9 | 91.5 | 91.8 | 67.8 |
| mg# | 15.2 | 15.2 | 15.2 | 15.2 | 15.2 | 15.2 | 15.2 | 15.2 | 15.2 | 15.2 | 15.2 | 15.2 | 15.2 | 15.2 | 15.2 | 15.2 |
| cr# | 15.2 | 15.2 | 15.2 | 15.2 | 15.2 | 15.2 | 15.2 | 15.2 | 15.2 | 15.2 | 15.2 | 15.2 | 15.2 | 15.2 | 15.2 | 15.2 |

Whole Rock Trace Elements

| Sample | LP08-03 | LP08-14 | LPE-028 | LPE-029 | LPE-042 | LPE-046 | LPE-048 | LPE-061 | LPE-062 | TAL-001 | TAL-014 | TAL-047 | TAL-052 | TAL-056 |
|--------|---------|---------|---------|---------|---------|---------|---------|---------|---------|---------|---------|---------|---------|---------|
| Rb | 0.395 | 0.866 | 1.735 | 0.415 | 0.169 | 0.308 | 0.882 | 0.453 | 0.374 | 0.316 | 0.267 | 0.274 | 0.426 | 0.171 |
| Sr | 9.300 | 27.771 | 25.741 | 11.618 | 8.507 | 8.382 | 22.148 | 15.106 | 19.345 | 10.083 | 7.151 | 3.775 | 4.601 | 6.157 |
| Y | 2.110 | 4.178 | 2.600 | 2.059 | 2.662 | 2.471 | 2.299 | 2.557 | 3.771 | 2.236 | 1.808 | 0.905 | 1.247 | 1.357 |
| Zr | 3.904 | 21.054 | 6.145 | 5.041 | 5.203 | 4.747 | 7.379 | 6.310 | 8.652 | 4.518 | 10.534 | 2.215 | 4.682 | 2.922 |
| Nb | 0.403 | 0.485 | 0.465 | 0.686 | 0.458 | 0.514 | 0.804 | 0.497 | 0.620 | 0.198 | 0.482 | 0.229 | 0.519 | 0.120 |
| Cs | 0.042 | 0.064 | 0.046 | 0.043 | 0.019 | 0.027 | 0.055 | 0.029 | 0.015 | 0.012 | 0.011 | 0.015 | 0.033 | 0.021 |
| Ba | 3.956 | 12.991 | 16.865 | 4.361 | 3.555 | 7.125 | 7.767 | 6.907 | 8.064 | 7.267 | 4.458 | 3.611 | 4.856 | 1.972 |
| La | 0.220 | 1.162 | 1.287 | 0.468 | 0.382 | 0.474 | 0.686 | 0.504 | 1.254 | 0.348 | 0.658 | 0.161 | 0.315 | 0.142 |
| Ce | 0.452 | 2.531 | 3.644 | 1.127 | 0.988 | 0.824 | 1.571 | 1.005 | 2.995 | 0.806 | 2.133 | 0.318 | 0.648 | 0.374 |
| Pr | 0.082 | 0.382 | 0.546 | 0.150 | 0.150 | 0.139 | 0.222 | 0.169 | 0.414 | 0.117 | 0.404 | 0.048 | 0.090 | 0.060 |
| Nd | 0.472 | 1.871 | 2.602 | 0.771 | 0.831 | 0.710 | 1.119 | 0.854 | 2.003 | 0.642 | 2.689 | 0.268 | 0.454 | 0.350 |
| Sm | 0.170 | 0.518 | 0.563 | 0.221 | 0.268 | 0.225 | 0.321 | 0.261 | 0.500 | 0.206 | 0.705 | 0.094 | 0.132 | 0.123 |
| Eu | 0.072 | 0.127 | 0.209 | 0.080 | 0.102 | 0.088 | 0.107 | 0.098 | 0.189 | 0.082 | 0.100 | 0.038 | 0.048 | 0.050 |
| Gd | 0.281 | 0.651 | 0.555 | 0.298 | 0.390 | 0.347 | 0.400 | 0.370 | 0.614 | 0.322 | 0.464 | 0.139 | 0.183 | 0.186 |
| Tb | 0.052 | 0.110 | 0.084 | 0.053 | 0.068 | 0.062 | 0.067 | 0.066 | 0.103 | 0.057 | 0.060 | 0.024 | 0.032 | 0.034 |
| Dy | 0.385 | 0.783 | 0.541 | 0.383 | 0.496 | 0.456 | 0.469 | 0.482 | 0.720 | 0.425 | 0.360 | 0.173 | 0.235 | 0.254 |
| Ho | 0.083 | 0.163 | 0.102 | 0.081 | 0.105 | 0.098 | 0.096 | 0.099 | 0.146 | 0.091 | 0.070 | 0.037 | 0.050 | 0.056 |
| Er | 0.248 | 0.474 | 0.288 | 0.244 | 0.313 | 0.293 | 0.277 | 0.296 | 0.426 | 0.272 | 0.213 | 0.108 | 0.150 | 0.168 |
| Tm | 0.038 | 0.069 | 0.041 | 0.036 | 0.046 | 0.043 | 0.041 | 0.044 | 0.061 | 0.040 | 0.031 | 0.016 | 0.023 | 0.025 |
| Yb | 0.240 | 0.435 | 0.251 | 0.240 | 0.306 | 0.288 | 0.266 | 0.283 | 0.392 | 0.264 | 0.210 | 0.108 | 0.159 | 0.172 |
| Lu | 0.041 | 0.072 | 0.042 | 0.041 | 0.051 | 0.049 | 0.043 | 0.047 | 0.067 | 0.046 | 0.036 | 0.019 | 0.028 | 0.030 |
| Hf | 0.103 | 0.375 | 0.151 | 0.122 | 0.143 | 0.130 | 0.193 | 0.151 | 0.216 | 0.126 | 0.310 | 0.062 | 0.129 | 0.084 |
| Ta | 0.003 | 0.022 | 0.018 | 0.005 | 0.004 | 0.003 | 0.024 | 0.004 | 0.021 | 0.006 | 0.005 | 0.006 | 0.021 | 0.005 |
| Pb | 0.043 | 0.871 | 0.326 | 0.255 | 0.234 | 0.042 | 0.366 | 0.274 | 5.556 | 0.993 | 0.185 | 0.156 | 0.248 | 0.257 |
| Th | 0.049 | 0.256 | 0.092 | 0.105 | 0.190 | 0.025 | 0.380 | 0.130 | 0.152 | 0.057 | 0.094 | 0.096 | 0.175 | 0.046 |
| U | 0.015 | 0.072 | 0.014 | 0.025 | 0.049 | 0.011 | 0.075 | 0.036 | 0.040 | 0.019 | 0.027 | 0.038 | 0.034 | 0.058 |

| Sample | TAL-077 | TAL-084 | TAL-094 | TAL-099 | TAL-102 | TAL-106 | TAL-110 | TAL-112 | TAL-125 | TAL-127 | TAL-131 | TAL-134 | TAL-143 | TAL-149 |
|--------|---------|---------|---------|---------|---------|---------|---------|---------|---------|---------|---------|---------|---------|---------|
| Rb | 0.343 | 0.274 | 0.268 | 0.488 | 0.141 | 0.632 | 0.134 | 0.151 | 0.296 | 0.248 | 0.432 | 0.141 | 0.117 | 0.612 |
| Sr | 2.658 | 3.125 | 3.509 | 5.545 | 3.122 | 5.968 | 3.136 | 6.771 | 5.147 | 8.025 | 6.020 | 6.524 | 4.313 | 4.564 |
| Y | 0.654 | 0.800 | 0.971 | 1.369 | 0.406 | 1.687 | 0.786 | 2.288 | 1.250 | 1.780 | 1.234 | 2.109 | 0.759 | 1.010 |
| Zr | 2.323 | 1.806 | 1.878 | 2.804 | 0.834 | 2.811 | 1.269 | 4.509 | 4.022 | 3.399 | 1.700 | 4.446 | 1.319 | 1.874 |
| Nb | 0.164 | 0.130 | 0.195 | 0.140 | 0.180 | 0.372 | 0.105 | 0.493 | 0.324 | 0.192 | 0.242 | 0.589 | 0.095 | 0.238 |
| Cs | 0.024 | 0.013 | 0.015 | 0.027 | 0.013 | 0.037 | 0.011 | 0.024 | 0.031 | 0.012 | 0.027 | 0.020 | 0.010 | 0.033 |
| Ba | 2.243 | 2.081 | 2.003 | 2.814 | 2.476 | 4.607 | 2.220 | 2.045 | 2.412 | 3.469 | 4.522 | 1.495 | 3.943 | 4.295 |
| La | 0.153 | 0.115 | 0.163 | 0.133 | 0.181 | 0.402 | 0.161 | 0.228 | 0.193 | 0.168 | 0.167 | 0.174 | 0.078 | 0.250 |
| Ce | 0.258 | 0.241 | 0.330 | 0.363 | 0.416 | 0.938 | 0.312 | 0.716 | 0.468 | 0.438 | 0.360 | 0.637 | 0.185 | 0.281 |
| Pr | 0.036 | 0.039 | 0.049 | 0.062 | 0.044 | 0.117 | 0.039 | 0.106 | 0.076 | 0.071 | 0.046 | 0.101 | 0.030 | 0.049 |
| Nd | 0.176 | 0.215 | 0.251 | 0.348 | 0.174 | 0.551 | 0.197 | 0.625 | 0.432 | 0.411 | 0.244 | 0.602 | 0.173 | 0.264 |
| Sm | 0.057 | 0.071 | 0.081 | 0.117 | 0.038 | 0.157 | 0.063 | 0.219 | 0.139 | 0.153 | 0.085 | 0.210 | 0.065 | 0.080 |
| Eu | 0.024 | 0.030 | 0.033 | 0.049 | 0.011 | 0.061 | 0.027 | 0.083 | 0.055 | 0.064 | 0.037 | 0.079 | 0.026 | 0.033 |
| Gd | 0.092 | 0.109 | 0.129 | 0.189 | 0.046 | 0.240 | 0.102 | 0.331 | 0.200 | 0.244 | 0.149 | 0.313 | 0.104 | 0.128 |
| Tb | 0.016 | 0.020 | 0.024 | 0.034 | 0.008 | 0.043 | 0.019 | 0.060 | 0.034 | 0.045 | 0.028 | 0.054 | 0.019 | 0.024 |
| Dy | 0.121 | 0.147 | 0.183 | 0.249 | 0.065 | 0.322 | 0.148 | 0.450 | 0.240 | 0.333 | 0.222 | 0.397 | 0.143 | 0.181 |
| Ho | 0.025 | 0.033 | 0.040 | 0.054 | 0.014 | 0.070 | 0.032 | 0.096 | 0.048 | 0.074 | 0.051 | 0.087 | 0.031 | 0.040 |
| Er | 0.077 | 0.100 | 0.122 | 0.161 | 0.049 | 0.206 | 0.099 | 0.285 | 0.146 | 0.217 | 0.152 | 0.256 | 0.091 | 0.122 |
| Tm | 0.012 | 0.015 | 0.020 | 0.024 | 0.009 | 0.031 | 0.016 | 0.044 | 0.022 | 0.032 | 0.024 | 0.039 | 0.014 | 0.019 |
| Yb | 0.080 | 0.104 | 0.132 | 0.156 | 0.064 | 0.205 | 0.105 | 0.279 | 0.140 | 0.221 | 0.166 | 0.252 | 0.092 | 0.127 |
| Lu | 0.014 | 0.019 | 0.024 | 0.028 | 0.012 | 0.035 | 0.018 | 0.047 | 0.026 | 0.037 | 0.029 | 0.044 | 0.016 | 0.022 |
| Hf | 0.061 | 0.048 | 0.056 | 0.072 | 0.017 | 0.087 | 0.036 | 0.142 | 0.101 | 0.094 | 0.053 | 0.118 | 0.041 | 0.049 |
| Ta | 0.004 | 0.003 | 0.005 | 0.004 | 0.006 | 0.014 | 0.002 | 0.003 | 0.004 | 0.006 | 0.007 | 0.002 | 0.002 | 0.005 |
| Pb | 0.078 | 0.166 | 0.279 | 0.256 | 0.368 | 0.367 | 0.236 | 0.285 | 0.047 | 0.158 | 0.178 | 0.200 | 0.113 | 0.080 |
| Th | 0.081 | 0.050 | 0.038 | 0.031 | 0.097 | 0.259 | 0.108 | 0.177 | 0.013 | 0.054 | 0.043 | 0.055 | 0.020 | 0.016 |
| U | 0.030 | 0.022 | 0.013 | 0.041 | 0.052 | 0.089 | 0.044 | 0.048 | 0.012 | 0.030 | 0.022 | 0.023 | 0.031 | 0.013 |

Clinopyroxene Trace Elements

| Sample | LP08-02 | LP08-12 | LP08-14 | LPE-028 | LPE-029 | LPE-042 | LPE-048 | LPE-061 | LPE-062 | TAL-001 | TAL-014 | TAL-047 | TAL-056 | TAL-084 |
|--------|---------|---------|---------|---------|---------|---------|---------|---------|---------|---------|---------|---------|---------|---------|
| Li | 4.663 | 35.84 | - | 25.43 | 10.67 | 21.33 | 3.092 | 10.43 | 4.100 | 5.756 | - | 6.652 | 5.037 | 4.078 |
| Rb | - | 0.143 | 0.014 | 1.999 | 0.008 | 0.017 | 0.289 | 0.214 | 0.015 | 0.011 | 0.007 | 0.021 | 0.011 | 0.632 |
| Sr | 3.323 | 103.5 | 19.42 | 147.1 | 64.70 | 41.23 | 9.175 | 6.197 | 43.17 | 7.458 | 5.167 | 56.51 | 11.45 | 53.71 |
| Y | 20.84 | 16.28 | 48.68 | 14.98 | 20.12 | 21.31 | 23.42 | 27.91 | 23.02 | 23.66 | 30.49 | 12.64 | 20.90 | 11.56 |
| Zr | 28.33 | 35.39 | 160.5 | 24.08 | 34.51 | 31.51 | 41.76 | 44.22 | 37.27 | 33.86 | 152.1 | 23.31 | 38.72 | 20.66 |
| Nb | 0.246 | 0.426 | 0.210 | 0.443 | 0.940 | 0.009 | 0.075 | 0.379 | 0.993 | 0.183 | 0.122 | 0.363 | 0.394 | 0.153 |
| La | 0.767 | 6.355 | 4.933 | 7.054 | 2.183 | 0.946 | 2.193 | 1.112 | 4.414 | 1.096 | 6.590 | 1.296 | 1.147 | 0.954 |
| Ce | 4.337 | 20.85 | 18.66 | 22.15 | 7.637 | 4.376 | 7.690 | 5.552 | 12.25 | 4.552 | 32.89 | 4.035 | 4.848 | 3.247 |
| Pr | 0.900 | 3.103 | 3.363 | 3.274 | 1.320 | 0.896 | 1.407 | 1.141 | 1.721 | 0.878 | 7.773 | 0.711 | 0.947 | 0.572 |
| Nd | 5.408 | 14.62 | 18.61 | 15.10 | 7.343 | 5.553 | 8.380 | 6.975 | 8.262 | 5.348 | 56.39 | 4.180 | 5.793 | 3.276 |
| Sm | 1.983 | 3.391 | 5.900 | 3.349 | 2.398 | 2.088 | 3.025 | 2.702 | 2.557 | 2.119 | 15.48 | 1.564 | 2.154 | 1.198 |
| Eu | 0.688 | 1.179 | 0.925 | 1.269 | 0.838 | 0.745 | 0.778 | 0.607 | 0.962 | 0.626 | 1.297 | 0.619 | 0.680 | 0.485 |
| Gd | 2.880 | 3.314 | 7.350 | 3.173 | 3.040 | 2.760 | 3.757 | 4.002 | 3.404 | 3.116 | 9.253 | 2.161 | 3.043 | 1.635 |
| Tb | 0.544 | 0.496 | 1.319 | 0.473 | 0.527 | 0.494 | 0.638 | 0.719 | 0.613 | 0.582 | 1.136 | 0.374 | 0.545 | 0.295 |
| Ti | 4034.5 | 5422.1 | 13662.1 | 3269.7 | 3267.7 | 6579.1 | 4501.4 | 5418.3 | 5048.5 | 3910.9 | 11019.6 | 2625.2 | 3442.7 | 1980.3 |
| Dy | 3.902 | 3.334 | 9.237 | 3.072 | 3.803 | 3.800 | 4.493 | 5.187 | 4.392 | 4.322 | 6.273 | 2.530 | 3.935 | 2.173 |
| Ho | 0.833 | 0.642 | 1.947 | 0.620 | 0.814 | 0.818 | 0.927 | 1.107 | 0.920 | 0.925 | 1.164 | 0.514 | 0.836 | 0.464 |
| Er | 2.405 | 1.724 | 5.327 | 1.701 | 2.267 | 2.472 | 2.551 | 3.139 | 2.576 | 2.630 | 3.053 | 1.381 | 2.333 | 1.312 |
| Tm | 0.351 | 0.248 | 0.738 | 0.240 | 0.315 | 0.401 | 0.358 | 0.437 | 0.364 | 0.382 | 0.414 | 0.187 | 0.329 | 0.184 |
| Yb | 2.213 | 1.554 | 4.373 | 1.578 | 1.973 | 2.710 | 2.202 | 2.793 | 2.288 | 2.455 | 2.428 | 1.166 | 2.031 | 1.174 |
| Lu | 0.312 | 0.221 | 0.626 | 0.226 | 0.275 | 0.441 | 0.300 | 0.386 | 0.323 | 0.335 | 0.343 | 0.160 | 0.285 | 0.166 |
| Hf | 0.904 | 1.111 | 3.285 | 0.749 | 1.066 | 1.148 | 1.442 | 1.538 | 1.265 | 1.008 | 6.437 | 0.728 | 1.024 | 0.616 |
| Ta | 0.044 | 0.077 | 0.135 | 0.050 | 0.052 | 0.002 | 0.014 | 0.025 | 0.083 | 0.059 | 0.028 | 0.038 | 0.063 | 0.017 |
| Pb | 0.010 | 0.165 | 0.303 | 0.245 | 0.067 | 0.113 | 0.128 | 0.055 | 0.399 | 0.016 | 0.029 | 0.024 | 0.017 | 0.021 |
| Th | 0.027 | 0.342 | 1.612 | 0.265 | 0.906 | 0.335 | 1.449 | 0.758 | 0.837 | 0.073 | 0.989 | 0.863 | 0.276 | 0.104 |
| U | 0.012 | 0.223 | 0.362 | 0.049 | 0.296 | 0.106 | 0.380 | 0.254 | 0.195 | 0.025 | 0.095 | 0.350 | 0.112 | 0.077 |

| Sample | TAL-127 | TAL-134 | 3H-2 | 3H-4 | 3H-8 | 5H-2 | 5H-3 | 5H-7 | 5H-9 | 5H-10 | 5H-13 |
|--------|---------|---------|-------|--------|--------|--------|-------|--------|--------|---------|--------|
| Li | 5.856 | 14.67 | 0.992 | - | 1.502 | 1.269 | 1.270 | 1.209 | 1.156 | 371.3 | 1.004 |
| Rb | 0.033 | 0.026 | 0.043 | 0.024 | 0.032 | 0.247 | 0.019 | 0.054 | 0.157 | 0.263 | 0.018 |
| Sr | 57.28 | 67.58 | 50.41 | 60.00 | 60.75 | 75.47 | 25.93 | 41.23 | 19.72 | 496.3 | 158.2 |
| Y | 15.03 | 20.43 | 5.260 | 19.96 | 16.80 | 16.73 | 7.460 | 10.81 | 8.413 | 144.0 | 8.650 |
| Zr | 26.35 | 32.62 | 15.25 | 26.70 | 25.89 | 22.97 | 4.596 | 7.848 | 9.487 | 267.5 | 52.41 |
| Nb | 0.213 | 0.124 | 0.291 | 0.102 | 0.279 | 0.648 | 0.311 | 0.063 | 0.079 | 10.25 | 2.698 |
| La | 1.122 | 1.830 | 1.357 | 0.319 | 1.212 | 1.349 | 0.879 | 0.331 | 0.141 | 26.96 | 8.088 |
| Ce | 3.611 | 6.785 | 3.720 | 2.154 | 4.320 | 3.675 | 2.247 | 1.269 | 0.688 | 76.74 | 18.50 |
| Pr | 0.631 | 1.237 | 0.579 | 0.545 | 0.790 | 0.577 | 0.293 | 0.244 | 0.176 | 12.15 | 2.409 |
| Nd | 3.701 | 7.127 | 3.127 | 3.818 | 4.680 | 3.308 | 1.284 | 1.515 | 1.356 | 67.83 | 10.62 |
| Sm | 1.423 | 2.437 | 1.005 | 1.741 | 1.722 | 1.335 | 0.357 | 0.655 | 0.777 | 21.26 | 2.348 |
| Eu | 0.549 | 0.855 | 0.362 | 0.730 | 0.675 | 0.571 | 0.142 | 0.292 | 0.312 | 8.697 | 0.752 |
| Gd | 2.063 | 3.192 | 1.202 | 2.726 | 2.447 | 2.163 | 0.646 | 1.090 | 1.296 | 23.74 | 2.271 |
| Tb | 0.383 | 0.546 | 0.190 | 0.509 | 0.436 | 0.413 | 0.139 | 0.222 | 0.237 | 4.463 | 0.320 |
| Ti | 2640.4 | 3560.3 | 721.9 | 3788.3 | 3841.5 | 3066.6 | 954.5 | 1707.0 | 3106.4 | 24223.7 | 1990.7 |
| Dy | 2.804 | 3.910 | 1.163 | 3.788 | 3.112 | 3.042 | 1.204 | 1.791 | 1.660 | 29.02 | 1.941 |
| Ho | 0.597 | 0.826 | 0.223 | 0.805 | 0.666 | 0.672 | 0.285 | 0.421 | 0.342 | 5.945 | 0.347 |
| Er | 1.726 | 2.302 | 0.559 | 2.348 | 1.915 | 1.927 | 0.896 | 1.291 | 0.931 | 15.53 | 0.877 |
| Tm | 0.249 | 0.331 | 0.074 | 0.338 | 0.274 | 0.281 | 0.141 | 0.201 | 0.129 | 2.150 | 0.116 |
| Yb | 1.624 | 2.074 | 0.448 | 2.207 | 1.792 | 1.810 | 0.950 | 1.365 | 0.804 | 13.965 | 0.689 |
| Lu | 0.227 | 0.282 | 0.065 | 0.314 | 0.253 | 0.265 | 0.143 | 0.204 | 0.117 | 2.003 | 0.097 |
| Hf | 0.798 | 1.086 | 0.531 | 0.982 | 0.853 | 0.798 | 0.105 | 0.182 | 0.495 | 6.892 | 1.339 |
| Ta | 0.049 | 0.021 | 0.035 | 0.006 | 0.037 | 0.037 | 0.032 | 0.007 | 0.004 | 1.072 | 0.479 |
| Pb | 0.012 | 0.067 | 0.043 | 0.034 | 0.046 | 0.043 | 0.045 | 0.021 | 0.024 | 0.270 | 0.080 |
| Th | 0.110 | 0.190 | 0.039 | 0.013 | 0.031 | 0.060 | 0.033 | 0.006 | 0.006 | 1.162 | 0.668 |
| U | 0.045 | 0.059 | 0.013 | 0.005 | 0.012 | 0.016 | 0.016 | 0.010 | 0.012 | 0.359 | 0.171 |

Convergent–destructive–margins–where two plates converge forming either subduction or continental collision zones – are one of the main tectonic scenarios along plate boundaries. Despite the enormous success of the plate tectonic theory in modern Earth sciences, essential questions still remain open concerning the evolution of continents in convergent settings and their role in the dynamics of the Earth's lithospheric mantle. The subcontinental lithospheric mantle (SCLM) is the part of the lithosphere below the crust up to asthenospheric depths. Small samples of this region – known as mantle xenoliths – can be entrained by volcanic rocks and provide direct sample of the SCLM from different tectonic settings such as intracontinental rifts and – less commonly – convergent settings. Thus, mantle xenoliths afford a unique opportunity to investigate petrology, structure and chemical composition of the SCLM.

The originality of this work relies on the multidisciplinary study of two mantle xenolith occurrences in convergent settings: the Sangilen Plateau of Tuva in Siberia and the SE Iberian Volcanic Province in South East Spain. The Tuva and SE Iberian Volcanic Province xenoliths give insight into ancient Ordovician and Neogene SCLM in different convergent geodynamic settings, respectively.

In this thesis I studied mantle xenoliths hosted in alkaline rocks produced during the latest stages of orogenic convergence, thereby providing a snapshot of the deformation, melting and metasomatism in these settings. I combined detailed petrological and petrostructural characterization of mantle xenoliths with geochemical characterization including bulk and mineral major, trace element, Sr-Nd-Pb radiogenic isotope and in situ Re-Os isotope analyses. These data are combined and mined to unveil the thermal, petrostructural and seismic characteristic of the SCLM beneath these regions, as well as used to identify the age and inheritance of melting events, melt-rock reaction and metasomatic processes involved in the compositional modification of the SCLM in convergent settings.



CSIC

CONSEJO SUPERIOR DE INVESTIGACIONES CIENTÍFICAS



UGR

Universidad
de **Granada**